Titel der Arbeit:

Many-body theory for the lattice thermal conductivity of crystalline thermoelectrics

Dissertation
zur Erlangung des akademischen Grades

doctor rerum naturalium

(Dr. rer. nat.)

im Fach Physik, Spezialisierung:

Theoretische Festkörperphysik

eingereicht an der

Mathematisch-Naturwissenschaftlichen Fakultät der Humboldt-Universität zu Berlin

von

M. Sc. Axel Felix Hübner, geb. am 13.11.1995 in Berlin

Präsidentin der Humboldt-Universität zu Berlin
Prof. Dr. Julia von Blumenthal

Dekanin der Mathematisch-Naturwissenschaftlichen Fakultät
Prof. Dr. Caren Tischendorf

GutachterInnen: 1.
2.
3.

Tag der mündlichen Prüfung:

AXEL HÜBNER

MANY-BODY THEORY FOR THE LATTICE THERMAL CONDUCTIVITY OF CRYSTALLINE THERMOELECTRICS

MANY-BODY THEORY FOR THE LATTICE THERMAL CONDUCTIVITY OF CRYSTALLINE THERMOELECTRICS

AXEL HÜBNER

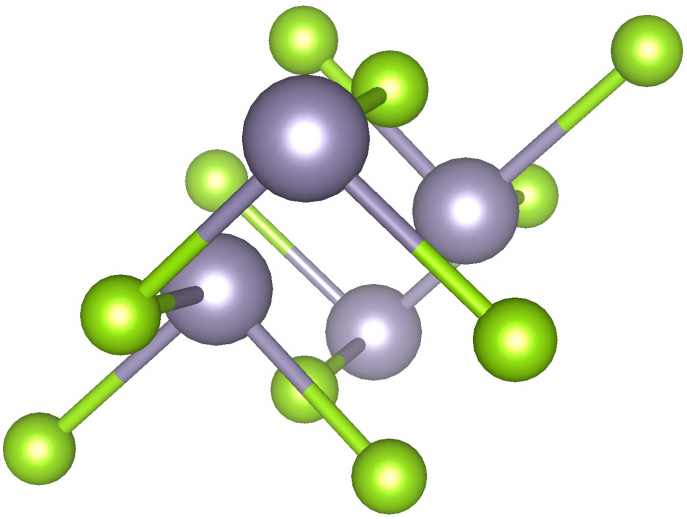

December 2022

LOCATION:
Berlin

TIME FRAME:
December 2022

We have a shared vision of change - creating a world that is fit for generations to come.

— Extinction Rebellion

To my mother, Yvonne Hübner.

ABSTRACT

Thermoelectrics (TE) are materials that can be used to generate electricity from waste heat. As a large portion of our energy resources is wasted as heat (250), TE can contribute to a more sustainable use of our energy resources, which is more urgent than ever. A key quantity to the efficiency, and therefore the applicability, of TE is the lattice thermal conductivity. In this work, I prove the invariance of the lattice thermal conductivity in the context of linear-response theory (LR). This invariance enables me to derive novel formulas for a correction to the widely used Boltzmann-transport equation (BTE) for lattice thermal transport in crystalline solids using LR. It turned out that these derivations cannot be performed by a human by hand, using the formalism I chose. To perform the necessary symbolic manipulations, I programmed a computer algebra system (CAS), that implements LR, starting from expectation values, over Feynman diagrams to mathematical formulas. The number of resulting terms turned out to be too large for an analysis of all limiting cases. Consequently, I aimed at evaluating *all* terms, with as few approximations as possible, to generate a simple, numerical result. To do so, I developed a software package to evaluate the formulas numerically without further approximation and applied it to long-serving as well as promising new TE, namely PbTe, Bi_2Te_3, SnSe, and B_4C. Additionally I investigated MgO and KF. The result can be summed up as follows:

The correction to the BTE for the lattice thermal conductivity has almost no influence in the investigated materials at any simulated temperature.

My investigation suggests that the BTE can be used for a wide range of materials, including the most anharmonic ones. Consequently, this work is in agreement with the literature, that the most anharmonic materials are exactly those with the lowest lattice thermal conductivity (37). It suggests that future theoretic work on lattice thermal conductivity should focus to find the correct phonon-propagator of strongly anharmonic systems.

ZUSAMMENFASSUNG

Thermoelektrika (TE) sind Materialien die Elektrizität aus Abwärme gewinnen können. Da ein großer Teil der weltweit generierten Energie als Abwärme verloren geht (250), können TE zu einer nachhaltigeren Nutzung unserer Energieressourcen beitragen. Eine wichtige Kenngröße für die Effizienz, und damit die Anwendbarkeit, von TE ist ihre Gitterwärmeleitfähigkeit. In meiner Doktorarbeit habe ich die Invarianz der Gitterwärmeleitfähigkeit im Kontext der Linear-Response Theorie (LR) bewiesen. Diese Invarianz ermöglichte es mir, eine Korrektur der weitverbreiteten Boltzmann-Transport Gleichung (BTE) für die Gitterwärmeleitfähigkeit in kristallinen Materialien mittels LR herzuleiten. Diese Korrektur ist wichtig um zu beurteilen, wie genau die BTE die Wärmeleitfähigkeit eines Kristalls vorhersagen kann. Es stellte sich heraus, dass die Herleitung im von mir gewählten Formalismus nicht sinnvoll durch einen Menschen per Hand durchgeführt werden kann. Um die dafür notwendigen symbolischen Umformungen durchzuführen, habe ich ein Computer-Algebra System (CAS) entwickelt, dass die LR implementiert, angefangen mit Erwartungswerten, über Feynman-Diagramme bis hin zu mathematischen Termen. Die Anzahl an Beiträgen zum finalen Resultat stellte sich als zu groß heraus um Grenzfälle zu analysieren oder prüfbare Approximationen herzuleiten. Aus diesem Grund habe ich *alle* Beiträge mit so wenigen Approximationen wie möglich ausgewertet, um ein einfaches numerisches Resultat zu erhalten. Dafür habe ich eine Software entwickelt, um diese Terme numerisch auszuwerten. Damit habe ich meine Korrektur für altbekannte wie auch vielversprechende TE ausgewertet, nämlich PbTe, Bi_2Te_3, SnSe und B_4C. Zusätzlich habe ich MgO und KF untersucht. Das Resultat lässt sich wie folgt zusammenfassen:

Die Korrektur zur BTE für die Gitterwärmeleitfähigkeit hat in keinem der untersuchten Materialien und bei keiner der simulierten Temperaturen einen nennenswerten Einfluss.

Meine Untersuchung legt nahe, dass die BTE für eine große Bandbreite an Materialien sicher angewandt werden kann, auch besonders stark Anharmonische. Folglich ist diese Arbeit in Übereinstimmung mit der Literatur, dass die am stärksten anharmonischen Materialien genau die mit der niedrigsten Wärmeleitfähigkeit sind (37). Es scheint daher sinnvoll, dass sich zukünftige Forschung weniger auf die Herleitung solcher Korrekturen zur BTE als vielmehr auf die korrekte Berechnung des Phononpropagators in stark anharmonischen Materialien konzentrieren sollte.

ACKNOWLEDGMENTS

I want to give special thanks to the people helping me with discussions and advice to accomplish the goals of this thesis. These include my supervisor, Prof. Dr. Claudia Draxl, my tutor, Dr. Santiago Rigamonti, PD Dr. Pasquale Pavone, Sebastian Tillack, Dr. Keith Gilmore, Dr. Nakib Haider Protik and Benedikt Moritz Maurer.

CONTENTS

ACRONYMS

ASE	Atomic simulation environment
beyBol	Beyond Boltzmann package
BFGS	Broyden-Fletcher-Goldfarb-Shanno algorithm
BO	Born-Oppenheimer (approximation)
BTE	Boltzmann transport equation
BZ	Brillouin zone
CAS	Computer algebra system
DFT	Density functional theory
DPA	Diagonal propagator approximation
EMT	Effective medium theory
FCC	Face centered cubic
FFT	Fast Fourier transform
GK	(the) Green-Kubo equation
IFC	Interatomic force constant
LDA	Local density approximation (to DFT)
LO	Longitudinal optical
LR	Linear response theory
MD	Molecular dynamics
MPI	Message processing interface
OOP	Object oriented programming
OPI	One-particle irreducible
PBEsol	Perdew-Burke-Ernzerhof functional, parametrized for solids, as approximation to DFT
RTA	Relaxation time approximation (to the BTE)
SCPT	Self-consistent phonon theory
SOTA	State-of-the-art
TDEP	Temperature dependent effective potential (method)

TE Thermoelectric (material)

TO Transverse optical (phonon mode)

Part I

BASICS

1 INTRODUCTION

To generate electricity in a reliable, safe, and sustainable fashion is a need for our society. One possibility to do this is the conversion of waste heat using the thermoelectric effect. Waste heat is created by engines in cars and airplanes, powerhouse turbines, various industrial processes such as smelting, especially in the chemical and construction industry and even in computing centres. Hence, we lose a significant amount of our energy resources (250) and thermoelectrics have an enormous potential to make our use of energy resources fit for the future.

When heat flows through a thermoelectric material, a voltage is generated due to the diffusion of charge carriers (62, 257, 260, 297). This effect can be used to generate electricity. The efficiency of the conversion is good, if the thermoelectric *figure of merit*

$$ZT = \frac{\sigma S^2}{\kappa} T \tag{1.1}$$

is large. S is the Seebeck coefficient, κ the thermal conductivity, σ the electrical conductivity, and T the temperature. Nowadays, most thermoelectric devices provide a figure of merit of approximately 1 (201, 257). This is too inefficient to be cost-effective in many applications (241). Would the figure of merit be 3 or higher, these devices could be used for many more applications (167, 275). The most promising candidates to reach such a value are semiconductors, with a low thermal but good electrical conductivity (250). The task is to find semiconductors that match these criteria. At this point it is important to understand, that the thermal conductivity κ is (approximately) made up of two components: an electronic one κ_e, caused by the diffusion of charge carriers, and a lattice part κ_l, caused by the lattice vibrations, the phonons:

$$\kappa = \kappa_e + \kappa_l. \tag{1.2}$$

The law of Wiedemann-Franz (148, 260, 281) states, that the electronic contribution to the thermal conductivity is proportional to the electrical conductivity σ, as the diffusing charge carriers also carry heat. This is one reason why it is not easy to optimize the figure of merit of a material, as a good electrical conductor is also a good thermal conductor. Despite this problem, one may find the best thermoelectrics by searching for materials with a low *lattice* thermal conductivity. This approach already led to groundbreaking findings (30, 167, 301). The other important option would be to maximize σS^2 (65, 165, 296), which is beyond the scope of this thesis.

The lattice thermal conductivity of a material is low, if the phonons are strongly scattered (95). In a pure crystal (without vacancies or disorder), there are two processes responsible for this: the scattering of phonons with phonons (anharmonicity) and electrons (electron-phonon interaction) (88). It is known that the predominant scattering mechanism in most crystalline systems (and especially in semiconductors) is the anharmonicity (303), and so, strongly anharmonic systems are especially promising for thermoelectric applications. An example is SnSe with a figure of merit of 2.6 at 930K (301). To suggest which other materials have a low lattice thermal conductivity, high-throughput calculations might be incredibly valuable (283). For these high-throughput calculations it is important to have fast and accurate theoretical methods (186).

State-of-the-art methods to calculate the lattice thermal conductivity are the classical Green-Kubo (GK) equation (147), non-equilibrium molecular dynamics (194), and the Boltzmann transport equation (BTE) (95). The BTE is the most often used method, as it is, compared to the other two approaches, numerically by far the cheapest. Traditionally, the assumption of the BTE is, that the phonons behave as in a gas, in which they do not scatter "too often" and behave almost like classical particles (6). This quasiparticle picture (204) enables to treat phonon modes (almost) independently and assign them a defined long lifetime, which leads to the relaxation time approximation (RTA) (261). With lifetime and dispersion (138) of the phonons, it is possible to calculate the lattice thermal conductivity of a material (95). The BTE gives very good results for many materials (32, 43, 150, 267, 302). However, the interpretation of phonons as quasiparticles becomes questionable, especially in bad thermal conductors (220). A more modern BTE exists (31, 246) that is independent of the quasiparticle picture. However, even this BTE only constitutes the 1^{st} order approximation of perturbation theory to Kubo's formula for thermal conduction (147, 161), while higher-order corrections are neglected. Such higher-order corrections are important in other cases, such as the scattering of electrons by impurities (166). The accuracy of approximating κ_l by the BTE can therefore only be assessed if a second-order correction is evaluated (25). The size of this correction hints when other methods, such as GK, are inevitable to calculate the lattice thermal conductivity. Especially in bad thermal conductors it remained unclear whether the BTE can be trusted (32).

First expressions for higher-order corrections have been derived already back in the 1960's (102, 253), but with approximations that especially limit the applicability in crystals with low lattice thermal conductivity. First steps to implement these corrections have been taken (31, 256). However, a full second-order approximation to Kubo's formula was not known before this work. Furthermore, to the best of my knowledge, known higher-order corrections have not been evaluated numerically, especially not for interesting thermoelectrics.

Many materials are used and designed for thermoelectric applications. These include materials with rather simple unit cells, such as PbTe, Bi_2Te_3 or the novel SnSe as well as more complex ones, such as chalcogenides (45), clathrates (18, 63, 104, 157, 200, 275), skutterudites (199, 242, 276), nanostructured materials (41, 116, 224, 278, 279, 295) and many others (27, 130, 160, 181, 277). The introduction of nanoparticles was studied (296), alloying (14, 82) and the application of strain (192, 293). Materials of lower dimension have been studied (153, 300), glasses and amorphous systems (5, 77), and the effect of polycrystallization (191).

In my PhD thesis, I derived the exact second-order approximation to the lattice thermal conductivity for an anharmonic crystal, based on the Born-Oppenheimer approximation (BO). I did *not* use any further approximations. To perform and test all necessary symbolic calculations in a controllable way, I programmed a computer-algebra system. I developed software to evaluate the derived formulas and applied it to six materials, including the thermoelectrics that are most used and most efficient today: PbTe, Bi_2Te_3, SnSe, and B_4C as well as MgO and KF. These materials all have a rather simple unit cell, which makes my calculations numerically tractable. However, they cover a wide range of characteristics: they are good, mediocre or bad thermal conductors, containing heavy or light atoms with large or small mass differences.

This thesis is organized as follows: In Sec. 2, the many-body formulation of quantum mechanics is recalled and necessary definitions are made. In Sec. 3, I formally derive a comprehensive theory of lattice thermal conduction. This theory is used to calculate a correction term to the BTE for an anharmonic solid using a computer algebra system, that I built (Sec. 4). In Sec. 5, the ingredients necessary to evaluate the correction to the BTE in real crystals are presented, and in Sec. 6, the numerical results for the systems of interest are shown. In Sec. 7, I conclude this thesis and lay out possible future research directions.

2 EXISTING METHODOLOGY

It must be possible to calculate the lattice thermal conductivity of a crystal from how the vibrations in the material propagate. In order to calculate this motion, the quantum many-body problem of the crystal must be solved. However, the solution for most materials is impossible nowadays. To approximate the solution, one can introduce the Born-Oppenheimer approximation (BO) to model the vibrations. In this thesis, only crystals are considered, and lattice vibrations are generally referred to as phonons. Based on BO, the many-body formulation of quantum mechanics is introduced using Green's functions, and the Matsubara technique (175) as a way to approximate solutions (Sec. 2.2). The definition of the thermal conductivity is given in Sec. 2.3. Only boson operators appear in the derivation, so the upcoming discussion is restricted to bosons. At the end of this section, competing state of the art methods are presented (Secs. 2.2.8 and 2.3.2).

If not stated differently, this thesis solely assumes anharmonic interactions between phonons. However, other effects may alter the phonon motion as well, such as dipole-dipole interactions in polar materials (3, 59, 285, 286), electron-phonon interactions (15, 88, 254, 303), structural disorder (73), impurities (95, 282), isotopes (52, 168) or boundary scattering in finite samples (10, 20, 158). The dipole-dipole interaction is introduced in Sec. 5.1.3. Different methods to model the motion of phonons and the lattice thermal conductivity are found in Refs. (54, 79, 86, 222, 234, 238, 251, 252, 256) and (31, 103, 230, 231, 253).

2.1 PHONONS AND THE ANHARMONIC CRYSTAL

To model crystalline systems, a commonly used approximation, is the Born-Oppenheimer approximation (BO) (23), that will be used throughout this thesis. In BO, the motion of the nuclei and the electrons is decoupled, by the assumption that the nuclei are much slower than the electrons, such that the electrons follow the nuclei adiabatically. Additionally, one assumes that the electrons remain in their ground-state. This approximation is valid, if the difference in energy between the first excited state of the electrons and the ground-state is large compared to the thermal excitation energy $\beta^{-1} = k_B T$ (23). This will be tacitly assumed throughout the text.

In BO, the energy of the crystal is a function of the displacements of the nuclei from their equilibrium position. This function is the Born-Oppenheimer energy surface E_B. The displacements are $u^{\alpha}_{\kappa,p}$, where the index p denotes the unit cell, κ nucleus in the unit cell and α is the displacement direction. This convention follows Ref. (88). Then E_B

may be Taylor-expanded around the equilibrium $E_B(\mathbf{u})_{\mathbf{u}=\mathbf{0}} = E_0 \equiv 0$, $\mathbf{u}$ be the vector of all displacements:

$$E_B(\mathbf{u}) \approx \sum_{l=2}^{N_B} \frac{1}{l!} \sum_{\{\kappa,\alpha,p\}} \left[\frac{\partial^l E_B}{\partial u^{\alpha_1}_{\kappa_1,p_1} ... \partial u^{\alpha_l}_{\kappa_l,p_l}} \right]_{\mathbf{u}=\mathbf{0}} u^{\alpha_1}_{\kappa_1,p_1} \times ... \times u^{\alpha_l}_{\kappa_l,p_l}. \tag{2.1}$$

The summation in curly braces $\{...\}$ means that all indices of the same type that occur in the expression are summed, so for $l = 2$, $\sum_{\{\kappa\}} \chi_{\kappa_1,\kappa_2} = \sum_{\kappa_1,\kappa_2} \chi_{\kappa_1,\kappa_2}$. The tensors

$$\Phi^{\kappa_1,p_1,...,\kappa_l,p_l}_{\alpha_1,...,\alpha_l} \equiv \left[\frac{\partial^l E_B}{\partial u^{\alpha_1}_{\kappa_1,p_1} ... \partial u^{\alpha_l}_{\kappa_l,p_l}} \right]_{\mathbf{u}=\mathbf{0}} \tag{2.2}$$

are the interatomic force constants. Because the energy of the crystal is invariant under rotations and translations, and as the crystal possesses a certain number of symmetry operations, the interatomic force constants fulfill a number of interrelations (23, 71), that are summed up in Appendix B.2.

If one truncates the Taylor expansion of E_B at $N_B = 2$, one gets the harmonic approximation. A harmonic crystal possesses vibrational eigenexcitations (more precisely collective modes (205)), called phonons. The motion of the nuclei can then be decomposed into eigenstates of the dynamical matrix

$$D_{\kappa_1,\alpha_1,\kappa_2,\alpha_2}(\mathbf{q}) = (M_{\kappa_1} M_{\kappa_2})^{-1/2} \sum_p \Phi^{\kappa_1,0,\kappa_2,p}_{\alpha_1,\alpha_2} e^{i\mathbf{q}\cdot(\mathbf{R}_p + \boldsymbol{\tau}_{\kappa_2} - \boldsymbol{\tau}_{\kappa_1})}, \tag{2.3}$$

where $\mathbf{q}$ denotes a crystal momentum, M_κ the mass of nucleus κ, $\mathbf{R}_p$ is the location of the p^{th} unit cell, and $\boldsymbol{\tau}_\kappa$ the position of nucleus κ in the unit cell. The dynamical matrix fulfills the well-known eigenvalue equation (50)

$$\sum_{\kappa_1,\alpha_1} D_{\kappa_1,\alpha_1,\kappa_2,\alpha_2}(\mathbf{q}) e^{\alpha_2}_{\kappa_2,\nu}(\mathbf{q}) = \omega^2_{\mathbf{q},\nu} e^{\alpha_1}_{\kappa_1,\nu}(\mathbf{q}), \tag{2.4}$$

where ν is a mode index, $e^{\alpha_1}_{\kappa_1,\nu}(\mathbf{q})$ is the phonon polarization, and $\omega_{\mathbf{q},\nu}$ is the phonon frequency. Already Born and Debye (214) argued, that a harmonic crystal does not have a well-defined thermal conductivity, which is why higher terms of the expansion in Eq. (2.1) must be considered. These higher, anharmonic terms lead to interactions between the phonons, introducing decay. This is similar to other transport problems, where the description using independent eigenexcitations is insufficient (138, 166).

To calculate the lattice thermal conductivity of a crystalline system, I model an interacting (bosonic) phonon system. At a finite temperature, the states of the system can be described by a grandcanonical ensemble, defined by a density matrix $\hat{\rho} = \exp(-\beta \hat{H})$ (124) (the phonons chemical potential is zero), where $\hat{H}$ is the system Hamiltonian, com-

posed of the kinetic energy of the nuclei and the potential energy of the system $\widehat{V}$. This potential energy is obtained by replacing the nuclei displacement u with the nuclei displacement operator $\widehat{u}$ in Eq. (2.1)

$$\widehat{u}^{\alpha}_{\kappa,p} = \sqrt{\frac{1}{2M_\kappa N_p}} \sum_{\mathbf{q},\nu} \exp\left(i\mathbf{q}\cdot(\mathbf{R}_p + \boldsymbol{\tau}_\kappa)\right) e^{\alpha}_{\kappa,\nu}(\mathbf{q}) \sqrt{\frac{\hbar}{\omega_{\mathbf{q},\nu}}} \widehat{U}_{\mathbf{q},\nu}, \tag{2.5}$$

where N_p is the number of unit cells in the supercell used for the calculations, $\widehat{U}_{\mathbf{q},\nu} = \widehat{a}_{\mathbf{q},\nu} + \widehat{a}^{\dagger}_{-\mathbf{q},\nu}$ is the phonon displacement operator, $\widehat{a}_{\mathbf{q}\nu}$ is a phonon destruction operator and $\widehat{a}^{\dagger}_{\mathbf{q}\nu}$ a phonon creation operator. This quantization accounts for the standard procedure of interpreting the nuclei as classical particles, but the phonons as quantized collective excitations (88). With the creation and annihilation operators, one can introduce the concept of second quantization, where every operator and every state of the system can be represented by $\widehat{a}_{\mathbf{q}\nu}$ and $\widehat{a}^{\dagger}_{\mathbf{q}\nu}$. For a detailed description see Ref. (203). The operators $\widehat{a}_{\mathbf{q}\nu}$ and $\widehat{a}^{\dagger}_{\mathbf{q}\nu}$ act on an eigenstate of the harmonic Hamiltonian $\widehat{H}_0$ (i.e. $N_B = 2$) with $n_{\mathbf{q}\nu}(\geq 0)$ excitations of the mode $\mathbf{q}\nu$ as follows

$$\begin{aligned}
\widehat{a}^{\dagger}_{\mathbf{q}\nu}|..., n_{\mathbf{q}\nu}, ...\rangle &= \sqrt{n_{\mathbf{q}\nu}+1}|..., n_{\mathbf{q}\nu}+1, ...\rangle \\
\widehat{a}_{\mathbf{q}\nu}|..., n_{\mathbf{q}\nu}, ...\rangle &= \sqrt{n_{\mathbf{q}\nu}}|..., n_{\mathbf{q}\nu}-1, ...\rangle.
\end{aligned} \tag{2.6}$$

All the eigenstates of $\widehat{H}_0$ can therefore be represented by an operator product multiplied with a state without any excitations $|0, ..., 0\rangle = |\rangle$, the vacuum. The set of all these states is the Fock space $\mathcal{F}$, and $\mathcal{F}$ spans the Hilbert space, as $\widehat{H}_0$ is hermitean. As the Fock space is complete, every operator may be expanded in $\widehat{H}_0$'s eigenbasis

$$\widehat{A} = \sum_{\xi,\gamma} |\xi\rangle\langle\xi|\widehat{A}|\gamma\rangle\langle\gamma|. \tag{2.7}$$

Both $|\xi\rangle$ and $|\gamma\rangle$ can be generated from the vacuum state by repeated application of a creation operator. Hence, every operator can be written as a summed product of matrix elements times a product

$$\widehat{a}^{\dagger}_{\mathbf{q}_1\nu_1}...|\rangle\langle|\widehat{a}_{\mathbf{q}_{n+1}\nu_{n+1}}... \tag{2.8}$$

From now on, all operators will be represented in terms of annihilation and creation operators. The second quantization allows one to avoid the explicit use of states in the formalism.

2.2 GREEN'S FUNCTIONS

At the heart of the many-body formulation of quantum mechanics is the Green's function. Green's functions G are defined in this thesis as in Ref. (204). I follow Ref. (204) in this section. There are several

Green's functions that appear in the formalism. The retarded Green's function is defined as

$$G^r_{\widehat{A}\widehat{B}}(t-t') = -i\theta(t-t')\langle\left[\widehat{A}(t),\widehat{B}(t')\right]\rangle, \tag{2.9}$$

where $\widehat{A}$ and $\widehat{B}$ are some operators in the Heisenberg picture, $\theta(x)$ denotes the Heaviside function, $[,]$ is the commutator and $\langle\widehat{O}\rangle = \mathrm{Tr}(\widehat{\rho})^{-1}\mathrm{Tr}(\widehat{\rho}\widehat{O})$. The advanced and averaged Green's functions are

$$G^a_{\widehat{A}\widehat{B}}(t-t') = i\theta(t'-t)\langle\left[\widehat{A}(t),\widehat{B}(t')\right]\rangle, \tag{2.10}$$

and

$$G_{\widehat{A}\widehat{B}}(t-t') = \frac{1}{2}\left[G^r_{\widehat{A}\widehat{B}}(t-t') + G^a_{\widehat{A}\widehat{B}}(t-t')\right]. \tag{2.11}$$

For example $\widehat{A}$ and $\widehat{B}$ may be phonon displacement operators. In this case I speak of the phonon propagator.

The Fourier transforms of the Green's functions can be related to an object called the spectral density via their spectral representation [1]

$$\begin{aligned} G^r_{\widehat{A}\widehat{B}}(\mathcal{E}) &= \int_{\mathbb{R}} d\mathcal{E}' \frac{\mathcal{S}_{\widehat{A}\widehat{B}}(\mathcal{E}')}{\mathcal{E}-\mathcal{E}'+i0^+}, \\ G^a_{\widehat{A}\widehat{B}}(\mathcal{E}) &= \int_{\mathbb{R}} d\mathcal{E}' \frac{\mathcal{S}_{\widehat{A}\widehat{B}}(\mathcal{E}')}{\mathcal{E}-\mathcal{E}'-i0^+}. \end{aligned} \tag{2.12}$$

0^+ is a positive infinitesimal. The spectral density is then

$$\begin{aligned} \mathcal{S}_{\widehat{A}\widehat{B}}(t-t') &= \frac{1}{2\pi}\langle\left[\widehat{A}(t),\widehat{B}(t')\right]\rangle \\ &= \frac{1}{2\pi\hbar}\int_{\mathbb{R}} d\mathcal{E}\mathcal{S}_{\widehat{A}\widehat{B}}(\mathcal{E})\exp(-\frac{i}{\hbar}\mathcal{E}(t-t')), \end{aligned} \tag{2.13}$$

with it's spectral representation

$$\begin{aligned} \mathcal{S}_{\widehat{A}\widehat{B}}(\mathcal{E}) = \frac{\hbar}{\mathrm{Tr}(\widehat{\rho})}\sum_{\gamma,\xi}\langle\gamma|\widehat{A}|\xi\rangle\langle\xi|\widehat{B}|\gamma\rangle\exp(-\beta E_\gamma)\left[1-\exp(-\beta\mathcal{E})\right] \\ \times\delta(\mathcal{E}-(E_\xi-E_\gamma)). \end{aligned} \tag{2.14}$$

In this thesis, discrete values of energies are denoted by E (eigenenergies with Greek subscript and Matsubara energies with no or Latin subscript). Continuous energy variables are denoted by $\mathcal{E}$. The above relations can easily be inverted via:

$$\frac{1}{x\pm i0^+} = \mathcal{P}\frac{1}{x} \mp i\pi\delta(x), \tag{2.15}$$

1 In this thesis, $f(t)$ and $f(\mathcal{E})$ are Fourier transforms of each other. The argument signals the domain.

where $\mathcal{P}$ denotes the principal value, and one finds

$$\mathcal{S}_{\widehat{A}\widehat{B}}(\mathcal{E}) = \frac{i}{2\pi}\left[G^r_{\widehat{A}\widehat{B}}(\mathcal{E}) - G^a_{\widehat{A}\widehat{B}}(\mathcal{E})\right]. \tag{2.16}$$

Later in this thesis, the phonon spectral density (corresponding to the phonon propagator) is approximated numerically. I check the plausibility of the used approximation with *spectral moments* (204). One defines the operator $\widehat{\mathcal{L}} = i\hbar\frac{\partial}{\partial t}$ and acts n times on Eq. (2.13):

$$\begin{aligned}
\frac{1}{2\pi}\langle\left[\left[...\left[\left[\widehat{A}(t),\widehat{H}\right],\widehat{H}\right]...\right],\widehat{B}(t')\right]\rangle &= \\
&= \frac{1}{2\pi\hbar}\int_{\mathbb{R}} d\mathcal{E}\mathcal{S}_{\widehat{A}\widehat{B}}(\mathcal{E})\mathcal{E}^n\exp(-\frac{i}{\hbar}\mathcal{E}(t-t')), \\
\Rightarrow \quad \langle\left[\left[...\left[\left[\widehat{A},\widehat{H}\right],\widehat{H}\right]...\right],\widehat{B}\right]\rangle &= \frac{1}{\hbar}\int_{\mathbb{R}} d\mathcal{E}\mathcal{S}_{\widehat{A}\widehat{B}}(\mathcal{E})\mathcal{E}^n \\
&=: M^{(n)}_{\widehat{A}\widehat{B}},
\end{aligned} \tag{2.17}$$

with $M^{(n)}_{\widehat{A}\widehat{B}}$ being the n^{th} spectral moment. The spectral moments can then be calculated explicitly and compared to the moments of $\mathcal{S}$.

2.2.1 *Correlation functions*

There is one important relation between the correlation functions in a system, and the spectral density, that is the spectral theorem (204):

$$\langle\widehat{B}(t')\widehat{A}(t)\rangle = \hbar^{-1}\int_{\mathbb{R}} d\mathcal{E}\frac{\mathcal{S}_{\widehat{A}\widehat{B}}(\mathcal{E})}{\exp(\beta\mathcal{E})-1}\exp(-\frac{i}{\hbar}\mathcal{E}(t-t')) + d. \tag{2.18}$$

The additional constant term d vanishs for $\widehat{A} = \widehat{B} = \widehat{U}$, as is shown in the Appendix C. Thereby one has a direct relation between a correlation function and the corresponding spectral density. This will be used later to test the many-body theory against molecular dynamics (MD) simulations (see Sec. 5.2.5).

2.2.2 *Matsubara technique*

Matsubara's formalism for perturbation theory at finite temperatures is based on the idea to evaluate thermal expectation values by expanding only a single quantity in the perturbation (175). To do this, Matsubara introduced a complex time variable, $\tau = it$, which will be a real number in the following calculations. Then, he defined the time evolution in the Heisenberg picture with this time for an operator $\widehat{A}$:

$$-\hbar\frac{\partial}{\partial\tau}\widehat{A}(\tau) = \left[\widehat{A}(\tau),\widehat{H}\right] \tag{2.19}$$

The Matsubara function of two operators $\widehat{A}$ and $\widehat{B}$ is defined as

$$G^M_{\widehat{A}\widehat{B}}(\tau-\tau') = -\langle T_\tau\left(\widehat{A}(\tau)\widehat{B}(\tau')\right)\rangle, \tag{2.20}$$

where T_τ is the Matsubara time-ordering operator, that is defined for two operators by

$$T_\tau\left(\widehat{A}(\tau)\widehat{B}(\tau')\right) = \theta(\tau-\tau')\widehat{A}(\tau)\widehat{B}(\tau') + \theta(\tau'-\tau)\widehat{B}(\tau')\widehat{A}(\tau). \tag{2.21}$$

If T_τ acts on more than two operators, it orders the operators according to their time argument, putting the earliest rightmost. The Matsubara function (always denoted by an M) is only defined for $\hbar\beta > \tau, \tau' > 0$. It is periodic in $\tau - \tau'$: if $\hbar\beta > \tau - \tau' > 0$, then

$$G^M_{\widehat{A}\widehat{B}}(\tau-\tau') = G^M_{\widehat{A}\widehat{B}}(\tau-\tau'-\hbar\beta). \tag{2.22}$$

This periodicity allows one to represent the function by a Fourier series:

$$G^M_{\widehat{A}\widehat{B}}(\tau) = \frac{1}{\hbar\beta}\sum_E \exp\left(-\frac{E\tau}{\hbar}\right) G^M_{\widehat{A}\widehat{B}}(E), \tag{2.23}$$

where $E = i\frac{2\pi n}{\beta}$ is a Matsubara energy, n is an integer. $G^M_{\widehat{A}\widehat{B}}(E)$ are the Matsubara components:

$$G^M_{\widehat{A}\widehat{B}}(E) = \int_0^{\hbar\beta} d\tau \exp\left(\frac{E}{\hbar}\tau\right) G^M_{\widehat{A}\widehat{B}}(\tau). \tag{2.24}$$

Equation (2.23) is the analytic continuation of the function $G^M_{\widehat{A}\widehat{B}}(\tau)$, especially for the case $\tau = 0$. One can write down the spectral representation of $\langle T_\tau(\widehat{A}(\tau)\widehat{B}(0))\rangle$, for $\tau > 0$:

$$\begin{aligned}\langle\widehat{A}(\tau)\widehat{B}(0)\rangle &= \frac{1}{\mathrm{Tr}(\widehat{\rho})}\sum_{\gamma,\xi}\langle\gamma|\widehat{A}|\xi\rangle\langle\xi|\widehat{B}|\gamma\rangle\exp\left(\tau\frac{E_\gamma - E_\xi}{\hbar} - \beta E_\gamma\right)\\ &= \frac{1}{\hbar}\int_{\mathbb{R}} d\mathcal{E}\frac{\mathcal{S}_{\widehat{A}\widehat{B}}(\mathcal{E})}{1-\exp(-\beta\mathcal{E})}\exp\left(-\frac{\mathcal{E}\tau}{\hbar}\right).\end{aligned} \tag{2.25}$$

If one changes to the Matsubara component:

$$\begin{aligned}G^M_{\widehat{A}\widehat{B}}(E) &= -\int_0^{\hbar\beta} d\tau \exp\left(\frac{E}{\hbar}\tau\right)\langle\widehat{A}(\tau)\widehat{B}(0)\rangle\\ &= \int_{\mathbb{R}} d\mathcal{E}\frac{\mathcal{S}_{\widehat{A}\widehat{B}}(\mathcal{E})}{E-\mathcal{E}},\end{aligned} \tag{2.26}$$

the retarded Green's function can be written in terms of it's spectral density as well:

$$G^r_{\widehat{A}\widehat{B}}(\mathcal{E}) = \int_{\mathbb{R}} d\mathcal{E}'\frac{\mathcal{S}_{\widehat{A}\widehat{B}}(\mathcal{E}')}{\mathcal{E}-\mathcal{E}'+i0^+}. \tag{2.27}$$

As a consequence, the Matsubara function can be analytically continued to the retarded function, by setting $E \to \mathcal{E} + i0^+$.

Finally, I want to sketch how the perturbation expansion can be expressed using Matsubara functions. A detailed description can be found in Ref. (204). To do this, recapitulate the equations of motion for an operator in the Heisenberg and Dirac picture (denoted by superscripts H and D on the operator):

$$\begin{aligned} \widehat{A}^H(\tau) &= \widehat{W}^D(0,\tau)\widehat{A}^D(\tau)\widehat{W}^D(\tau,0) \\ \widehat{W}^D(\tau,\tau') &= \exp\left(\frac{\tau\widehat{H}_0}{\hbar}\right)\exp\left(\frac{-\widehat{H}(\tau-\tau')}{\hbar}\right)\exp\left(\frac{-\tau'\widehat{H}_0}{\hbar}\right). \end{aligned} \tag{2.28}$$

Especially, one finds an equation of motion for the time-evolution operator $\widehat{W}^D(\tau,\tau')$ that can be solved ($\widehat{H}_i = \widehat{H} - \widehat{H}_0$):

$$\begin{aligned} -\hbar\frac{\partial}{\partial\tau}\widehat{W}^D(\tau,\tau') &= \widehat{H}_i^D(\tau)\widehat{W}^D(\tau,\tau') \\ \widehat{W}^D(\tau,\tau') &= \sum_{n=0}^{\infty}\frac{1}{n!}\left(-\frac{1}{\hbar}\right)^n\int_{\tau'}^{\tau}d\tau_1...d\tau_n T_\tau\left[\widehat{H}_i^D(\tau_1)...\widehat{H}_i^D(\tau_n)\right]. \end{aligned} \tag{2.29}$$

The second line is a solution to the equation in the first, where the boundary condition $\widehat{W}^D(\tau,\tau) = \mathbb{I}$ has been used. Note that

$$\widehat{W}^D(\tau_1,\tau_2)\widehat{W}^D(\tau_2,\tau_3) = \widehat{W}^D(\tau_1,\tau_3). \tag{2.30}$$

Most importantly, one obtains

$$\begin{aligned} \exp\left(-\frac{\tau}{\hbar}\widehat{H}\right) &= \exp\left(-\frac{\tau}{\hbar}\widehat{H}_0\right)\widehat{W}^D(\tau,0) \\ &\Rightarrow \widehat{\rho} = \widehat{\rho}_0\widehat{W}^D(\hbar\beta,0), \end{aligned} \tag{2.31}$$

where $\widehat{\rho}_0$ is the density matrix of the harmonic system. This can be used as follows: Consider the Matsubara function, for $\tau - \tau' > 0$

$$\begin{aligned} G^M_{\widehat{A}\widehat{B}}(\tau-\tau') &= -\frac{1}{\mathrm{Tr}(\widehat{\rho})}\mathrm{Tr}\left[\widehat{\rho}T_\tau\left(\widehat{A}^H(\tau)\widehat{B}^H(\tau')\right)\right] \\ &= -\frac{1}{\mathrm{Tr}(\widehat{\rho})}\mathrm{Tr}\left(\widehat{\rho}\widehat{A}^H(\tau)\widehat{B}^H(\tau')\right) \\ &= -\frac{1}{\mathrm{Tr}(\widehat{\rho})}\mathrm{Tr}(\widehat{\rho}_0\widehat{W}^D(\hbar\beta,\tau)\widehat{A}^D(\tau)\widehat{W}^D(\tau,\tau')\times \\ &\qquad\qquad \widehat{B}^D(\tau')\widehat{W}^D(\tau',0)) \\ &= -\frac{1}{\mathrm{Tr}(\widehat{\rho})}\mathrm{Tr}\left(\widehat{\rho}_0 T_\tau(\widehat{W}^D(\hbar\beta,0)\widehat{A}^D(\tau)\widehat{B}^D(\tau'))\right) \end{aligned} \tag{2.32}$$

where the last step is possible, because the operators are already in correct order. Then, one obtains the perturbation expansion

$$G^M_{\widehat{A}\widehat{B}}(\tau-\tau') = -\frac{1}{\mathrm{Tr}(\widehat{\rho})}\sum_{n=0}^{\infty}\frac{1}{n!}\left(-\frac{1}{\hbar}\right)^n\int_0^{\hbar\beta} d\tau_1...d\tau_n \times \\ \mathrm{Tr}\left[\widehat{\rho}_0 T_\tau(\widehat{H}_i^D(\tau_1)...\widehat{H}_i^D(\tau_n)\widehat{A}^D(\tau)\widehat{B}^D(\tau'))\right]. \tag{2.33}$$

The D, referring to Dirac's picture, will be omitted from now on for convenience. To evaluate this equation perturbatively, some more theorems are necessary. The most important is Wick's theorem for thermal quantum mechanics, that allows to evaluate traces of operator products. The idea of Wick's theorem is, to recursively reduce the complexity of a trace of operator products, down to the "simplest" possible correlation function. For this, one defines this simplest correlation function, as the "contraction" of two operators:

$$\langle T_\tau\left(\widehat{A}(\tau_A)\widehat{B}(\tau_B)\right)\rangle^{(0)}, \tag{2.34}$$

where $\langle ...\rangle^{(0)}$ is the expectation value in the harmonic, non-interacting system. Then Wick's theorem states, that if $\widehat{A}_1...\widehat{A}_{2n}$ are single creation or annihilation operators (or a linear combination of them) then (time arguments are omitted for convenience),

$$\langle T_\tau\left(\widehat{A}_1...\widehat{A}_{2n}\right)\rangle^{(0)} = \sum\{\text{full contraction}\}, \tag{2.35}$$

where "full contraction" means, that all operators are paired in all possible ways. For example

$$\begin{aligned}\langle T_\tau\left(\widehat{A}_1\widehat{A}_2\widehat{A}_3\widehat{A}_4\right)\rangle^{(0)} =& \langle T_\tau\left(\widehat{A}_1\widehat{A}_2\right)\rangle^{(0)}\langle T_\tau\left(\widehat{A}_3\widehat{A}_4\right)\rangle^{(0)} \\ &+ \langle T_\tau\left(\widehat{A}_1\widehat{A}_3\right)\rangle^{(0)}\langle T_\tau\left(\widehat{A}_2\widehat{A}_4\right)\rangle^{(0)} \\ &+ \langle T_\tau\left(\widehat{A}_1\widehat{A}_4\right)\rangle^{(0)}\langle T_\tau\left(\widehat{A}_2\widehat{A}_3\right)\rangle^{(0)}.\end{aligned} \tag{2.36}$$

Wick's theorem for this case is proven in Appendix D.

2.2.3 *Feynman diagrams*

It can now be used to calculate expectation values, occurring in Eqns. (2.31) and (2.33). However, without additional theorems, the workload is overwhelming. These additional theorems are obtained by introducing Feynman diagrams and related concepts of topology and self-energy. I want to derive Feynman rules for an interacting phonon system with the Hamiltonian

$$\widehat{H} = \widehat{T} + \widehat{V}, \tag{2.37}$$

with

$$\widehat{V} = \widehat{V}^{(0)} + \widehat{V}^{(2)} + \widehat{V}^{(3)} + ..., \tag{2.38}$$

where the potential energy for the n-body interaction is

$$\widehat{V}^{(n)} = \frac{1}{n!} \sum_{\{\kappa,\alpha,p\}} \Phi^{\kappa_1,p_1,...,\kappa_n,p_n}_{\alpha_1,...,\alpha_n} \widehat{u}^{\alpha_1}_{\kappa_1,p_1} \times ... \times \widehat{u}^{\alpha_n}_{\kappa_n,p_n}. \tag{2.39}$$

$\widehat{T}$ is the kinetic energy operator of the nuclei. I follow Ref. (267), where $\widehat{V}^{(n)}$ is represented in terms of phonon displacement operators

$$\widehat{V}^{(n)} = \frac{N_p^{1-\frac{n}{2}}}{n!} \left(\frac{\hbar}{2}\right)^{n/2} \sum_{\{\mathbf{q}\nu\}} \frac{\tilde{\Phi}(\mathbf{q}_1,\nu_1,...,\mathbf{q}_n,\nu_n)}{\sqrt{\omega_{\mathbf{q}_1,\nu_1}...\omega_{\mathbf{q}_n,\nu_n}}} \widehat{U}_{\mathbf{q}_1,\nu_1}...\widehat{U}_{\mathbf{q}_n,\nu_n}. \tag{2.40}$$

$\tilde{\Phi}$ are the inverse space force constants

$$\tilde{\Phi}(\mathbf{q}_1,\nu_1,...,\mathbf{q}_n,\nu_n) = \sum_{\{\kappa,\alpha\}} \prod_{l=1}^{n} e^{\alpha_l}_{\kappa_l,\nu_l}(\mathbf{q}_l) \varphi^n(\mathbf{q}_1,\kappa_1,\alpha_1,...,\mathbf{q}_n,\kappa_n,\alpha_n), \tag{2.41}$$

with

$$\varphi^n(\mathbf{q}_1,\kappa_1,\alpha_1,...,\mathbf{q}_n,\kappa_n,\alpha_n) = \sum_{\{p\}} (M_{\kappa_1}...M_{\kappa_n})^{-\frac{1}{2}} \Phi^{\kappa_1,0,...,\kappa_n,p_n}_{\alpha_1,...,\alpha_n} \times \exp\left(i \sum_{l=2}^{n} \mathbf{q}_l \cdot (\mathbf{R}_{p_l} + \boldsymbol{\tau}_{\kappa_l} - \boldsymbol{\tau}_{\kappa_1})\right) \Delta(\sum_i \mathbf{q}_i). \tag{2.42}$$

Δ is 1 only if it's argument is a reciprocal lattice vector. I define the momentum operator of the phonons as in Refs. (246, 253)

$$\widehat{P}_{\mathbf{q},\nu} = i\omega_{\mathbf{q},\nu}(\widehat{a}^{\dagger}_{-\mathbf{q},\nu} - \widehat{a}_{\mathbf{q},\nu}), \tag{2.43}$$

which will later be necessary for thermal conductivity calculations. Another important relation is

$$\left[\widehat{U}_{\mathbf{q},\nu}, \widehat{H}\right] = i\hbar\widehat{P}_{\mathbf{q},\nu}. \tag{2.44}$$

Once Wick's theorem has been applied to the expectation values, they can be identified with diagrams as follows: Assume I want to compute the expectation value

$$\langle T_\tau \left(\widehat{A}(\tau_A)\widehat{B}(\tau_B)\right)\rangle^{(0)}, \tag{2.45}$$

where both $\widehat{A}$ and $\widehat{B}$ can be represented as a monomial of phonon displacement and momentum operators times a prefactor. One may

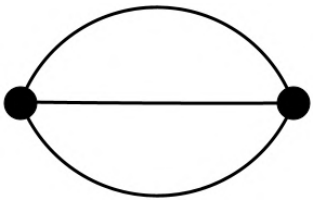

Figure 2.1: Diagram corresponding to the expectation value in Eq. (2.47). The number of loops of this diagram is 2, that is, the minimum number of edges/lines to be removed, before the graph has no cycles anymore. The diagram therefore belongs to the second order of perturbation theory.

choose $\widehat{A} = \widehat{B} = \widehat{V}^{(3)}$. Then, the expectation value can be rephrased using (appropriately chosen) prefactors $v^{(3)}$, as ($\tau_A > \tau_B$)

$$\sum_{\{\mathbf{q}\nu\}} v^{(3)}(\mathbf{q}_1,\nu_1,\mathbf{q}_2,\nu_2,\mathbf{q}_3,\nu_3)v^{(3)}(\mathbf{q}_4,\nu_4,\mathbf{q}_5,\nu_5,\mathbf{q}_6,\nu_6)\times \\ \langle \widehat{U}_{\mathbf{q}_1,\nu_1}(\tau_A)\widehat{U}_{\mathbf{q}_2,\nu_2}(\tau_A)\widehat{U}_{\mathbf{q}_3,\nu_3}(\tau_A)\widehat{U}_{\mathbf{q}_4,\nu_4}(\tau_B)\widehat{U}_{\mathbf{q}_5,\nu_5}(\tau_B)\widehat{U}_{\mathbf{q}_6,\nu_6}(\tau_B)\rangle^{(0)} \tag{2.46}$$

and can be contracted according to Wick's theorem. One contribution to this is found by contracting the operators with the indices 1 and 4, 2 and 5, as well as 3 and 6, as

$$\sum_{\{\mathbf{q}\nu\}} v^{(3)}(\mathbf{q}_1,\nu_1,\mathbf{q}_2,\nu_2,\mathbf{q}_3,\nu_3)v^{(3)}(\mathbf{q}_4,\nu_4,\mathbf{q}_5,\nu_5,\mathbf{q}_6,\nu_6)\times \\ \langle \widehat{U}_{\mathbf{q}_1,\nu_1}(\tau_A)\widehat{U}_{\mathbf{q}_4,\nu_4}(\tau_B)\rangle^{(0)}\langle \widehat{U}_{\mathbf{q}_2,\nu_2}(\tau_A)\widehat{U}_{\mathbf{q}_5,\nu_5}(\tau_B)\rangle^{(0)}\times \\ \langle \widehat{U}_{\mathbf{q}_3,\nu_3}(\tau_A)\widehat{U}_{\mathbf{q}_6,\nu_6}(\tau_B)\rangle^{(0)}. \tag{2.47}$$

Now it is necessary to compute the fundamental correlation function $\widehat{A} = \widehat{U}_{\mathbf{q},\nu}$ and $\widehat{B} = \widehat{U}_{\mathbf{q}'\nu'}$ in the non-interacting system, the "bare" phonon propagator. This has been done in Appendix E.1. In Fourier component representation, this is

$$\mathcal{G}^{M,(0)}_{\mathbf{q},\nu,\mathbf{q}',\nu'}(E) = \hbar\left(\frac{1}{E-\hbar\omega_{\mathbf{q},\nu}} - \frac{1}{E+\hbar\omega_{\mathbf{q},\nu}}\right)\delta_{\nu,\nu'}\delta_{\mathbf{q},-\mathbf{q}'+\mathbf{R}_\mathbf{q}}, \tag{2.48}$$

where $\mathbf{R}_\mathbf{q}$ is a reciprocal lattice vector. The other fundamental contractions will later be related to the phonon propagator, which is why they are not written down here. In general, the expectation values, built from two operators of the type $\widehat{P}$ and/or $\widehat{U}$, will be denoted by $\mathcal{G}^{\widehat{A}\widehat{B}}$. The expectation value Eq. (2.47) may be represented by the diagram shown in Fig. 2.1 by identifying the function v as the dots on the side and the contractions as the lines between the dots. The diagrammatic representation of all contractions occurring in this thesis is shown in Fig. 2.2. The interactions used in my calculations can be displayed with the vertices shown in Fig. 2.3, namely the 3-phonon and 4-phonon vertices, corresponding to $\widehat{V}^{(3)}$ and $\widehat{V}^{(4)}$. One may take several steps to simplify the perturbation expansion. To compute an expectation value

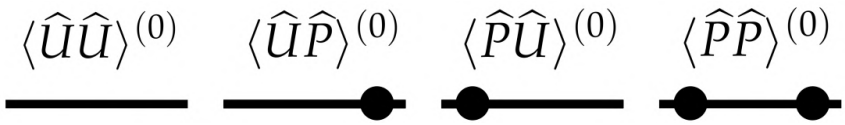

Figure 2.2: Fundamental contractions. Later, especially for the calculation of the thermal conductivity, the contractions may be replaced by expectation values in the interacting system.

Figure 2.3: Interaction vertices in this theory, representing the interactions $\widehat{V}^{(3)}$ on the left, and $\widehat{V}^{(4)}$ on the right.

$\langle \widehat{A}(\tau_A)\widehat{B}(\tau_B) \rangle$ in the interacting system, one only needs to compute connected diagrams (204), exemplified by Fig. 2.4. The idea is, that in Eq. (2.33), the denominator $\mathrm{Tr}(\widehat{\rho})$ cancels all disconnected diagrams in the expansion.

The prefactor of a diagram (referring to Eq. (2.33)) with n_3, n_4, and n_5 vertices with 3, 4, and 5 arms is always one. The vertices can be interchanged without changing the expression in $n_3!n_4!n_5!$ ways. On the other hand, the number of expressions with n_3, n_4, and n_5 vertices is the multinomial coefficient $\frac{n!}{n_3!n_4!n_5!}$. Then the total prefactor is $\frac{1}{n!}\frac{n!}{n_3!n_4!n_5!}n_3!n_4!n_5! = 1$. This can be generalized, for other interactions.

To simplify further, one can use the Matsubara components of the Green's functions. To transfer the complex time expression, write each propagator in terms of their Matsubara components and assign the time dependence in the way presented in Fig. 2.5. If the propagators are represented by their Matsubara components, all integrals from 0 to $\hbar\beta$ (from Eq. (2.33)) can be associated to a vertex and give a factor

$$\int_0^{\hbar\beta} \exp(\hbar^{-1}\sum E_i\tau)d\tau = \hbar\beta\delta_{\sum E_i}, \tag{2.49}$$

where δ is one, if its subscript is zero, otherwise it is zero. In the Matsubara representation, every vertex is said to "conserve the Matsubara

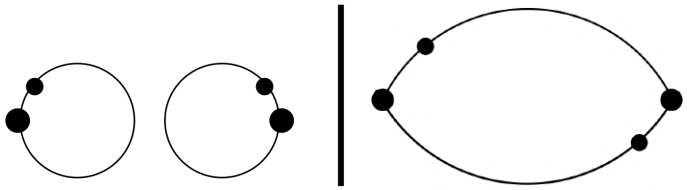

Figure 2.4: Disconnected (left) and connected (right) diagram. $\widehat{A}$ and $\widehat{B}$ both contain one $\widehat{U}$ and one $\widehat{P}$ in the examples.

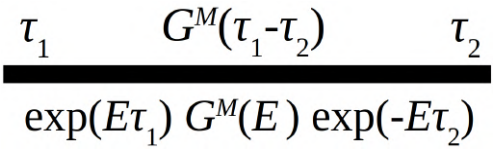

Figure 2.5: Illustration of the relation between the complex time representation and the Matsubara component representation of a diagram. The left vertex be at time τ_1, the right one at τ_2. The propagator has the value $\mathcal{G}^M(\tau_1 - \tau_2) = \sum_E \exp(E\tau_1)\mathcal{G}^M(E)\exp(-E\tau_2)$. One can then multiply each vertex with all the exponentials that carry its time, and assign the propagator the value $\mathcal{G}^M(E)$.

energy". Every Green's function is represented by its Matsubara components. A number of summations remain, the *Matsubara summations*, that will be discussed later. The number of independent Matsubara summations is the *order* of the contribution. The order is identical to the number of loops of the diagram. All contributions of order n to a quantity are the n^{th} order approximation to this quantity. Examples for quantities are the self-energy, or the lattice thermal conductivity.

2.2.4 *Feynman rules for the propagator*

One obtains rules for the diagrams, that are the Feynman rules for the phonon propagator in the interacting system $\mathcal{G}^M_{\mathbf{q},\nu,\nu'}(E_n)$. The propagator is diagonal in $\mathbf{q}$, without loss of generality because of translation invariance.

- Draw all diagrams that connect two end-points corresponding to $\widehat{U}$ operators.
- For every interaction vertex $\widehat{V}^{(i)}$, one obtains a factor $-\beta$.
- Every propagator carries a factor $(\hbar\beta)^{-1}$.
- The correlation function carries an overall factor (-1), from the definition and a factor $\hbar\beta$ from the decomposition into Matsubara components.
- Every vertex $\widehat{V}^{(i)}$ conserves crystal momentum (up to reciprocal lattice vectors) and energies of the connected Green's functions.
- The prefactor of every vertex is given in the definition of the relevant $\widehat{V}^{(i)}$, without the operators. This prefactor is called $v^{(i)}$.
- All momenta and Matsubara energies (that the correlation function does not depend on) are integrated / summed.

2.2.5 *Dyson's equation and self-energy*

A practical way to improve the approximation to $\mathcal{G}^M_{\mathbf{q},\nu,\nu'}(E_n)$ is the introduction of the concept of self-energy. This concept allows to consider the impact of interactions, and especially decay, in the phonon propagator. This is imperative for thermal conductivity calculations.

Figure 2.6: Diagrammatic representation of Dyson's equation. The double line is the phonon propagator in the interacting system. The simple line is the bare phonon propagator. Σ is the phonon self-energy.

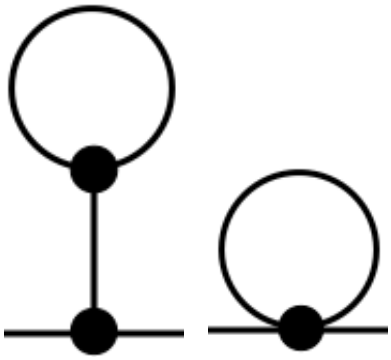

Figure 2.7: Diagrams that contribute to the self-energy.

The self-energy appears in Dyson's equation that may be represented diagrammatically as shown in Fig. 2.6. The double line in the figure denotes the (dressed) phonon propagator in the interacting system while the simple line denotes the (bare) phonon propagator in the harmonic system. This equation can be iterated by inserting the dressed phonon propagator on the left hand side. It is to be determined what Σ is. In index notation Dyson's equation reads

$$\mathcal{G}^{M}_{\mathbf{q},\nu,\nu'}(E) = \mathcal{G}^{M,(0)}_{\mathbf{q},\nu,\nu'}(E) + \sum_{\nu''} \frac{1}{\hbar\beta} \mathcal{G}^{M,(0)}_{\mathbf{q},\nu,\nu}(E) \alpha \Sigma^{M}_{\mathbf{q},\nu,\nu''}(E) \mathcal{G}^{M}_{\mathbf{q},\nu'',\nu'}(E), \tag{2.50}$$

where α is a prefactor. This can be rephrased in matrix form

$$\mathcal{G}^{M}_{\mathbf{q}}(E) = \left[1 - \frac{\alpha}{\hbar\beta} \mathcal{G}^{M,(0)}_{\mathbf{q}}(E) \Sigma^{M}_{\mathbf{q}}(E)\right]^{-1} \mathcal{G}^{M,(0)}_{\mathbf{q}}(E), \tag{2.51}$$

and I choose $\alpha = \beta$. Then, the function $\Sigma^{M}_{\mathbf{q}}(E)$ is a set of diagrams, multiplied with β^{-1}. This is a useful convention, as the units of the self-energy are Joule.

The diagrams that compose Σ are called *one-particle irreducible* (OPI). Recall Eq. (2.33): every diagram that contributes to $\mathcal{G}$ has the prefactor 1, so that all diagrams have to be counted exactly once. Self-energy diagrams, such as those in Fig. 2.7 have the property, that one cannot cut one particle-line to obtain two independent self-energy diagrams - hence, they are termed OPI. A diagram such as the one in Fig. 2.8 is not a self-energy diagram, as it can be decomposed into other self-energy diagrams. If it would be included in the self-energy, it would

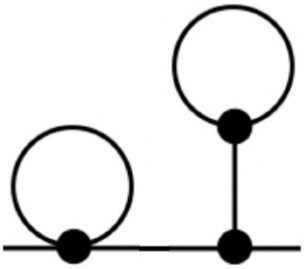

Figure 2.8: One particle reducible diagram. By removing the line in the middle the diagram can be reduced into two independent self-energy diagrams.

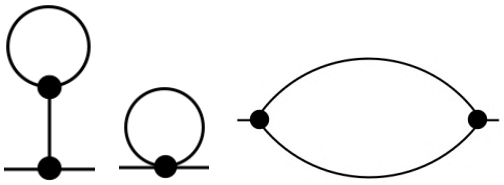

Figure 2.9: Anharmonic contributions to the self-energy, at first loop-order perturbation theory, in diagrammatic form. Diagrams containing electron-phonon interactions are neglected, as they will, in most cases, not have a major impact on the phonon self-energy (143, 303). The black circles denote vertex functions, while the lines represent propagators. The values of the diagrams are denoted as D^1, D^2 and D^3, from left to right. The left 'tadpole' diagram vanishs in crystals that possess inversion symmetry (169).

be counted twice in $\mathcal{G}$. By convention, the OPI diagrams are not multiplied with the propagators that contract with them. A diagrammatic approximation to Σ may be used, if the perturbation is small "enough". What enough means, will be discussed in Appendix F.

Often, the cross-terms $\Sigma_{\mathbf{q},\nu,\nu'}(E)$ with $\nu \neq \nu'$ will be neglected, so that the functions in the above equations are simple numbers. I call this the diagonal propagator approximation (DPA).

The self-energy and the phonon propagator have specific symmetry properties, discussed in Appendices E.2 and E.3. In the case of an anharmonic crystal, the self-energy contributions to first order are given by the diagrams in Fig. 2.9. The constant contribution to the self-energy (from the left and the middle diagram) is given by

$$\Sigma^c_{\mathbf{q},\nu,\nu'} = D^1_{\mathbf{q},\nu,\nu'} + D^2_{\mathbf{q},\nu,\nu'}, \tag{2.52}$$

where

$$D^1_{\mathbf{q},\nu,\nu'} = -72\sum_{\nu_1} v^{(3)}(\mathbf{q},\nu;-\mathbf{q},\nu';0,\nu_1)(\hbar\omega_{0,\nu_1})^{-1}\times \sum_{\mathbf{q}_1,\nu_2} v^{(3)}(\mathbf{q}_1,\nu_2;-\mathbf{q}_1,\nu_2;0,\nu_1)n_B(\hbar\omega_{\mathbf{q}_1,\nu_2})$$
$$D^2_{\mathbf{q},\nu,\nu'} = -24\sum_{\mathbf{q}_1,\nu_1} v^{(4)}(\mathbf{q},\nu;-\mathbf{q},\nu';\mathbf{q}_1,\nu_1,-\mathbf{q}_1,\nu_1)n_B(\hbar\omega_{\mathbf{q}_1,\nu_1}). \tag{2.53}$$

The variable contribution to the self-energy is found from the third diagram and can be written as (267)

$$D^{M,3}_{\mathbf{q},\nu,\nu'}(E_n) = -18\sum_{\mathbf{q}_1,\nu_1,\nu_2} \mathcal{F}^M(E_n,\omega_{\mathbf{q}_1\nu_1},\omega_{\mathbf{q}-\mathbf{q}_1\nu_2}) \times v^{(3)}(-\mathbf{q},\nu;\mathbf{q}_1,\nu_1;\mathbf{q}-\mathbf{q}_1,\nu_2)v^{(3)}(\mathbf{q},\nu';-\mathbf{q}_1,\nu_1;\mathbf{q}_1-\mathbf{q},\nu_2), \tag{2.54}$$

with

$$\mathcal{F}^M(E,\omega_1,\omega_2) = \sum_{\sigma=\pm1}\left(\frac{n_B(\hbar\omega_1)+n_B(\hbar\omega_2)}{E+\sigma(\omega_1+\omega_2)} + \frac{n_B(\hbar\omega_2)-n_B(\hbar\omega_1)}{E+\sigma(\omega_1-\omega_2)}\right). \tag{2.55}$$

Here, n_B is the boson occupation factor $n_B(\mathcal{E}) = \frac{1}{2}\coth(\frac{\beta\mathcal{E}}{2})$. From now on, if not mentioned differently, the propagator $\mathcal{G}$ means the solution to Dyson's equation.

2.2.6 *Weak interactions and quasiparticles*

In the case of weak interactions, i.e. small self-energies, the spectral density of a phonon mode $\mathbf{q}\nu$ may be very well approximated by a (sharply peaked) Lorentzian

$$\begin{aligned}
\mathcal{S}_{\mathbf{q},\nu,\nu'}(\mathcal{E}) &\approx \frac{-\delta_{\nu\nu'}}{\pi}\mathrm{Im}\left(\mathcal{G}^r_{\mathbf{q},\nu,\nu}(\mathcal{E})\right)\\
&\approx \frac{\delta_{\nu\nu'}}{\pi}\mathrm{Im}\left(\frac{-2\hbar^2\omega_{\mathbf{q},\nu}}{\mathcal{E}^2-(\hbar\omega_{\mathbf{q},\nu})^2+2\hbar\omega_{\mathbf{q},\nu}\Sigma^r_{\mathbf{q},\nu,\nu}(\mathcal{E})}\right)\\
&\approx \frac{\delta_{\nu\nu'}}{\pi}\mathrm{Im}\left(\frac{-2\hbar^2\omega_{\mathbf{q},\nu}}{2\hbar\omega_{\mathbf{q},\nu}(\mathcal{E}-\hbar\omega_{\mathbf{q},\nu})+2\hbar\omega_{\mathbf{q},\nu}\Sigma^r_{\mathbf{q},\nu,\nu}(\mathcal{E})}\right)\\
&= -\frac{\hbar\delta_{\nu\nu'}}{\pi}\mathrm{Im}\left(\frac{1}{(\mathcal{E}-\hbar\omega_{\mathbf{q},\nu})+\Sigma^r_{\mathbf{q},\nu,\nu}(\mathcal{E})}\right)\\
&\approx \frac{\hbar\delta_{\nu\nu'}}{\pi}\frac{\mathrm{Im}(\Sigma^r_{\mathbf{q},\nu,\nu}(\hbar\omega_{\mathbf{q},\nu}))}{(\mathcal{E}-\hbar\omega_{\mathbf{q},\nu})^2+\mathrm{Im}(\Sigma^r_{\mathbf{q},\nu,\nu}(\hbar\omega_{\mathbf{q},\nu}))^2},
\end{aligned} \tag{2.56}$$

and one may define the lifetime of this phonon as

$$\tau_{\mathbf{q},\nu} = \frac{\hbar}{2\,\mathrm{Im}(\Sigma^r_{\mathbf{q},\nu,\nu}(\hbar\omega_{\mathbf{q},\nu}))}. \tag{2.57}$$

In other words, one can characterize a phonon spectral density by the phonon frequency $\omega_{\mathbf{q},\nu}$, and lifetime $\tau_{\mathbf{q},\nu}$. This may later be used to simplify equations that contain the phonon spectral density or propagator. In this case, the imaginary part of a trace self-energy element may be interpreted as the decay rate of a phonon mode. It is known that this interpretation holds true in the limit of long lifetimes (205, 220).

2.2.7 *Strong interactions*

For many materials, such as simple cubic Ca (70) but also in presence of strong interactions, perturbation theory may not be suitable to model the phonon motion in the crystal. In order to model such systems, I resort to self-consistent phonon theory (SCPT), described by Werthamer (289) and applied for example by Tadano (267). There exist multiple other methods to model the phonon motion in crystals, for example the temperature dependent effective potential method (TDEP) (113, 114), which may be more well-suited in certain materials and will be discussed in more detail in Sec. 6.

The idea of SCPT is, that the self-energy alters the phonon propagator according to Dyson's equation. But the self-energy itself is calculated from the phonon propagator. One may therefore solve Dyson's equation with the self-energy as a functional of the dressed propagator self-consistently. If the self-energy is approximated by its constant contributions, one needs to solve the SCP equation (267)

$$\begin{aligned} \det\left(\omega^2 - V_{\mathbf{q}}\right) &= 0 \\ V_{\mathbf{q}\nu\nu'} &= \omega^2_{\mathbf{q}\nu}\delta_{\nu\nu'} - (2\omega_{\mathbf{q}\nu})^{1/2}(2\omega_{\mathbf{q}\nu'})^{1/2}\Sigma^c_{\mathbf{q}\nu\nu'}. \end{aligned} \tag{2.58}$$

The new SCP phonon frequencies are then used to calculate the self-energy and the equation is iterated for convergence. A self-consistent solution may not be the *physical* solution. The physical solution would be the self-consistent solution that minimizes the free energy of the system (251).

2.2.8 *Alternative methods*

There are many methods to calculate the propagator, that are not used in this thesis. These include old ones, where many of them are not in use today, to the best of my knowledge (79, 86). There has especially been the trial to solve ladder diagrams for the phonon propagator (252) that are claimed to give leading contributions to the

phonon self-energy, based on phase space arguments from Ref. (2). There are approaches that extend many-body theory by including second-loop-order corrections to the phonon scattering rates (234) that are especially important at high temperatures (13). These methods scale extremely fast with the number of nuclei in the unit cell of the simulated material. Another idea would be to develop a cumulant expansion for the anharmonic phonon self-energy (9, 33, 109, 145). The quality of an approximation can be judged by the value of the free energy it corresponds to. This value should be as small as possible and can be calculated with a famous formula from Ref. (251).

There also exist methods to obtain better IFCs for a specific task. For example, the temperature-dependent effective potential (TDEP) method (113), has proven useful in strongly interacting systems. In TDEP, a MD trajectory is created for each temperature, and then IFCs (usually up to third order) are fitted to the DFT forces that occur in the MD simulation. This method seems to be more stable in a strongly interacting system, than the many-body approach presented in this thesis. On the other hand, TDEP is numerically much more expensive, because of the need to simulate a MD trajectory at each temperature.

2.3 LATTICE THERMAL CONDUCTIVITY

2.3.1 *Formulation*

To describe the conduction of heat or energy at the quantum level is a formidable task for multiple reasons: Linear response theory usually assumes a system in thermal equilibrium, for which formulas can be derived routinely, see Refs. (144, 304, 305). This is not the case if we consider thermal transport. Even though it is clear, that the thermal conductivity exists in the limit of a vanishing temperature gradient (166), the unambiguous derivation of a correlation function to be used in Kubo's equations (147) is non-trivial and for this reason repeated in Appendix G.

The correlation function for the lattice thermal conductivity, perfectly suited for the BO approximation, was derived by Hardy (102). His heat-flux operator is

$$\widehat{\mathbf{J}} = \frac{1}{2\Omega}\left\{\sum_i \frac{\widehat{\mathbf{p}}_i}{M_i}\left(\frac{\widehat{\mathbf{p}}_i^2}{2M_i} + \widehat{V}_i\right) + \sum_{i,j}(\widehat{\mathbf{r}}_i - \widehat{\mathbf{r}}_j)\frac{1}{i\hbar}\left[\frac{\widehat{\mathbf{p}}_i^2}{2M_i}, \widehat{V}_j\right]\right\} + \text{h.c.}, \tag{2.59}$$

where $\widehat{\mathbf{p}}_j$, $\widehat{\mathbf{r}}_j$ and $\widehat{V}_j$ are the momentum, position, and local potential energy operator of the nucleus j. $\widehat{V}_j$ can be altered by assigning different portions of the interaction energy to different participating nuclei. As a result, the heat-flux operator is not uniquely defined. Please note, that in this thesis, the terms *heat flux* and *energy flux* are used indis-

criminately, which is correct as transfer of matter is not considered within the formalism (270).

The thermal conductivity can be written as (4, 161)

$$\kappa^{ij} = \frac{\Omega}{T} \int_0^\beta d\lambda \int_0^\infty dt \, \langle \widehat{J}^i \widehat{J}^j (t + i\hbar\lambda) \rangle, \tag{2.60}$$

where $\widehat{J}^j$ is meant in the Heisenberg picture. It remained unclear so far, under which circumstances κ^{ij} is independent of the specific definition of the $\widehat{V}_j$. This problem is addressed in Sec. 3.1.

It has been shown for similar cases in Ref. (166) and is shown for our case explicitly in Appendix G.2 that Eq. (2.60) can be rephrased as

$$\kappa^{ij} = -\frac{1}{T} \lim_{\mathcal{E}\to 0} \frac{1}{\mathcal{E}} \mathrm{Im}(\Pi_r^{ij}(\mathcal{E})), \tag{2.61}$$

where $\Pi_r^{ij}(\mathcal{E})$ is the Fourier transform of the retarded heat-flux autocorrelation function

$$\Pi_r^{ij}(t - t') = -i\Omega\theta(t - t') \langle \left[\widehat{J}^i(t), \widehat{J}^j(t') \right] \rangle. \tag{2.62}$$

This formulation will be used to derive a perturbation theory for the lattice thermal conductivity from first principles in the next chapter. I conclude this chapter with a brief review of the state-of-the-art methods to measure and compute the thermal conductivity, that were not used in my work.

2.3.2 *Alternative methods*

Many methods to calculate the thermal conductivity, are not used in this thesis. These include old ones, that are, to the best of my knowledge, not in use nowadays (112, 146, 230, 231). Again, a ladder diagram approach to the thermal conductivity has been proposed in Ref. (253), that aims to solve a Bethe-Salpeter equation. Investigations on a Fokker-Planck equation have been done (298). There have been mathematical developments (119). Hardy (103) developed a perturbation expansion, that expands more than one quantity in the interaction at once.

The most important competing method to the BTE and many-body theory, is GK using MD (32, 93, 94). It is known that GK and the BTE are related to the current many-body formalism as discussed in Appendix G.2 and Ref. (244) and have been compared for many materials (228). MD, especially when using DFT calculations for every time step, is known to be numerically extremely expensive because the supercells needed for the simulations must be large (for example $12 \times 12 \times 12$ in silicon) (42, 245). MD can be corrected for quantum effects as well (40). For not too high temperatures it should be possible to use the virial approximation to the thermal conductivity (121, 230). If,

additionally, the heat-flux is approximated as harmonic, the numerical effort for MD calculations can be significantly reduced (32). Also, electron-phonon interactions can be included in MD (174). MD is a non-perturbative approach and therefore the "gold-standard", that the results of this work can be compared to. A related approach is the Green-Kubo modal analysis (162, 163, 249).

Non-equilibrium approaches that are conceptually quite simple (193) turn out to be numerically extremely intensive. To the best of my knowledge these methods are not widely used to determine the thermal conductivity of crystalline solids (61, 107, 194). More approaches have been attempted using many-body potentials (74) or non-equilibrium Greens functions (247).

The theory of thermal conduction is well-understood in simple materials like diamond (287) or silicon (72).

Thermal conductivity measurements, especially if not at room temperature, are nowadays usually based on the laser-flash technique (149, 208). The results of laser-flash measurements are the ultimate reference for any theoretic calculation. New methods are still in development nowadays (11, 106, 159), but the laser-flash technique has proven reliable, as it reduces the impact of Kapitza resistance at the coating-sample-interface (133, 266, 295) and surface heat-losses through short measuring times.

Part II

RESULTS

3

THEORY ADVANCEMENTS

The aim of this thesis is to develop a methodology suited to calculate the lattice thermal conductivity of promising crystalline thermoelectrics. These materials should have a low lattice thermal conductivity (167) and are (most likely) semiconductors (257). The main question to be addressed here is, whether the thermal conductivity can be calculated with some type of Boltzmann transport equation (BTE), or whether higher-order corrections are necessary for the materials under investigation. To do so, it is first important to reason whether the interatomic force constants are indeed everything that is necessary to calculate the lattice thermal conductivity:

Anticipating that the BO approximation is valid, the electrons of the system adjust adiabatically to the positions of the nuclei, and always stay in their ground-state. The nuclei positions effectively determine the state of the electrons. As the state of both the electrons and nuclei is determined only by the nuclei positions, one can depict the system as one of effectively interacting nuclei. All properties of the system, related to the nuclei, must be calculatable from this effective interaction, such as the lattice thermal conductivity and the energy. The energy of the system is then determined by the displacements of the nuclei from their equilibrium position, which is encoded in the BO energy surface $E_B(\mathbf{u})$. As discussed in Sec. 2.1, this surface may be Taylor-expanded around the equilibrium in powers of the nuclei-displacements, and the coefficients of this expansion are the interatomic force constants. Hence these interatomic force constants determine the BO energy surface near the groundstate $\mathbf{u} = \mathbf{0}$. If the crystal is in thermal equilibrium the excited states of the system belong to a grand-canonical ensemble (124, 139, 202), and are likely to have an energy close to that of the groundstate. Therefore the states with an energy near to that of the groundstate determine the motion of the nuclei. As these states are determined by the interatomic force constants, the latter determine all properties of the system, such as the lattice thermal conductivity. This means that, given the interatomic force constants, the existence of a method to calculate the lattice thermal conductivity, without further approximation, is guaranteed.

I did not assume anything about the existence of collective vibrational modes, their decay, or the interaction strength in a crystal. Not even the periodicity of the system has been used. Accordingly, I expect that a generalization of the method to amorphous systems should be possible, and first steps have been done in Refs. (4, 256).

On this basis I construct a new approach to lattice thermal transport. I use the methods of linear response and Matsubara perturbation

theory as described in Sec. 2. In contrast to linear response theory in equilibrium, the correlation function for the thermal conductivity is not uniquely defined (see Sec. 2.3 and Appendix G). Consequently, the first task is to prove the invariance of the lattice thermal conductivity (Sec. 3.1). In Sec. 3.2, I assemble a new many-body methodology to calculate thermal conductivities, entirely from first principles. To do so, I first derive the heat-flux operator for a general crystal in the BO approximation and then prove a few necessary identities for the phonon propagator. To rule out further doubts on the approach, in Sec. 3.3, I show that the theory actually recovers the BTE. Finally, I discuss what is necessary to go beyond (Sec. 3.4).

3.1 INVARIANCE PROOF

The following considerations have been published in Ref. (125) and I closely follow this reasoning. During the writing of this thesis a similar, but not identical, consideration appeared in the literature (31).

This part was inspired by the proof of the invariance for the classical limit of the thermal conductivity (69, 173). To prove the invariance in the quantum case for the trace elements of the thermal conductivity tensor, I will do the following steps. First, I will compute a quantum Einstein relation, relating the thermal conductivity to the trace of the product of two operators. This will enable me to use a generalized version of the Cauchy-Schwarz inequality for matrices. Finally, I will define two thermal conductivities, corresponding to two definitions of the heat-flux operator $\widehat{\mathbf{J}}$, and show that they are identical. The invariance of the tensor κ follows from the invariance of it's trace elements.

The starting point of the proof is Eq. (2.60)

$$\kappa^{ij} = \frac{\Omega}{T \operatorname{Tr}(\widehat{\rho})} \int_0^\beta d\lambda \int_0^\infty dt \operatorname{Tr}\left(\widehat{\rho}\widehat{J}^i \widehat{J}^j(t + i\hbar\lambda)\right).$$

The vector operator $\widehat{\mathbf{J}}$ is meant in the Heisenberg-picture and can be obtained from the volume average of a *local* heat-flux operator which fulfills a continuity equation (102)

$$\frac{1}{i\hbar}\left[\widehat{\mathcal{H}}(\mathbf{x}), \widehat{H}\right] = -\nabla \cdot \widehat{\mathbf{j}}(\mathbf{x}), \tag{3.1}$$

where $\widehat{\mathcal{H}}(\mathbf{x})$ is a local Hamiltonian density that is only constrained by the fact that its volume integral is $\widehat{H}$. There remains a gauge freedom to $\widehat{\mathcal{H}}(\mathbf{x})$, as the interaction energy can be located at any of the

involved particles or spatial coordinates. Multiplying Eq. (3.1) with $\mathbf{x}$ and integrating over space, using partial integration, leads to

$$\begin{aligned}\frac{1}{i\hbar}\left[\frac{1}{\Omega}\int_\Omega d\mathbf{x}\,\mathbf{x}\widehat{\mathcal{H}}(\mathbf{x}),\widehat{H}\right] &= \\ -\frac{1}{\Omega}\int_\Omega d\mathbf{x}\,\mathbf{x}\nabla\cdot\widehat{\mathbf{j}}(\mathbf{x}) &= \\ \frac{1}{\Omega}\int_\Omega d\mathbf{x}\,\widehat{\mathbf{j}}(\mathbf{x}) &= \widehat{\mathbf{J}}.\end{aligned} \tag{3.2}$$

As the integrand $\mathbf{x}\widehat{\mathbf{j}}(\mathbf{x})$ vanishes outside the system, the surface term in Eq. (3.2) vanishs (102). As $\widehat{\mathcal{H}}(\mathbf{x})$ pertains a gauge freedom, $\widehat{\mathbf{J}}$ is not uniquely defined. An example is Hardy's heat-flux operator, see Eq. (2.59), where the local potential energies $\widehat{V}_i$ are not uniquely defined:

$$\widehat{\mathbf{J}} = \frac{1}{2\Omega}\left\{\sum_i \frac{\widehat{\mathbf{p}}_i}{M_i}\left(\frac{\widehat{\mathbf{p}}_i^2}{2M_i}+\widehat{V}_i\right)+\sum_{i,j}(\widehat{\mathbf{r}}_i-\widehat{\mathbf{r}}_j)\frac{1}{i\hbar}\left[\frac{\widehat{\mathbf{p}}_i^2}{2M_i},\widehat{V}_j\right]\right\}+\text{h.c.}$$

I define the auxiliary quantity

$$\widehat{K}^i(t) = \alpha\int_0^\beta d\lambda\int_0^t dt'\widehat{J}^i(t'-i\hbar\lambda), \tag{3.3}$$

where α is a constant. To derive the quantum Einstein relation, I want to prove that the thermal conductivity κ^{ij} is related to $\text{Re}\langle\widehat{K}^i(t)\widehat{K}^j(t)\rangle$. With the aid of (112)

$$\int_0^y dx_1dx_2\,f(x_1-x_2) = \int_{-y}^y d\gamma\,(y-|\gamma|)f(\gamma), \tag{3.4}$$

one finds

$$\begin{aligned}\text{Tr}\left(\widehat{\rho}(\widehat{K}^i(t)\widehat{K}^j(t))\right) &= \\ &= \alpha^2\int_{-\beta}^\beta d\phi(\beta-|\phi|)\int_{-t}^t d\sigma(t-|\sigma|)\text{Tr}\left(\widehat{\rho}\widehat{J}^i(\sigma-i\hbar\phi)\widehat{J}^j\right).\end{aligned} \tag{3.5}$$

I take the limit $t\to\infty$ of Eq. (3.5) and apply the relation

$$\lim_{t\to\infty}\int_{-t}^t d\sigma\left(1-\frac{|\sigma|}{t}\right)\exp(i\omega\sigma) = 2\pi\delta(\omega). \tag{3.6}$$

In the eigenfunction representation of $\widehat{H}$, I obtain

$$\begin{aligned}&\lim_{t\to\infty}\frac{1}{t}\text{Tr}\left(\widehat{\rho}(\widehat{K}^i(t)\widehat{K}^j(t))\right) = \\ &= 2\pi\hbar\alpha^2\int_{-\beta}^\beta d\phi(\beta-|\phi|)\sum_{\gamma,\xi}\exp(-\beta E_\gamma)\exp((E_\gamma-E_\xi)\phi) \\ &\qquad \delta(E_\gamma-E_\xi)\widehat{J}^i_{\gamma,\xi}\widehat{J}^j_{\xi,\gamma},\end{aligned} \tag{3.7}$$

where $E_{\gamma/\xi}$ is an eigenvalue of $\widehat{H}$ and $\widehat{J}^i_{\gamma,\xi}$ is a matrix element of the heat-flux operator between $\widehat{H}$'s eigenstates $|\xi\rangle$ and $|\gamma\rangle$. The integration is straightforward due to the δ-function, leading to

$$\lim_{t\to\infty}\frac{1}{t}\mathrm{Tr}\left(\widehat{\rho}(\widehat{K}^i(t)\widehat{K}^j(t))\right) = 2\pi\hbar\alpha^2\beta^2\sum_{\gamma,\xi}\exp(-\beta E_\gamma)\delta(E_\gamma - E_\xi)\widehat{J}^i_{\gamma,\xi}\widehat{J}^j_{\xi,\gamma}. \tag{3.8}$$

This limit is identical to the thermal conductivity, as defined in Eq. (2.60), if $\alpha = (\Omega k_B/2\mathrm{Tr}\widehat{\rho})^{1/2}$:

$$\lim_{t\to\infty}\frac{1}{t}\mathrm{Tr}\left(\widehat{\rho}(\widehat{K}^i(t)\widehat{K}^j(t))\right) = \kappa^{ij}. \tag{3.9}$$

This is the quantum Einstein relation, that I wanted to prove.

Now, there is just one more step needed: Assume there are two different heat fluxes, causing two different conductivities, κ^{ii}_1 and κ^{ii}_2, corresponding to $\widehat{K}^i_1$ and $\widehat{K}^i_2$, respectively. I define $\widehat{K}^i_2 - \widehat{K}^i_1 = \widehat{\Psi}^i$. Then

$$\begin{aligned}
\kappa^{ii}_{12} &= \lim_{t\to\infty}\frac{1}{t}\mathrm{Tr}\left(\widehat{\rho}(\widehat{K}^i_1(t) + \widehat{K}^i_2(t))^2\right)\\
&= \kappa^{ii}_1 + \kappa^{ii}_2 + \lim_{t\to\infty}\frac{1}{t}\mathrm{Tr}\left(\widehat{\rho}(\widehat{K}^i_1(t)\widehat{K}^i_2(t) + \widehat{K}^i_2(t)\widehat{K}^i_1(t))\right)\\
&= 2\,(\kappa^{ii}_1 + \kappa^{ii}_2) - \lim_{t\to\infty}\frac{1}{t}\mathrm{Tr}\left(\widehat{\rho}\widehat{\Psi}^i(t)\widehat{\Psi}^i(t)\right)\\
&= 2\,(\kappa^{ii}_1 + \kappa^{ii}_2).
\end{aligned} \tag{3.10}$$

The last step is possible, because $\widehat{\Psi}^i$ is bounded, and t grows infinitely. I will elaborate on this point further below. Comparing the second with the fourth line, I find

$$\lim_{t\to\infty}\frac{1}{t}\mathrm{Tr}\left(\widehat{\rho}(\widehat{K}^i_1\widehat{K}^i_2 + \widehat{K}^i_2\widehat{K}^i_1)\right) = \kappa^{ii}_1 + \kappa^{ii}_2. \tag{3.11}$$

I use the Cauchy-Schwarz inequality

$$4\ \mathrm{Tr}\left(\widehat{\rho}\widehat{A}^2\right)\mathrm{Tr}(\widehat{\rho}\widehat{B}^2) \geq \mathrm{Tr}\left(\widehat{\rho}(\widehat{A}\widehat{B} + \widehat{B}\widehat{A})\right)^2, \tag{3.12}$$

and arrive at:

$$\begin{aligned}
&2\sqrt{\kappa^{ii}_1\kappa^{ii}_2} \geq \kappa^{ii}_1 + \kappa^{ii}_2\\
\Rightarrow\ &0 \geq (\kappa^{ii}_1 - \kappa^{ii}_2)^2 \quad \blacksquare
\end{aligned} \tag{3.13}$$

The invariance of the tensor κ^{ij} follows immediately from Eq. (3.13) which is true for all directions, not just the cartesian axes. Let us assume two different thermal conductivity tensors, κ^{ij}_1 and κ^{ij}_2. According to Eq. (3.13), the diagonal values of both tensors are identical. This holds true for all rotations in space. As both tensors are real

and symmetric (55), their difference A is also symmetric and has an eigenbasis. For this eigenbasis, A must be zero, according to Eq. (3.13). As it vanishes in this basis, it vanishs in general. Therefore, $\kappa_1^{ij} = \kappa_2^{ij}$. ■

Thus, it is finally clear, that the thermal conductivity does not depend on the gauge choice of the local Hamiltonian density $\widehat{\mathcal{H}}(\mathbf{x})$.

I will now elaborate on the assumptions about the bounded operator $\widehat{\Psi}^i$ and how its expectation value can be estimated. The heat-flux operator can be changed, by changing $\widehat{\mathcal{H}}(\mathbf{x})$ that contains a kinetic and a potential part

$$\widehat{\mathcal{H}}(\mathbf{x}) = \widehat{\mathcal{T}}(\mathbf{x}) + \widehat{\mathcal{V}}(\mathbf{x}). \tag{3.14}$$

I define the local kinetic energy of the nuclei as $\widehat{\mathcal{T}}(\mathbf{x}) = \sum_i \widehat{T}_i \delta(\mathbf{x} - \mathbf{r}_i)$, where $\widehat{T}_i$ is the kinetic energy operator of nucleus i. $\widehat{\mathcal{V}}$ can be defined by considering a general many-body Hamiltonian in second quantization in real space (139)

$$\begin{aligned}
\widehat{H} &= \widehat{T} + \widehat{V} \\
&= \widehat{T} + \sum_n \frac{1}{n!} \int_\Omega d\mathbf{x}_1 ... d\mathbf{x}_n \widehat{a}^\dagger_{\mathbf{x}_1} ... \widehat{a}^\dagger_{\mathbf{x}_n} V_n(\mathbf{x}_1 ... \mathbf{x}_n) \widehat{a}_{\mathbf{x}_1} ... \widehat{a}_{\mathbf{x}_n} \\
&= \widehat{T} + \int_\Omega d\mathbf{x}\ \widehat{\mathcal{V}}(\mathbf{x}),
\end{aligned} \tag{3.15}$$

where $\widehat{a}_{\mathbf{x}}$ ($\widehat{a}^\dagger_{\mathbf{x}}$) is a particle destruction (creation) operator. The many-body potential function V_n is not uniquely defined. The freedom in defining V_n leads to a gauge freedom of the heat-flux operator $\widehat{\mathbf{J}}$. An allowed change of $\widehat{\mathbf{J}}$ has the form:

$$\begin{aligned}
\delta\widehat{\mathbf{J}} &= \frac{1}{i\hbar} \left[\frac{1}{\Omega} \int_\Omega d\mathbf{x}\ \mathbf{x} (\widehat{\mathcal{H}}(\mathbf{x}) - \widehat{\mathcal{H}}'(\mathbf{x})), \widehat{H} \right] \\
&= \frac{1}{i\hbar} \left[\frac{1}{\Omega} \int_\Omega d\mathbf{x}\ \mathbf{x} (\widehat{\mathcal{V}}(\mathbf{x}) - \widehat{\mathcal{V}}'(\mathbf{x})), \widehat{H} \right] \\
&= \frac{1}{i\hbar} \left[\widehat{\Phi}, \widehat{H} \right],
\end{aligned} \tag{3.16}$$

where $\widehat{\mathcal{V}}(\mathbf{x})$ has been changed to $\widehat{\mathcal{V}}'(\mathbf{x})$. The operator $\widehat{\Phi}$ is bound, because, following Ref. (4), one cannot assign local interaction energies to particles in macroscopic distance of the interacting particles, because, when partitioning a crystal into macroscopic chunks, the energy of each chunk would be a measurable quantity. As a measurable quantity cannot depend on the specific definition of $\widehat{\mathcal{H}}(\mathbf{x})$, this limits the allowed definitions of $\widehat{\mathcal{H}}(\mathbf{x})$. Assuming that the interaction distance

of particles is smaller than a (macroscopic) constant c, the operator $\widehat{\Phi}$ can be related to the potential energy in the system

$$\begin{aligned}\widehat{\Phi} &= \frac{1}{\Omega}\int_{\Omega} d\mathbf{x}\ \mathbf{x}(\widehat{\mathcal{V}}(\mathbf{x}) - \widehat{\mathcal{V}}'(\mathbf{x})) \\ &\ '\leq' \frac{\mathbf{c}}{\Omega}\int_{\Omega} d\mathbf{x}\ \widehat{\mathcal{V}}(\mathbf{x}) \\ &= \mathbf{c}\widehat{V},\end{aligned} \tag{3.17}$$

where $\leq$ means, that one cannot shift the assigned energy further away than the maximum distance c. Replacing $\widehat{K}^i$ with $\widehat{\Psi}^i$ in Eq. (3.5), one finds (similar to Eq. (3.8))

$$\begin{aligned}\lim_{t\to\infty}\frac{1}{t}\mathrm{Tr}(\widehat{\rho}(\widehat{\Psi}^i(t)\widehat{\Psi}^i(t))) = \\ -2\pi\hbar\alpha^2\beta^2\sum_{\gamma,\xi}\exp(-\beta E_\gamma)\delta(E_\gamma - E_\xi)|\widehat{\Phi}^i_{\gamma,\xi}|^2(E_\gamma - E_\xi)^2.\end{aligned} \tag{3.18}$$

This is zero, because the value of $\widehat{\Phi}^i_{\gamma,\xi}$ is finite. A similar consideration for $\widehat{K}^i$ is not feasible, because the position $\mathbf{x}$ in the system is unbounded, other than c – so the commutator in Eq. (3.2) cannot be separated in the eigenfunction representation as for $\widehat{\Psi}^i$. q.e.d.

3.2 PERTURBATION THEORY

To present the perturbation theory, first the vertex functions are calculated, and then the elementary correlation functions. Both are necessary to define Feynman rules.

3.2.1 *Heat-flux vertex functions*

The definition of the heat-flux operator, from Eq. (2.59)

$$\widehat{\mathbf{J}} = \frac{1}{2\Omega}\left\{\sum_i \frac{\widehat{\mathbf{p}}_i}{M_i}\left(\frac{\widehat{\mathbf{p}}_i^2}{2M_i} + \widehat{V}_i\right) + \sum_{i,j}(\widehat{\mathbf{r}}_i - \widehat{\mathbf{r}}_j)\frac{1}{i\hbar}\left[\frac{\widehat{\mathbf{p}}_i^2}{2M_i}, \widehat{V}_j\right]\right\} + \text{h.c.}$$

is to be Fourier transformed so that the heat-flux vertices can be interpolated in reciprocal space. This reciprocal space interpolation allows (as will be seen later) for a faster convergence of the final result with respect to the size of the simulated (DFT) supercells. This interpolation to a denser $\mathbf{q}$-grid is possible, because the IFCs are short-ranged. I use the following notation:

$$\widehat{p}^{\alpha}_{\kappa,p} = \sqrt{\frac{M_\kappa}{N_p}}\sum_{\mathbf{q}}\exp\left(i\mathbf{q}\cdot(\mathbf{R}_p + \boldsymbol{\tau}_\kappa)\right)\widehat{P}^{\alpha}_{\mathbf{q},\kappa}, \tag{3.19}$$

$$\widehat{u}^{\alpha}_{\kappa,p} = \sqrt{\frac{1}{M_\kappa N_p}} \sum_{\mathbf{q}} \exp\left(i\mathbf{q}\cdot(\mathbf{R}_p + \boldsymbol{\tau}_\kappa)\right) \widehat{U}^{\alpha}_{\mathbf{q},\kappa}. \tag{3.20}$$

This can be translated to the mode representation via

$$\widehat{A}^{\alpha}_{\mathbf{q},\kappa} = \sum_{\nu} e^{\alpha}_{\kappa\nu}(\mathbf{q}) \sqrt{\frac{\hbar}{2\omega_{\mathbf{q}\nu}}} \widehat{A}_{\mathbf{q}\nu}, \tag{3.21}$$

where $\widehat{A}$ is either $\widehat{U}$ or $\widehat{P}$. The Fourier transformation is performed in Appendix H.1. The heat-flux operator can then be written as

$$\widehat{\mathbf{J}} = \frac{1}{2\Omega}\left[\widehat{\mathbf{J}}^1 + \widehat{\mathbf{J}}^2 + \widehat{\mathbf{J}}^3 + \widehat{\mathbf{J}}^4\right] + \text{h.c.}, \tag{3.22}$$

where the operators $\widehat{\mathbf{J}}^1$, $\widehat{\mathbf{J}}^2$, and $\widehat{\mathbf{J}}^4$ can be decomposed into a sum of operators depending on the order of the interatomic force constant that causes the contribution as

$$\widehat{J}^{i,k} = \sum_{n} \widehat{J}^{i,k}_{n}, \tag{3.23}$$

where the n runs over all positive integers. φ^n is given by Eq. (2.42), and I use the convention $\varphi^1 = 0$. The contributions are

$$\widehat{J}^{i,1}_{n-1} = \frac{N_p^{-n/2}}{(n-1)!}(-i)\frac{n-1}{n} \sum_{\{\kappa,\alpha,\mathbf{q}\}} \widehat{P}^{\alpha_1}_{\kappa_1,\mathbf{q}_1} \prod_{l=2}^{n} \widehat{U}^{\alpha_l}_{\kappa_l,\mathbf{q}_l} \times \frac{d}{d\mathbf{q}_n^i}\varphi^n(\mathbf{q}_1,\kappa_1,\alpha_1;\ldots;\mathbf{q}_n,\kappa_n,\alpha_n), \tag{3.24}$$

$$\begin{aligned}\widehat{J}^{i,2}_{n} = {} & \frac{N_p^{-(n+1)/2}}{n!}(1-n) \sum_{\{\kappa,\alpha,\mathbf{q}\}} \widehat{P}^{\alpha_n}_{\kappa_n,\mathbf{q}_n} \widehat{U}^{i}_{\kappa_n,\mathbf{q}_0} \prod_{l=1}^{n-1} \widehat{U}^{\alpha_l}_{\kappa_l,\mathbf{q}_l} M_{\kappa_n}^{-1/2} \\ & \times \varphi^n(\mathbf{q}_1,\kappa_1,\alpha_1;\ldots;\mathbf{q}_0+\mathbf{q}_n,\kappa_n,\alpha_n) \\ & + \frac{N_p^{-(n+1)/2}}{n!}(n-1) \sum_{\{\kappa,\alpha,\mathbf{q}\}} \widehat{P}_{\kappa_n,\alpha_n,\mathbf{q}_n} \widehat{U}^{i}_{\kappa_{n-1},\mathbf{q}_0} \prod_{l=1}^{n-1} \widehat{U}_{\kappa_l,\alpha_l,\mathbf{q}_l} M_{\kappa_{n-1}}^{-1/2} \\ & \times \varphi^n(\mathbf{q}_1,\kappa_1,\alpha_1;\ldots;\mathbf{q}_0+\mathbf{q}_{n-1},\kappa_{n-1},\alpha_{n-1};\mathbf{q}_n,\kappa_n,\alpha_n),\end{aligned} \tag{3.25}$$

$$\widehat{J}^{i,3} = \frac{1}{2} N_p^{-1/2} \sum_{\kappa,\alpha,\{\mathbf{q}\}} M_\kappa^{-1/2} \widehat{P}_{\kappa i\mathbf{q}_1} \widehat{P}_{\kappa\alpha\mathbf{q}_2} \widehat{P}_{\kappa\alpha(-\mathbf{q}_1-\mathbf{q}_2)}, \tag{3.26}$$

and

$$\widehat{J}_n^{i,4} = \frac{N_p^{-(n+1)/2}}{n!} \sum_{\{\kappa,\alpha,\mathbf{q}\}} \widehat{P}^i_{\kappa_n,\mathbf{q}_0} \prod_{l=1}^{n} \widehat{U}^{\alpha_l}_{\kappa_l,\mathbf{q}_l} M_{\kappa_n}^{-1/2} \times \varphi^n(\mathbf{q}_1,\kappa_1,\alpha_1;...;\mathbf{q}_0+\mathbf{q}_n,\kappa_n,\alpha_n). \tag{3.27}$$

For these vertices, I use the following abbreviations

$$\widehat{J}_n^{i,k} = \sum_{\{\kappa,\alpha,\mathbf{q}\}} \widehat{P}^{\alpha_0}_{\kappa_0,\mathbf{q}_0} \prod_{l=1}^{n} \widehat{U}_{\kappa_l,\alpha_l,\mathbf{q}_l} J_n^{i,k}(\mathbf{q}_0,\kappa_0,\alpha_0;...;\mathbf{q}_n,\kappa_n,\alpha_n), \tag{3.28}$$

$$\widehat{J}^{i,3} = \sum_{\{\kappa,\alpha,\mathbf{q}\}} J^{i,3}(\mathbf{q}_1,\kappa_1,\alpha_1;\mathbf{q}_2,\kappa_2,\alpha_2;\mathbf{q}_3,\kappa_3,\alpha_3) \widehat{P}^{\alpha_1}_{\kappa_1,\mathbf{q}_1} \widehat{P}^{\alpha_2}_{\kappa_2,\mathbf{q}_2} \widehat{P}^{\alpha_3}_{\kappa_3,\mathbf{q}_3}, \tag{3.29}$$

$$J_n^i(\mathbf{q}_0,\kappa_0,\alpha_0;...;\mathbf{q}_n,\kappa_n,\alpha_n) = \sum_{k=1,2,4} J_n^{i,k}(\mathbf{q}_0,\kappa_0,\alpha_0;...;\mathbf{q}_n,\kappa_n,\alpha_n). \tag{3.30}$$

The vertex functions of the interaction are given by φ^n. The virial approximation to the heat-flux operator is to neglect $\widehat{J}^{i,3}$ and $\widehat{J}^{i,4}$, which is reasonable for not too high temperatures (230, 231) and is used in some GK-MD simulations (32). Different from any other reference I saw (e.g. (31, 217, 253)) I do not approximate the heat-flux operator as $\widehat{J}_1^{i,1}$.

3.2.2 *Spectral densities and propagators*

After the vertex functions have been transformed, there are four different propagators and spectral densities that occur in the calculation after the Wick contractions have been performed. Symbolically, they are

$$\begin{aligned}
\mathcal{G}^{\hat{P}\hat{P}}(\tau) &= \langle T_\tau \left(\widehat{P}(\tau)\widehat{P}(0) \right) \rangle, \\
\mathcal{G}^{\hat{P}\hat{U}}(\tau) &= \langle T_\tau \left(\widehat{P}(\tau)\widehat{U}(0) \right) \rangle, \\
\mathcal{G}^{\hat{U}\hat{P}}(\tau) &= \langle T_\tau \left(\widehat{U}(\tau)\widehat{P}(0) \right) \rangle, \text{ and} \\
\mathcal{G}^{\hat{U}\hat{U}}(\tau) &= \langle T_\tau \left(\widehat{U}(\tau)\widehat{U}(0) \right) \rangle.
\end{aligned} \tag{3.31}$$

The corresponding spectral densities are $\mathcal{S}^{\widehat{P}\widehat{P}}$, $\mathcal{S}^{\widehat{U}\widehat{P}}$, $\mathcal{S}^{\widehat{P}\widehat{U}}$, and $\mathcal{S}^{\widehat{U}\widehat{U}}$. The interrelations between these objects are derived in Appendix E, and are tabulated here:

$$\begin{aligned}
\mathcal{G}^{r/a,\widehat{P}\widehat{U}}_{\mathbf{q},\nu,\nu'}(\mathcal{E}) &= -\frac{i\mathcal{E}}{\hbar}\mathcal{G}^{r/a}_{\mathbf{q},\nu,\nu'}(\mathcal{E}),\\
\mathcal{G}^{r/a,\widehat{U}\widehat{P}}_{\mathbf{q},\nu,\nu'}(\mathcal{E}) &= \frac{i\mathcal{E}}{\hbar}\mathcal{G}^{r/a}_{\mathbf{q},\nu,\nu}(\mathcal{E}),\\
\mathcal{G}^{r/a,\widehat{P}\widehat{P}}_{\mathbf{q},\nu,\nu'}(\mathcal{E}) &= \frac{\mathcal{E}^2}{\hbar^2}\mathcal{G}^{r/a}_{\mathbf{q},\nu,\nu'}(\mathcal{E}) - 2\omega_{\mathbf{q},\nu}\delta_{\nu,\nu'},\\
\mathcal{S}^{\widehat{P}\widehat{U}}_{\mathbf{q},\nu,\nu'}(\mathcal{E}) &= -\frac{i\mathcal{E}}{\hbar}\mathcal{S}_{\mathbf{q},\nu,\nu'}(\mathcal{E}),\\
\mathcal{S}^{\widehat{U}\widehat{P}}_{\mathbf{q},\nu,\nu'}(\mathcal{E}) &= -\mathcal{S}^{\widehat{P}\widehat{U}}_{\mathbf{q},\nu,\nu'}(\mathcal{E}), \text{ and}\\
\mathcal{S}^{\widehat{P}\widehat{P}}_{\mathbf{q},\nu,\nu'}(\mathcal{E}) &= \frac{\mathcal{E}^2}{\hbar^2}\mathcal{S}_{\mathbf{q},\nu,\nu'}(\mathcal{E}).
\end{aligned} \tag{3.32}$$

These relations hold, importantly, for the interacting system. That means, if the standard phonon-propagator is known, all occurring contractions can be computed right away. The interacting phonon propagator is obtained from Dyson's equation, as explained in Sec. 2.2.5 (and Sec. 5.2).

The phonon propagator and spectral density, corresponding to operators $\widehat{U}_{\mathbf{q}\nu}$ and $\widehat{U}^{\alpha}_{\mathbf{q}\kappa}$, can be related as well (K is $\mathcal{G}$ or $\mathcal{S}$),

$$K^{\alpha\alpha'}_{\mathbf{q}\kappa\kappa'}(\mathcal{E}) = \frac{\hbar}{2}\sum_{\nu\nu'} e^{\alpha}_{\kappa\nu}(\mathbf{q})e^{\alpha'}_{\kappa'\nu'}(-\mathbf{q})(\omega_{\mathbf{q}\nu}\omega_{\mathbf{q}\nu'})^{-1/2}K_{\mathbf{q}\nu\nu'}(\mathcal{E}). \tag{3.33}$$

$K^{\alpha\alpha'}_{\mathbf{q}\kappa\kappa'}(\mathcal{E})$ is written in the *displacement basis*, while $K_{\mathbf{q}\nu\nu'}(\mathcal{E})$ is in the *mode basis*.

3.2.3 *Correlation function*

To calculate $\Pi^{ij}_M(E)$, first note, that the heat-flux operator is no monomial in the operators $\widehat{U}$ and $\widehat{P}$. The heat-flux operator can be written as

$$\widehat{J}^i = \sum_l \phi^i_l \widehat{\mathcal{O}}_l, \tag{3.34}$$

and $\widehat{\mathcal{O}}_l$ is a monomial in $\widehat{U}$ and $\widehat{P}$. In consequence, Π^{ij}_M can be written as a sum

$$\begin{aligned}
\Pi^{ij}_M(\tau-\tau') &= -\Omega\langle T_\tau\left(\widehat{J}^i(\tau)\widehat{J}^j(\tau')\right)\rangle\\
&= -\Omega\sum_{l,l'}\phi^i_l\phi^j_{l'}\langle T_\tau\left(\widehat{\mathcal{O}}_l(\tau)\widehat{\mathcal{O}}_{l'}(\tau')\right)\rangle\\
&= \sum_{l,l'}\phi^i_l\phi^j_{l'}\Pi^M_{l,l'}(\tau-\tau').
\end{aligned} \tag{3.35}$$

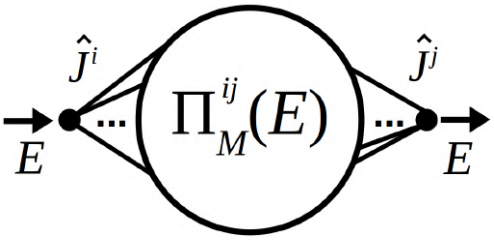

Figure 3.1: Diagrams corresponding to the correlation function $\Pi_M^{ij}(E)$. The frequency entering the external vertex to the left, is the sum of the other frequencies at this vertex. $\hat{J}$ must be replaced by any $\hat{\mathcal{O}}_l$, and every possible diagram has to be drawn.

The decomposition is possible for any $\tau - \tau'$, so it can be done in general (even though T_τ is not linear). The subscripts l and l' stand for operators $\hat{\mathcal{O}}_l$ that are monomials in the momentum and displacement operators of the phonons. The starting point for drawing diagrams for $\Pi^M_{l,l'}$ is then, that the construction operators for $\hat{\mathcal{O}}_l$ stand to the left and the operators for $\hat{\mathcal{O}}_{l'}$ to the right. $\Pi^M_{l,l'}(\tau)$ can be represented by its Matsubara components Eq. (2.23)

$$\Pi^M_{l,l'}(\tau) = \frac{1}{\hbar\beta} \sum_{\{E,\tilde{E}\}} \exp\left(-\hbar^{-1} \sum_{j=1}^{s} E_j \tau\right) \Pi^M_{l,l'}(E_1, ..., E_s, \tilde{E}_1, ..., \tilde{E}_{s'}), \tag{3.36}$$

where $\hat{\mathcal{O}}_l$ is a monomial of s operators. The Matsubara transform of this object is

$$\begin{aligned} \Pi^M_{l,l'}(E) &= \int_0^{\hbar\beta} \Pi^M_{l,l'}(\tau) \exp\left(\hbar^{-1} E\tau\right) d\tau \\ &= \sum_{\{E,\tilde{E}\}} \delta_{(E - \sum_{j=1}^{s} E_j)} \Pi^M_{l,l'}(E_1, ..., E_s, \tilde{E}_1, ..., \tilde{E}_{s'}). \end{aligned} \tag{3.37}$$

Hence, the diagrams that I need to draw, are connected diagrams, as depicted in Fig. 3.1. The energies at the $\hat{\mathcal{O}}_l$ ($\hat{\mathcal{O}}_{l'}$) vertex sum up to $+E$ ($-E$). The vertex of the operator $\hat{\mathcal{O}}_l$ does not conserve the Matsubara energy of the connected contractions. This is very similar to the calculation of the electrical conductivity presented in Ref. (166).

To summarize, the Feynman rules to compute the correlation function $\Pi^{ij}_M(E)$ in the following way:

- An interaction vertex has the value $-\beta\varphi^n$.
- A heat-flux vertex has the value J^i_n with n $\hat{U}$-arms and one $\hat{P}$ or it has the value $J^{i,3}$ and three $\hat{P}$-arms.
- A propagator has the value $(\hbar\beta)^{-1}\mathcal{G}^{M,\hat{A}\hat{B}}_{\mathbf{q},\kappa,\alpha,\kappa',\alpha'}(E)$. It has, at the beginning, its own Matsubara energy and momentum. $\hat{A}$ and $\hat{B}$ can be either $\hat{P}$ or $\hat{U}$. After the application of the conservation of

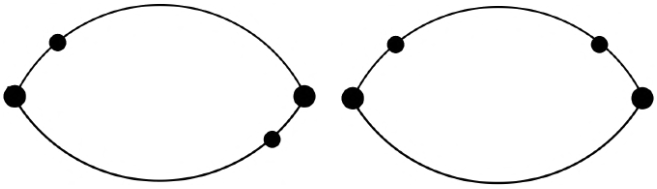

Figure 3.2: Diagrams that correspond to the BTE. The dot on the line denotes a $\widehat{P}$-contraction. The propagators are dressed, such that the lifetime of the phonons is finite. The vertices to the left and right correspond to $\widehat{J}_1^{i,1}$.

momenta and energies at the vertices, the Matsubara energies and momenta become dependent on each other.

- An overall factor of $(-\hbar\beta)$ has to be multiplied.
- Every interaction vertex conserves the crystal momentum and Matsubara energies of the connected contractions.
- Heat-flux vertices conserve the crystal momentum of the connected contractions. The sum of the energies on these vertices is the argument of the correlation function $\Pi_M^{ij}(E)$.
- All crystal momenta are to be integrated, and all Matsubara energies (but the argument of the correlation function) are to be summed.

A similar definition in the mode representation is equally possible.

3.3 IMPROVED BOLTZMANN TRANSPORT EQUATION

With the aid of the Feynman rules a BTE can be obtained from the formalism developed above. The starting point are the two diagrams that contribute to the lattice thermal conductivity to first order, shown in Fig. 3.2. The corresponding vertex function was calculated above and can be written as

$$\widehat{J}_1^{i,1} = -\frac{i\hbar}{2} \sum_{\mathbf{q}\nu\nu'} \widehat{P}_{-\mathbf{q}\nu} \widehat{U}_{\mathbf{q},\nu'} J_1^{i,1}(-\mathbf{q},\nu;\mathbf{q},\nu'). \tag{3.38}$$

In Appendix H.1.1, it is shown, that if this is approximated by diagonal terms then

$$\widehat{J}_1^{i,1} \approx -\frac{i\hbar}{2} \sum_{\mathbf{q}\nu} \widehat{P}_{-\mathbf{q}\nu} \widehat{U}_{\mathbf{q},\nu} \partial_{\mathbf{q}} \omega_{\mathbf{q},\nu}. \tag{3.39}$$

The task is now to evaluate the diagrams, shown in Fig. 3.2. With the Feynman rules, I write them as

$$D_1^{M,ij}(E) = -\frac{1}{\hbar N_p \Omega_c \beta} \sum_{\mathbf{q},\{\nu\}} J_1^{i,1}(-\mathbf{q},\nu_1;\mathbf{q},\nu_4) J_1^{j,1}(-\mathbf{q},\nu_3;\mathbf{q},\nu_2) \times \left(\sum_{E_1} \mathcal{G}^{M,\widehat{P}\widehat{U}}_{-\mathbf{q},\nu_1,\nu_2}(-E_1) \mathcal{G}^{M,\widehat{U}\widehat{P}}_{\mathbf{q},\nu_4,\nu_3}(E+E_1) \right). \tag{3.40}$$

Ω_c is the volume of the unit cell. The second diagram is

$$D_2^{M,ij}(E) = -\frac{1}{\hbar N_p \Omega_c \beta} \sum_{\mathbf{q},\{\nu\}} J_1^{i,1}(\mathbf{q},\nu_1;-\mathbf{q},\nu_4) J_1^{j,1}(-\mathbf{q},\nu_2;\mathbf{q},\nu_3) \times \left(\sum_{E_1} \mathcal{G}^{M}_{-\mathbf{q},\nu_4,\nu_3}(-E_1) \mathcal{G}^{M,\widehat{P}\widehat{P}}_{\mathbf{q},\nu_1,\nu_2}(E+E_1) \right). \tag{3.41}$$

For $D_2^{M,ij}(E)$ one of the vertex momenta is flipped (and that the vertex function $J_1^{i,1}$ is odd under momentum inversion). Then the task is to execute $\sum_{E_1}$. For this I use Eq. (2.26):

$$\begin{aligned} I^{M,ab}_{\mathbf{q}\nu_1\nu_2\nu_3\nu_4}(E) &= \sum_{E_1} \mathcal{G}^{a}_{-\mathbf{q},\nu_1\nu_2}(-E_1) \mathcal{G}^{b}_{\mathbf{q},\nu_3\nu_4}(E+E_1) \\ &= \sum_{E_1} \int_{\mathbb{R}} d\mathcal{E}_0 d\mathcal{E}_1 \frac{\mathcal{S}^{a}_{-\mathbf{q},\nu_1\nu_2}(\mathcal{E}_0)}{-E_1-\mathcal{E}_0} \frac{\mathcal{S}^{b}_{\mathbf{q},\nu_3\nu_4}(\mathcal{E}_1)}{(E_1+E)-\mathcal{E}_1}. \end{aligned} \tag{3.42}$$

I take the sum in and execute it:

$$\sum_{E_1} \frac{1}{-E_1-\mathcal{E}_0} \frac{1}{(E_1+E)-\mathcal{E}_1} = -\beta \frac{n_B(\mathcal{E}_0)+n_B(\mathcal{E}_1)}{\mathcal{E}_1+\mathcal{E}_0+E}. \tag{3.43}$$

This can be analytically continued and reinserted:

$$I^{r,ab}_{\mathbf{q}\nu_1\nu_2\nu_3\nu_4}(\mathcal{E}) = -\beta \int_{\mathbb{R}} d\mathcal{E}_0 d\mathcal{E}_1 \mathcal{S}^{a}_{-\mathbf{q},\nu_1\nu_2}(\mathcal{E}_0) \mathcal{S}^{b}_{\mathbf{q},\nu_3\nu_4}(\mathcal{E}_1) \frac{n_B(\mathcal{E}_0)+n_B(\mathcal{E}_1)}{\mathcal{E}_1+\mathcal{E}_0+\mathcal{E}+i0^+}. \tag{3.44}$$

I need to take the imaginary part of the diagram, as given by Eq. (2.61). This can be done by solely taking the imaginary part of the denominator in the equation, see Appendix I. Then

$$\begin{aligned} \mathrm{Im}(I^{r,ab}_{\mathbf{q}\nu_1\nu_2\nu_3\nu_4}(\mathcal{E})) &= \pi\beta \int_{\mathbb{R}} d\mathcal{E}_0 d\mathcal{E}_1 \mathcal{S}^{a}_{-\mathbf{q},\nu_1\nu_2}(\mathcal{E}_0) \mathcal{S}^{b}_{\mathbf{q},\nu_3\nu_4}(\mathcal{E}_1) \\ &\qquad \times (n_B(\mathcal{E}_0)+n_B(\mathcal{E}_1))\, \delta(\mathcal{E}_1+\mathcal{E}_0+\mathcal{E}) \\ &= \pi\beta \int_{\mathbb{R}} d\mathcal{E}_0 \mathcal{S}^{a}_{-\mathbf{q},\nu_1\nu_2}(\mathcal{E}_0) \mathcal{S}^{b}_{\mathbf{q},\nu_3\nu_4}(-\mathcal{E}_0-\mathcal{E}) \\ &\qquad \times (n_B(\mathcal{E}_0)-n_B(\mathcal{E}_0+\mathcal{E}))\,. \end{aligned} \tag{3.45}$$

The fact that the occupation n_B is an odd function has been used. If now the limit in Eq. (2.61) is taken, one obtains (if the spectral densities are well-behaved)

$$\lim_{\mathcal{E}\to 0} -\frac{\mathrm{Im}(I^{r,ab}_{\mathbf{q}\nu_1\nu_2\nu_3\nu_4}(\mathcal{E}))}{\mathcal{E}} = \pi\beta \int_{\mathbb{R}} d\mathcal{E}_0 \mathcal{S}^{a}_{-\mathbf{q},\nu_1\nu_2}(\mathcal{E}_0)\mathcal{S}^{b}_{\mathbf{q},\nu_3\nu_4}(-\mathcal{E}_0)n'_B(\mathcal{E}_0). \tag{3.46}$$

It is time to set $a = \widehat{P}\widehat{U}$ and $b = \widehat{U}\widehat{P}$ and $a = \widehat{U}\widehat{U}$ and $b = \widehat{P}\widehat{P}$, respectively and use the relations between the spectral densities:

$$\begin{aligned}
\lim_{\mathcal{E}\to 0} -\frac{\mathrm{Im}(I^{r,\widehat{U}\widehat{P},\widehat{P}\widehat{U}}_{\mathbf{q}\nu_1\nu_2\nu_3\nu_4}(\mathcal{E}))}{\mathcal{E}} &= \\
&= \hbar^{-2}\pi\beta \int_{\mathbb{R}} d\mathcal{E}_0 \mathcal{E}_0^2 \mathcal{S}_{-\mathbf{q},\nu_1\nu_2}(\mathcal{E}_0)\mathcal{S}_{\mathbf{q},\nu_3\nu_4}(-\mathcal{E}_0)n'_B(\mathcal{E}_0) \\
&= -\hbar^{-2}\pi\beta \int_{\mathbb{R}} d\mathcal{E}_0 \mathcal{E}_0^2 \mathcal{S}_{\mathbf{q},\nu_2\nu_1}(\mathcal{E}_0)\mathcal{S}_{\mathbf{q},\nu_3\nu_4}(\mathcal{E}_0)n'_B(\mathcal{E}_0) \\
&= -\lim_{\mathcal{E}\to 0} -\frac{\mathrm{Im}(I^{r,\widehat{U}\widehat{U},\widehat{P}\widehat{P}}_{\mathbf{q}\nu_1\nu_2\nu_3\nu_4}(\mathcal{E}))}{\mathcal{E}}.
\end{aligned} \tag{3.47}$$

In general, the BTE becomes

$$\begin{aligned}
\kappa^{ij}_{\mathrm{BTE}} = \frac{\pi\hbar}{2N_p\Omega_c} \sum_{\mathbf{q}\{\nu\}} & J^{i,1}_1(-\mathbf{q},\nu_1;\mathbf{q},\nu_4)J^{j,1}_1(-\mathbf{q},\nu_3;\mathbf{q},\nu_2) \\
& \times \int_{\mathbb{R}} d\mathcal{E}\mathcal{E}^2 \mathcal{S}_{\mathbf{q},\nu_1,\nu_2}(\mathcal{E})\mathcal{S}_{\mathbf{q},\nu_3,\nu_4}(\mathcal{E})n'_B(\mathcal{E}),
\end{aligned} \tag{3.48}$$

which may also be expressed in the displacement basis.

Now, the BTE-RTA will be derived from this expression in the quasi-harmonic limit. I assume the case of weak interaction. The only region where the spectral density is large is near $\mathcal{E}_0 = \hbar\omega_{\mathbf{q},\nu}$. In this region, one may approximate (Eq. (2.56))

$$\mathcal{S}_{\mathbf{q},\nu,\nu'}(\mathcal{E}) \approx \frac{\hbar\delta_{\nu,\nu'}}{\pi} \frac{\mathrm{Im}(\Sigma^{\mathrm{ret}}_{\mathbf{q},\nu,\nu}(\hbar\omega_{\mathbf{q},\nu}))}{(\mathcal{E}-\hbar\omega_{\mathbf{q},\nu})^2 + \mathrm{Im}(\Sigma^{\mathrm{ret}}_{\mathbf{q},\nu,\nu}(\hbar\omega_{\mathbf{q},\nu}))^2}. \tag{3.49}$$

In the peak-region, one has

$$\begin{aligned}
\mathcal{E}_0^2 &\approx (\hbar\omega_{\mathbf{q},\nu})^2, \\
n'_B(\mathcal{E}_0) &\approx n'_B(\hbar\omega_{\mathbf{q},\nu}).
\end{aligned} \tag{3.50}$$

On top of this, I only consider diagonal terms of the heat-flux operator. In this approximation, the integral can be carried out (if not all indices are identical, the integral must vanish):

$$\begin{aligned}\lim_{\mathcal{E}\to 0} -\frac{\mathrm{Im}(I^{r,\widehat{U}\widehat{P},\widehat{P}\widehat{U}}_{\mathbf{q}\nu_1\nu_1\nu_1\nu_1}(\mathcal{E}))}{\mathcal{E}} &\approx \\ &\approx -2\hbar^{-2}\pi\beta(\hbar\omega_{\mathbf{q},\nu_1})^2 n'_B(\hbar\omega_{\mathbf{q},\nu_1})\int_0^\infty d\mathcal{E}_0 \mathcal{S}_{\mathbf{q},\nu_1,\nu_1}(\mathcal{E}_0)^2 \\ &\approx -\hbar^{-2}\beta(\hbar\omega_{\mathbf{q},\nu_1})^2 n'_B(\hbar\omega_{\mathbf{q},\nu_1})\mathrm{Im}(\Sigma^{\mathrm{ret}}_{\mathbf{q},\nu_1,\nu_1}(\hbar\omega_{\mathbf{q},\nu_1}))^{-1}.\end{aligned} \tag{3.51}$$

Inserting this into the equations for the diagrams leads to

$$\begin{aligned}\lim_{\mathcal{E}\to 0} -\frac{D_1^{ij}(\mathcal{E})+D_2^{ij}(\mathcal{E})}{\mathcal{E}} \approx -\frac{\hbar}{2N_p\Omega_c}\sum_{\mathbf{q}\nu}(\hbar\omega_{\mathbf{q}\nu})^2\left(\partial_{\mathbf{q}}\omega_{\mathbf{q}\nu}\right)^i\left(\partial_{\mathbf{q}}\omega_{\mathbf{q}\nu}\right)^j \\ \times n'_B(\hbar\omega_{\mathbf{q}\nu})\mathrm{Im}(\Sigma^{\mathrm{ret}}_{\mathbf{q},\nu,\nu}(\hbar\omega_{\mathbf{q},\nu}))^{-1}.\end{aligned} \tag{3.52}$$

I introduce the mode heat-capacity (95)

$$C_{\mathbf{q},\nu} = -\frac{(\hbar\omega_{\mathbf{q},\nu})^2}{T}n'_B(\hbar\omega_{\mathbf{q},\nu}), \tag{3.53}$$

to finally obtain the standard BTE-RTA,

$$\kappa^{ij}_{\mathrm{BTE}} \approx \frac{1}{N_p\Omega_c}\sum_{\mathbf{q}\nu}\left(\partial_{\mathbf{q}}\omega_{\mathbf{q}\nu}\right)^i\left(\partial_{\mathbf{q}}\omega_{\mathbf{q}\nu}\right)^j C_{\mathbf{q},\nu}\tau_{\mathbf{q},\nu}. \tag{3.54}$$

In Ref. (244) it has been shown, that the BTE-RTA can be obtained from a very similar formalism (102), but they did not find the improved BTE. In contrast, Refs. (31, 246) present a formula very similar to the one to be found in this section. However, off-diagonal elements of the spectral density have been neglected in their derivations.

3.4 GOING BEYOND THE BTE

After I have shown that the above formalism correctly recovers the BTE in the RTA, it is now the task to go beyond the BTE. Indeed, the BTE cannot give insight whether a perturbation expansion leads to a reasonable result. To make a more justified judgement, it is necessary to compute higher terms of the expansion as well. If these higher terms give a significantly smaller contribution than the BTE, it can be claimed that the BTE yields a good approximation to the investigated quantity, in the spirit of Ref. (25) and similar to most approaches in condensed matter physics (108, 110) (see also Appendix F).

To obtain the second order contribution to the thermal conductivity it is necessary to include other heat-flux and interaction vertices. These additional vertices give rise to a plenty of different diagrams that must

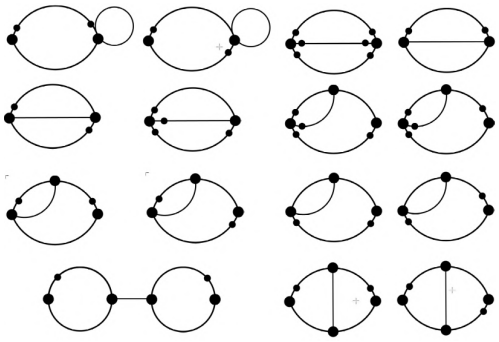

Figure 3.3: Some diagrams of the second-order correction of the lattice thermal conductivity. There exist numerous other diagrams that need to be considered for the heat-flux autocorrelation function.

be evaluated, as depicted in the Fig. 3.3. The diagrams shown there only contain dressed propagators. All these diagrams need two Matsubara summations. The number of symbolic manipulations makes it really hard for a human being to solve these diagrams explicitly by hand. It would be an error-prone, Sisyphean task. To speed up the development, safe effort, and improve reliability, I decided to build a computer algebra system (CAS) to generate all contributing diagrams and identify them with mathematical expressions. The next section of this manuscript will guide through the functionality of the CAS.

The idea of going beyond the BTE is not new (253), but the attempt to actually calculate all second-order diagrams, especially without an approximation, is novel, to the best of my knowledge.

4

SYMBOLIC DERIVATIONS AND COMPUTER ALGEBRA

The CAS that I have planned and developed aims at generating equations for the lattice thermal conductivity up to second order perturbation theory as well as source-code for their numerical evaluation. To obtain these equations, I start in Sec. 4.1 with the expectation values that contribute to $\Pi^{ij}_M(E)$, according to the Sec. 3.2.3. These are then expanded in the interaction up to second loop order using Eq. (2.33). The expectation values are Wick-contracted by Eq. (2.35) and interpreted as Feynman diagrams. The set of Feynman diagrams is then reduced in Sec. 4.2. The diagrams are transferred to mathematical objects in Sec. 4.3, using the Feynman rules, defined in Sec. 3.2.3. Finally, the resulting term objects are manipulated to make them numerically tractable, and they are automatically coded into `Fortran`. All occurring calculations will be presented with examples, that are as simple as possible. The corresponding `beyBol` package (the beyond Boltzmann package) together with the full second order calculation is available (126). [1]

There exist many automated diagram calculators in quantum field theory. Most of them are restricted to first loop order, for different quantities of interest (28, 51, 68, 99). For special theories, other approaches for the generation of Feynman diagrams exist (53, 89, 135, 140), as well as general group-theoretical approaches (198). In this work, I aim at second order at finite temperature. While I did tests on the third order contribution, I did not attempt to solve the corresponding integral, as the solution of the second order already exhausts my computational resources and would be tiny compared to the third order contribution.

The CAS is written in `Python` and uses concepts of object-oriented programming (OOP) (178) throughout. The classes of the subsystems are organized to mimic the construction of expressions usual to many-body theory (see Sec. 2):

- `ExpectationValue` objects are created at the beginning of the calculation, to contain all contributions up to a certain complexity (here the second order). These `ExpectationValues` are stored in an instance of a list class (`ExpectationValueList`) that is responsible for executing the Wick-contractions.
- The fully contracted `ExpectationValue` objects are used to initialize `FeynmanDiagram` objects, that are stored in the FeynmanDiagramList.

1 The source code and the full second order derivation can be obtained upon request.

- Finally, `Term` objects are initialized using `FeynmanDiagrams`. All `Term` objects are stored in a `TermList`.

While the objects, such as the `FeynmanDiagrams`, have methods that manipulate themself, the corresponding list classes are used to store the set of objects and manipulate the ensemble of objects together. The list classes are `Singleton` objects.

4.1 EXPECTATION VALUES

As a first step, I identify which expectation values can contribute to the thermal conductivity at the given order of approximation. Those are the expectation values that lead to terms with at most two Brillouin zone or Matsubara summations. The number of Brillouin zone or Matsubara summations is just the number of loops of the corresponding diagram: The number of conditions to be fulfilled by the loop momenta is the number of vertices $V = \sum_n v_n$, where v_n is the number of each vertex type. As the diagram is connected, there is one condition trivially fulfilled, because the others are. The number of independent energies/momenta at the beginning equals the number of propagators P. As each propagator connects to two vertex legs, the number of propagators is half the number of vertex legs of the diagram

$$L = P - (V - 1) = 1 + \sum_n v_n \left(\frac{l_n}{2} - 1 \right), \tag{4.1}$$

where l_n is the number of legs of a vertex. This L is just identical to the circuit rank of the corresponding graph (i.e. the number of loops). So, given the number of vertices v_n of each type n, the number of loops is fixed, and all combinations $\{v_1, ...v_n\}$ that lead to $L \leq 2$ are generated.

In our example of the heat-flux autocorrelation, the heat-flux vertex has contributions of the type $\widehat{P}\widehat{U}^m$ with $m \geq 1$ and $\widehat{P}\widehat{P}\widehat{P}$. The interactions I consider stem from the third and fourth order term of the BO surface, corresponding to $\widehat{U}^n$, $n = 3, 4$. So, one contribution to Π_M^{ij} can be written as (strongly simplified notation)

$$\left\langle T_\tau \left(\widehat{P}(\tau)\widehat{U}(\tau)\widehat{U}(\tau) \right) \left(\widehat{P}(\tau')\widehat{U}(\tau') \right) \right\rangle. \tag{4.2}$$

This is then expanded via Eq. (2.33) - with only one contribution of the form

$$\int d\tau_1 \langle T_\tau \left(\widehat{P}(\tau)\widehat{U}(\tau)\widehat{U}(\tau) \right) \left(\widehat{U}(\tau_1)\widehat{U}(\tau_1)\widehat{U}(\tau_1) \right) \left(\widehat{P}(\tau')\widehat{U}(\tau') \right) \rangle^{(0)}. \tag{4.3}$$

At that stage it is possible to start Wick-contracting the expectation values, as explained in Sec. 2.2.2. In order to implement this, I resort to an algorithm, described in Ref. (292). To represent the expectation

value at each step of the algorithm, I define three classes, implemented in the `beyBol` package:

1. A `BaseOperator` object (an enumerated type), that corresponds either to $\widehat{U}$ or $\widehat{P}$.
2. A `CompositeOperator` type, that contains a list of `BaseOperator` objects and an index for the time argument. It corresponds to an interaction or a heat-flux vertex.
3. A `Contraction` class, that contains two `BaseOperator` objects and two time indices.

One may further simplify the notation of the upper example ($\tau = \tau_0$ and $\tau_2 = \tau'$):

$$\langle T_\tau \left(\widehat{P}_0\widehat{U}_0\widehat{U}_0\right)\left(\widehat{U}_1\widehat{U}_1\widehat{U}_1\right)\left(\widehat{P}_2\widehat{U}_2\right)\rangle^{(0)}. \tag{4.4}$$

An `ExpectationValue` is then initialized with two lists: one with the contained `CompositeOperator` objects (here 3), and a list for the `Contraction` objects, which is empty at the beginning.

One may apply the Wick-contraction algorithm of Ref. (292) to this example. It takes the first `BaseOperator` of the first `CompositeOperator`, and contracts it with all other `BaseOperators` that appear in the expectation value. To reduce the workload, a multiplicity is stored with the expectation value, such that identical contractions are stored only once. For example, contracting $\widehat{P}_0$ with any of the $\widehat{U}_1$'s results in a contribution

$$3\langle T_\tau \left(\widehat{U}_0\widehat{U}_0\right)\left(\widehat{U}_1\widehat{U}_1\right)\left(\widehat{P}_2\widehat{U}_2\right)\rangle^{(0)}\left\{\langle T_\tau\widehat{P}_0\widehat{U}_1\rangle^{(0)}\right\}, \tag{4.5}$$

where any object in the curly braces is a contraction. In the second step one of the contributions is (by contracting the leftmost operators)

$$3\langle T_\tau() \left(\widehat{U}_1\widehat{U}_1\right)\left(\widehat{P}_2\widehat{U}_2\right)\rangle^{(0)}\left\{\langle T_\tau\widehat{P}_0\widehat{U}_1\rangle^{(0)}\langle T_\tau\widehat{U}_0\widehat{U}_0\rangle^{(0)}\right\}. \tag{4.6}$$

The Wick contraction process is iterated until there are no operators to be contracted (here: outside the curly braces).

At the end of the procedure, every `ExpectationValue` only contains `Contraction` objects, but no `CompositeOperator` objects that have a non-empty `BaseOperator` list. To second order in perturbation theory, there is a large number of these expectation values to handle, after the Wick contractions are finished. These fully contracted `ExpectationValues` can then be used to initialize `FeynmanDiagram` objects.

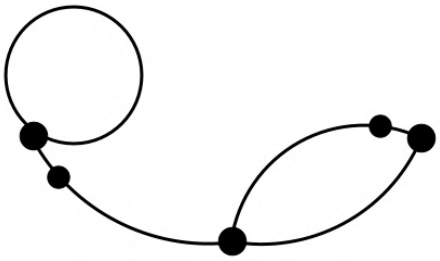

Figure 4.1: Diagram corresponding to the expectation value in Eq. (4.7).

4.2 FEYNMAN DIAGRAMS

To identify an expectation value with a Feynman diagram, the Wick contractions have to be continued to the end. Say, I contracted the above expectation value Eq. (4.6) further to find

$$3\left\{\langle T_\tau \hat{P}_0 \hat{U}_1\rangle^{(0)}\langle T_\tau \hat{U}_0 \hat{U}_0\rangle^{(0)}\langle T_\tau \hat{U}_1 \hat{P}_2\rangle^{(0)}\langle T_\tau \hat{U}_1 \hat{U}_2\rangle^{(0)}\right\}. \tag{4.7}$$

Then, every index can be interpreted as a vertex, and the expectation values are the propagators, i.e. the lines between the vertices of the diagram. The propagators are graphically represented as in Fig. 2.2 (Sec. 2.2.3), and the diagram corresponding to Eq. (4.7) is shown in Fig. 4.1. The simple graphical form of the diagrams enables to identify similar contributions to the perturbation expansion, via a normal form of Feynman diagrams. As normal forms will occur later in the manipulation of terms, I construct them here step by step.

A *normal form* is a unique representation of an object, such that two objects that are *similar* in some sense, can be identified with each other.

For example, two diagrams are said to be similar, if there exists a relabeling of the integrated Matsubara times such that the diagrams are identical, except for the multiplicity. For example, they may have a different multiplicity and different vertex labelings (time 1 in the above example may be called time 3), but are otherwise identical. If both these diagrams are brought to a normal form, they can be identified with each other. Then the list of Feynman diagrams is updated, by adding up the multiplicities, and deleting one of the diagrams from the list. I construct now the normal form for the diagrams.

To do this, the first thing I need is to define an order relation "<" for an object, e.g. a `BaseOperator`. I arbitrarily define that

$$\hat{P} < \hat{U} \tag{4.8}$$

is true, while any other comparison ($\hat{U} < \hat{P}$, $\hat{U} < \hat{U}$ or $\hat{P} < \hat{P}$) is wrong. This can be implemented in `Python`, using the magic method *__lt__*. In general, two objects A and B are *similar*, if not $A < B$ and not $B < A$.

From the order relation of a sub-object, the order relation of a composed object can be found, for example, as follows: A contraction, may have the the form

$$\langle T_\tau \widehat{U}_0 \widehat{P}_1 \rangle^{(0)}. \tag{4.9}$$

To define an order relation for contractions, I first define an order relation on an operator-index set (an operator with a time argument), that is, the index is dominant over the operator type, e.g. $\widehat{U}_0 < \widehat{P}_1$ and $\widehat{P}_1 < \widehat{P}_2$. The contraction above is identical to

$$\langle T_\tau \widehat{P}_1 \widehat{U}_0 \rangle^{(0)}. \tag{4.10}$$

To uniquely identify two contractions with the order relation, I define a *normal form of a contraction*: The first operator-index set must not be larger than the second, according to "<". Then I may define an order relation on contraction objects (in their normal form) as: If the first operator-index set of the first contraction O_1^1 is not similar to the first operator-index set of the second contraction O_2^1, then if $O_1^1 < O_2^1$ the first contraction C_1 and the second contraction C_2 fulfill $C_1 < C_2$. Otherwise if $O_2^1 < O_1^1$, then $C_2 < C_1$. If the first two operator-index sets are similar, then I start comparing the second set. If they are similar as well, the two contractions must be similar. As a result, I derived an order relation for contractions. The type of comparison, that I compare first the first elements, then the second, and so forth, I call *element-wise comparison*. This is easily implemented in an OOP language, such as `Python`.

The order relation of the Feynman diagrams can then be derived, by using the order relation of the contractions. A diagram is practically a list of contractions, and one multiplicity. The multiplicity does not matter for the similarity. To compare two diagrams, the first step is to order the list of contractions in each diagram, according to "<" of the contractions. Then, two diagrams can be compared, by comparing their contractions element-wise, which defines again an order relation. For the similarity of two diagrams, the labeling of the vertices is arbitrary. Then, it is possible to define a *normal form of a Feynman diagram*: For each diagram D, I count the number of vertices V_D of the diagram. Then, the vertex labels may be any permutation of the set $\{1, ...V_D\}$. For each permutation p, a diagram copy D_p is generated. For each D_p the list of contractions is ordered according to the order relation of the contractions. The normal form of the diagram D is a diagram copy D^* that fulfills (not $D_p < D^*$) for all p. A normal form always exists, and, if a number of permutations fulfill the upper relation, then the resulting diagram objects must be similar, as < constitutes an order relation.

Assume I have a set of `FeynmanDiagrams`, stored in the FeynmanDiagramList. If all `FeynmanDiagrams` are in normal form (achieved using the method `apply_normal_form`), it is possible to automatically identify similar diagrams using "<". If two diagrams are similar, the

multiplicity of one of them is updated to be the sum of both, and the other diagram is deleted. After this procedure, there remain numerous diagrams that vanish and are deleted, as listed in Appendix K for different reasons. With this reduced `FeynmanDiagramList`, I move forward to initialize a `TermList`, that contains the mathematical expressions of interest.

4.3 TERM OBJECTS

The `Term` and `TermList` class are by far the most complicated in `beyBol`'s CAS. The `Term` object contains a `Prefactor` and multiple lists that contain mathematical objects. The corresponding classes are `Denominator`, `OccupationFactor`, `Propagator`, `SpectralDensity` and `Vertex` such that each occurring mathematical object has its own list.

As all mathematical functions here contain an argument, I resort to `sympy` (180) to manipulate the argument objects. All classes that correspond to mathematical objects have a method to generate a LaTeX-string for themself, that enables to print the intermediate results of the calculation. This is central to validate the CAS. To exemplify mathematical manipulations, I will use the Boltzmann transport contribution D_1 whenever possible. Where it is not possible, I will use a contribution from the diagram shown in Fig. J.1 - but not to disrupt the flow of reading, the entire corresponding calculation is moved to Appendix J, and intermediate results may be taken from there.

4.3.1 *Application of the Feynman rules*

As a first step in the calculation, I apply the Feynman rules as defined in Sec. 3.2.3. The `Prefactor` is generated from the Feynman rules and the multiplicity of the `FeynmanDiagram`. In the case of the diagram D_1, the multiplicity of the diagram is 1. Then, the prefactor becomes

$$(-\hbar\beta)(-\beta)^0(\hbar\beta)^{-2}(N_p\Omega_c)^{-1} = \frac{-1}{\hbar N_p \Omega_c \beta}. \tag{4.11}$$

The propagators are then first initialized with an independent momentum and Matsubara energy. At each vertex, momentum and energy conservation is enforced (at each heat-flux vertex the sum of the ener-

gies is the argument of the correlation function $\pm E$). Then, in the case of D_1, the diagram value becomes

$$\begin{aligned} D_1^{M,ij}(E) = -\frac{1}{\hbar N_p \Omega_c \beta} \sum_{\mathbf{q},\{\nu\}} & J_1^{i,1}(\mathbf{q},\nu_1;-\mathbf{q},\nu_3)\times \\ & J_1^{j,1}(\mathbf{q},\nu_4;-\mathbf{q},\nu_2)\times \\ & \sum_{E_n} \mathcal{G}^{M,\widehat{P}\widehat{U}}_{\mathbf{q},\nu_1,\nu_2}(E_n)\times \\ & \times \mathcal{G}^{M,\widehat{U}\widehat{P}}_{-\mathbf{q},\nu_3,\nu_4}(E-E_n). \end{aligned} \tag{4.12}$$

The `Propagator` objects are stored in the (private) `Term` member `_propagators` and can be accessed by a public method. All other lists that occur are accessed in a similar way. The `Prefactor` is stored as member `_prefactor`.

4.3.2 *Application of the spectral representation*

As discussed in Sec. 3.4, it is only possible to achieve finite results for the thermal conductivity if the calculation proceeds with dressed propagators. Consequently, I apply the spectral representation Eq. (2.12) to each propagator that occurs in the diagram, as Mahan suggests (166). Then, all propagators are replaced by spectral densities and denominator objects (i.e. the list for the `Propagator` objects is emptied, and the `SpectralDensity`- and `Denominator`-lists are filled). In our example, the diagram becomes

$$\begin{aligned} D_1^{M,ij}(E) = & \frac{-1}{\beta\hbar N_p \Omega_c} \int_{\mathbb{R}} d\mathcal{E}_1 d\mathcal{E}_2 \sum_{\mathbf{q},\{\nu\}} \\ & J_1^{i,1}(\mathbf{q},\nu_1;-\mathbf{q},\nu_3)\times \\ & J_1^{j,1}(\mathbf{q},\nu_4;-\mathbf{q},\nu_2)\times \\ & \mathcal{S}^{\widehat{P}\widehat{U}}_{\mathbf{q},\nu_1,\nu_2}(+\mathcal{E}_1)\mathcal{S}^{\widehat{U}\widehat{P}}_{-\mathbf{q},\nu_3,\nu_4}(+\mathcal{E}_2)\times \\ & \sum_{E_1} (E_1-\mathcal{E}_1)^{-1}(E-E_1-\mathcal{E}_2)^{-1}. \end{aligned} \tag{4.13}$$

4.3.3 *Automated Matsubara summation*

It is now possible to execute the Matsubara summation on the denominator product in Eq. (4.13)

$$\sum_{E_1} (E_1-\mathcal{E}_1)^{-1}(E-E_1-\mathcal{E}_2)^{-1}. \tag{4.14}$$

In this case, the sum can be done as in Sec. 2.2.2, but here I take an automatable approach, following Ref. (196). I adjusted the approach slightly, to simplify the calculations of the computer algebra. The

value of any diagram, as a function of the Matsubara energies, can be written as

$$\sum_{\{E\}} f(E_1 ... E_L) = \sum_i h_i \sum_{\{E\}} \prod_{R_i=1}^{N_i} \left(\sum_{l=1}^{L} \sigma_l^{R_i} E_l + a^{R_i} \right)^{-1}, \tag{4.15}$$

where σ_i^l is either 1, 0, or -1, a^l is a real number, the sum i runs over all contributions, and h_i is some function that is independent of the Matsubara energies. At the beginning there is one contribution and all a^l are linear independent. The poles of f with respect to E_L are easily found as ($\sigma_L^{R_i} \neq 0$)

$$z_{R_i} = E_L^{(0)} = -\sigma_L^{R_i} \left(\sum_{l=1}^{L-1} \sigma_l^{R_i} E_l + a^{R_i} \right). \tag{4.16}$$

Then, the summation yields

$$\frac{1}{\beta} \sum_{E_L} f(E_1, ..., E_L) = - \sum_{R_i : \sigma_L^{R_i} \neq 0} \mathrm{Res}_{z=z_{R_i}} \left(f(E_1, ..., z) n_B(z) \right). \tag{4.17}$$

Equation (4.17) can always be applied, as the phonon propagator is expected to behave like the non-interacting one for large energy arguments (204).

The residues above can be calculated easily, as the poles are simple. The sum of resulting terms of the Matsubara summation again has the form of Eq. (4.15), because every denominator that has not been removed by the residue operation carries again its own independent a^{R_i} object. As a result, the poles of the function always remain simple, at every step of the iteration.

In the example Eq. (4.14), I have one Matsubara energy, and two poles. The position of the poles are

$$\begin{aligned} z_1 &= \mathcal{E}_1 \text{ and} \\ z_2 &= E - \mathcal{E}_2, \end{aligned} \tag{4.18}$$

and the corresponding residues are (only taking the denominators into account)

$$\begin{aligned} r_1(E) &= n_B(\mathcal{E}_1)(E - \mathcal{E}_1 - \mathcal{E}_2)^{-1} \text{ and} \\ r_2(E) &= -n_B(E - \mathcal{E}_2)(E - \mathcal{E}_1 - \mathcal{E}_2)^{-1} \\ &= n_B(\mathcal{E}_2)(E - \mathcal{E}_1 - \mathcal{E}_2)^{-1}. \end{aligned} \tag{4.19}$$

The Matsubara summations are completely automatized in `beyBol`. The periodicity of the occupation function removes all dependencies on other Matsubara energies immediately. At the end of the Matsubara summation, the only remaining Matsubara energy is the argument of the correlation function that is to be evaluated.

4.3.4 *Imaginary part*

The imaginary part of $\Pi_r^{ij}(\mathcal{E})$ can be found by taking the imaginary part of the denominator product of the diagram value, as shown in Appendix I.

The two resulting residues above give rise to two new `Term` objects, and the analytic continuation operation is very straightforward, by inserting $E \to \mathcal{E} + i0^+$ (compare Eq. (2.26), and note, that $\Pi_r^{ij}(\mathcal{E})$ is only evaluated in the immediate vicinity of 0, which is a Matsubara energy). As it is only necessary to take the imaginary part of the denominator product, the imaginary part operation can be executed. For $r_1(\mathcal{E})$

$$\mathrm{Im}(r_1(\mathcal{E})) = -\pi n_B(\mathcal{E}_1)\delta(\mathcal{E} - \mathcal{E}_1 - \mathcal{E}_2). \tag{4.20}$$

In general, there may be three denominators left, giving rise to a $\delta(x)\delta(y)\delta(z)$ term. In the second order example, that is presented in Appendix J (Eq. (J.3)), one contribution has a denominator product of the form

$$\frac{n_B(\mathcal{E}_0)n_B(\mathcal{E}_2)}{(\mathcal{E} - \mathcal{E}_0 - \mathcal{E}_1)\,(\mathcal{E}_0 - \mathcal{E}_2 - \mathcal{E}_3)\,(\mathcal{E} + \mathcal{E}_2 - \mathcal{E}_0 - \mathcal{E}_4)}, \tag{4.21}$$

and the imaginary part of this contribution is

$$\begin{aligned}&\frac{-\pi n_B(\mathcal{E}_0)n_B(\mathcal{E}_2)\delta(\mathcal{E} - \mathcal{E}_0 - \mathcal{E}_1)}{(\mathcal{E} + \mathcal{E}_2 - \mathcal{E}_0 - \mathcal{E}_4)\,(\mathcal{E}_0 - \mathcal{E}_2 - \mathcal{E}_3)} + \\ &\frac{-\pi n_B(\mathcal{E}_0)n_B(\mathcal{E}_2)\delta(\mathcal{E} + \mathcal{E}_2 - \mathcal{E}_0 - \mathcal{E}_4)}{(\mathcal{E} - \mathcal{E}_0 - \mathcal{E}_1)\,(\mathcal{E}_0 - \mathcal{E}_2 - \mathcal{E}_3)}.\end{aligned} \tag{4.22}$$

4.3.5 *Reintegration of spectral representations*

In the case of the second order (e.g. in Eq. (4.22)), there remain denominators in the product. To remove them, I use the spectral representation of the propagators:

$$\mathcal{G}^{\hat{A}\hat{B}}_{\mathbf{q}\nu\nu'}(\mathcal{E}) = \mathcal{P}\int_{\mathbb{R}} d\mathcal{E}_1 \frac{\mathcal{S}^{\hat{A}\hat{B}}_{\mathbf{q}\nu\nu'}(\mathcal{E}_1)}{\mathcal{E} - \mathcal{E}_1} = \frac{1}{2}\left[\mathcal{G}^{r,\hat{A}\hat{B}}_{\mathbf{q}\nu\nu'}(\mathcal{E}) + \mathcal{G}^{a,\hat{A}\hat{B}}_{\mathbf{q}\nu\nu'}(\mathcal{E})\right]. \tag{4.23}$$

$\mathcal{P}$ denotes a principal value. Every denominator can be matched with a spectral density, such that Eq. (4.23) can be employed. In the example of Appendix J, one contribution is

$$\begin{aligned} D^{M,ij}(E) = \frac{1}{\hbar^4 N_p^2 \Omega_c^2} \int_{\mathbb{R}} d\mathcal{E} \sum_{\{\mathbf{q}\nu\}} (-36)\, J_1^i(-\mathbf{q}_0,\nu_0;\mathbf{q}_0,\nu_2)\times \\ v^3(\mathbf{q}_0,\nu_1;-\mathbf{q}_2,\nu_4;\mathbf{q}_2-\mathbf{q}_0,\nu_6)\times \\ v^3(-\mathbf{q}_0,\nu_3;\mathbf{q}_2,\nu_5;\mathbf{q}_0-\mathbf{q}_2,\nu_8)\times \\ J_1^j(\mathbf{q}_0-\mathbf{q}_2,\nu_7;\mathbf{q}_2-\mathbf{q}_0,\nu_9)\times \\ \mathcal{S}^{\widehat{P}\widehat{U}}_{\mathbf{q}_0,\nu_0,\nu_1}(\mathcal{E}_0)\mathcal{S}_{-\mathbf{q}_0,\nu_2,\nu_3}(\mathcal{E}_1)\times \\ \mathcal{S}_{\mathbf{q}_2,\nu_4,\nu_5}(\mathcal{E}_2)\mathcal{S}^{\widehat{U}\widehat{P}}_{\mathbf{q}_0-\mathbf{q}_2,\nu_6,\nu_7}(\mathcal{E}_3)\times \\ \mathcal{S}_{\mathbf{q}_2-\mathbf{q}_0,\nu_8,\nu_9}(\mathcal{E}_4)\times \\ \frac{-\pi n_B(\mathcal{E}_0)n_B(\mathcal{E}_2)\delta(\mathcal{E}-\mathcal{E}_0-\mathcal{E}_1)}{(\mathcal{E}+\mathcal{E}_2-\mathcal{E}_0-\mathcal{E}_4)(\mathcal{E}_0-\mathcal{E}_2-\mathcal{E}_3)}. \end{aligned} \tag{4.24}$$

The integration energies that can be reintegrated via Eq. (4.23) are $\mathcal{E}_3$ and $\mathcal{E}_4$. The corresponding denominators and spectral densities are highlighted. The result is

$$\begin{aligned} \frac{1}{\hbar^4 N_p^2 \Omega_c^2} \int_{\mathbb{R}} d\mathcal{E} \sum_{\{\mathbf{q}\nu\}} (36\pi)\, J_1^i(-\mathbf{q}_0,\nu_0;\mathbf{q}_0,\nu_2)\times \\ v^3(\mathbf{q}_0,\nu_1;-\mathbf{q}_2,\nu_4;\mathbf{q}_2-\mathbf{q}_0,\nu_6)\times \\ v^3(-\mathbf{q}_0,\nu_3;\mathbf{q}_2,\nu_5;\mathbf{q}_0-\mathbf{q}_2,\nu_8)\times \\ J_1^j(\mathbf{q}_0-\mathbf{q}_2,\nu_7;\mathbf{q}_2-\mathbf{q}_0,\nu_9)\times \\ \mathcal{S}^{\widehat{P}\widehat{U}}_{\mathbf{q}_0,\nu_0,\nu_1}(\mathcal{E}_0)\mathcal{S}_{-\mathbf{q}_0,\nu_2,\nu_3}(\mathcal{E}-\mathcal{E}_0)\times \\ \mathcal{S}_{\mathbf{q}_2,\nu_4,\nu_5}(\mathcal{E}_2)n_B(\mathcal{E}_0)n_B(\mathcal{E}_2)\times \\ \mathcal{G}^{\widehat{U}\widehat{P}}_{\mathbf{q}_0-\mathbf{q}_2,\nu_6,\nu_7}(\mathcal{E}_0-\mathcal{E}_2)\times \\ \mathcal{G}_{\mathbf{q}_2-\mathbf{q}_0,\nu_8,\nu_9}(\mathcal{E}+\mathcal{E}_2-\mathcal{E}_0). \end{aligned} \tag{4.25}$$

4.3.6 *Propagator interrelations and the limit*

To simplify the final equations, the next step is to use the interrelations between the different spectral densities and propagator objects (Sec. 3.2.2). All objects that contain a $\widehat{P}$ operator can be transformed into

the phonon propagator or phonon spectral density. I switch back to the example of D_1, for conciseness. In this case, the diagram value is

$$\lim_{\mathcal{E}\to 0}\frac{\mathrm{Im}(D_1^{r,ij}(\mathcal{E}))}{\mathcal{E}} = \frac{-\pi}{\hbar N_p \Omega_c}\int_{\mathbb{R}} d\mathcal{E}_1 \sum_{\mathbf{q},\{\nu\}} J_1^{i,1}(\mathbf{q},\nu_1;-\mathbf{q},\nu_3)\times J_1^{j,1}(\mathbf{q},\nu_4;-\mathbf{q},\nu_2)\times \mathcal{S}^{\hat{P}\hat{U}}_{\mathbf{q},\nu_1,\nu_2}(\mathcal{E}_1)\mathcal{S}^{\hat{U}\hat{P}}_{-\mathbf{q},\nu_3,\nu_4}(-\mathcal{E}_1)\times \lim_{\mathcal{E}\to 0}\frac{n_B(\mathcal{E}_1)-n_B(\mathcal{E}_1-\mathcal{E})}{\mathcal{E}}, \quad (4.26)$$

and becomes

$$\lim_{\mathcal{E}\to 0}\frac{\mathrm{Im}(D_1^{r,ij}(\mathcal{E}))}{\mathcal{E}} = \frac{-\pi}{\hbar N_p \Omega_c}\int_{\mathbb{R}} d\mathcal{E}_1 \mathcal{E}_1^2 \sum_{\mathbf{q},\{\nu\}} J_1^{i,1}(\mathbf{q},\nu_1;-\mathbf{q},\nu_3)\times J_1^{j,1}(\mathbf{q},\nu_4;-\mathbf{q},\nu_2)\times \mathcal{S}_{\mathbf{q},\nu_1,\nu_2}(\mathcal{E}_1)\mathcal{S}_{-\mathbf{q},\nu_3,\nu_4}(-\mathcal{E}_1)\times n_B'(\mathcal{E}_1). \quad (4.27)$$

Note that, for the lattice thermal conductivity κ^{ij} the constant contribution $-2\omega_{\mathbf{q},\nu}\delta_{\nu,\nu'}$ in

$$\mathcal{G}^{r/a,\hat{P}\hat{P}}_{\mathbf{q},\nu,\nu'}(\mathcal{E}) = \frac{\mathcal{E}^2}{\hbar^2}\mathcal{G}^{r/a}_{\mathbf{q},\nu,\nu'}(\mathcal{E}) - 2\omega_{\mathbf{q},\nu}\delta_{\nu,\nu'},$$

can be ignored, see Appendix L.

4.3.7 *Transformation into a normal form*

The `Term` objects that result at this point are evaluable (see Eqns. (4.27) and (J.6)). In practice, however, it is favorable to simplify the second order contributions further. For this, I construct a normal form for terms, in the same spirit as for Feynman diagrams. The most important thing to note is, that the integration energies in the final terms can be arranged, such that the integration momenta and energies become four-momenta like. This is an empiric observation, that I did not manage to prove.

The precise definition of the order relations is not important for the results and described in Appendix M. Here I present how it is build up: I define a normal form for any `sympy` argument. This enables to compare argument-dependent objects: `SpectralDensities`, `Propagators`, and `OccupationFactors` (for each type independently). For the `Vertices`, I use additionally the order relation defined for the `BaseOperators`. Then, all objects that occur in a term possess an

order relation. The prefactor is again not important for the similarity. This enables an element-wise comparison of all `SpectralDensities`, `Propagators`, `OccupationFactors`, and `Vertices` in all `Terms`, as for the `Contractions` in `FeynmanDiagram` objects. To identify more terms with each other, I use the identities of the different objects that occur in a term. For example,

- the occupation factors n_B possess odd parity,
- the `Propagators` and `SpectralDensities` are either odd or even under combined index, momentum and energy inversion,
- the `Vertex` $J_1^{1,i}$ that occurs in the BTE is odd in it's momentum argument. Other vertex arguments may be permuted if they correspond to the same operator type (such as $\widehat{P}$).

It is then possible, at second order perturbation theory, to force all objects to only have positive arguments that add up. E.g., one may have a spectral density $\mathcal{S}_{\mathbf{q}_1+\mathbf{q}_2}(\mathcal{E}_1+\mathcal{E}_2)$ but not $\mathcal{S}_{\mathbf{q}_1-\mathbf{q}_2}(\mathcal{E}_1-\mathcal{E}_2)$ (196). To further specify the normal form, and as the arguments of the occupation functions must be linearly independent of each other (because the a^l are, see Sec. 4.3.3), the energies are transformed such that the occupation functions depend on only one integration energy. The indices are relabelled such that the vertex indices are increasing. Then, a contribution to the second order is, for example (see Appendix J, Eq. (J.8))

$$\begin{aligned}\frac{1}{\hbar^6 N_p^2 \Omega_c^2}\int_{\mathbb{R}} d\mathcal{E} \sum_{\{\mathbf{q}\nu\}} &(36\mathcal{E}_0\pi(\mathcal{E}_0+\mathcal{E}_1))\, J_1^i(\mathbf{q}_0,\nu_0;-\mathbf{q}_0,\nu_1)\times \\ &J_1^j(\mathbf{q}_0+\mathbf{q}_1,\nu_2;-\mathbf{q}_0-\mathbf{q}_1,\nu_3)\times \\ &v^3(\mathbf{q}_0,\nu_4;\mathbf{q}_1,\nu_5;-\mathbf{q}_0-\mathbf{q}_1,\nu_6)\times \\ &v^3(\mathbf{q}_0+\mathbf{q}_1,\nu_7;-\mathbf{q}_1,\nu_8;-\mathbf{q}_0,\nu_9)\times \\ &\mathcal{S}_{\mathbf{q}_1,\nu_8,\nu_5}(\mathcal{E}_1)\mathcal{S}_{\mathbf{q}_0,\nu_1,\nu_4}(\mathcal{E}_0)\times \\ &\mathcal{S}^{(1)}_{\mathbf{q}_0,\nu_9,\nu_0}(\mathcal{E}_0)n_B(\mathcal{E}_1)n_B(\mathcal{E}_0)\times \\ &\mathcal{G}_{\mathbf{q}_0+\mathbf{q}_1,\nu_6,\nu_2}(\mathcal{E}_0+\mathcal{E}_1)\times \\ &\mathcal{G}_{\mathbf{q}_0+\mathbf{q}_1,\nu_3,\nu_7}(\mathcal{E}_0+\mathcal{E}_1). \end{aligned} \tag{4.28}$$

Given this normal form, it is possible to identify similar contributions to the final result. The prefactors of the different terms (that have not been considered in the normal form) are then added up. There remains however a freedom to manipulate the ensemble of terms.

4.3.8 *Reduction by partial integration*

One may note the following about the occurring integrands: They all vanish for large values of any integration energy $\mathcal{E}_i$ (as the spectral densities become zero in my approximation, see Sec. 5.2). As a con-

sequence, the integrand P without the derivative must fulfill (in Eq. (4.28), the second spectral density carries a derivative)

$$\int_{\mathbb{R}} d\mathcal{E}_1 d\mathcal{E}_2 \frac{d}{d\mathcal{E}_i} P(\mathcal{E}_1, \mathcal{E}_2) = 0, \tag{4.29}$$

because of partial integration. This however, leaves the opportunity, to add a specific zero to the list of all terms, trying to minimize the total number of contributions. It turns out, that all contributions can be written in a form, where only derivatives of occupation functions occur, such as this one:

$$\begin{aligned}\frac{1}{\hbar^6 N_p^2 \Omega_c^2} \int_{\mathbb{R}} d\mathcal{E} \sum_{\{\mathbf{q}\nu\}} (-144\mathcal{E}_1 \pi(\mathcal{E}_0 + \mathcal{E}_1))\, J_1^i(\mathbf{q}_0, \nu_0; -\mathbf{q}_0, \nu_1) \times \\ J_1^j(\mathbf{q}_0 + \mathbf{q}_1, \nu_2; -\mathbf{q}_0 - \mathbf{q}_1, \nu_3) \times \\ v^3(\mathbf{q}_0, \nu_4; \mathbf{q}_1, \nu_5; -\mathbf{q}_0 - \mathbf{q}_1, \nu_6) \times \\ v^3(\mathbf{q}_0 + \mathbf{q}_1, \nu_7; -\mathbf{q}_1, \nu_8; -\mathbf{q}_0, \nu_9) \times \\ \mathcal{S}_{\mathbf{q}_1,\nu_1,\nu_5}(\mathcal{E}_1) \mathcal{S}_{\mathbf{q}_1,\nu_8,\nu_0}(\mathcal{E}_1) \times \\ \mathcal{S}_{\mathbf{q}_0,\nu_9,\nu_4}(\mathcal{E}_0) n_B^{(1)}(\mathcal{E}_1) n_B(\mathcal{E}_0) \times \\ \mathcal{G}_{\mathbf{q}_0+\mathbf{q}_1,\nu_3,\nu_7}(\mathcal{E}_0 + \mathcal{E}_1) \times \\ \mathcal{G}_{\mathbf{q}_0+\mathbf{q}_1,\nu_6,\nu_2}(\mathcal{E}_0 + \mathcal{E}_1).\end{aligned} \tag{4.30}$$

The same code that has been used here to manipulate equations for the thermal conductivity can be used to calculate contributions to the phonon self-energies. Indeed, I have let this code implement the entire second-loop order perturbation theory result for the self-energy that has, in my implementation, about 78000 lines of `Fortran` code. Neither I managed to converge the second order contribution to the self-energy, nor I was able to check it thoroughly for correctness. The missing self-energy of second order might lead to underestimation of phonon linewidths, especially at high temperature (13). Decay rates of second order perturbation theory have been calculated in Ref. (234).

4.4 VALIDATION OF THE COMPUTER ALGEBRA

To validate the CAS implementation, I did unit tests for most of the source code, such that the code coverage level reaches about 90%. On top of this, tests against the known first order contributions to the thermal conductivity and self-energy have been performed. To make sure, that the calculations are not wrong, the second order calculation has been written out, step-by-step, in order to allow by-hand checks of every calculation step. The `Term` objects are, for this reason named (with a descriptive string), such that terms can be traced through the calculation. The second order step-by-step calculation will be uploaded to the web and one can obtain it on request.

5 IMPLEMENTATION

The task of this section is to enable the numerical evaluation of the formulas derived with the methods described in Sec. 4. To see what is necessary to evaluate the correction to the BTE, one can look at the representative example Eq. (4.30):

1. The vertex functions V and J, corresponding to interaction and heat-flux vertices, need to be evaluated for arbitrary momentum in the Brillouin zone.
2. The phonon spectral densities and propagators must be evaluated for arbitrary momentum and energy.
3. The indices of the expression must be summed.
4. The integral over all energies and momenta of the results must be taken. To do this with reasonable resources, steps 1-3 should be done in a short amount of time.

To calculate the vertex functions, the interatomic force constants (IFCs) of the crystal are needed. The finite-displacement method to calculate them is presented in Appendix B.1. With this, I will introduce the vertex functions in Sec. 5.1. Symmetrized exponential functions, that I call star functions are shown in Sec. 5.1.1, and the different implemented options of the vertex functions and their symmetry properties are tabulated in Sec. 5.1.2. Proofs of these properties are found in Appendix B.2. Spectral densities and propagators can be calculated via Dyson's Eq. (2.51) from a self-energy, which is in my work solely based on anharmonic interactions. The calculation of the self-energy, its properties, approximations, and tests are presented in Sec. 5.2. When the self-energy, and therefore the propagators, are known, the thermal conductivity can be calculated. The details of this implementation are presented in Sec. 5.3.

The validation and test approach to these implementations is presented at the end of each section. For the numerical implementation, `Fortran` 2018 is used (except for the optimization of the index multiplication scheme that uses `Python`).

5.1 IMPLEMENTATION OF THE VERTEX FUNCTIONS

In this section, I will show how the vertex functions φ^n are calculated for arbitrary $\mathbf{q}$-values. Their properties (symmetry transformations, translation, and permutation invariance) will be discussed. To make the vertex functions fulfill these properties in general, it is not enough to simply multiply the force constants with ordinary exponentials, which can be exemplified with the dynamical matrix, that may be

interpreted as the simplest vertex with two legs. The dynamical matrix is given by Eq. (2.3), for arguments $\mathbf{q}$ on a grid *commensurate* with the supercell in which the IFCs are calculated. There are a number of constraints on the transformation laws of the dynamical matrix under the space-group of the crystal (171). These transformation laws are not satisfied for the above formula, if the argument $\mathbf{q}$ is off the grid commensurate with the supercell. To achieve correct symmetry transformations, one has to use star functions. These star functions are used for the vertex functions V and J as well. I only show here the list of properties that the functions must fulfill and how they are implemented. In Appendix H.2, I show the properties of the mathematical vertex function and its implementation.

5.1.1 *Introduction of star functions*

I define a star function as

$$\theta(\mathbf{q}, \mathbf{R}) = \frac{1}{|S|} \sum_{S} \sum_{\mathbf{x} \sim S\mathbf{R}} w(\mathbf{R}) \exp(iS\mathbf{q} \cdot \mathbf{x}), \tag{5.1}$$

where $\mathbf{R}$ is some nuclei position in the supercell, $\mathbf{q}$ is the crystal momentum, S is a rotation of a symmetry operation of the crystal. $|S|$ is the number of symmetry operations. If $\mathbf{x} \sim \mathbf{y}$ for some vector $\mathbf{y}$, then $\mathbf{x}$ is the vector inside the first supercell, that can be transformed to $\mathbf{y}$ by translations of the supercell. If $\mathbf{y}$ is at the boundary of the supercell, the sum over all equivalent $\mathbf{x}$ is taken. The function w counts the number of similar vectors to some $\mathbf{y}$, and divides by it. The symmetry operations of the crystal are found using `spglib` (273). By the use of `spglib` (273), I avoid the use of tables of space-groups (36, 152, 210, 263). The formalism assumes, that the supercell is closed under the symmetry operations of the unit cell, i.e. after any symmetry operation has been applied, the supercell must still have the same shape. For example, in a face-centered cubic (fcc) crystal, a supercell can only be of the type $n \times n \times n$ (for some n), but not $2 \times 3 \times 4$. This is an important constraint on the simulation, as otherwise, the final result of the calculation may violate the symmetry properties of the simulated crystal system, see Appendix H.2.

The derivative of the star function is found by the analytical derivative of θ. The star functions are identical to the exponential functions on the $\mathbf{q}$-grid commensurate with the supercell. Using a different definition of the dynamical matrix,

$$D_{\kappa_1,\alpha_1,\kappa_2,\alpha_2}(\mathbf{q}) = (M_{\kappa_1} M_{\kappa_2})^{-1/2} \sum_{p} \Phi^{\kappa_1,0,\kappa_2,p}_{\alpha_1,\alpha_2} \theta(\mathbf{q}, \mathbf{R}_p + \boldsymbol{\tau}_{\kappa_2} - \boldsymbol{\tau}_{\kappa_1}), \tag{5.2}$$

it fulfills the transformation laws (171) on every $\mathbf{q}$-point, such that this definition enables a symmetrized interpolation of the dynamical matrix to the entire Brillouin zone (see Appendix H.2).

5.1.2 *Implemented vertex functions*

The vertex function calculation is more involved, as the vertices must fulfill a number of properties. These properties are easily proven in the infinite crystal system. That my implementation fulfills these constraints, is shown in Appendix H.2. The translation invariance of the force constants leads to

$$\sum_{\kappa} \varphi^n(\mathbf{q}_1, \kappa_1, \alpha_1, ..., \mathbf{0}, \kappa, \alpha, ...) = 0. \tag{5.3}$$

The transformations of the space-group force the vertex function to fulfill, for some symmetry operation $\mathcal{O} = \{S|\mathbf{v}_S\}$

$$\varphi^n(S\mathbf{q}_1, \mathcal{O}(\kappa_1), \mu_1, ..., S\mathbf{q}_n, \mathcal{O}(\kappa_n), \mu_n) = \sum_{\{\alpha\}} \left(\prod_{l=1}^{n} S_{\mu_l, \alpha_l} \right) \times \varphi^n(\mathbf{q}_1, \kappa_1, \alpha_1, ..., \mathbf{q}_n, \kappa_n, \alpha_n), \tag{5.4}$$

which can be shown by Fourier transforming the corresponding equation for the interatomic force constants. $\mathcal{O}(\kappa)$ means the corresponding index of the nucleus, after the transformation has been applied. Due to the permutation invariance of the force constants one has

$$\varphi^n(\mathbf{q}_{P(1)}, \kappa_{P(1)}, \alpha_{P(1)}, ..., \mathbf{q}_{P(n)}, \kappa_{P(n)}, \alpha_{P(n)}) = \varphi^n(\mathbf{q}_1, \kappa_1, \alpha_1, ..., \mathbf{q}_n, \kappa_n, \alpha_n), \tag{5.5}$$

for a permutation P on the set $\{1, ..., n\}$. To obtain an interpolation of these vertices that fulfills all these requirements, I define,

$$\varphi(\mathbf{q}_1, \kappa_1, \alpha_1, ..., \mathbf{q}_n, \kappa_n, \alpha_n) = \sum_{\{p\}} \Phi^{0, p_2, ..., p_n}_{\kappa_1, \alpha_1, ..., \kappa_n, \alpha_n} \vartheta^{\kappa_1, ..., \kappa_n}_{p_2, ..., p_n}(\mathbf{q}_1, ..., \mathbf{q}_n), \tag{5.6}$$

where the phase factor ϑ is a shorthand for

$$\vartheta^{\kappa_1, ..., \kappa_n}_{p_2, ..., p_n}(\mathbf{q}_1, ..., \mathbf{q}_n) = N_p^{-1} \sum_{p_1} \theta(\mathbf{q}_1, \mathbf{R}_{p_1}) \prod_{l=2}^{n} \theta(\mathbf{q}_l, \mathbf{R}_{p_l} + \mathbf{R}_{p_1} + \boldsymbol{\tau}_{\kappa_l} - \boldsymbol{\tau}_{\kappa_1}). \tag{5.7}$$

N_p is the number of unit cells in the supercell. With this factor ϑ, the vertex functions fulfill all theoretical constraints exactly, see Appendix H.2. An alternative implementation is given by

$$\vartheta^{\kappa_1, ..., \kappa_n}_{p_2, ..., p_n}(\mathbf{q}_1, ..., \mathbf{q}_n) = \prod_{l=2}^{n} \theta(\mathbf{q}_l, \mathbf{R}_{p_l} + \boldsymbol{\tau}_{\kappa_l} - \boldsymbol{\tau}_{\kappa_1}). \tag{5.8}$$

This partially breaks the permutation invariance (as permuting with the first index is not possible) and also the translation invariance, if the first momentum argument is zero. These properties are proven in

the Appendix H.2. In all calculations, the second interpolation scheme is used, as it leads to good results compared to MD simulations (see Sec. 5.2.5), and needs less computational resources.

5.1.3 *Correction in polar materials*

All crystals of interest for this work are polar, that is, the atoms in the crystal carry an effective charge that leads to an interaction between the nuclei. This changes the values of the vertex functions. For the dynamical matrix the correction is (symmetrized for all $\mathbf{q}$-points) (286)

$$D^{N}_{\kappa,\alpha,\kappa',\alpha'}(\mathbf{q}) = 4\pi e \frac{[Z_\kappa \mathbf{q}]_\alpha \, [Z_{\kappa'} \mathbf{q}]_{\alpha'}}{\sqrt{M_\kappa M_{\kappa'}} \Omega_c \mathbf{q} \cdot \epsilon_\infty \cdot \mathbf{q}} N_p^{-1} \sum_p \theta(\mathbf{q}, \mathbf{R}_p + \boldsymbol{\tau}_{\kappa'} - \boldsymbol{\tau}_\kappa), \tag{5.9}$$

where effective charges Z_κ and macroscopic dielectric tensor ϵ_∞ may be calculated with the `exciting`-code (96). Corrections for higher order vertices have been calculated in Ref. (59), but are not considered in this work. As the heat-flux vertex is directly related to the vertex function φ^2 and its derivative, the heat-flux can be corrected accordingly.

5.1.4 *Exploiting sparsity*

Vertex functions can be calculated with two different methods in `beyBol`. There is a dense implementation, that just stores the force constants as long arrays, computes all necessary prefactors, and then implements the definition of these vertex functions. However, in large supercells and complicated materials, this approach is numerically increasingly costly. Hence, `beyBol` has also a sparse implementation of vertex functions that can be used for vertices of order 3 or higher. This sparse implementation uses only non-zero interatomic force constants and minimizes the number of calculations of the prefactor ϑ that turns out to be the most costly step. Looking at (any of) the prefactor definition(s) shows that the prefactor ϑ is independent of the direction indices α. That means, all interatomic force constants for a set of $\{p_2, ..., p_n, \kappa_1, ..., \kappa_n\}$, can be grouped together. This grouping is independent of the momentum arguments of ϑ - such that it can be precomputed for each interatomic force constant and stored. As the force constants are well approximated as short-range interactions, only a few sets $\{p_2, ..., p_n\}$ must be considered, and this causes a significant speed-up.

5.2 THE CALCULATION OF THE SELF-ENERGY

To calculate the self-energy of a phonon fast and as accurate as possible, the first task is to understand its mathematical properties properly. The properties of the anharmonic self-energy of the phonon system

can be found from the properties of the phonon propagator, that have been derived in Ref. (170). The self-energy, that is defined through Dyson's Eq. (2.51) has the properties (see Appendix E and Ref. (170) for the space-group transformation laws)

$$\begin{aligned}
\Sigma^r_{\mathbf{q}\nu\nu'}(\mathcal{E}) &= \Sigma^a_{\mathbf{q}\nu'\nu}(\mathcal{E})^*, \\
\Sigma^r_{\mathbf{q}\nu\nu'}(\mathcal{E}) &= \Sigma^r_{-\mathbf{q}\nu\nu'}(-\mathcal{E})^*, \\
\Sigma^r_{S\mathbf{q}\nu\nu'}(\mathcal{E}) &= \Sigma^r_{\mathbf{q}\nu\nu'}(\mathcal{E}),
\end{aligned} \tag{5.10}$$

for any space-group rotation S of the crystal. To calculate Σ, I use "ordinary" diagrammatic perturbation theory in Sec. 5.2.1, and self-consistent phonon theory on the phonon band energies in Sec. 5.2.6.

5.2.1 *First-order perturbation theory*

To first order, the self-energy can be calculated from the diagrams, shown in Fig. 2.9. Reference (172) has shown, that the self-energy can be expanded into Legendre polynomials and functions (1). In my formulation, I define a constant and a variable contribution to the self-energy Σ^c, Σ^v and matrices $\mathbb{A}^n$ such that

$$\begin{aligned}
\Sigma^r_{\mathbf{q}\nu\nu'}(\mathcal{E}) &= \Sigma^c_{\mathbf{q}\nu\nu'} + \Sigma^v_{\mathbf{q}\nu\nu'}(\mathcal{E}) \\
&= \Sigma^c_{\mathbf{q}\nu\nu'} + \sum_n A^n_{\mathbf{q}\nu\nu'}(Q_n(x) + iP_n(x)),
\end{aligned} \tag{5.11}$$

where $x = \frac{\mathcal{E}}{\mathcal{E}_{\max}}$ for some maximum value $\mathcal{E}_{\max}$ of the expansion, which is in my case twice the maximum phonon frequency of the material (explained below). P_n is a Legendre polynomial (that vanishs for absolute arguments larger than 1) and Q_n the respective Legendre function. These functions can be computed from Bonnet recursion (1) (K_n is P_n or Q_n)

$$(n+1)K_{n+1}(x) = (2n+1)xK_n(x) - nK_{n-1}(x), \tag{5.12}$$

and the start values of the recusions are

$$\begin{aligned}
P_0(x) &= 1, \\
P_1(x) &= x, \\
Q_0(x) &= \frac{1}{2}\log\left|\frac{1+x}{1-x}\right|, \\
Q_1(x) &= xQ_0(x) - 1.
\end{aligned} \tag{5.13}$$

As the Bonnet recursion for Legendre functions becomes numerically unstable for too large absolute values x (111, 207), I introduce a cutoff after which the values of Q_n are set to zero (usually $x_{\max} = 0.95$, which is well converged). Legendre polynomials can be obtained stably (22).

To first order in perturbation theory, the constant contribution to the self-energy is given in Sec. 2.2.5. The variable contribution to the self-energy is found from the third diagram, see Eq. (2.54)

$$D^{M,3}_{\mathbf{q},\nu,\nu'}(E) = -18 \sum_{\mathbf{q}_1,\nu_1,\nu_2} \mathcal{F}^M(E, \omega_{\mathbf{q}_1\nu_1}, \omega_{\mathbf{q}-\mathbf{q}_1\nu_2}) \times v^{(3)}(-\mathbf{q},\nu;\mathbf{q}_1,\nu_1;\mathbf{q}-\mathbf{q}_1,\nu_2) v^{(3)}(\mathbf{q},\nu';-\mathbf{q}_1,\nu_1;\mathbf{q}_1-\mathbf{q},\nu_2),$$

with

$$\mathcal{F}^M(E,\omega_1,\omega_2) = \sum_{\sigma=\pm 1} \left(\frac{n_B(\hbar\omega_1)+n_B(\hbar\omega_2)}{E+\sigma(\omega_1+\omega_2)} + \frac{n_B(\hbar\omega_2)-n_B(\hbar\omega_1)}{E+\sigma(\omega_1-\omega_2)} \right).$$

After analytic continuation of E to $\mathcal{E}$, the imaginary part of $\mathcal{F}^r$ can be evaluated as

$$\begin{aligned} \mathrm{Im}\left(\mathcal{F}^r(\mathcal{E},\omega_1,\omega_2)\right) = -\pi \sum_{\sigma=\pm 1} & \left(n_B(\hbar\omega_1)+n_B(\hbar\omega_2)\right) \\ & \times \delta(\mathcal{E}+\sigma(\omega_1+\omega_2)) \\ & + \left(n_B(\hbar\omega_2)-n_B(\hbar\omega_1)\right) \\ & \times \delta(\mathcal{E}+\sigma(\omega_1-\omega_2)). \end{aligned} \tag{5.14}$$

Because the phonon frequencies in a material are limited by a maximum value $\omega_{\max}$, this function can be expanded in Legendre polynomials P_n, defined in the interval $[-\mathcal{E}_{\max}, +\mathcal{E}_{\max}]$, with $\mathcal{E}_{\max} = 2\hbar\omega_{\max}$, via

$$\begin{aligned} &\mathrm{Im}\left(\mathcal{F}^r(\mathcal{E},\omega_1,\omega_2)\right) = \sum_{n=0}^{\infty} a_n(\omega_1,\omega_2) P_n(\mathcal{E}/\mathcal{E}_{\max}) \quad \text{and} \\ &a_n(\omega_1,\omega_2) = \frac{1}{2n\mathcal{E}_{\max}} \int_{-\mathcal{E}_{\max}}^{\mathcal{E}_{\max}} d\mathcal{E}\, \mathrm{Im}\left(\mathcal{F}^r(\mathcal{E},\omega_1,\omega_2)\right) P_n(\mathcal{E}/\mathcal{E}_{\max}). \end{aligned} \tag{5.15}$$

This means if

$$D^{r,3}_{\mathbf{q}}(\mathcal{E}) = \sum_n \mathbb{A}^n_{\mathbf{q}} (Q_n(\mathcal{E}/\mathcal{E}_{\max}) + iP_n(\mathcal{E}/\mathcal{E}_{\max})), \tag{5.16}$$

one readily finds the expression for the matrices $\mathbb{A}^n_{\mathbf{q}}$ to be

$$A^n_{\mathbf{q}\nu\nu'} = -18 \sum_{\mathbf{q}_1,\nu_1,\nu_2} a_n(\omega_{\mathbf{q}_1\nu_1}, \omega_{\mathbf{q}-\mathbf{q}_1\nu_2}) \times v^{(3)}(-\mathbf{q},\nu;\mathbf{q}_1,\nu_1;\mathbf{q}-\mathbf{q}_1,\nu_2) v^{(3)}(\mathbf{q},\nu';-\mathbf{q}_1,\nu_1;\mathbf{q}_1-\mathbf{q},\nu_2). \tag{5.17}$$

It is my aim to compute these matrices on a $\mathbf{q}$-grid in the Brillouin zone and then interpolate them to any $\mathbf{q}$-point. Because of the possible degeneracy of the phonon modes, this interpolation is done in the

displacement basis (see Eqns. (E.4) and (E.26)). Accordingly, the $\mathbb{A}^n_{\mathbf{q}}$-matrices, in the displacement basis have the form

$$A^{n,\alpha\alpha'}_{\mathbf{q}\kappa\kappa'} = \frac{2}{\hbar}\sum_{\nu\nu'} e^{\alpha}_{\kappa\nu}(\mathbf{q}) e^{\alpha'}_{\kappa'\nu'}(-\mathbf{q})(\omega_{\mathbf{q}\nu}\omega_{\mathbf{q}\nu'})^{1/2} A^{n}_{\mathbf{q}\nu\nu'}. \tag{5.18}$$

The actual calculation of the matrices $\mathbb{A}^n_{\mathbf{q}}$ proceeds with the `cuhre` routine (19) of the `CUBA`-library (100, 101). This deterministic algorithm uses Genz-Malik rules (83) and proves extremely performant in computing all elements of all $\mathbb{A}^n_{\mathbf{q}}$ ($n \leq n_{\max} = O(100)$) for one $\mathbf{q}$ at a time.

As the symmetry transformation laws of the self-energy imply that the matrices $\mathbb{A}^n_{\mathbf{q}}$ transform (in displacement basis) like the dynamical matrix, I can apply the results of Ref. (171) to calculate all $\mathbb{A}^n_{\mathbf{q}}$: They need only be calculated on symmetrically inequivalent $\mathbf{q}$-points. Additionally, on high-symmetry points in the Brillouin zone, the values of the matrices are constrained by the small-group of the $\mathbf{q}$-point. The procedure to constrain the matrices is presented in the next section.

5.2.2 *High-symmetry points*

Different from the dynamical matrix, the matrices $\mathbb{A}^n_{\mathbf{q}}$ are calculated via numerical integration and are, as a result, not exact. In the perfectly converged form, however, they are constrained by the small-group of the point $\mathbf{q}$. This group is given as this subset of symmetry operations of the crystal, that leaves the point $\mathbf{q}$ invariant (modulo reciprocal lattice vectors). This can be formulated as a commutation relation: Just like the dynamical matrix D, any of the other matrices of interest must commute with the transformation matrices of the dynamical matrix that correspond to rotations that leave the $\mathbf{q}$-vector invariant (see Eq. (E.23))

$$\left[\mathbb{A}^n_{\mathbf{q}}, \Gamma_S(\mathbf{q})\right] = 0, \tag{5.19}$$

for all S in the small group of $\mathbf{q}$. The same holds for the constant contribution to the self-energy. To enforce the symmetry, I rely on a modified algorithm from Ref. (164). As Eq. (5.19) is linear in the elements of $\mathbb{A}^n_{\mathbf{q}}$, I can define a vectorization operation for the matrix, such that the vector $\mathbf{a}$ contains all elements of $\mathbb{A}^n_{\mathbf{q}}$. Then, an operator $T_S(\mathbf{q})$ corresponding to $\Gamma_S(\mathbf{q})$ can be defined such that Eq. (5.19) can be written as

$$T_S(\mathbf{q})\mathbf{a} = 0. \tag{5.20}$$

Because $T_S(\mathbf{q})^\dagger T_S(\mathbf{q})$ is positive semidefinite, the sum

$$M(\mathbf{q}) = \sum_{S(\mathbf{q})} T_S(\mathbf{q})^\dagger T_S(\mathbf{q}), \tag{5.21}$$

is positive semidefinite as well (where the sum runs over the symmetry operations of the small group). I can calculate a set of orthonormal vectors that span the nullspace of $M(\mathbf{q})$, that is $\{\mathbf{n}_1, ..., \mathbf{n}_d\}$. Then, the symmetry-corrected vector $\mathbf{a}$ is given by the calculated one $\mathbf{a}_c$ as

$$\mathbf{a} = \sum_{l=1}^{d} \mathbf{a}_c \mathbf{n}_l^\dagger \mathbf{n}_l. \tag{5.22}$$

It is clear, that the matrix $\mathbb{A}_\mathbf{q}^n$, reconstructed from this vector $\mathbf{a}$, must fulfill Eq. (5.19) for all symmetry operations S of the small group. Indeed, the symmetry constraint could have been enforced using

$$\mathbb{A}_\mathbf{q}^{n,c} = \frac{1}{|S(\mathbf{q})|} \sum_{S(\mathbf{q})} \Gamma_S^\dagger(\mathbf{q}) \mathbb{A}_\mathbf{q}^n \Gamma_S(\mathbf{q}). \tag{5.23}$$

In my implementation, I tested whether the matrices $\mathbb{A}_\mathbf{q}^n$ converge against a matrix $\mathbb{A}_\mathbf{q}^{n,c}$ by increasing the accuracy of the integration routine. The set of matrices on all $\mathbf{q}$-points can be used, to generate a symmetrical Fourier interpolation of the self-energy for the entire Brillouin zone and arbitrary energies. It is thereby possible to calculate the phonon propagator and spectral density of the crystal for all energy and momentum arguments under the given approximation to the self-energy.

5.2.3 *Diagonal propagator approximation*

The numerically most complex step is the calculation of the matrix elements of $\mathbb{A}_\mathbf{q}^n$ for the variable part of the self-energy. The integrand has to be evaluated at a number of $\mathbf{q}$-points ($N_\mathbf{q}$), for all n and all indices ν, ν', ν_1, and ν_2. As the number of modes n_dof is the number of degrees of freedom of the unit cell, the overall complexity is $\mathcal{O}(N_\mathbf{q} n_\mathrm{max} n_\mathrm{dof}^4)$. If one assumes, that the final propagator is diagonal in the mode basis, contributions for all ν, ν_1, and ν_2 must be evaluated, leading to a complexity $\mathcal{O}(N_\mathbf{q} n_\mathrm{max} n_\mathrm{dof}^3)$, which constitutes a significant improvement, e.g. for SnSe in the low temperature phase (referred to as Sn_4Se_4, with a factor of $3 \times 8 = 24$ times speed-up).

In this thesis, stoichiometric formulas that carry the number of atoms in the unit cell, such as Sn_4Se_4, refer to structures, while those that contain the relative amount of each atomic type (SnSe) refer to the material.

5.2.4 *Convergence tests and validation*

The convergence of the self-energy is tested routinely in `beyBol` against the number of evaluations of the integrand, the number of Legendre polynomials in the expansion, and the $\mathbf{q}$-grid density on which the matrices $\mathbb{A}_\mathbf{q}^n$ of the self-energy in the crystal are evaluated. To compare

two different self-energy interpolations, I compare the matrix valued functions

$$I_{\mathbf{q}}(\mathcal{E}) = \Sigma^c_{\mathbf{q}} + i\sum_n \mathbb{A}^n_{\mathbf{q}} P_n(\mathcal{E}/\mathcal{E}_{\max}), \tag{5.24}$$

because the convolution of P_n and Q_m is hard to derive (1). Two of these functions are to be compared on a number of $\mathbf{q}$-points, in the sense of an L^2 norm on the interval $[-\mathcal{E}_{\max}, \mathcal{E}_{\max}]$:

$$\begin{aligned}\varepsilon^2_{\mathbf{q}} = ||I^1_{\mathbf{q}} - I^2_{\mathbf{q}}||^2_2 &= n^{-2}_{\text{dof}} \sum_{\nu,\nu'} \int_{-\mathcal{E}_{\max}}^{\mathcal{E}_{\max}} d\mathcal{E} |I^1_{\mathbf{q}\nu\nu'}(\mathcal{E}) - I^2_{\mathbf{q}\nu\nu'}(\mathcal{E})|^2 \\ &= n^{-2}_{\text{dof}} \sum_{\nu,\nu'} \int_{-\mathcal{E}_{\max}}^{\mathcal{E}_{\max}} d\mathcal{E} |\Sigma^{c,1}_{\mathbf{q}\nu\nu'} - \Sigma^{c,2}_{\mathbf{q}\nu\nu'} + \\ &\quad + i\sum_n (A^{n,1}_{\mathbf{q}\nu\nu'} - A^{n,2}_{\mathbf{q}\nu\nu'}) P_n(\mathcal{E}/\mathcal{E}_{\max})|^2.\end{aligned} \tag{5.25}$$

As the Legendre polynomials are orthonormal and $\mathbb{A}^0_{\mathbf{q}} = 0$, one has

$$\begin{aligned}\varepsilon^2_{\mathbf{q}} = n^{-2}_{\text{dof}}(2\mathcal{E}_{\max}) \sum_{\nu,\nu'} (&|\Sigma^{c,1}_{\mathbf{q}\nu\nu'} - \Sigma^{c,2}_{\mathbf{q}\nu\nu'}|^2 + \\ &+ \sum_n (2n+1)^{-1} |A^{n,1}_{\mathbf{q}\nu\nu'} - A^{n,2}_{\mathbf{q}\nu\nu'}|^2).\end{aligned} \tag{5.26}$$

This comparison is then done for a number of random $\mathbf{q}$-points ($N_{\mathbf{q}}$) in the Brillouin zone:

$$\varepsilon = N^{-1}_{\mathbf{q}} \sum_{\mathbf{q}'} \varepsilon_{\mathbf{q}'}, \tag{5.27}$$

and this is compared to the respective norm of a self-energy

$$\zeta^2_{\mathbf{q}} = n^{-2}_{\text{dof}}(2\mathcal{E}_{\max}) \sum_{\nu,\nu'} \left(|\Sigma^{c,1}_{\mathbf{q}\nu\nu'}|^2 + \sum_n (2n+1)^{-1} |A^{n,1}_{\mathbf{q}\nu\nu'}|^2 \right), \tag{5.28}$$

and the relative error ε/ζ is tested. In this fashion, the convergence against the number of Legendre polynomials, the convergence of $\Sigma^c_{\mathbf{q}}$ and $\mathbb{A}^n_{\mathbf{q}}$ at a calculated $\mathbf{q}$-point, and the density of the $\mathbf{q}$-grid can be converged at a time. I call a value $\varepsilon/\zeta < 0.03$ converged. This is somewhat arbitrary but consistently leads to converged results for the thermal conductivity in aluminium. It remains questionable whether aluminium is representative.

To visualize the above consideration, I exemplify the results with calculations in aluminium. I calculated the self-energy at the X point and halfway between X and Γ for the mode with the lowest frequency. The input force constants were created with the effective medium theory (EMT) calculator `ASAP3` from `ASE` (151). In Fig. 5.1, the self-energy for different highest orders of the Legendre polynomials are compared at X, while in Fig. 5.2 different radial cutoffs of the force constants in

the fits are compared. The number of Legendre polynomials should not be increased much above 250, as for higher orders the convergence of the parameter matrices $\mathbb{A}^n_{\mathbf{q}}$ is hard to achieve. Also, in this case, the cutoff radius for the force constants used in the calculations can be securely set to 13 Bohr.

It turns out, that the self-energy is especially hard to converge against the $\mathbf{q}$-grid density. Grid sizes of $12 \times 12 \times 12$ in PbTe or even $16 \times 16 \times 8$ in Bi_2Te_3 show that the $\mathbb{A}^n_{\mathbf{q}}$-matrices are hard to interpolate in inverse space. Also, the thermal conductivity calculated from these values saturates only for these very dense $\mathbf{q}$-grids. Such a very dense $\mathbf{q}$-grid corresponds to a very large effective supercell for which the calculation is performed. The convergence of the thermal conductivity only for the very largest effective supercells is reminiscent of the saturation of the thermal conductivity with respect to the cell sizes needed for MD simulations (42). On the other hand, the IFCs are easily converged in much smaller cells. This is a hint, that the bare interactions between the nuclei are very well localized in most systems, but their impact on the effective phonon motion is long-ranged. The advantage of many-body theory over MD simulations would then be explained by the fact that the MD simulation must use DFT in the effective supercell, while many-body theory can resort to supercells not much larger than the range of the bare interaction.

The self-energy is rather easy to converge, compared to the spectral density, and is smoothely dependent on the input IFCs. The spectral density is not: as the phonon frequencies and the positions of the peaks of the self-energy vary, the spectral density changes in a strongly nonlinear fashion. This is reminiscent of the report of very unstable BTE calculations with respect to changing input IFCs (294). An example of this instability is shown in Fig. 5.4: the phonon frequency is just at 4meV, which is nearby a strong change in the phonon self-energy. Minor changes in the self-energy will have a large impact on the corresponding spectral densities.

In order to validate the implementation, I compared the results of my calculation with those of `phono3py` (271) with input IFCs from EMT (128) or the case of aluminium, see Fig. 5.3. The two imaginary self-energies are very similar. For PbTe, the real-part of the transverse-optical (TO) phonon self-energy at the Γ-point (Fig. 5.4) is almost identical to the result of Ref. (155) (with calculation parameters in Appendix N).

5.2.5 *Comparison to molecular dynamics*

Beyond comparing similar implementations of the self-energy calculations, I also aimed at comparing the calculated spectral densities $\mathcal{S}$ against results from MD. The MD simulations have been performed with the `ASAP3` calculator from `ASE`. To compare the spectral densities, recall the spectral theorem Eq. (2.18) that relates the phonon

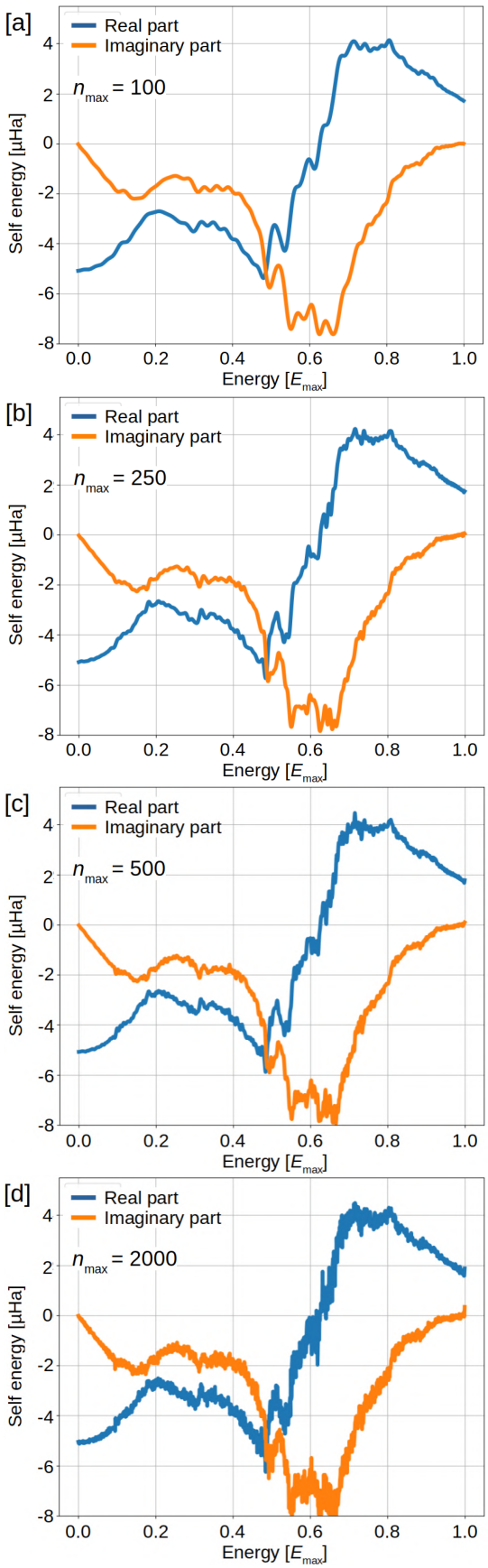

Figure 5.1: Self-energy of aluminium at the X point at 300K. The number of Legendre polynomials $n_{\max}$ varies from (a) 100, (b) 250, (c) 500 and (d) 2000.

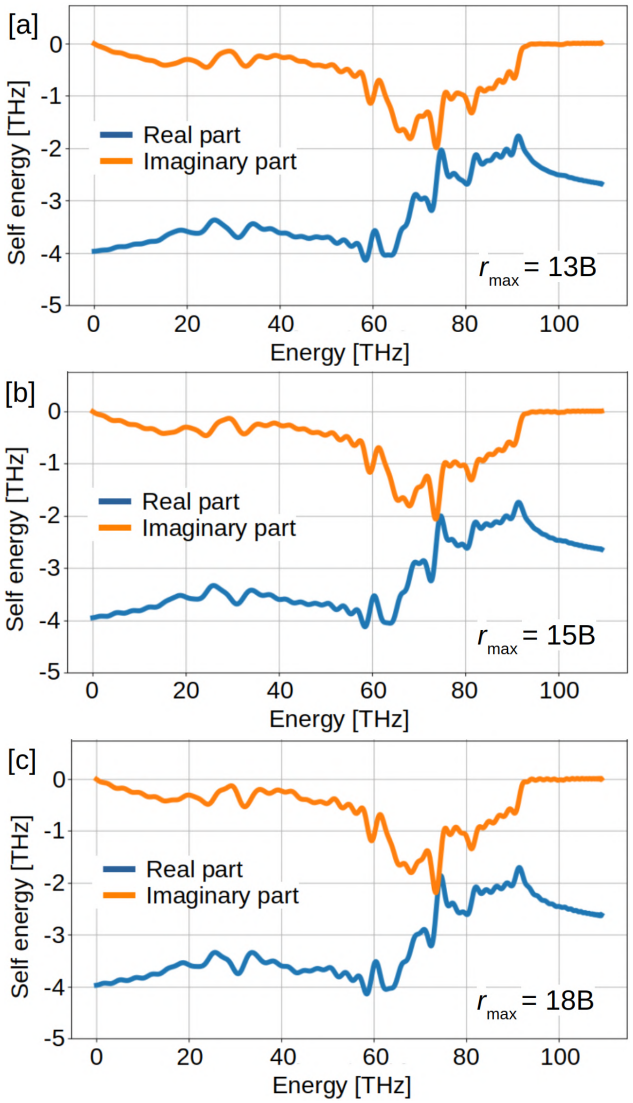

Figure 5.2: Self-energy of aluminium halfway between Γ and *X* point at 300K. The cutoff radii for the force constants are (a) 13B, (b) 15B and (c) 18B.

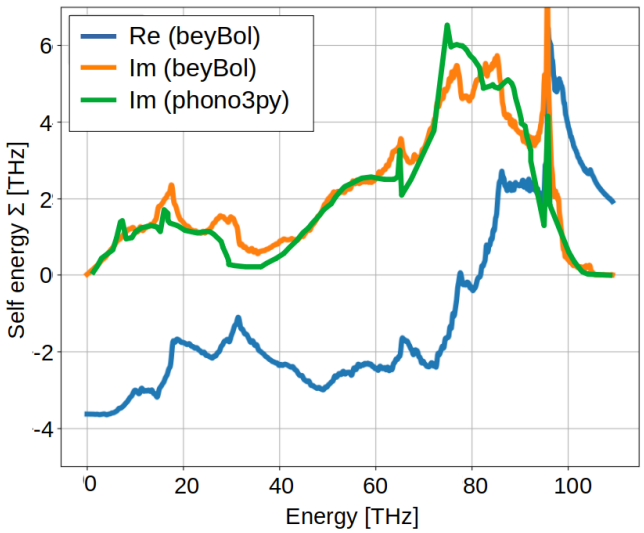

Figure 5.3: Imaginary part of the self-energy, calculated and `beyBol` and `phono3py`, respectively. `beyBol` expands the δ function of D^3, while `phono3py` uses tetrahedron integration. For completeness also the real part is shown. The calculations have been performed at 900K. The two imaginary part curves are multiplied with -1.

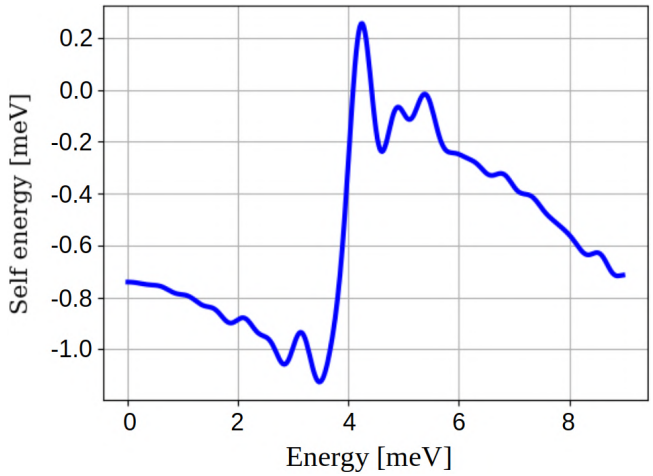

Figure 5.4: PbTe real part of the self-energy of the (ferroelectric) transverse-optical (TO) phonon at the Γ point. My calculation parameters can be found in Appendix N.

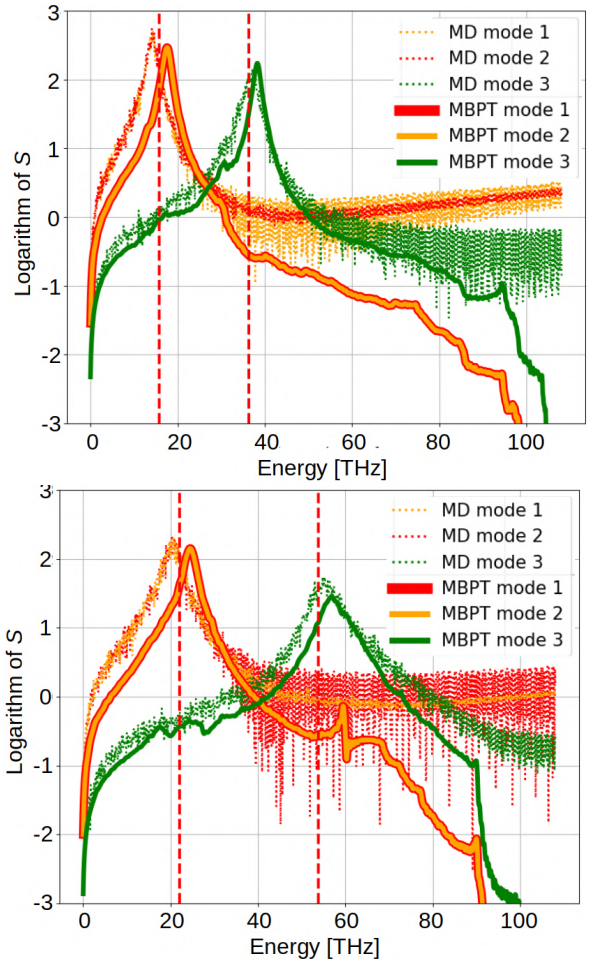

Figure 5.5: Comparison of the spectral density trace elements (for mode one, two and three) of two different **q**-points between the spectral density computed from an MD run and the spectral density computed from many body theory. The red and orange curves are identical, by symmetry. The material is aluminium (EMT) at 900K. The logarithm of the spectral density is plotted. Only the peak-region is important for the calculation of the lattice thermal conductivity. The red dashed lines denote the phonon frequencies.

displacement autocorrelation function to the spectral density of the phonons

$$\langle \widehat{U}_{\mathbf{q}\nu}(t)\widehat{U}_{-\mathbf{q}\nu'}(t')\rangle = \hbar^{-1}\int_{\mathbb{R}} d\mathcal{E}\frac{\mathcal{S}_{\mathbf{q}\nu\nu'}(\mathcal{E})}{\exp(\beta\mathcal{E})-1}\exp(-\frac{i}{\hbar}\mathcal{E}(t-t')), \tag{5.29}$$

where the left side can be calculated from MD, and can then be compared to the result from many-body theory (the constant term d is zero in this case, see Appendix C). By inverting the spectral theorem, I obtain two spectral densities. The spectral density encodes all the information about the phonon motion. At high temperatures the two spectral densities are almost identical, see Fig. 5.5.

As the comparison shows, the qualitative similarity is crushing, but the spectral densities are not perfectly identical. While I tested for size-convergence, I assume that the slight difference between the equipartition distribution of phonons in MD and the Bose-Einstein distribution in many-body theory mainly causes the discrepancy. It might also be because higher terms of the constant self-energy contribution have been neglected, or that the MD with its friction parameters can never give the exact same result, no matter how small the friction is. An alternative to be checked is, whether a simulation using TDEP may resolve the discrepancies. As you will see, the correction to the BTE calculation is too small to be found with such a 3% difference between the spectral densities in both approaches, such that a direct comparison between the thermal conductivity results of MD and many-body theory will not test the BTE correction (which I aimed at, first).

5.2.6 *Self-consistent phonon theory*

In very anharmonic materials, such as PbTe, the direct application of first order perturbation theory may fail, when the self-energy of the phonon does not just slightly change the phonon energy. In PbTe for example, the direct application of first order perturbation theory leads to an instability of the crystal for temperatures larger than 238K. This is due to a large constant self-energy contribution, see Fig. 6.2. The impact of thermal expansion has been neglected, see also Sec. 6.1. To overcome this, I used self-consistent phonon theory (SCPT) (see also Sec. 2.2.7). In SCPT, a self-consistent Dyson equation is solved. However, the true solution of the self-consistent Dyson equation, that minimizes the free energy of the system (251) is very hard to find in a realistic system (262). Therefore, I rely on the principle of adiabatic continuity (6): The dynamical matrix of the system is first calculated at 0K. The self-energy is calculated and the dynamical matrix is changed to become the effective dynamical matrix. Then, the temperature is increased by a step δT, and the equation is iterated once. This iteration is performed to high temperatures. The results of the phonon bands become reproducible for small enough temperature steps. The phonon bands created by this procedure may not be the correct physical ones of the real system as structural transformations, and volume changes have not been considered.

I sum up the algorithm: In order not to recompute the vertex functions φ in every step, the calculation is performed on a predefined $\mathbf{q}$-grid.

1. Compute all values of φ on a defined $\mathbf{q}$-grid.
2. Start at a very small temperature (preferably 0K).
3. From the harmonic dynamical matrix, compute the constant part of the self-energy.
4. From this self-energy, generate an effective dynamical matrix D^e.

5. Compute the self-energy for this effective dynamical matrix and update D^e.
6. Store D^e together with the temperature.
7. Increase the temperature by δT.
8. Update D^e for the new temperature, by computing the new self-energy from the last effective dynamical matrix for the new temperature.
9. Jump to step 6, and repeat until a maximum temperature T_{max} is reached.

Even in this case, the phonon bandstructure might show instabilities. In this occasion (that happens in our examples only in bismuth-telluride), the bandstructure is interpolated on a denser than the original **q**-grid. On **q**-points, where the dynamical matrix has negative eigenvalues, a similar, but stable dynamical matrix is constructed as follows:

1. Calculate all the eigenvalues of the dynamical matrix.
2. If an eigenvalue is negative, take the absolute value of the eigenvalue.
3. Reconstruct a new dynamical matrix.
4. Symmetrize D to find an effective dynamical matrix with the correct symmetry. (This uses the algorithm of Sec. 5.2.2.)
5. Jump to step 1 for the effective dynamical matrix, until the matrix has not been changed anymore.

From the set of effective dynamical matrices, new force constants are reconstructed in a larger effective supercell. These force constants can then be used in the calculations. Another option to obtain better, more physical bands, is given by a smooth interpolation scheme, proposed in Ref. (39). Even more physical would it be to resort to density functional perturbation theory to find the harmonic force constants on a dense **q**-grid (16), or the use of TDEP. The implementation of self-consistent phonon theory in `beyBol` is parallelized via the message-processing interface (MPI).

5.3 CALCULATION OF THE THERMAL CONDUCTIVITY

This section will be concerned with the calculation of the correction term to the thermal conductivity, arising from second order perturbation theory.

5.3.1 *Multiplication scheme optimization*

In order to calculate the correction term efficiently, the first step is to examine the resulting terms. One of the 32 contributions is

$$\begin{aligned}\frac{1}{\hbar^6 N_p^2 \Omega_c^2} \int_{\mathbb{R}} d\mathcal{E} \sum_{\{\mathbf{q}\nu\}} (-144\mathcal{E}_1 \pi(\mathcal{E}_0+\mathcal{E}_1))\, J_1^i(\mathbf{q}_0,\nu_0;-\mathbf{q}_0,\nu_1)\times \\ J_1^j(\mathbf{q}_0+\mathbf{q}_1,\nu_2;-\mathbf{q}_0-\mathbf{q}_1,\nu_3)\times \\ v^3(\mathbf{q}_0,\nu_4;\mathbf{q}_1,\nu_5;-\mathbf{q}_0-\mathbf{q}_1,\nu_6)\times \\ v^3(\mathbf{q}_0+\mathbf{q}_1,\nu_7;-\mathbf{q}_1,\nu_8;-\mathbf{q}_0,\nu_9)\times \\ \mathcal{S}_{\mathbf{q}_1,\nu_1,\nu_5}(\mathcal{E}_1)\mathcal{S}_{\mathbf{q}_1,\nu_8,\nu_0}(\mathcal{E}_1)\times \\ \mathcal{S}_{\mathbf{q}_0,\nu_9,\nu_4}(\mathcal{E}_0) n_B^{(1)}(\mathcal{E}_1) n_B(\mathcal{E}_0)\times \\ \mathcal{G}_{\mathbf{q}_0+\mathbf{q}_1,\nu_3,\nu_7}(\mathcal{E}_0+\mathcal{E}_1)\times \\ \mathcal{G}_{\mathbf{q}_0+\mathbf{q}_1,\nu_6,\nu_2}(\mathcal{E}_0+\mathcal{E}_1).\end{aligned}$$

Two things must be noted here. First, the evaluation of the integrand requires to sum up to 10 indices. The summation of all indices at a time would of course scale to order 10 in the number of degrees of freedom of the unit cell, n_{dof}. To reduce the work needed for a tensor summation is, however, a very common problem in condensed matter physics (17, 46, 47, 117, 118). In fact, there are implementations available such as the `iTensor` package (76), but these turn out not to be flexible enough to cover all tensor multiplication cases that occur in this work (especially when more than two objects carry an index, as in the case of the self-energy calculation). To minimize the workload, I implemented a (slightly generalized) version of an algorithm described in Ref. (219), that maximally reduces the number of operations, using a branch-and-bound technique (122) (which is necessary as the tensor network multiplication problem is $\mathcal{NP}$-hard).

To further reduce the workload in the integration routine, transposition operations for the occuring tensors in the calculation have been minimized automatically by penalizing transpositions in the branch-and-bound algorithm, which further increases the performance of the final routine.

The term forms a *convolution* in the energy arguments, as it can be written as $g(\mathcal{E}_1)h(\mathcal{E}_1+\mathcal{E}_2)k(\mathcal{E}_2)$. This is true for all terms of second order, and the reason is that in the BO approximation the vertex functions do not depend on the energies (which means that the phonon-phonon interaction is approximated as instantaneous). In order to integrate a convolution, it is possible to fast-Fourier-transform (FFT) all the occurring functions. Because the spectral densities and propagators that occur in the calculation have a strongly varying character around the phonon energy $\hbar\omega_{\mathbf{q}\nu}$, the number of points needed per energy axis in the energy integration is $N_{\mathcal{E}} = O(1000)$. The FFT reduces the workload for the integration of both energies from $\mathcal{O}(N_{\mathcal{E}}^2)$ to $\mathcal{O}(N_{\mathcal{E}}\log(N_{\mathcal{E}}))$ (which turns out to be practically linear). Thereby

I won a crucial speed-up of a factor of 1000 that only enables the calculation of the correction to the BTE.

In order to take advantage of all these in the numerical integration, and avoid typos and coding mistakes, the code for the integrand is written automatically. The code-writing routine proceeds in the following steps:

1. Split every term into four components, dependent on $\mathcal{E}_1$, $\mathcal{E}_2$, $\mathcal{E}_1 + \mathcal{E}_2$ and those objects independent of all of that.
2. For each energy dependent component, take energy-independent objects to minimize the number of indices.
3. Optimize the multiplication scheme for each component, and evaluate each object for all energy values on an equidistant grid.
4. Fourier transform each energy-dependent component (where the component that depends on the sum of energies is inversely transformed to the others), such that the Fourier transformed objects depend on a parameter x.
5. Optimize the multiplication scheme for the objects that are left.
6. Find objects that have to be calculated for more than one term and make sure they are created only once.
7. Multiply them for each Fourier argument x, and take the sum.

In this way, the overall complexity of the evaluation of the integral is reduced to $\mathcal{O}(N_{\mathbf{q}} N_{\mathcal{E}} \log(N_{\mathcal{E}}) n_{\text{dof}}^2 + N_{\mathbf{q}} N_{\mathcal{E}} n_{\text{dof}}^4)$ ($N_{\mathbf{q}}$ being the number of sets of $\{\mathbf{q}_1, \mathbf{q}_2\}$ points that are evaluated).

Further performance gains are obtained by the use of *Just-in-time* BLAS code and batched matrix multiplication routines (127). An additional speed-up is optionally obtained by using the DPA, which leads to an overall complexity of $\mathcal{O}(N_{\mathbf{q}} N_{\mathcal{E}} \log(N_{\mathcal{E}}) n_{\text{dof}}^2 + N_{\mathbf{q}} N_{\mathcal{E}} n_{\text{dof}}^3)$ and is very important for systems, such as Sn_4Se_4 or C_3B_{12}.

The whole integration is then performed by using the `suave` or `vegas` routine from the integration library `CUBA` (101), that use stratified and importance sampling techniques (226, 237). The routines interpret the energy integrated term above as the integrand of a 6-dimensional integral over the set $\{\mathbf{q}_1, \mathbf{q}_2\}$. The selection of point-sets $\{\mathbf{q}_1, \mathbf{q}_2\}$ is left to the `CUBA` library.

5.3.2 *Using symmetry*

The transformation rule for any space-group rotation of the crystal S for the thermal conductivity is given by

$$\kappa = S\kappa S^T, \tag{5.30}$$

which is true, because the thermal gradient transforms like any normal vector $\nabla T \to S\nabla T$. In other words, the thermal conductivity must commute with all space-group rotations of the crystal. To assure the calculated tensor fulfills this property, I use the same algorithm as

for the matrices $\mathbb{A}^n_{\mathbf{q}}$ (see Sec. 5.2.2). For example, for any fcc crystal the thermal conductivity can be written as $\kappa^{ij} = \alpha\delta^{ij}$, where α is a constant.

To further simplify the calculation, I used the fact that the correction integrand transforms under space-group operations $\{\mathbf{q}_1, \mathbf{q}_2\} \to \{S\mathbf{q}_1, S\mathbf{q}_2\}$, as a normal tensor (as every element in mode basis is invariant under this transformation, except for the heat-flux operators). This means, that the final result can also be obtained by restricting the integration of $\mathbf{q}_1$ to the irreducible wedge of the Brillouin zone. Then the result κ^I of this wedge and the full result are related via $\kappa = \sum_S S\kappa^I S^T$.

To restrict the integration to the irreducible Brillouin zone is, however, not as simple as for usual grid-sums (where the equivalence of two $\{\mathbf{q}_1, \mathbf{q}_2\}$ can be tested easily). These grid-sums are not preferable for integrations in 6 dimensions, as the error of the integral scales like $\mathcal{O}(N_{\mathbf{q}}^{-1/3})$, while that of quasi-Monte-Carlo integration scales like $\mathcal{O}(N_{\mathbf{q}}^{-1}\log(N_{\mathbf{q}})^6)$ (29, 189, 284). As a result, it is preferable to combine the quasi-Monte-Carlo integration technique with the restriction of the integration region, which is possible as follows: I construct the polytope of the irreducible Brillouin zone of the crystal. For this, I implemented an algorithm explained in Ref. (131) (using Minkowski reduction (195)). Then, the integrand is set to zero, if $\mathbf{q}_1$ does not lie inside the polytope of the irreducible Brillouin zone.

The use of this technique is optional. The reason is, that the variability of the integrand near the boundary of the irreducible Brillouin zone causes the integration routine to use significant resources trying to resolve the actual contribution from this region. Many times the integrand is a smooth function of $\{\mathbf{q}_1, \mathbf{q}_2\}$ if $\mathbf{q}_1$ is not restricted and therefore it is only beneficial to use the above method if the adaptive slicing of the `suave`-routine exactly isolates the irreducible Brillouin zone, which is, for example, the case in orthorhombic system, such as Sn_4Se_4. It might be possible to find a continuous map of the irreducible Brillouin zone polytope on the unit cube, in which case this technique would always be beneficial as the `CUBA` library integrates only on unit-cubes.

5.3.3 *Convergence tests and validation*

The implementation was again tested for Al against the `phono3py`-code (272), which uses the relaxation time approximation and the linearized Boltzmann transport equation (38). Additionally, the unit-cell of aluminium was chosen to have either one or two nuclei, and the results for the thermal conductivity have been compared. While these two descriptions of the same system must, of course, lead to the same results, all calculation steps are completely independent, starting from the calculation of the IFCs. The result for the thermal conductivity computed by `beyBol` is independent of that, see Fig. 5.6.

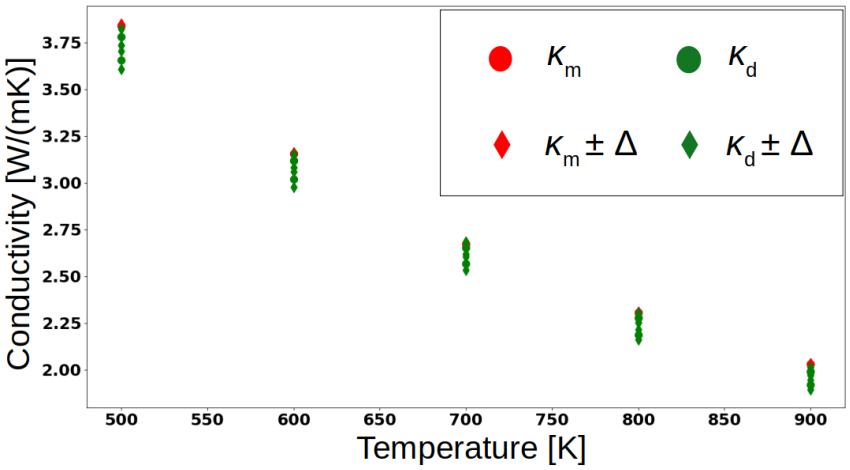

Figure 5.6: Comparison of the thermal conductivity of aluminium calculated with one (red) and with two (green) atoms in the unit cell. The thermal conductivity $\pm$ the uncertainty of the integration routine is denoted by a rhombus. The full symmetry of aluminium is *not* enforced for the two-atom case, which is why different directions have different values (that are almost identical as expected).

Additionally, the thermal conductivity is isotropic in both cases, as expected. Therefore, the definition of the unit cell in `beyBol` does not affect the final calculation result.

6 APPLICATIONS

In this section, I want to show and discuss the application of the previously introduced theory and implementation. The numerical results of my work are presented material by material. First, the phonon propagator is shown, with a discussion on what approximations have been used to obtain the results, and then the thermal conductivity calculations are presented and compared to available literature. The results for the second-order correction are summed up in Sec. 6.8. The calculation parameters, necessary to reproduce the results, are tabulated in Appendix N. To relax the crystal structures, I used the BFGS algorithm of `FHI-aims`, relaxing lattice vectors and nuclei positions together. All IFCs have been computed using a finite-displacement approach. For all materials, DFT calculations have been performed, using the PBEsol functional. For PbTe, I additionally performed calculations using the LDA functional.

6.1 LEAD TELLURIDE

PbTe is one of the most often used thermoelectrics and has been studied for a long time (66, 149). It crystallizes in the fcc structure. PbTe has been reported to show characteristics of a ferroelectric instability (7, 26, 60, 185) similar to germanium telluride (54). This is due to the second-order Jahn-Teller effect (129, 154, 239, 265). PbTe is known to have a high Grüneisen parameter (149). The Grüneisen parameter describes the impact of the volume change of the crystal lattice on its vibrations. Also, quartic anharmonicity has been reported to play a crucial role (291).

In my calculations, the thermal expansion of the material was not considered. The self-energy has been calculated with first-order perturbation theory (Sec. 5.2.1) and SCPT (Sec. 2.2.7). The calculation of the renormalized phonon bands with SCPT has been performed both with LDA and PBEsol (see Appendix O). Harmonic phonon frequencies as a function of $\mathbf{q}$ are shown in Fig. 6.1. The SCPT renormalized phonon frequencies as a function of $\mathbf{q}$ at 238K are shown in Fig. 6.2. Note that SCPT includes the zero-point motion of the nuclei, so that the harmonic phonon bands are not identical to the 0K SCPT bands, even though they are very close. With the phonon dispersion and third and fourth-order IFCs, I calculated the phonon spectral densities (Sec. 5.2.1), which are presented for PBEsol without SCPT in Fig. 6.3. The thermal conductivity has been calculated using the BTE as a function of temperature for different approximations to DFT and the self-energy and is presented in Fig. 6.4.

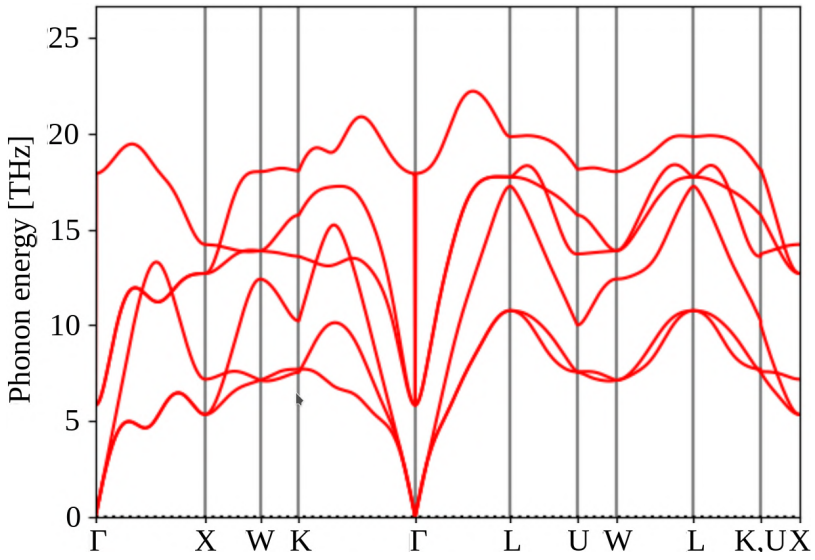

Figure 6.1: Harmonic phonon band structure of PbTe (with PBEsol). Born effective charges have been included as calculated in Ref. (255).

In Fig. 6.1 one can see, that the harmonic phonon frequencies in PbTe are always real. In Fig. 6.2 this is also the case for the SCPT phonon bands at 238K. However, in Fig. 6.2 it can be seen, that the frequency of the acoustic phonon modes at the X point undergoes a large renormalization and is almost zero. This is due to strong fourth-order IFCs that lead to a large constant part of the self-energy $\Sigma^c_{\mathbf{q}}$. Using first-order perturbation theory, this leads to negative eigenvalues of the effective dynamical matrix $D(\mathbf{q}) - \Sigma^c_{\mathbf{q}}$ at X for temperatures above 238K. This means, in first-order perturbation theory, the crystal structure is predicted to be unstable above 238K, and so this level of theory cannot be used for calculations. Using SCPT, the phonon frequency of the acoustic mode at the X point increases again for temperatures above 238K. For comparison, a calculation of the SCPT band structure using LDA gives a similar behavior for the acoustic phonon frequency at the X point, becoming imaginary for temperatures larger than 224K in first-order perturbation theory. In order to compare first-order perturbation theory with SCPT at temperatures above 238K (using PBEsol), I discarded the constant contribution to the self-energy $\Sigma^c_{\mathbf{q}}$ in first-order perturbation theory. This is a rather crude approximation, as $\Sigma^c_{\mathbf{q}}$ is large. Nonetheless this approximation was used before, for example in Ref. (155).

In Fig. 6.3, the trace of the spectral density matrix $\mathrm{Tr}\mathcal{S}$ is depicted as a heat-map depending on the energy $\mathcal{E}$ and the crystal momentum $\mathbf{q}$ plotted along the standard ASE bandpath (i.e. the bandpath that is suggested by ASE (151) for this type of crystal structure). The harmonic phonon frequencies are shown as red lines in the same plot. Large values of $\mathrm{Tr}\mathcal{S}$ are visible as bright areas and reflect renormalized phonon frequencies. $\mathrm{Tr}\mathcal{S}$ is larger if the phonon lifetime is larger. I call this type of plot a *spectral density plot*, and it will be shown for all

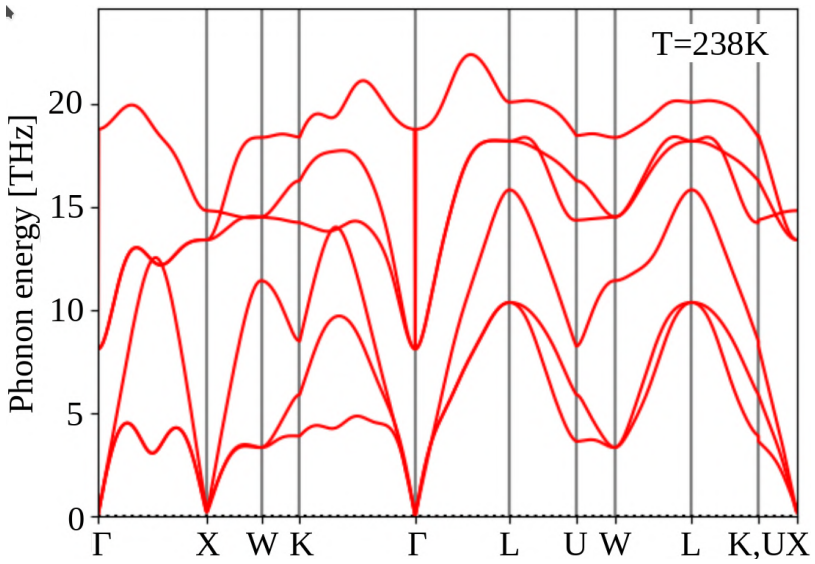

Figure 6.2: Phonon band structure of PbTe (using PBEsol) at 238K calculated with SCPT. Born effective charges have been included as calculated in Ref. (255).

presented materials. For Fig. 6.3 I used first-order perturbation theory. Recall that I discarded the constant contribution to the self-energy $\Sigma^c_{\mathbf{q}}$. It can be seen, that the phonon lifetimes decrease with temperature. This is expected as larger occupation numbers of the phonons tend to increase the scattering rates. The scattering is especially strong for the high-energy phonon modes, as they tend to have a larger scattering phase space. At 800K, Tr$\mathcal{S}$ does not show a well-localized maximum for these high-energy modes anymore, and these modes lose their band-like character.

Additionally, the renormalized phonon frequencies increase with the temperature. At this level of theory this is expected as well: The real part of the self-energy is the Kramers-Kronig transform of the imaginary part

$$\mathrm{Re}\Sigma(\mathcal{E}) = \frac{1}{\pi}\mathcal{P}\int_{\mathbb{R}} \frac{\mathrm{Im}\Sigma(\mathcal{E}')}{\mathcal{E}'-\mathcal{E}}d\mathcal{E}' = \frac{2}{\pi}\mathcal{P}\int_{-\infty}^{0} \frac{\mathcal{E}'\mathrm{Im}\Sigma(\mathcal{E}')}{(\mathcal{E}')^2-\mathcal{E}^2}d\mathcal{E}'$$

where I used that the imaginary part of the self-energy is an odd function of the energy. For negative $\mathcal{E}'$, the imaginary part is positive. The absolute value of the imaginary part tends to be larger for energies higher than the maximum phonon frequency of the system, as can be seen in Figs. 5.1, 5.2 and 5.3. As higher energy excitations tend to have a larger scattering phase space, the real part of the self-energy tends to be negative. This tendency can be observed for the TO phonon mode at 300K, as presented in Fig. 5.4. The renormalized phonon frequencies are the square root of the eigenvalues of the effective dynamical matrix $D(\mathbf{q}) - \mathrm{Re}\Sigma^v_{\mathbf{q}}(\hbar\omega_{\mathbf{q}\nu})$, and therefore tend to be larger than the harmonic phonon frequencies. As the imaginary part increases with temperature, the renormalized phonon frequencies increase as well.

In inelastic neutron scattering measurements, a satellite has been found below the minimum of the TO-phonon mode at Γ for 300K (60). It has been reproduced using TDEP (155, 238), but is not seen in my calculations. In TDEP, effective third-order IFCs are obtained by a fit to an MD trajectory. As the nuclei are displaced from their equilibrium positions along the MD trajectory, the fitted IFCs also contain the influence of higher-order IFCs. They are therefore different from the IFCs obtained through the finite-displacement approach. As especially the fourth-order IFCs are large in PbTe, it is reasonable to expect a significant impact on the effective third-order IFCs already at room temperature. Additionally, the spectral density is sensitive for the small changes in these IFCs especially in the TO phonon mode at Γ, depicted in Fig. 5.4: As the TO phonon frequency is near the self-energy peak position, small differences of one of the two may have a large impact on the spectral density. It is therefore reasonable that the spectral densities calculated with IFCs from TDEP and a finite-displacement approach show different qualitative behavior at Γ. These qualitative deviations of the spectral densities do not impact, however, the main conclusions of this thesis, see Secs. 6.8 and 7.

With the spectral densities, I calculated the thermal conductivity using the BTE as a function of temperature. The results are presented in Fig. 6.4. Experimental results are taken from Ref. (213). The thermal conductivity is isotropic, as PbTe crystallizes in an fcc structure. To investigate the effects of the exchange-correlation functional on the computed conductivity, Fig. 6.4 shows SCPT results for PBEsol and LDA. Additionally, the conductivity is presented in a calculation with PBEsol without SCPT and discarding $\Sigma^c_{\mathbf{q}}$, to compare to calculations from the literature with the same approximation to Σ (255). This result is in good agreement with other *ab initio* calculations (255) and experiments (233, 259). The SCPT calculations underestimate the thermal conductivity.

Comparing the LDA and the PBEsol calculations for low temperatures, one can see that the LDA results are significantly smaller. It is reasonable to assume that this is caused by higher phonon frequencies obtained by the PBEsol approximation. These higher frequencies are not obtained due to different equilibrium volumes of the unit cell, as these were identical for both LDA and PBEsol. Note that I did relax the lattice vectors for both cases independently. The significant difference between the results for the conductivity is still reasonable, as the conductivity shows a strong dependence on the input IFCs (294), and minor differences in the IFCs due to different exchange-correlation functionals are plausible. At larger temperatures, the renormalized phonon bands are in closer agreement and the results for the conductivity are also more similar.

The PBEsol calculation without SCPT and discarding $\Sigma^c_{\mathbf{q}}$ leads to results that are closer to experiment than those that utilize SCPT (which includes the effect of $\Sigma^c_{\mathbf{q}}$). However, neglecting the constant contribution $\Sigma^c_{\mathbf{q}}$ is a crude approximation, as it has a large impact on the

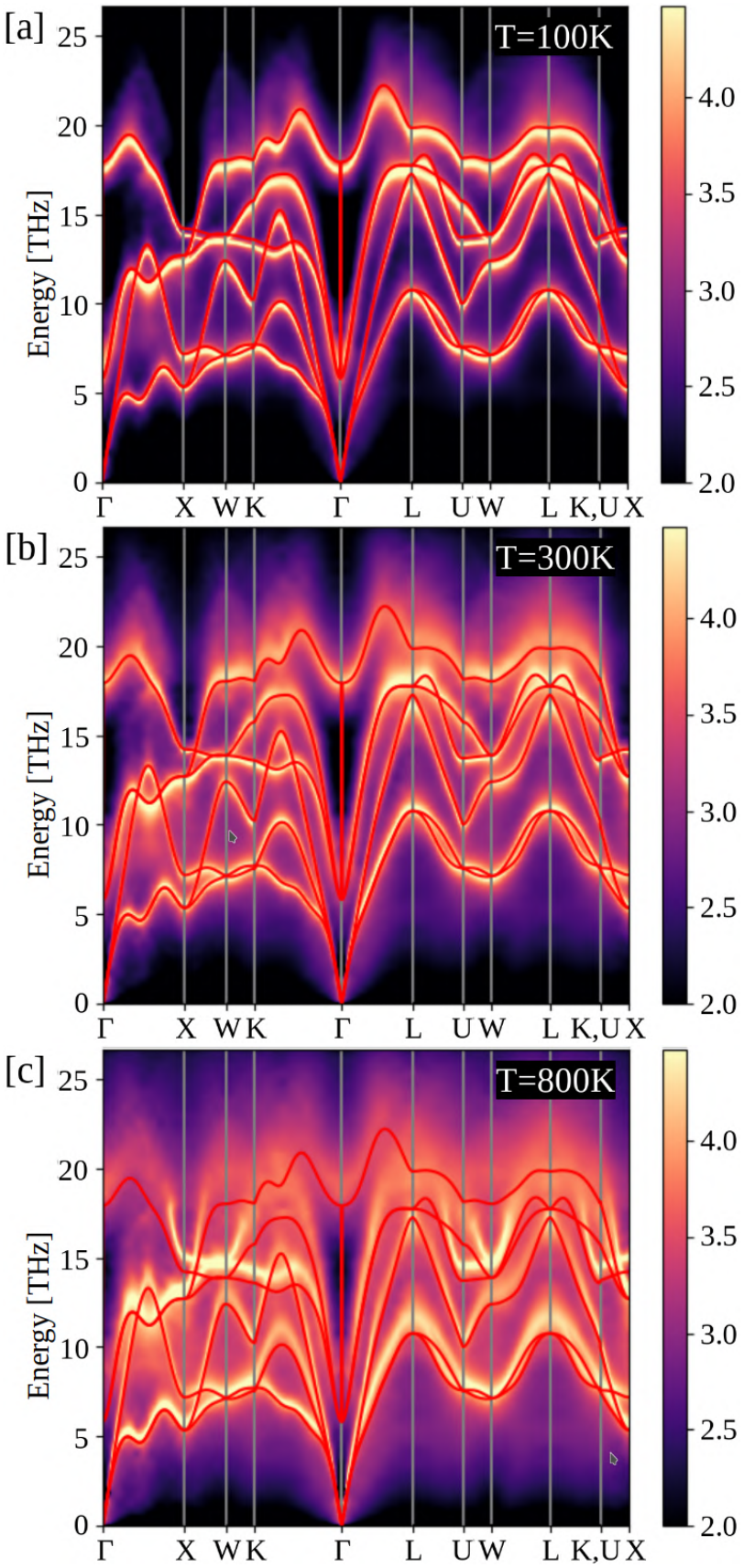

Figure 6.3: Renormalization of the phonon bands in PbTe for (a) 100K, (b) 300K and (c) 800K. The red line corresponds to the harmonic phonon dispersion. As a decoration, the logarithm with base 10 of the trace of the spectral density matrix in the mode basis is presented as background color. The value corresponds to the value depicted by the colorbar on the right. SCPT has not been used and the constant part of the self-energy $\Sigma^c_{\mathbf{q}}$ has been neglected.

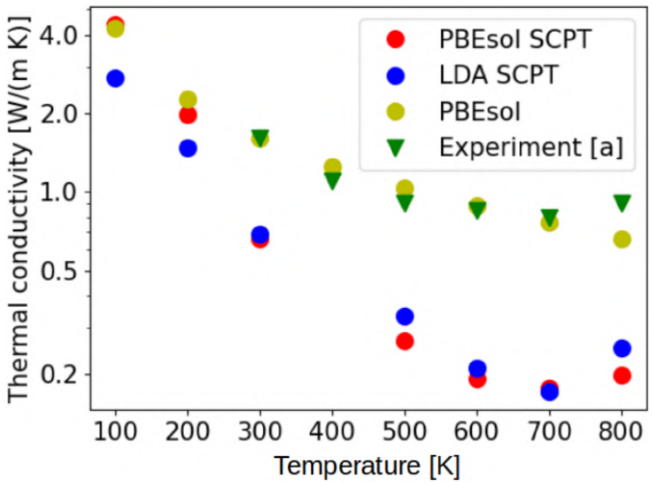

Figure 6.4: Lattice thermal conductivity as calculated with the BTE by different types of calculations: PBEsol with SCPT (red symbols), LDA with SCPT (blue symbols), and PBEsol without SCPT and discarding $\Sigma^c_{\mathbf{q}}$ (yellow symbols) compared to experimental results from Ref. (213) (green symbols). Note that LDA and PBEsol with SCPT could not be used for calculations at 400K, as the renormalized phonon band structures showed instabilities.

renormalized phonon frequencies. I expect that either the constant contribution $\Sigma^c_{\mathbf{q}}$ is reduced by higher terms in the perturbation expansion of the self-energy, or compensated by the thermal expansion.

The common $1/T$ behavior of the thermal conductivity for large temperatures (229) is recovered for PBEsol without SCPT and $\Sigma^c_{\mathbf{q}}$, for all temperatures and by experiment up to 700K, while the SCPT calculations do not. This is another hint, that SCPT is yet not enough to quantitatively model the phonons in PbTe at higher temperatures. Also, the SCPT phonon bandstructures of LDA and PBEsol both show instabilities at 400K, so no conductivity calculation was performed for this temperature. Between 700K and 800K there is an increase of the thermal conductivity in the SCPT calculations and experiment.

The second-order correction to the lattice thermal conductivity is of the size of $10^{-3} W/mK$, independent of the temperature. Therefore, it has negligible effect on the thermal conductivity of PbTe. As this is a common finding in all materials studied in this thesis, I will reason in Sec. 6.8 why this is the case. PbTe is a role model for materials that are strongly anharmonic, simple in structure, and containing heavy atoms. I therefore expect that also other materials of this kind are unlikely to have a large second-order contribution.

In future work, it could be interesting to consider the impact of disorder, as for example thallium impurities have been reported to enhance the power factor (115). Also alloying can increase the thermoelectric performance further (149). Intrinsic defects can, on the other hand, decrease the thermal conductivity (75).

6.2 BISMUTH TELLURIDE

Bi_2Te_3 and other Bi-chalcogenides possess a special layered topological structure. They are of interest for superconducting, thermomagnetic, and of course, thermoelectric applications (179, 184, 197, 299). Bi_2Te_3 is, together with its alloys with Bi_2Se_3 and Sb_2Te_3, the thermoelectric with the highest performance at room temperature (264, 290). Due to its importance for applications, the electronic and vibrational properties have been investigated in detail (182, 258). The thermal conductivity was measured (78, 90, 243) and computed using GK-MD simulations (123).

In Fig. 6.5 a unit cell of Bi_2Te_3 is depicted, showing the characteristic layered structure. The Bi atoms are enclosed between Te atoms in each layer. Below this the Brillouin zone (BZ) of Bi_2Te_3 is presented, with the bandpath (in red) that was used to create other plots in this section.

In Fig. 6.6, the absolute values of the phonon frequencies as a function of $\mathbf{q}$ are plotted along the ASE bandpath, presented in Fig. 6.5. It exhibits a set of phonon bands with lower energy that is separated by a gap from higher energy phonons, already reported in Ref. (258). Other characteristics of this calculation also match those reported in Ref. (258): The maximum phonon frequency is comparable and the maxima of the phonon frequencies are at the same high-symmetry points (Z and Γ). The group velocities of the phonons are in general quite small, except near the Γ point. However, in my work, one can see along the Γ-Y path near Γ, that the absolute frequency reaches zero not exactly at Γ. This part of the bandpath is not presented in Ref. (258). One eigenvalue of the dynamical matrix is negative for some $\mathbf{q}$ values along this path, at this level of approximation. This however means, that the crystal is not stable against distortions and it is not possible to study an unstable crystal system with many-body theory. To obtain this result I used the PBEsol functional, but it also appeared in LDA calculations and with different calculation parameters. Because of the importance of Bi_2Te_3 I decided to continue with the calculations in the following way. I chose to manipulate the phonon bandstructure of Bi_2Te_3 using the algorithm presented in Sec. 5.2.6. In Fig. 6.7 the resulting phonon frequencies are presented using an effective supercell of size $5 \times 10 \times 10$. The instability near Γ is gone, and the bandstructure changed minimally. However, this new dispersion does not exhibit the characteristic linear dispersion of the acoustic phonon modes near Γ. Nonetheless, this dispersion can be used for calculating the thermal conductivity with the BTE and the second-order correction, to see whether the second-order correction has an impact.

Based on this "stabilized" phonon dispersion, I calculated effective phonon dispersions using SCPT for temperatures up to 500K. It turned out that SCPT has no significant impact on the phonon bandstructure. Therefore I relied on first-order perturbation theory.

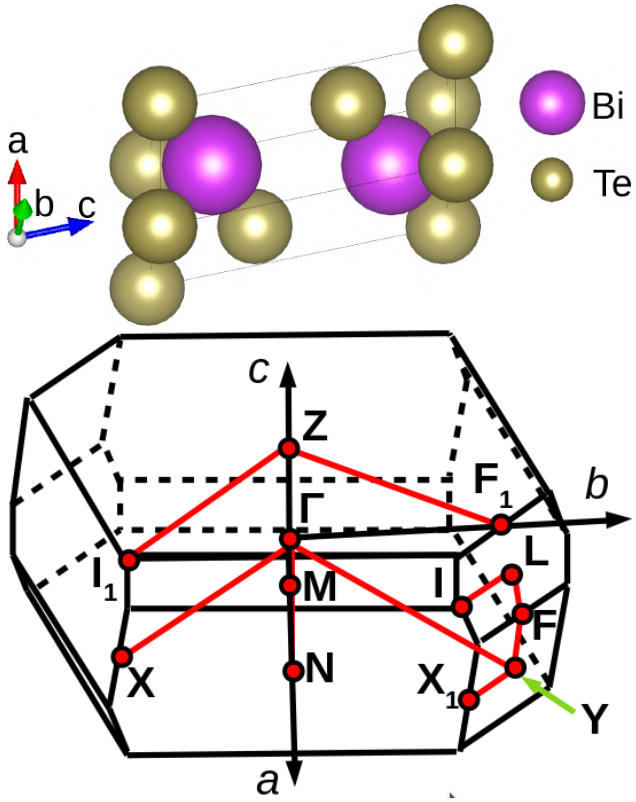

Figure 6.5: Unit cell of Bi_2Te_3 (top). The picture was created with VESTA (183). Brillouin zone and bandpath used to compute the phonon dispersion (Fig. 6.6) (bottom). Red lines denote the bandpath that connects the high-symmetry points (red dots).

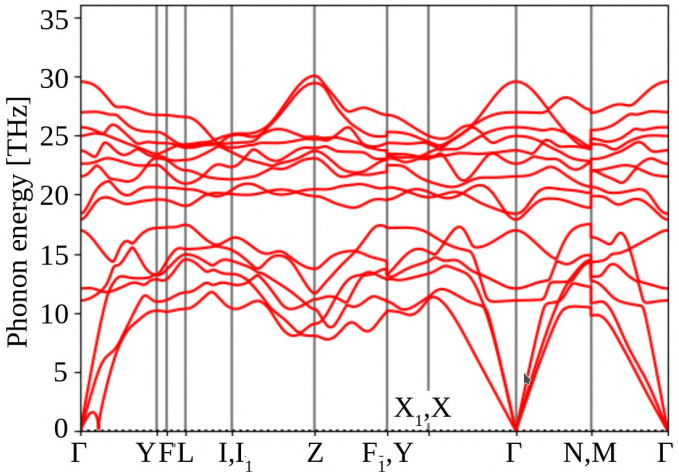

Figure 6.6: Phonon band structure of Bi_2Te_3 obtained with PBEsol. Note the instability of the harmonic crystal along the Γ-Y-path near Γ.

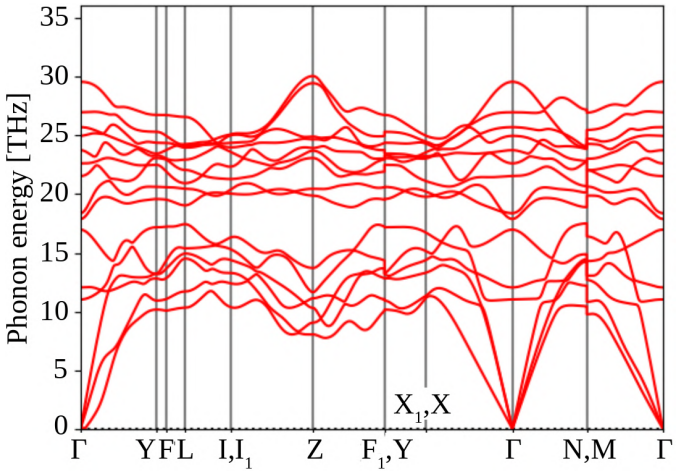

Figure 6.7: Phonon band structure of Bi_2Te_3, stabilized using the algorithm presented in Sec. 5.2.6.

In Fig. 6.8 the spectral density plot (as explained in Sec. 6.1) of Bi_2Te_3 is shown for 50K and 500K. Significant broadening can be observed especially for the higher-energy phonons, at higher temperatures. This is as expected again because higher-energy phonons tend to have larger scattering phase space, and because higher temperatures tend to increase the scattering rates. In this sense, the spectral densities exhibit a behavior very similar to those of PbTe.

In Fig. 6.9, the resulting average thermal conductivity for the in-plane directions of Bi_2Te_3 is displayed, calculated by the BTE, as a function of temperature and compared to experimental data. To the best of my knowledge there is no other BTE calculation for the lattice thermal conductivity of Bi_2Te_3 in the literature. The result slightly underestimates the experimental values from Refs. (243, 290). This may be a consequence of the stabilized phonon dispersion. Additionally, the $1/T$ behavior of the conductivity is not met. This means, according to Ref. (229), that the lifetimes of the phonons that carry the heat do not significantly decrease with the temperature. There is increased broadening of the spectral densities for the high-energy phonon modes. Thus it can only be caused by the low-energy modes near Γ. I therefore expect this uncommon behavior to be a result of the stabilization of the phonon modes near Γ.

The out-of-plane thermal conductivity is overestimated (see Appendix N). The harmonic phonon dispersion can be well compared to experiment (232). I expect scattering rates of the phonons are the reason. These could, in my interpretation, be underestimated because some interactions that lead to scattering of a phonon propagating through the layers of Bi_2Te_3 are neglected. This is because such a phonon is transmitted between atoms that are in a comparably large distance. These atoms may participate in a third-order interaction that leads to scattering. If their distance from each other is larger than the cutoff radius, used for the calculation of the IFCs (see Appendices B.1

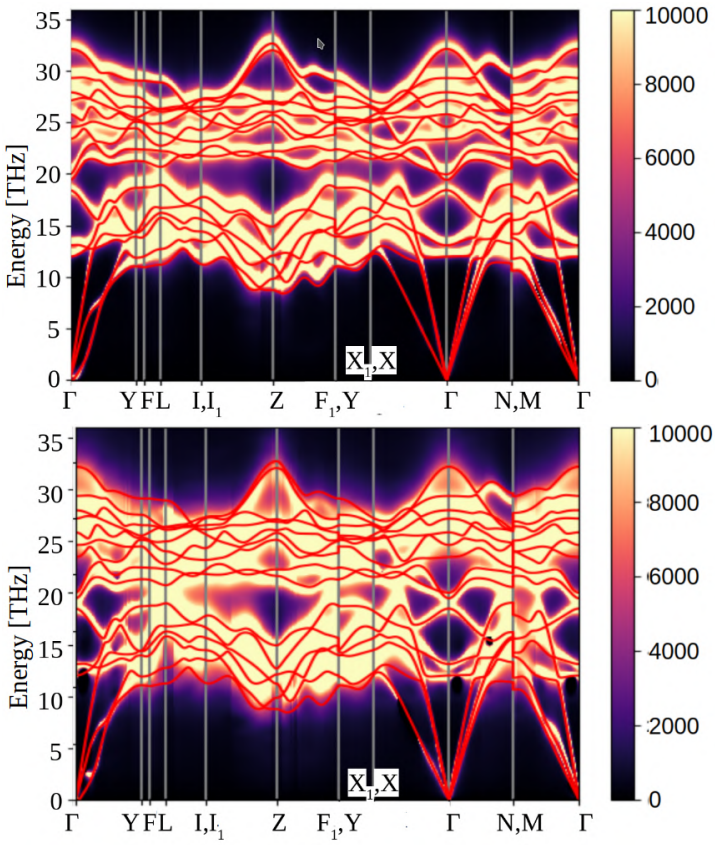

Figure 6.8: Renormalization of the phonon bands in Bi_2Te_3 for 50K (upper figure) and 500K (lower figure). The red line corresponds to the harmonic phonon dispersion. As a decoration, the trace of the spectral density matrix in the mode basis is presented as background color. The value corresponds to the value depicted by the colorbar on the right. Note that in this plot, values above 10000 are displayed as black.

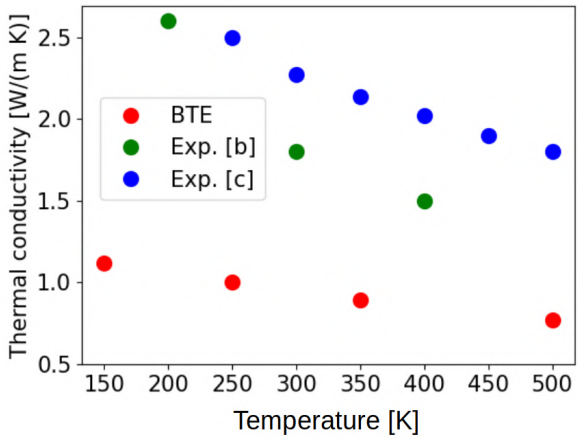

Figure 6.9: Lattice thermal conductivity of Bi_2Te_3, averaged over the in-plane directions, calculated with the BTE (red). Experiments are shown for comparison. Ref. [b] corresponds to Ref. (243) (green) and Ref. [c] is Ref. (290) (blue).

and N), then this interaction is neglected. As the third-order IFCs are the only sources of scattering at this level of approximation, this may lead to a significant overestimation of phonon lifetimes. This argument is supported by an investigation of SnSe (156), where the lattice thermal conductivity shrinks significantly when the cutoff radius for the third-order IFCs is increased above a certain distance. The reason of the high thermal conductivity in the direction perpendicular to the layers may then be due to the fact that certain scattering processes are not represented, as the corresponding IFCs are neglected.

Even though there is a mismatch between some theoretical expectations and the result of my calculations, the predictions of the thermal conductivity using the BTE are rather close to the experimental data, and the spectral densities exhibit most characteristic behaviors. I therefore expect that the size of the second-order correction can be estimated.

My correction formula did not lead to a significant contribution to the thermal conductivity in Bi_2Te_3. The correction is even smaller than in PbTe, and of the size of $10^{-4} W/mK$. The result suggests that less stiff and less anharmonic materials with less simple structure are also unlikely to exhibit a large second-order contribution.

In future work, it should be investigated if improved force models improve the agreement of the calculation results with experiment. The first step would, however, be to fix the phonon dispersion with more sophisticated methods, such as DFPT for larger supercells or TDEP.

6.3 TIN SELENIDE

Tin selenide is the best currently known thermoelectric with $ZT = 2.6$ (301), due to its extremely low lattice thermal conductivity. The

origins of the extreme anharmonicity in SnSe are discussed in Ref. (156). SnSe crystallizes at low temperatures in an orthorhombic *Pnma*-structure (Sn_4Se_4), and at higher temperature in *Cncm* (Sn_2Se_2), with higher symmetry. My calculations have been performed for the low temperature phase.

In Fig. 6.10 the unit cell of this low temperature phase of SnSe is depicted. Sn_4Se_4 exhibits a layered structure similar to that of Bi_2Te_3. The layered structure can not be seen, because a top view is shown. Below this, the BZ of SnSe is depicted, which is a cuboid, as the crystal structure is orthorhombic. The bandpath is presented as a red line, which encircles in this case exactly the irreducible BZ of the Sn_4Se_4. Below this, on the bottom, the phonon frequencies of Sn_4Se_4 are depicted as a function of $\mathbf{q}$ plotted along the bandpath, in the harmonic approximation. The phonon bandstructure is reminiscent of Bi_2Te_3, in that there are higher and lower energy phonon modes that are separated. However, in Sn_4Se_4 no gap in the phonon density of states is observed. In this approximation Sn_4Se_4 exhibits larger phonon frequencies than PbTe and Bi_2Te_3.

State-of-the-art calculations (156) rely on inelastic neutron scattering measurements of the phonon band structure and a fit of effective temperature dependent IFCs. The effect of the temperature dependent phonon dispersions and thereby strongly affected phonon scattering rates must be considered for a quantitative analysis of SnSe.

In my calculations, the thermal expansion has been neglected. I tried to study the self-energy in Sn_4Se_4 with SCPT as well as first-order perturbation theory. In my calculations, the renormalized phonon frequencies in SCPT rapidly increased with temperature, so that the maximum phonon frequency doubled already at 300K. I expect, as in PbTe, that either the constant contribution $\Sigma^c_{\mathbf{q}}$ is reduced by higher terms in the perturbation expansion of the self-energy, or compensated by the thermal expansion. As the increase of the renormalized phonon frequencies is too drastic to be considered reasonable, I resort to first-order perturbation theory and discarded the constant contribution to the self-energy $\Sigma^c_{\mathbf{q}}$. This is a severe approximation.

The resulting spectral density plots are presented in Fig. 6.11 for 100K, 300K, and 800K. One can see very broad spectral densities already at room temperature. At 800K, some phonon bands get so broad that they cannot be distinguished from others anymore.

In Fig. 6.12, the in-plane thermal conductivity predicted by the BTE is shown as a function of the temperature. There is a rather close quantitative agreement between the experimental results and the calculation. Because of the approximations, this might be coincidence. Note that in a similar study (156), it was found that the thermal conductivity is further reduced, if a larger cutoff for the third-order IFCs is used. This may lead to a still better agreement between experiment and calculation.

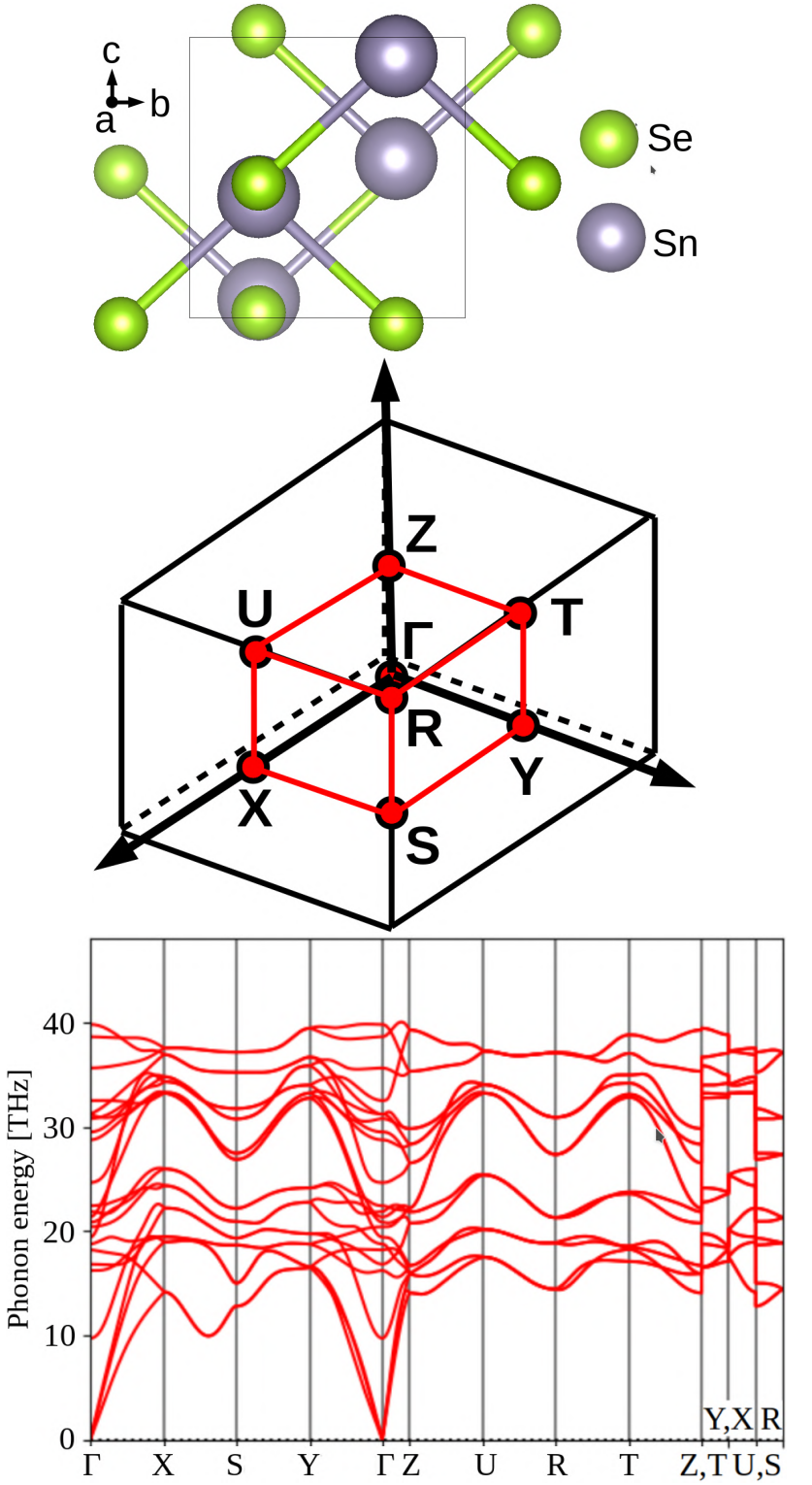

Figure 6.10: Unit cell of Sn_4Se_4 (top). Brillouin zone and bandpath used to compute the phonon dispersion (middle). Red lines denote the bandpath that connects the high-symmetry points (red dots). Harmonic phonon band structure of Sn_4Se_4 (bottom).

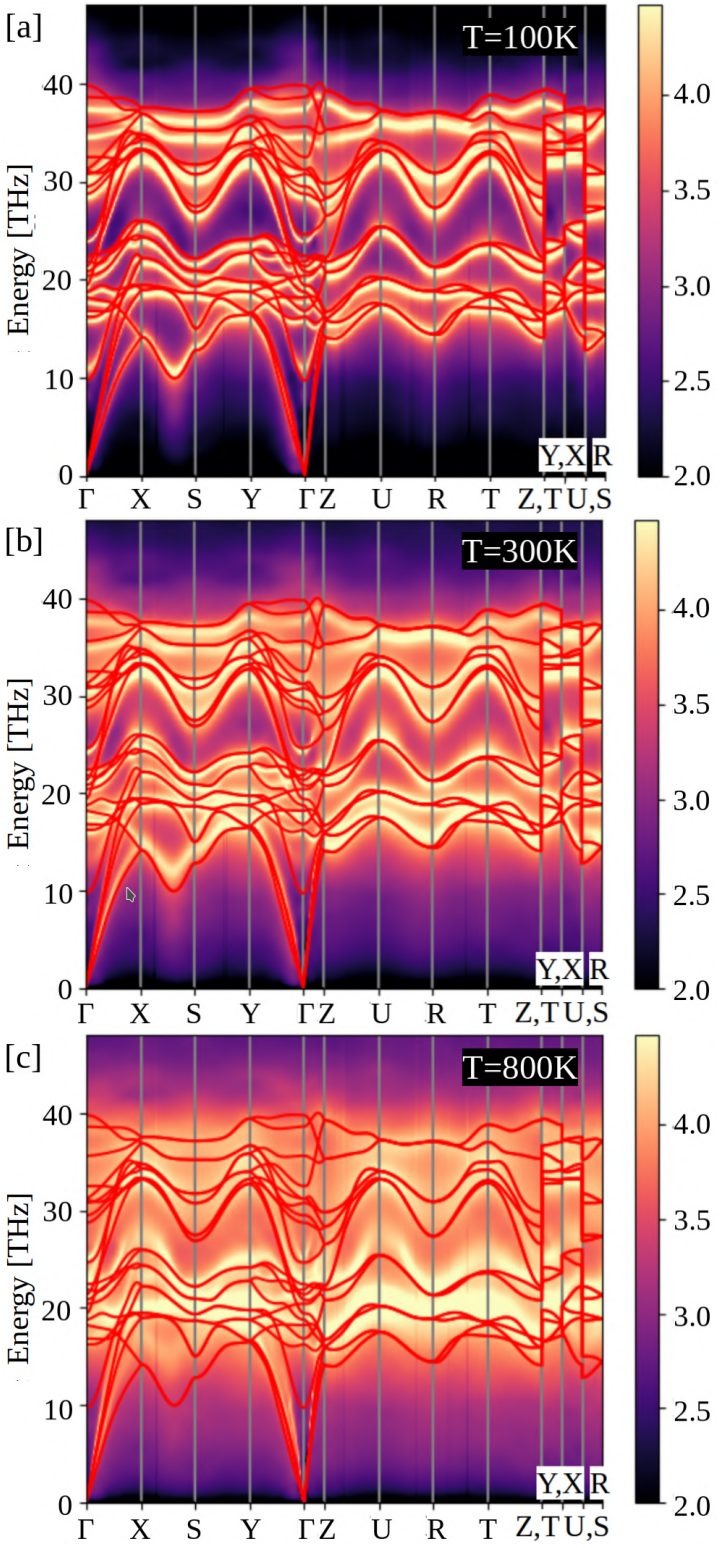

Figure 6.11: Renormalization of the phonon bands in Sn_4Se_4 for (a) 100K, (b) 300K and (c) 800K. The red line corresponds to the harmonic phonon dispersion. As a decoration, the logarithm with base 10 of the trace of the spectral density matrix in the mode basis is presented as background color. The value corresponds to the value depicted by the colorbar on the right.

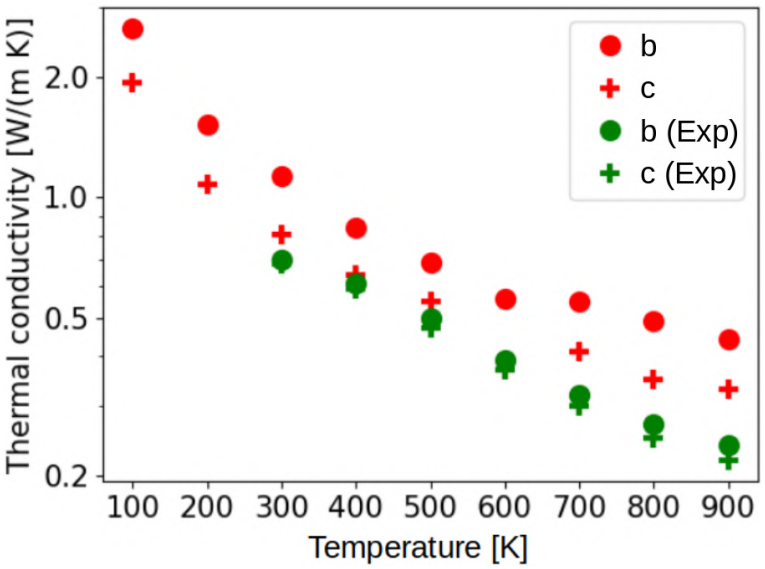

Figure 6.12: Lattice thermal conductivity for the in-plane directions (as shown in Fig. 6.10) in Sn_4Se_4 calculated with the BTE (red) and compared to experiment (green). Experimental data from Ref. (301).

Similar to Bi_2Te_3, the thermal conductivity in the out-of-plane direction is overestimated. One can see in Ref. (156), that the anisotropy of the thermal conductivity significantly depends on the third-order IFC cutoff radius. I therefore assume that certain important third-order IFCs have been neglected in my calculation, and this leads to this overestimation. Nonetheless, this calls for future work, using more sophisticated force models and larger simulation supercells.

In total, there is a good qualitative agreement with experimental (301) and other theoretical work (156). Therefore it seems reasonable to assume, that the order of magnitude of the second-order result should be reliable.

Looking at Fig. 6.11 again, one can see, that the spectral densities exhibit large values for large regions in $(\mathbf{q}, \mathcal{E})$-space. When I then recall a contribution to second-order, such as Eq. (4.30), it is likely that there are regions, where all contributing functions in the product are large. However, the second-order correction in Sn_4Se_4 is never larger than $2 \cdot 10^{-3} W/mK$. This hints that the correction does *not* increase in bad thermal conductors. As even one of the most anharmonic crystals known today does not exhibit a significant contribution, it seems unlikely that very anharmonic systems will.

6.4 BORON CARBIDE

Boron carbides are candidates for thermoelectric applications at high temperatures (188, 240, 288). From the manifold of possible configurations, I choose the stiffest boron-carbide, B_4C (176). In Fig. 6.13, it

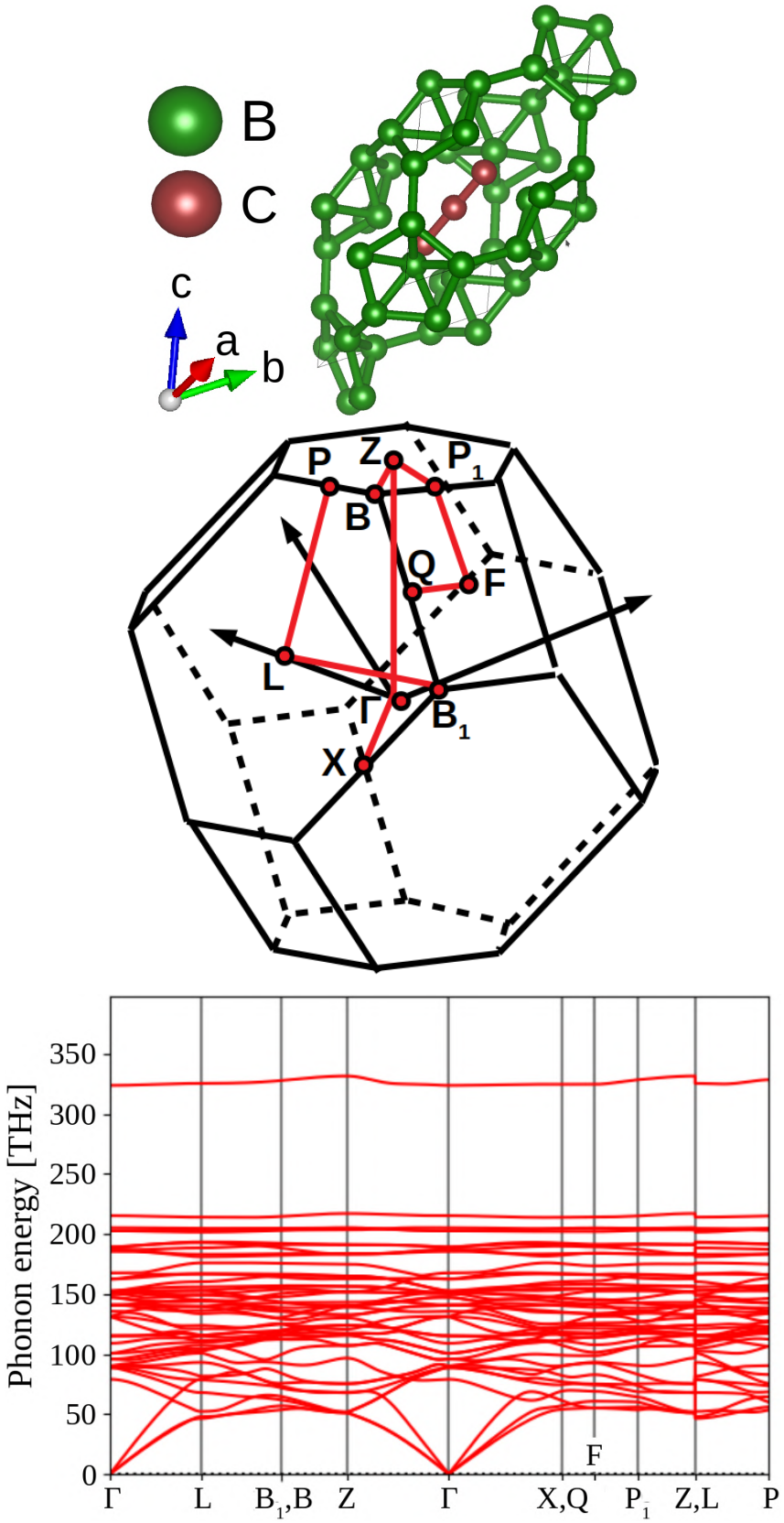

Figure 6.13: Unit supercell of B_4C (top). On the left, the lattice vectors are indicated. Brillouin zone and bandpath used to compute the phonon dispersion (middle). Red lines denote the bandpath that connects the high-symmetry points (red dots). Harmonic phonon band structure of B_4C (bottom).

is shown that it crystallizes in a rhombohedral structure, $B_{12}C_3$ (176), where the boron atoms form icosahedra, while the carbon atoms form a line of three. Below this, the BZ is presented including special points and the bandpath. Below this, the phonon frequencies are presented along these bandpaths.

Because of the structure many symmetrically distinct IFCs are included already at low cutoff-distances. The fit of the IFCs using `ALM` turned out to be very memory consuming, and I had to resort to small cutoff-distances of the third-order IFCs (6 B). The maximum phonon frequency of B_4C is very large. Many high-energy phonons have a frequency that only slowly varies as a function of $\mathbf{q}$. To compute the self-energy, I used first-order perturbation theory. As fourth order force constants were not fitted, the constant contribution $\Sigma^c_{\mathbf{q}}$ could not be calculated.

The spectral density plots are displayed in Fig. 6.14 for 300K and 600K along a small part of the bandpath. Note the wiggly behavior of the renormalized acoustic phonon frequencies near Γ. This seems to be a sign of a not fully converged self-energy. To calculate the self-energy, within the DPA, I used 30000 core hours. Also the spectral density of the highest-energy phonon mode exhibits an unusual structure with many peaks and valleys. In my opinion, this also hints at convergence problems. These might also be caused by the large maximum phonon frequency of the material - as then more Legendre polynomials are needed to accurately model the self-energy. However, the spectral density remains positive for all (positive) energy arguments. The broadening of the spectral densities grows with temperature. This is, as for the other materials, expected.

In Fig. 6.15, the average of the trace elements of the lattice thermal conductivity calculated with the BTE is presented as a function of the temperature. The predicted thermal conductivity is underestimated. This could be a consequence of the underconvergence issues described above. As all lattice directions lead to very similar results of the conductivity, I plot the mean value of the trace elements of the thermal conductivity. The typical $1/T$ behavior is reproduced by the simulation. Despite slight fluctuations of the BTE result, the order of magnitude of the second-order contribution should be trustworthy.

The second-order contribution is significantly larger in B_4C than in any other investigated material, with up to $3 \cdot 10^{-2} W/mK$. Nonetheless this is negligible compared to the BTE. B_4C is a material made up of light atoms in a complex unit cell, that has high phonon frequencies. This may hint that also these materials are unlikely to have significant second-order contribution.

Further investigations could be performed in the future, with larger computational resources to obtain a more quantitative assessment of the properties of B_4C. Additionally different boron carbides could be studied.

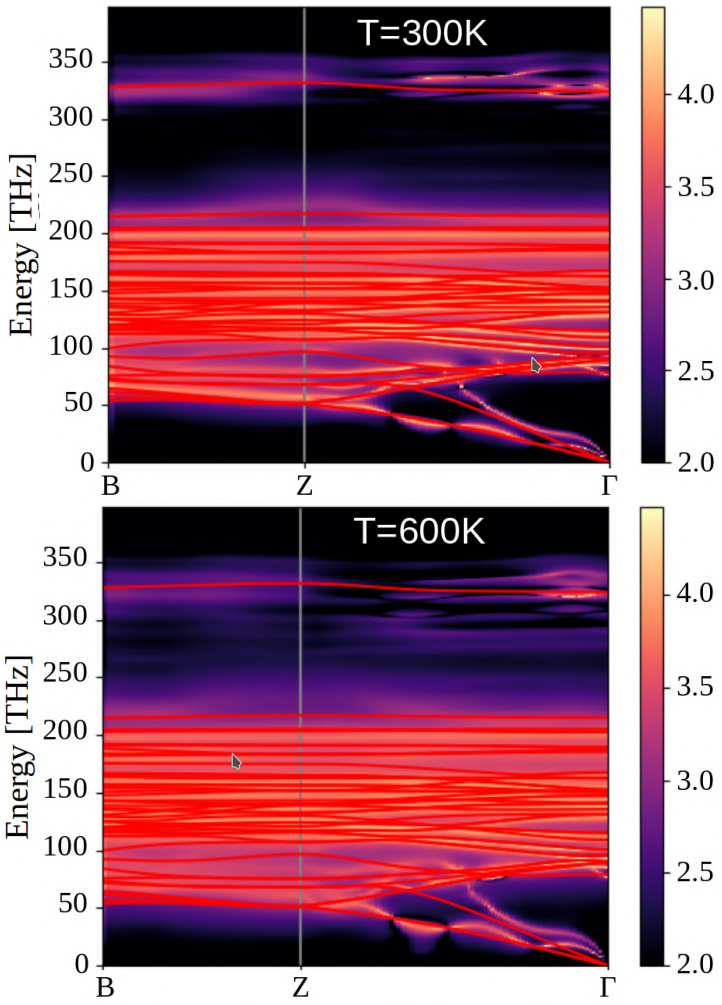

Figure 6.14: Renormalization of the phonon bands in B_4C for 300K (upper figure) and 600K (lower figure). The red line corresponds to the harmonic phonon dispersion. As a decoration, the logarithm with base 10 of the trace of the spectral density matrix in the mode basis is presented as background color. The value corresponds to the value depicted by the colorbar on the right.

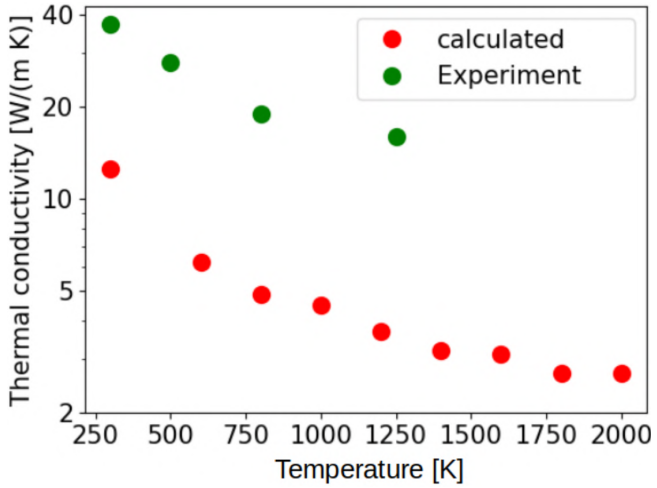

Figure 6.15: Average of the trace of the lattice thermal conductivity in B_4C calculated with the BTE as a function of the temperature (red). Experimental data from Ref. (24) (green).

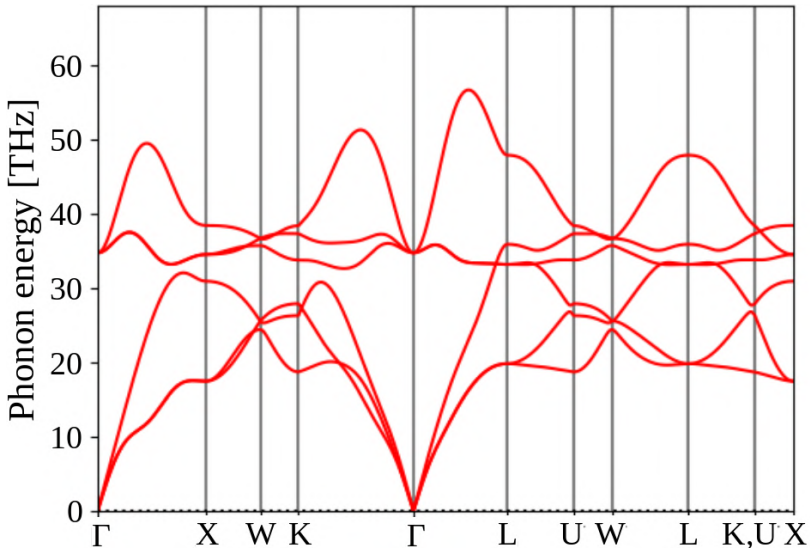

Figure 6.16: Phonon band structure of KF (PBEsol).

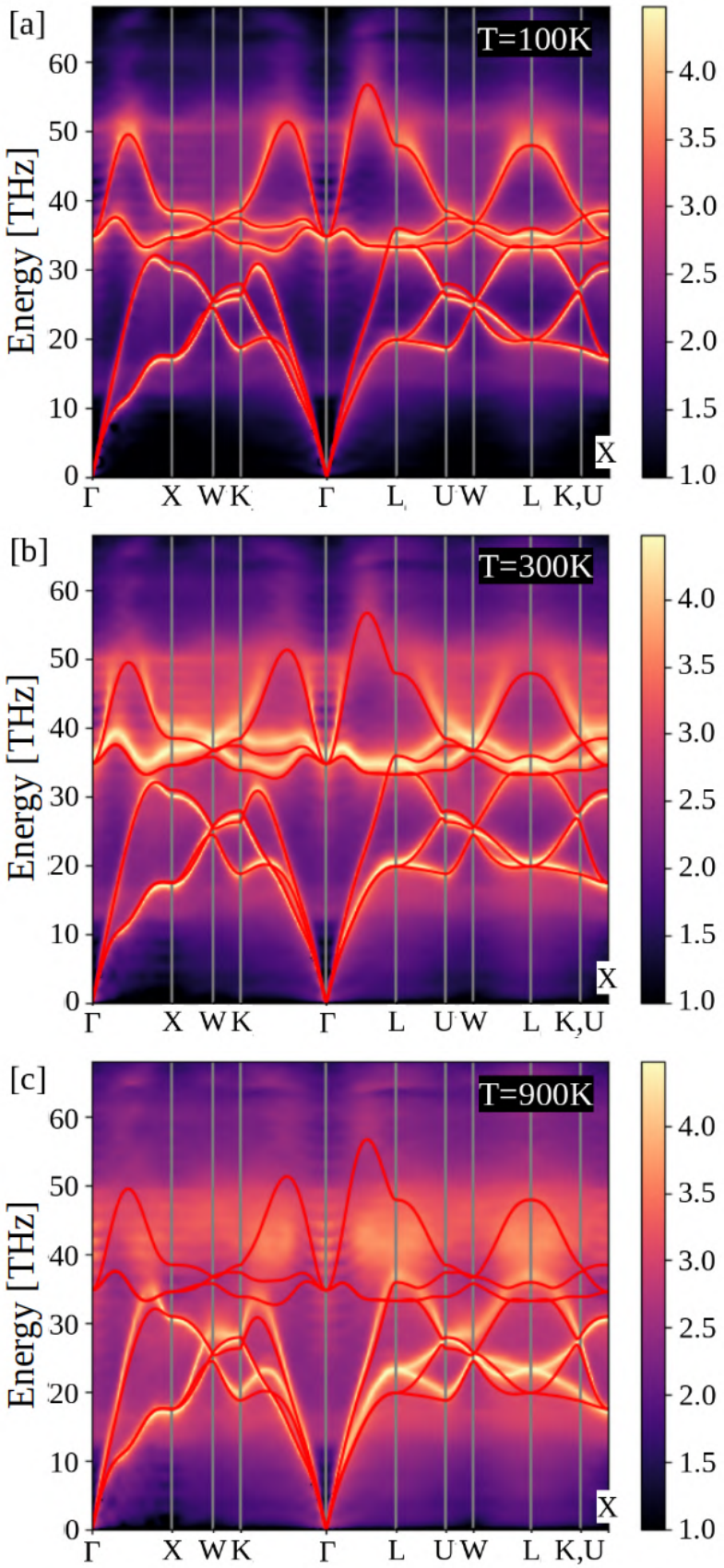

Figure 6.17: Renormalization of the phonon bands in KF for (a) 100K (b) 300K and (c) 900K. The red line corresponds to the harmonic phonon dispersion. As a decoration, the logarithm with base 10 of the trace of the spectral density matrix in the mode basis is presented as background color. The value corresponds to the value depicted by the colorbar on the right.

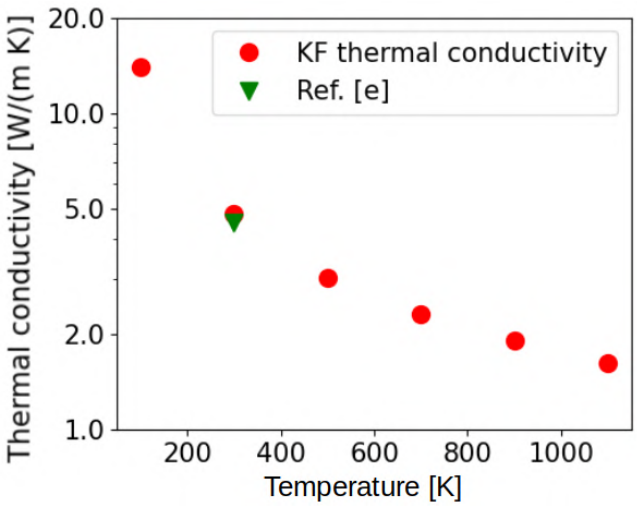

Figure 6.18: Lattice thermal conductivity of KF calculated with the BTE (red). Experimental data indicated by [e] is taken from Ref. (141) (green).

6.5 POTASSIUM FLOURIDE

KF is a chemical compound that has no thermoelectric applications nowadays. Nevertheless it is a role-model as a material with a mediocre thermal conductivity (141) where atoms have large relative mass differences. KF crystallizes in an fcc structure.

In Fig. 6.16, the phonon bands are presented. The maximum phonon frequency of 56THz is moderate. I used first-order perturbation theory to calculate the self-energy of this material. In Fig. 6.17, the spectral density plots are displayed for 100K, 300K, and 900K. The renormalized phonon frequencies grow slowly with increasing temperature. The broadening of the spectral densities is rather small, and grows as well. These observations are, as for the other materials, expected (see discussion in Sec. 6.1).

In Fig. 6.18 the thermal conductivity calculated with the BTE is presented as a function of temperature. The only reference calculation (141), at 300K, is in good agreement. This should be, as the reference calculation was performed with PBEsol using `FHI-aims` (using GK-MD). The expected $1/T$ dependence of the conductivity can be observed. As all theoretical expectations are met, it is reasonable to assume that the phonon propagator was modelled accurately. Therefore I expect, that the correction can be calculated quite accurately. It turns out that the second-order correction, with less than $10^{-4} W/mK$, is also in this material negligible. We observe with this example, that also a material with nuclei of largely different mass does not exhibit a significant second-order correction.

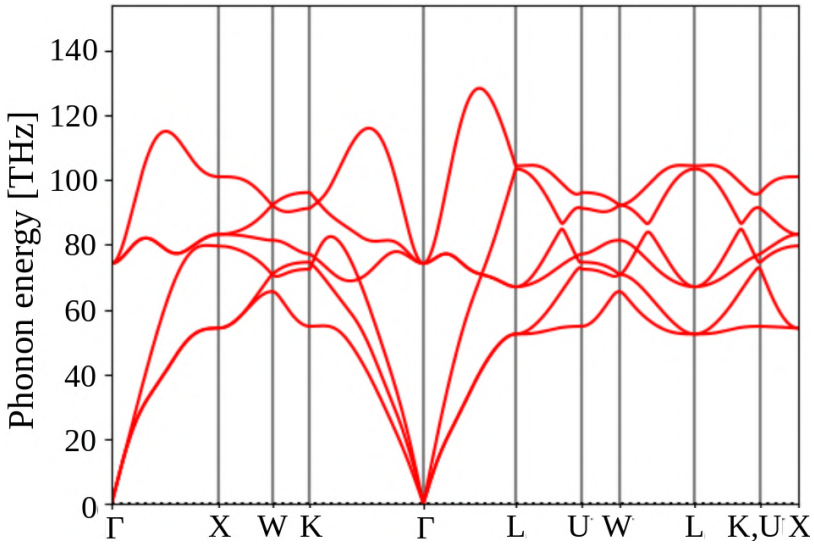

Figure 6.19: Phonon band structure of MgO (PBEsol).

6.6 MAGNESIUM OXIDE

MgO is a material with a high lattice thermal conductivity and low electrical conductivity. It is stable at high temperatures and used as refractory. It is a role model as a good thermal conductor, to calculate the correction to the BTE at high temperatures (e.g. 3000K). MgO crystallizes in an fcc structure.

In Fig. 6.19 the phonon frequencies are presented as a function of $\mathbf{q}$. The maximum phonon frequency of the material is large, with 128THz. I used first-order perturbation theory to compute the self-energy in MgO.

In Fig. 6.20, the spectral density plots for MgO are shown. The renormalized phonon frequencies increase significantly with temperature. The broadening is not very large, but also increases with temperature. Both these observations are, as for the other materials, expected (see discussion in Sec. 6.1).

In Fig. 6.21 the lattice thermal conductivity calculated with the BTE is presented as a function of the temperature. Another calculation (141) with GK-MD agrees very well with the result of my calculation at room temperature. Especially at low temperatures, the agreement of the calculation with experiment is good. At high temperatures, there is a discrepancy between my calculation and the experiment. This is reasonable because the effect of fourth order IFCs on the phonon decay is probably not negligible anymore (13, 234). The $1/T$ dependence can be observed in experiment (136), but not in my BTE calculation. This may be due to the high phonon frequencies in the material, so that the mode heat-capacity of the high-energy phonon modes saturates only for high temperatures.

As most theoretical expectations are met, it seems reasonable to assume that the phonon propagator was modelled accurately in

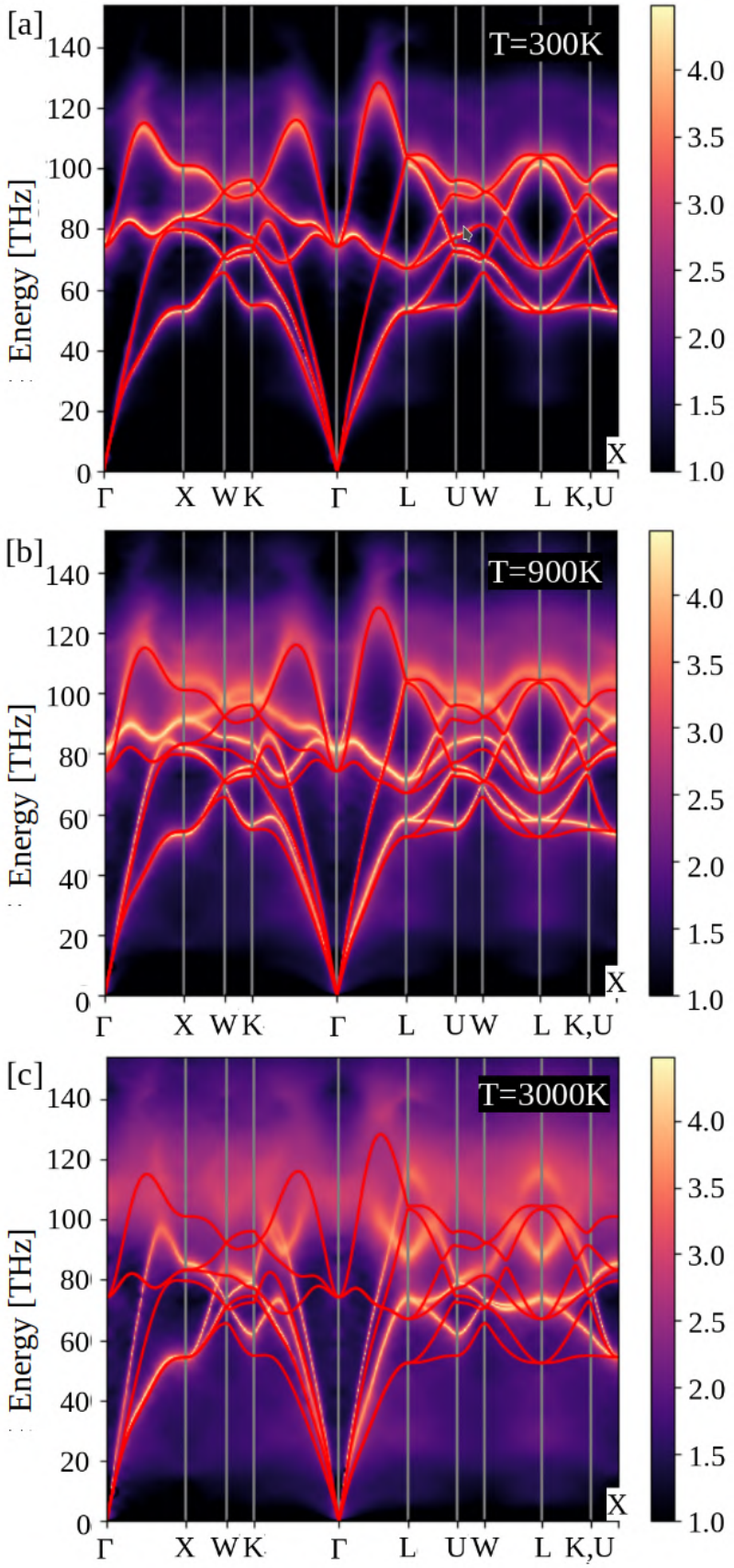

Figure 6.20: Renormalization of the phonon bands in MgO for (a) 300K (b) 900K and (c) 3000K. The red line corresponds to the harmonic phonon dispersion. As a decoration, the logarithm with base 10 of the trace of the spectral density matrix in the mode basis is presented as background color. The value corresponds to the value depicted by the colorbar on the right.

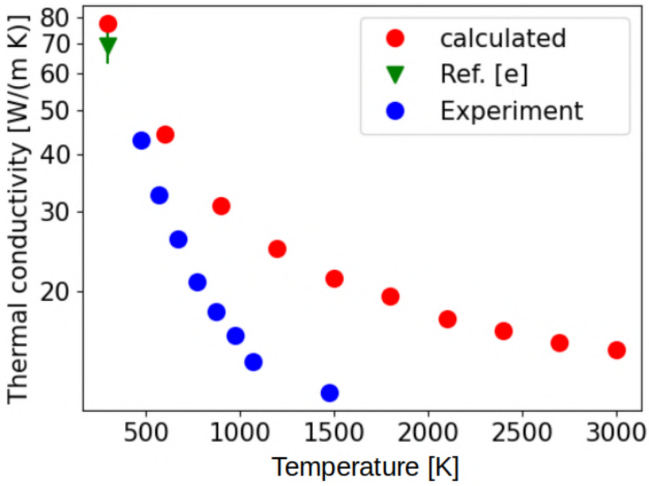

Figure 6.21: Lattice thermal conductivity in MgO calculated with the BTE (red). Reference [e] is Ref. (141) (GK-MD) (green) and experimental data is taken from Ref. (136) (blue).

this system. Therefore the second-order correction can be evaluated rather accurately. Also in this material it is negligible, being less than $10^{-2} W/mK$. I conclude that also a material with a large thermal conductivity may not exhibit a significant second-order correction.

6.7 FAILED ATTEMPTS

I describe here also attempted calculations that failed. They give a hint, what may be improved in the future.

6.7.1 *Silver chloride*

AgCl serves in AgCl-electrodes. These are common reference electrodes in electrochemistry. AgCl can be used to manufacture photographic paper. It has no specific thermoelectric application but is known for its low thermal conductivity.

In Fig 6.22, the phonon bandstructure in the harmonic approximation is shown. The behavior of the absolute frequencies is caused by large intervals along the bandpath where the eigenvalues of the dynamical matrix become negative. These intervals are so large, that I did not renormalize the phonon frequencies, as this would mean a drastic manipulation of the phonon band-structure.

At higher pressure, the bands of AgCl may become stable using the harmonic approximation. But then, there is no chance to compare to the MD calculations of Ref. (141) under normal conditions anymore. For this reason, I did not perform further analysis for AgCl.

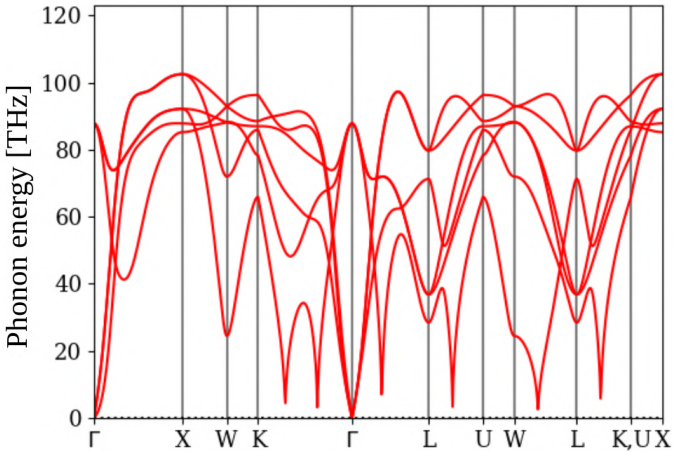

Figure 6.22: Harmonic phonon band structure of AgCl.

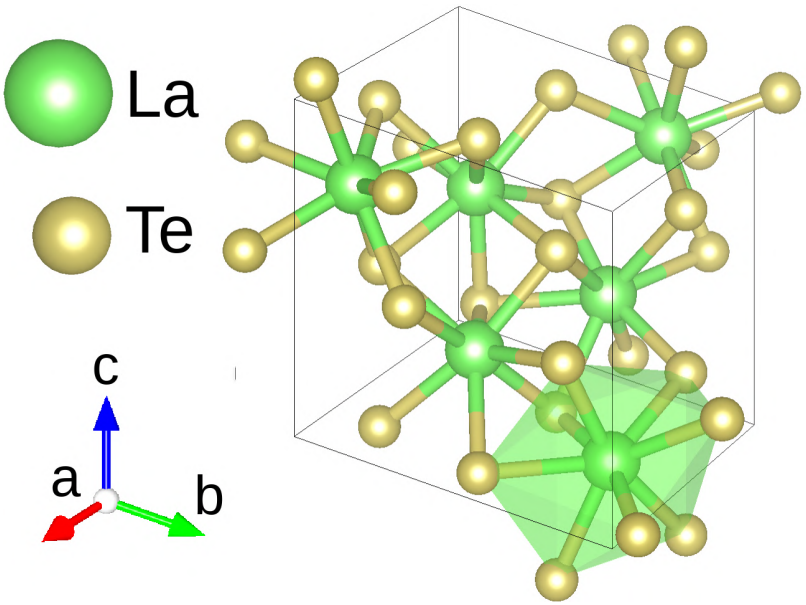

Figure 6.23: Unit cell of La_3Te_4. The coordination polyhedron of a La-atom is shown.

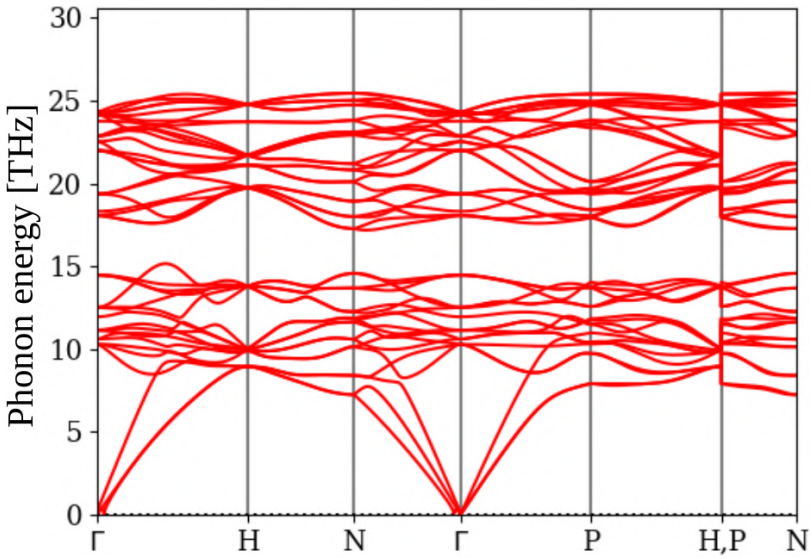

Figure 6.24: Phonon band structure of La_3Te_4.

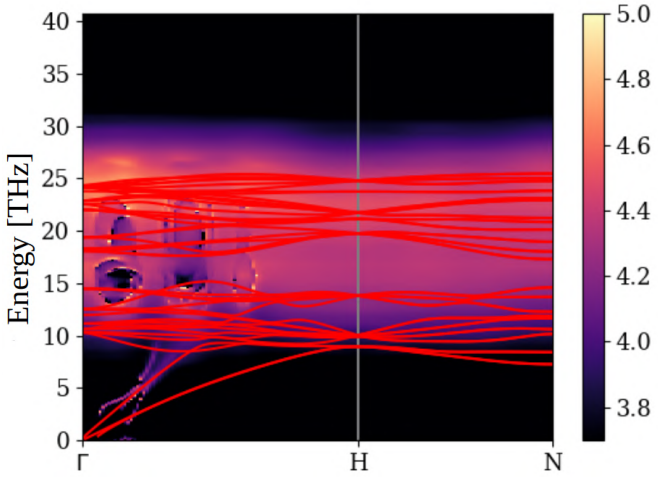

Figure 6.25: Renormalization of the phonon bands in La_3Te_4 for 300K. The red line corresponds to the harmonic phonon dispersion. As a decoration, the logarithm with base 10 of the trace of the spectral density matrix in the mode basis is presented as background color. The value corresponds to the value depicted by the colorbar on the right.

6.7.2 *Lanthanum telluride*

$La_{3-x}Te_4$ is a promising high-temperature thermoelectric (280) known to have a low lattice thermal conductivity (177). Up to 1/9 of the La atomic positions in the crystal structure can be vacant (177) and these vacancies can lead to increased phonon scattering. I tried to study La_3Te_4.

In Fig. 6.23 the body-centered cubic crystal structure of La_3Te_4 is depicted, where a coordination polyhedron of a La atom is highlighted. In Fig. 6.24, the phonon bands are presented. To compute the self-energy, I used first-order perturbation theory discarding the constant contribution to the self-energy $\Sigma^c_{\mathbf{q}}$. In Fig. 6.25, the resulting spectral density plots are presented. They exhibit circular features, that are not seen in other spectral density plots. This is due to a lack of convergence, as the spectral density changes sign. This change in sign should not occur, as it signals that the imaginary part of the self-energy has the wrong sign which in turn means, that causality is violated.

Nonetheless, thermal conductivity calculations, using the BTE and the correction to the BTE, have been performed (see Appendix N). The results for the BTE are, however, unrealistically low. To investigate this material, larger computational resources are necessary (I used 30000 core hours, with the DPA).

6.8 SECOND ORDER CORRECTION

The results for the correction to the BTE can be summed up as follows:

The correction to the BTE for the lattice thermal conductivity has almost no influence in the investigated materials at any simulated temperature.

The precise numerical results can be found in Appendix N, in Tables N.16, N.17, N.18, N.20, N.22, N.24, and N.26. The correction never overcomes the value of $3 \cdot 10^{-2} W/(mK)$. Before performing these calculations, I did not find an convincing argument, hinting at the size of the correction term. In the view of the results, I may, however, give possible reasons. Lets recall the contribution to the lattice thermal conductivity, Eq. (4.30), from Sec. 4

$$\frac{1}{\hbar^6 N_p^2 \Omega_c^2} \int_{\mathbb{R}} d\mathcal{E} \sum_{\{\mathbf{q}\nu\}} \left(-144\mathcal{E}_1 \pi(\mathcal{E}_0 + \mathcal{E}_1)\right) J_1^j(\mathbf{q}_0, \nu_0; -\mathbf{q}_0, \nu_1) \times$$
$$J_1^j(\mathbf{q}_0 + \mathbf{q}_1, \nu_2; -\mathbf{q}_0 - \mathbf{q}_1, \nu_3) \times$$
$$v^3(\mathbf{q}_0, \nu_4; \mathbf{q}_1, \nu_5; -\mathbf{q}_0 - \mathbf{q}_1, \nu_6) \times$$
$$v^3(\mathbf{q}_0 + \mathbf{q}_1, \nu_7; -\mathbf{q}_1, \nu_8; -\mathbf{q}_0, \nu_9) \times$$
$$\mathcal{S}_{\mathbf{q}_1,\nu_1,\nu_5}(\mathcal{E}_1) \mathcal{S}_{\mathbf{q}_1,\nu_8,\nu_0}(\mathcal{E}_1) \times$$
$$\mathcal{S}_{\mathbf{q}_0,\nu_9,\nu_4}(\mathcal{E}_0) n_B^{(1)}(\mathcal{E}_1) n_B(\mathcal{E}_0) \times$$
$$\mathcal{G}_{\mathbf{q}_0+\mathbf{q}_1,\nu_3,\nu_7}(\mathcal{E}_0 + \mathcal{E}_1) \times$$
$$\mathcal{G}_{\mathbf{q}_0+\mathbf{q}_1,\nu_6,\nu_2}(\mathcal{E}_0 + \mathcal{E}_1).$$

Three reasons, that may cause the small size of the correction, are:

- The correction term contains two integrals over energies $\mathcal{E}$, and the integrand is only non-zero within the range $[-\mathcal{E}_{\max}, \mathcal{E}_{\max}]$. For the BTE, there is only one such integral. For the correction there are two. As the value of an integral is proportional to the size of the integration region, the correction is of the order of $\mathcal{E}_{\max}^2/\mathrm{Ha}^2$, while the BTE is of the order $\mathcal{E}_{\max}/\mathrm{Ha}$. As the phonon frequencies are very small compared to a Hartree the correction should be smaller.
- For the trace elements of the thermal conductivity tensor, the integrand of the BTE is positive *everywhere* - which may not be the case for the correction.
- If one assumes the virial approximation (that is supposed to be reasonable for crystalline solids), the correction to the BTE contains at least two anharmonic force constants. Their value in natural units (Ha B^{-n}) is probably much smaller than 1.

One more observation can be made: the correction is significantly smaller in bad thermal conductors, such as SnSe. I want to give a possible reason here: If one recalls Eq. (4.30), the integrand is a product of spectral densities and vertex functions. In a bad conductor, the vertex functions are larger than in a good one. But at the same time, the scattering rates for the phonons rise (proportional to the square of the anharmonic vertices), which leads to a stronger broadening of the spectral densities in their peak-region. If the contribution of the correction to the thermal conductivity is dominated by those peaks in the integration region, then the broadening of the spectral densities would decrease the correction to the thermal conductivity. As there are at least three spectral densities, but at most two anharmonic vertices, the broadening of the spectral densities may dominate the increase of the anharmonic vertices, and therefore the correction to the BTE is dwarfed even further in strongly anharmonic materials. This trend would only be stopped, if further damping of the spectral densities is no longer possible (as there are spectral moments that must be fulfilled)

such that the contribution grows with the anharmonic vertex functions only. This regime seems not to occur in any of the investigated crystals.

I use a simple model now, to check when the correction to the BTE may become important. This is superior to the artificial increase of the temperature or anharmonic IFC strength, as in this case perturbation theory would break down. Consider a model where the spectral density is maximally flattened with one parameter ($\mathcal{E}_m$)

$$\mathcal{S}_{\mathbf{q},\nu,\nu'}(\mathcal{E}) = c_{\mathbf{q},\nu,\nu'}\mathrm{sgn}(\mathcal{E})\theta(\mathcal{E}_m - |\mathcal{E}|), \tag{6.1}$$

where sgn is the sign function. By fitting $c_{\mathbf{q},\nu,\nu'}$ to the first spectral moment, I find

$$c_{\mathbf{q},\nu,\nu'} = \frac{2\hbar\omega_{\mathbf{q},\nu}\delta_{\nu,\nu'}}{\mathcal{E}_m^2}. \tag{6.2}$$

This model is physical, as the behavior of the phonon propagator at large energies is not changed:

$$\begin{aligned}\mathcal{G}_{\mathbf{q},\nu,\nu'}(\mathcal{E}) &= c_{\mathbf{q},\nu,\nu'}\left[\log(1-\mathcal{E}_m/\mathcal{E}) + \log(1+\mathcal{E}_m/\mathcal{E})\right] \\ &= \mathcal{O}(\mathcal{E}^{-2}) \quad \text{for large } \mathcal{E}.\end{aligned} \tag{6.3}$$

This model is non-perturbative, and $\mathcal{E}_m$ is not related to the maximum phonon frequency of the system. Inserting this into Eq. (4.30) or any other term of second-order, the scaling with respect to $\mathcal{E}_m$ becomes

$$c(\mathcal{E}_m)^n\mathcal{E}_m^2\mathcal{E}_m^p n_B(\mathcal{E}_m)n_B^{(1)}(\mathcal{E}_m), \tag{6.4}$$

where n is the number of spectral densities and propagators in the term, which is 3, 4, or 5. $\mathcal{E}_m^2$ comes from the integration, and $\mathcal{E}_m^p$ from the prefactor (p is at least 2 and at most 6). However, the $p = 6$ term corresponds to kinetic energy transport due to the motion of the nuclei, which should be small, and therefore, in practice the maximum p is 4. For small $\mathcal{E}_m$, the correction scales in between $\mathcal{E}_m^{-3}$ and $\mathcal{E}_m^{-9}$. In comparison, the BTE scales like $\mathcal{E}_m^{-2}$. That means, if $\mathcal{E}_m$ is really small, the correction becomes more important. The correction should also matter more in this model, when the temperature is increased (as it carries two instead of one occupation factor). Larger anharmonic vertex functions would increase the correction in this model, as well as larger phonon frequencies. Whether there are physical conditions that can be described with this model is unclear, to the best of my knowledge. Nonetheless, it shows that, mathematically, it should be possible to obtain a large correction term.

7 CONCLUSIONS AND OUTLOOK

In this work, I investigated the lattice thermal conductivity of crystalline solids by means of many-body theory. I was able to derive a BTE from the definition of the lattice thermal conductivity as well as a new second-order correction without any but the BO approximation. I did *not* further approximate the phonon propagator or the heat-flux operator to derive both formulas. To model the phonons in the crystals, I calculated the phonon propagator with perturbation theory and SCPT. The thermal conductivity was evaluated with the BTE and my new correction for interesting thermoelectrics, PbTe, Bi_2Te_3, SnSe and B_4C and other materials, MgO and KF. The `beyBol` package that I developed for these calculations will be available online (126).

My results show that the second-order correction is for all investigated materials negligible compared to the BTE. This suggests that the BTE is a very good approximation to the lattice thermal conductivity, given the correct phonon propagator, because the perturbation expansion constitutes an asymptotic series, and therefore it is unlikely that higher terms of the expansion would be meaningful *and* significant at a time (see Appendix F). This means that vertex corrections for phonon thermal transport as suggested in Refs. (31) and (253) are likely to be negligible as well, as they constitute a further approximation to the correction. This is different from electronic transport (223). These considerations are especially applicable for the most anharmonic solids. This work agrees with the literature (37), stating that more anharmonic materials generally have a lower lattice thermal conductivity, as the correction is not larger in materials with stronger phonon-phonon scattering. Hence, if it is possible to obtain a realistic phonon propagator for a strongly anharmonic thermoelectric, the BTE might well be sufficient to model the thermal conductivity, and there is no need for numerically intense MD simulations. This may facilitate high-throughput calculations of the lattice thermal conductivity. Whether it is possible to obtain the phonon propagator in strongly anharmonic systems by numerically less intense methods remains, however, unclear.

The materials, studied in this thesis, cover a wide range of characteristics. The most efficient and most used thermoelectrics, known today, have been modelled. However, what all modelled materials have in common is, that they have rather small unit cells, so the numerical calculations remained feasible. In future work, more complicated systems might be investigated with faster and more stable calculation methods. Such methods might be the singular value decomposition of tensors (for the correction calculation) (12) or fast sparse multiplication

schemes (80, 92, 97). Also graphical processing units could be useful (134).

Structurally disordered materials such as β-ZnSb (73) may be modelled using means of many-body theory (204, 248), by introducing additional self-energy terms to account for the disorder. In the same spirit impurities (225) and isotope mass differences (168) may be handled. The theory for lattice thermal conduction that I have developed is additionally independent of the notion of a phonon, once the vibration propagator is known. As a result, it is probably possible to extend the theory in the spirit of Ref. (256), but this may, as usual in science, need a bunch of new concepts (8).

The theory considered in this thesis heavily relies on the applicability of the BO approximation in solids. It is, however, known that this approximation cannot be used for all materials, and breaks for example in graphene (221). It would be interesting to extend the current theory beyond the BO approximation. The calculation of the electronic contribution to the thermal conductivity and the entangled electron-phonon thermal transport problem are other, possible extensions of this work, that would introduce the effects of electron-phonon coupling (88).

Part III

APPENDIX

A

GENERAL DEFINITIONS

In my notation I follow Giustino (88), who defines the ion index as $\{\kappa, \alpha, p\}$, where κ is the index of the nucleus in the unit cell, α is any Cartesian direction and p is the index of the unit cell itself. The following equations are important.

$$\sum_{\nu} \left(e^{\alpha}_{\kappa,\nu}(\mathbf{q})\right)^{*} e^{\alpha'}_{\kappa',\nu}(\mathbf{q}) = \delta_{\kappa,\kappa'}\delta^{\alpha,\alpha'} \tag{A.1}$$

$$\sum_{\kappa,\alpha} \left(e^{\alpha}_{\kappa,\nu}(\mathbf{q})\right)^{*} e^{\alpha}_{\kappa,\nu'}(\mathbf{q}) = \delta_{\nu,\nu'} \tag{A.2}$$

$$\left(e^{\alpha}_{\kappa,\nu}(\mathbf{q})\right)^{*} = e^{\alpha}_{\kappa,\nu}(-\mathbf{q}) \tag{A.3}$$

$$\widehat{p}^{\alpha}_{\kappa,p} = \sqrt{\frac{M_\kappa}{N_p}} \sum_{\mathbf{q},\nu} \exp\left(i\mathbf{q}\cdot(\mathbf{R}_p + \boldsymbol{\tau}_\kappa)\right) \widehat{P}^{\alpha}_{\mathbf{q},\kappa} \tag{A.4}$$

$$\widehat{P}^{\alpha}_{\mathbf{q},\kappa} = \sum_{\nu} e^{\alpha}_{\kappa,\nu}(\mathbf{q}) \sqrt{\frac{\hbar}{2\omega_{\mathbf{q},\nu}}} \widehat{P}_{\mathbf{q},\nu} \tag{A.5}$$

$$\widehat{u}^{\alpha}_{\kappa,p} = \sqrt{\frac{1}{M_\kappa N_p}} \sum_{\mathbf{q}} \exp\left(i\mathbf{q}\cdot(\mathbf{R}_p + \boldsymbol{\tau}_\kappa)\right) \widehat{U}^{\alpha}_{\mathbf{q},\kappa} \tag{A.6}$$

$$\widehat{U}^{\alpha}_{\mathbf{q},\kappa} = \sum_{\nu} e^{\alpha}_{\kappa,\nu}(\mathbf{q}) \sqrt{\frac{\hbar}{2\omega_{\mathbf{q},\nu}}} \widehat{U}_{\mathbf{q},\nu} \tag{A.7}$$

$$\sum_{\mathbf{q}} \exp(i\mathbf{q}\cdot\mathbf{R}_p) = N\delta_{p,0} \quad \text{and} \quad \sum_{p} \exp(i\mathbf{q}\cdot\mathbf{R}_p) = N\Delta(\mathbf{q}) \tag{A.8}$$

Here, N_p is the number of unit cells, in the considered super-cell, e is the phonon polarization and $\Delta(\mathbf{q})$ is a boolean asking whether $\mathbf{q}$ is a reciprocal lattice vector.

B

INTERATOMIC FORCE CONSTANTS

B.1 CALCULATION OF THE INTERATOMIC FORCE CONSTANTS

The interatomic force constants (IFCs) are the derivatives of the Born-Oppenheimer surface, see Sec. 2.1.

To obtain a reasonable approximation to the IFCs I use the density functional theory (DFT) (48, 120, 211) and a finite displacement approach (209, 274). DFT is not guaranteed to obtain the correct physical IFCs. It is however a standard method in modern materials science and is usually a good model for the electronic properties of a system (see Appendix O). The DFT calculations must run in supercells that are a set of repeated unit cells. In these supercells some atoms are displaced. These displacements from the equilibrium position lead to forces on all atoms of the supercell, that can be calculated within DFT.

To obtain the IFCs I rely on Tadano's `ALM` code (268), and so I follow here the reference. Tadano defines the vector $\mathbf{b} = \frac{\partial E_B}{\partial \mathbf{\Phi}}$ where $\mathbf{\Phi}$ is the vector of IFCs. Then, the IFCs $\mathbf{\Phi}$ are adjusted to minimize the difference with respect to the forces calculated by DFT (F_{DFT}):

$$||F_{\mathbf{\Phi}} - F_{\mathrm{DFT}}||_2 = \left|\left|\frac{\partial \mathbf{b}}{\partial \mathbf{u}}\mathbf{\Phi} - F_{\mathrm{DFT}}\right|\right|_2, \tag{B.1}$$

and the matrix $\frac{\partial \mathbf{b}}{\partial \mathbf{u}}$ depends on the configuration $\mathbf{u}$. The vector $\mathbf{\Phi}$ is then chosen to minimize the error with linear regression techniques. `ALM` also provides a tool to choose configurations $\mathbf{u}$, such that the fit error of the IFCs is minimized and the symmetries of the IFCs are taken into account (`ALM`s `suggest` method). I interfaced my code with the `ALM` system and used the atomic simulation environment (`ASE`) (151) to generate input files and read output files for the DFT code `FHI-aims` (21, 105). More explicitly, the `geometry.in` file is written, and the `aims.out` file is read. After the DFT calculations have been performed, the forces are read from the `aims.out` file, so they can be used by `ALM`s `optimize` method to obtain a list of IFCs. This list of IFCs is written into input files for the `beyBol` system.

To reduce the number of necessary DFT calculations, the symmetry of the crystal is exploited (see Appendix B.2) and assumptions are made about the IFCs: IFCs of order 3 and higher are not taken into account, if the distance between the interacting atoms is larger than a cutoff distance r_{max}, depending on the atom types in the interaction. A further reduction of the number of calculations is achieved by limiting the interactions to a number of m_o particles (for each order of the IFCs independently), where m_o can be lower than the order of the respective

IFC. The information about the cutoff-distances and excluded multi-body interactions is called the force model of the calculation. The parameters of the force model have to be converged with respect to the self-energy and thermal conductivity, which can lead to a large number of DFT calculations, especially in complex, low-symmetry crystals. The computational expense of the DFT calculations easily outweighs all forthcoming calculations. As the same IFCs that my system needs are necessary to evaluate the BTE in the RTA, I conclude that my system is computationally only marginally more expensive than the older BTE.

An alternative approach to calculate the IFCs of a crystal is given by density functional perturbation theory (16, 58, 91), which has not been used in this work. In most implementations, only second order IFCs can be calculated (`VASP` (98), `siesta` (81), `FHI-aims` (21)) and only the `d3q` package (212) of `QuantumEspresso` (84, 85) is able to calculate third order constants. Higher-order constants have, to the best of my knowledge, not been computed using density functional perturbation theory.

In finite-displacement approaches compressed sensing techniques (64, 268, 302) for the solution of Eq. (B.1) have been proposed, to further reduce the number of DFT calculations necessary. However, it is known in the literature, that the result of the thermal conductivity is very sensitive on the accuracy of the forces (down to $1 \mu eV/\text{Å}$) (294) so that usual fit errors of about 2% as given by compressed sensing approaches (302) are hardly recommendable for this study. More on this topic, and an explanation why the results are so sensitive is given in Sec. 5.2.

B.2 PROPERTIES OF THE INTERATOMIC FORCE CONSTANTS

In this Appendix, the properties of the IFCs due to the invariances of the crystal energy are summed up (23). There is permutation invariance, as E_B is a continuous function, and so, derivatives can be interchanged:

$$\Phi^{\kappa_1,p_1,\dots,\kappa_n,p_n}_{\alpha_1,\dots,\alpha_n} = \Phi^{\kappa_{P(1)},p_{P(1)},\dots,\kappa_{P(n)},p_{P(n)}}_{\alpha_{P(1)},\dots,\alpha_{P(n)}}, \tag{B.2}$$

for any permutation P of the set $\{1,\dots,n\}$. The translation invariance guarantees a vanishing net force on the unit cells:

$$\sum_{\kappa_i,p_i} \Phi^{\kappa_1,p_1,\dots,\kappa_n,p_n}_{\alpha_1,\dots,\alpha_n} = 0, \tag{B.3}$$

for any i in the set $\{1, ..., n\}$. The space-group symmetries lead to more relations: If one has a symmetry operation that leaves the crystal lattice invariant $\mathcal{O} = \{S|v_S\}$ in Seitz notation, then

$$\Phi^{\mathcal{O}(\kappa_1),\mathcal{O}(p_1),...,\mathcal{O}(\kappa_n),\mathcal{O}(p_n)}_{\alpha_1,...,\alpha_n} = \sum_{\{\mu\}} \left(\prod_{l=1}^{n} S^{\mu_l}_{\alpha_l} \right) \Phi^{\kappa_1,p_1,...,\kappa_n,p_n}_{\mu_1,...,\mu_n}, \tag{B.4}$$

where $\mathcal{O}(p)$ is the unit cell that the nuclei from unit cell p with index κ is mapped to by the operation, and $\mathcal{O}(\kappa)$ is the new nuclei index. Rotation invariance has not been used in this thesis (but is used by `ALM` (268)).

C

VANISHING CONSTANT TERM

According to Ref. (204), the constant term in the spectral theorem reads (for the phonon case)

$$\lim_{\mathcal{E}\to 0} \mathcal{E}\mathcal{G}_{\mathbf{q}\nu\nu'}(\mathcal{E}) = 2\hbar d, \tag{C.1}$$

and d is to be calculated. Now $\mathcal{G}_{\mathbf{q}\nu\nu'}(\mathcal{E})$ is well behaved at $\mathcal{E} = 0$:

$$\mathcal{G}_{\mathbf{q}\nu\nu'}(0) = \int_{\mathbb{R}} d\mathcal{E}' \frac{\mathcal{S}_{\mathbf{q}\nu\nu'}(\mathcal{E}')}{\mathcal{E}'}, \tag{C.2}$$

and the phonon spectral density is an odd function, such that the integrand is finite everywhere, and so is $\mathcal{G}$ as the integration domain is finite. Then, the above integral is finite and so is $\mathcal{G}_{\mathbf{q}\nu\nu'}(0)$. As a result, $d = 0$.

D

NON-ZERO TEMPERATURE WICK THEOREM

I follow here Ref. (204). The proof of Wick's theorem works as follows: be $\widehat{A}_1(\tau_1)...\widehat{A}_{2n}(\tau_{2n})$ already time ordered (without loss of generality), then the times of the operators are $\tau_1 > \tau_2 ... > \tau_{2n}$. The time evolution of a creation or annihilation operator is

$$\widehat{A}_i(\tau_i) = \gamma_i(\tau_i)\widehat{\alpha}_i, \tag{D.1}$$

where $\widehat{\alpha}_i$ may be a creation or annihilation operator, and $\gamma_i(\tau_i) = \exp(\sigma_i \frac{E_i}{\hbar}\tau_i)$, with $\sigma_i = \pm 1$ with positive sign for a creation operator. The time evolution of a contraction is trivial

$$\begin{aligned}\langle \widehat{A}_i(\tau_i)\widehat{A}_j(\tau_j)\rangle^{(0)} &= \gamma_i(\tau_i)\gamma_j(\tau_j)\langle \widehat{\alpha}_i\widehat{\alpha}_j\rangle^{(0)} \\ &= \gamma_i(\tau_i)\gamma_j(\tau_j)\frac{\left[\widehat{\alpha}_i, \widehat{\alpha}_j\right]}{1-\gamma_i(\hbar\beta)},\end{aligned} \tag{D.2}$$

where the second line follows after computing all relevant expectation values, and the combination of the result. [...] means the commutator.

$$\begin{aligned}\frac{\langle \widehat{A}_1(\tau_1)...\widehat{A}_{2n}(\tau_{2n})\rangle^{(0)}}{\gamma_1(\tau_1)...\gamma_{2n}(\tau_{2n})} &= \langle \widehat{\alpha}_1...\widehat{\alpha}_{2n}\rangle^{(0)} \\ &= \sum_{i=2...2n}\langle \widehat{\alpha}_2...[\widehat{\alpha_1}, \widehat{\alpha}_i]...\widehat{\alpha}_{2n}\rangle^{(0)} \\ &+ \langle \widehat{\alpha}_2...\widehat{\alpha}_{2n}\widehat{\alpha}_1\rangle^{(0)}.\end{aligned} \tag{D.3}$$

$\widehat{\alpha}_1$ can be commuted with $\widehat{\rho}_0$ by noting that $\widehat{\alpha}_1\widehat{\rho}_0 = \gamma_1(\hbar\beta)\widehat{\rho}_0\widehat{\alpha}_1$. Then

$$\begin{aligned}\frac{\langle \widehat{A}_1(\tau_1)...\widehat{A}_{2n}(\tau_{2n})\rangle^{(0)}}{\gamma_1(\tau_1)...\gamma_{2n}(\tau_{2n})}(1-\gamma_1(\hbar\beta)) &= \sum_{i=2...2n}\langle \widehat{\alpha}_2...[\widehat{\alpha_1}, \widehat{\alpha}_i]...\widehat{\alpha}_{2n}\rangle^{(0)} \\ \Rightarrow \langle \widehat{A}_1(\tau_1)...\widehat{A}_{2n}(\tau_{2n})\rangle^{(0)} &= \sum_{i=2...2n}\langle \widehat{A}_2...\widehat{A}_{i-1}\widehat{A}_{i+1}...\widehat{A}_{2n}\rangle^{(0)}\times \\ &\times \langle \widehat{A}_1\widehat{A}_i\rangle^{(0)}.\end{aligned} \tag{D.4}$$

The time arguments in the last line have been omitted for convenience. The expectation value is zero if the number of operators is odd, as the free Hamiltonian $\widehat{H}_0$ commutes with the number operator of all particles. Another important fact is that Wick's theorem applies to operators of the type

$$\widehat{A} = \xi_1\widehat{\alpha} + \xi_2\widehat{\alpha}^\dagger, \tag{D.5}$$

which is easily seen by decomposing the expectation value into the composing creation and annihilation operators and recollecting terms

thereafter. The example used in this thesis, are the displacement and momentum operators of the phonons $\widehat{U}$ and $\widehat{P}$.

E

SPECTRAL DENSITY AND PROPAGATOR

E.1 NON-INTERACTING PROPAGATOR

As a starting point of the calculation, the non-interacting propagators of the theory are computed. Those can be easily found from the fundamental contractions (166)

$$\begin{aligned}
\alpha_{\mathbf{q},\nu,\mathbf{q}',\nu'}(\tau) &= \langle \widehat{a}^{\dagger}_{\mathbf{q},\nu}(\tau)\widehat{a}_{\mathbf{q}',\nu'}\rangle^{(0)} \\
&= \exp(\omega_{\mathbf{q},\nu}\tau)n_B(\hbar\omega_{\mathbf{q},\nu})\delta_{\nu,\nu'}\delta_{\mathbf{q},-\mathbf{q}'} \text{ and} \\
\beta_{\mathbf{q},\nu,\mathbf{q}',\nu'}(\tau) &= \langle \widehat{a}_{\mathbf{q},\nu}(\tau)\widehat{a}^{\dagger}_{\mathbf{q}',\nu'}\rangle^{(0)} \\
&= \exp(-\omega_{\mathbf{q},\nu}\tau)(n_B(\hbar\omega_{\mathbf{q},\nu})+1)\delta_{\nu,\nu'}\delta_{\mathbf{q},-\mathbf{q}'},
\end{aligned} \tag{E.1}$$

where n_B is the boson occupation factor. This result is obtained from elementary statistical mechanics. Writing this in Matsubara components (Eq. (2.33)) results in

$$\begin{aligned}
\alpha_{\mathbf{q},\nu,\mathbf{q}',\nu'}(E_n) &= \int_0^{\hbar\beta} d\tau \alpha_{\mathbf{q},\nu,\mathbf{q}',\nu'}(\tau)\exp(i\frac{E_n}{\hbar}\tau) \\
&= \frac{-\hbar}{E_n+\hbar\omega_{\mathbf{q},\nu}}\delta_{\nu,\nu'}\delta_{\mathbf{q},-\mathbf{q}'} \text{ and} \\
\beta_{\mathbf{q},\nu,\mathbf{q}',\nu'}(E_n) &= \frac{\hbar}{E_n-\hbar\omega_{\mathbf{q},\nu}}\delta_{\nu,\nu'}\delta_{\mathbf{q},-\mathbf{q}'}.
\end{aligned} \tag{E.2}$$

The phonon propagator is therefore

$$\begin{aligned}
\mathcal{G}^{M,(0)}_{\mathbf{q},\nu,\mathbf{q}',\nu'}(E_n) &= \alpha_{\mathbf{q},\nu,\mathbf{q}',\nu'}(E_n)+\beta_{\mathbf{q},\nu,\mathbf{q}',\nu'}(E_n) \\
&= \hbar\left(\frac{1}{E_n-\hbar\omega_{\mathbf{q},\nu}}-\frac{1}{E_n+\hbar\omega_{\mathbf{q},\nu}}\right)\delta_{\nu,\nu'}\delta_{\mathbf{q},-\mathbf{q}'}.
\end{aligned} \tag{E.3}$$

As the propagator is diagonal in the momentum, the second momentum argument is usually omitted in this thesis.

E.2 GENERAL PROPERTIES

The propagator and spectral density (K is $\mathcal{G}$ or $\mathcal{S}$) in displacement and in mode basis relate as

$$K^{\alpha\alpha'}_{\mathbf{q}\kappa\kappa'}(\mathcal{E}) = \frac{\hbar}{2}\sum_{\nu\nu'} e^{\alpha}_{\kappa\nu}(\mathbf{q})e^{\alpha'}_{\kappa'\nu'}(-\mathbf{q})(\omega_{\mathbf{q}\nu}\omega_{\mathbf{q}\nu'})^{-1/2}K_{\mathbf{q}\nu\nu'}(\mathcal{E}). \tag{E.4}$$

All occurring spectral densities can be related to the phonon spectral density, using $\left[\widehat{U}_{\mathbf{q},\nu}, \widehat{H}\right] = \left[\widehat{U}_{\mathbf{q},\nu}, \widehat{H}_0\right] = i\hbar\widehat{P}_{\mathbf{q},\nu}$, use Eq. (2.14):

$$\begin{aligned}
\mathcal{S}^{\widehat{U}\widehat{P}}_{\mathbf{q},\nu,\nu'}(\mathcal{E}) &= \frac{\hbar}{\mathrm{Tr}(\widehat{\rho})}\sum_{\alpha,\beta}\langle\alpha|\widehat{U}_{\mathbf{q},\nu}|\beta\rangle\langle\beta|\widehat{P}_{-\mathbf{q},\nu'}|\alpha\rangle\exp(-\beta E_\alpha)\times \\
&\qquad [1-\exp(-\beta\mathcal{E})]\,\delta(\mathcal{E}-(E_\beta-E_\alpha)) \\
&= \frac{-i}{\mathrm{Tr}(\widehat{\rho})}\sum_{\alpha,\beta}\langle\alpha|\widehat{U}_{\mathbf{q},\nu}|\beta\rangle\langle\beta|\left[\widehat{U}_{-\mathbf{q},\nu'},\widehat{H}\right]|\alpha\rangle\exp(-\beta E_\alpha)\times \\
&\qquad \times[1-\exp(-\beta\mathcal{E})]\,\delta(\mathcal{E}-(E_\beta-E_\alpha)) \\
&= \frac{-i}{\mathrm{Tr}(\widehat{\rho})}\sum_{\alpha,\beta}\langle\alpha|\widehat{U}_{\mathbf{q},\nu}|\beta\rangle\langle\beta|\widehat{U}_{-\mathbf{q},\nu'}|\alpha\rangle\exp(-\beta E_\alpha)\times \\
&\qquad [1-\exp(-\beta\mathcal{E})]\,(E_\alpha-E_\beta)\delta(\mathcal{E}-(E_\beta-E_\alpha)) \\
&= \frac{i\mathcal{E}}{\hbar}\mathcal{S}_{\mathbf{q},\nu,\nu'}(\mathcal{E}). \qquad \text{(E.5)}
\end{aligned}$$

Similarly, one obtains

$$\begin{aligned}
\mathcal{S}^{\widehat{P}\widehat{U}}_{\mathbf{q},\nu,\nu'}(\mathcal{E}) &= -\frac{i\mathcal{E}}{\hbar}\mathcal{S}_{\mathbf{q},\nu,\nu'}(\mathcal{E}) \text{ and} \\
\mathcal{S}^{\widehat{P}\widehat{P}}_{\mathbf{q},\nu,\nu'}(\mathcal{E}) &= \frac{\mathcal{E}^2}{\hbar^2}\mathcal{S}_{\mathbf{q},\nu,\nu'}(\mathcal{E}). \qquad \text{(E.6)}
\end{aligned}$$

From the spectral representation of the propagator

$$\mathcal{G}^{r,\widehat{A}\widehat{B}}_{\mathbf{q}\nu\nu'}(\mathcal{E}) = \int_{\mathbb{R}} d\mathcal{E}'\,\frac{\mathcal{S}^{\widehat{A}\widehat{B}}_{\mathbf{q}\nu\nu'}(\mathcal{E}')}{\mathcal{E}+i0^+-\mathcal{E}'}, \qquad \text{(E.7)}$$

one can then derive the relations between the corresponding propagators.

$$\begin{aligned}
\mathcal{G}^{r,\widehat{P}\widehat{U}}_{\mathbf{q},\nu,\nu'}(\mathcal{E}) &= -\frac{i}{\hbar}\int_{\mathbb{R}} d\mathcal{E}'\,\frac{\mathcal{E}'\mathcal{S}_{\mathbf{q}\nu\nu'}(\mathcal{E}')}{\mathcal{E}+i0^+-\mathcal{E}'} \\
&= -\frac{i\mathcal{E}}{\hbar}\int_{\mathbb{R}} d\mathcal{E}'\,\frac{\mathcal{S}_{\mathbf{q}\nu\nu'}(\mathcal{E}')}{\mathcal{E}+i0^+-\mathcal{E}'} + \frac{i}{\hbar}\int_{\mathbb{R}} d\mathcal{E}'\,\mathcal{S}_{\mathbf{q}\nu\nu'}(\mathcal{E}') \\
&= -\frac{i\mathcal{E}}{\hbar}\mathcal{G}^r_{\mathbf{q},\nu,\nu'}(\mathcal{E}). \qquad \text{(E.8)}
\end{aligned}$$

The last step is possible because $\mathcal{S}$ is odd in its energy argument.

$$\mathcal{G}^{r/a,\widehat{U}\widehat{P}}_{\mathbf{q},\nu,\nu'}(\mathcal{E}) = \frac{i\mathcal{E}}{\hbar}\mathcal{G}^{r/a}_{\mathbf{q},\nu,\nu}(\mathcal{E}), \qquad \text{(E.9)}$$

and the slightly more involved

$$\begin{aligned}\mathcal{G}^{r,\widehat{P}\widehat{P}}_{\mathbf{q},\nu,\nu'}(\mathcal{E}) &= \hbar^{-2}\int_{\mathbb{R}} d\mathcal{E}' \frac{(\mathcal{E}')^2 \mathcal{S}_{\mathbf{q}\nu\nu'}(\mathcal{E}')}{\mathcal{E}+i0^+-\mathcal{E}'} \\ &= \frac{\mathcal{E}^2}{\hbar^2}\int_{\mathbb{R}} d\mathcal{E}' \frac{\mathcal{S}_{\mathbf{q}\nu\nu'}(\mathcal{E}')}{\mathcal{E}+i0^+-\mathcal{E}'} - \hbar^{-2}\int_{\mathbb{R}} d\mathcal{E}'(\mathcal{E}+\mathcal{E}')\mathcal{S}_{\mathbf{q}\nu\nu'}(\mathcal{E}') \\ &= \frac{\mathcal{E}^2}{\hbar^2}\mathcal{G}^{r}_{\mathbf{q},\nu,\nu'}(\mathcal{E}) - 2\omega_{\mathbf{q},\nu}\delta_{\nu,\nu'}. \end{aligned} \tag{E.10}$$

It was used again, that $\mathcal{S}$ is odd. Additionally, the first spectral moment has been used

$$2\hbar\omega_{\mathbf{q},\nu}\delta_{\nu,\nu'} = \frac{1}{\hbar}\int_{\mathbb{R}} d\mathcal{E}\mathcal{E}\mathcal{S}_{\mathbf{q},\nu,\nu'}(\mathcal{E}). \tag{E.11}$$

This can be calculated easily using Eq. (2.17) and

$$\left[\widehat{U}_{\mathbf{q}\nu}, \widehat{H}\right] = \left[\widehat{U}_{\mathbf{q}\nu}, \widehat{H}_0\right] = i\hbar\widehat{P}_{\mathbf{q}\nu} \text{ and} \tag{E.12}$$

$$\left[\widehat{U}_{\mathbf{q}\nu}, \widehat{P}_{\mathbf{q}'\nu'}\right] = 2i\omega_{\mathbf{q},\nu}\delta_{\mathbf{q},-\mathbf{q}'}\delta_{\nu\nu'}. \tag{E.13}$$

The first phonon spectral moment is calculated routinely in my implementation to test the results.

Two properties of $\mathcal{S}_{\mathbf{q},\nu,\nu'}(\mathcal{E})$ are the behavior under reflection of $\mathcal{E}$ and $\mathbf{q}$:

$$\begin{aligned}\mathcal{S}_{\mathbf{q},\nu,\nu'}(-\mathcal{E}) &= \frac{\hbar}{\mathrm{Tr}(\widehat{\rho})}\sum_{\alpha,\beta}\langle\alpha|\widehat{U}_{\mathbf{q},\nu}|\beta\rangle\langle\beta|\widehat{U}_{-\mathbf{q},\nu'}|\alpha\rangle \exp(-\beta E_\alpha)\times \\ &\qquad \times\left[1-\exp(\beta\mathcal{E})\right]\delta(-\mathcal{E}-(E_\beta-E_\alpha)) \\ &= \frac{\hbar}{\mathrm{Tr}(\widehat{\rho})}\sum_{\alpha,\beta}\langle\alpha|\widehat{U}_{\mathbf{q},\nu}|\beta\rangle\langle\beta|\widehat{U}_{-\mathbf{q},\nu'}|\alpha\rangle \exp(-\beta E_\alpha)\times \\ &\times\exp(\beta(E_\alpha-E_\beta))\left[\exp(-\beta\mathcal{E})-1\right]\delta(\mathcal{E}-(E_\alpha-E_\beta)) \\ &= \frac{\hbar}{\mathrm{Tr}(\widehat{\rho})}\sum_{\alpha,\beta}\langle\alpha|\widehat{U}_{\mathbf{q},\nu}|\beta\rangle\langle\beta|\widehat{U}_{-\mathbf{q},\nu'}|\alpha\rangle \exp(-\beta E_\beta)\times \\ &\qquad \times\left[\exp(-\beta\mathcal{E})-1\right]\delta(\mathcal{E}-(E_\alpha-E_\beta)) \\ &= \frac{\hbar}{\mathrm{Tr}(\widehat{\rho})}\sum_{\beta,\alpha}\langle\alpha|\widehat{U}_{-\mathbf{q},\nu'}|\beta\rangle\langle\beta|\widehat{U}_{\mathbf{q},\nu}|\alpha\rangle \exp(-\beta E_\alpha)\times \\ &\qquad \times\left[\exp(-\beta\mathcal{E})-1\right]\delta(\mathcal{E}-(E_\beta-E_\alpha)) \\ &= -\mathcal{S}_{-\mathbf{q},\nu',\nu}(\mathcal{E}), \end{aligned} \tag{E.14}$$

and under complex conjugation I have:

$$\begin{aligned}(\mathcal{S}_{\mathbf{q},\nu,\nu'}(\mathcal{E}))^* &= \frac{\hbar}{\mathrm{Tr}(\widehat{\rho})}\sum_{\alpha,\beta}(\langle\alpha|\widehat{U}_{\mathbf{q},\nu}|\beta\rangle\langle\beta|\widehat{U}_{-\mathbf{q},\nu'}|\alpha\rangle)^* \exp(-\beta E_\alpha)\times \\ &\qquad [1-\exp(-\beta\mathcal{E})]\,\delta(\mathcal{E}-(E_\beta-E_\alpha)) \\ &= \frac{\hbar}{\mathrm{Tr}(\widehat{\rho})}\sum_{\alpha,\beta}\langle\alpha|\widehat{U}_{\mathbf{q},\nu'}|\beta\rangle\langle\beta|\widehat{U}_{-\mathbf{q},\nu}|\alpha\rangle \exp(-\beta E_\alpha)\times \\ &\qquad [1-\exp(-\beta\mathcal{E})]\,\delta(\mathcal{E}-(E_\beta-E_\alpha)) \\ &= \mathcal{S}_{\mathbf{q},\nu',\nu}(\mathcal{E}). \end{aligned} \tag{E.15}$$

These properties mean for the averaged propagator (that is the average between retarded and advanced propagator)

$$\begin{aligned}(\mathcal{G}_{\mathbf{q},\nu,\nu'}(\mathcal{E}))^* &= \mathcal{G}_{\mathbf{q},\nu',\nu}(\mathcal{E}), \\ \mathcal{G}_{\mathbf{q},\nu,\nu'}(\mathcal{E}) &= \mathcal{G}_{-\mathbf{q},\nu',\nu}(-\mathcal{E}). \end{aligned} \tag{E.16}$$

Maradudin (170) has proven another powerful property of the phonon propagator:

$$\begin{aligned}\mathcal{G}^M_{\mathbf{q},\nu,\nu'}(\tau) &= \langle T_\tau \widehat{U}_{\mathbf{q},\nu}(\tau)\widehat{U}^\dagger_{\mathbf{q},\nu'}(0)\rangle \\ &= \langle T_\tau \widehat{U}_{\mathbf{q},\nu}(0)(\widehat{U}_{\mathbf{q},\nu'}(\tau))^\dagger\rangle \\ &= \langle T_\tau \widehat{U}_{-\mathbf{q},\nu'}(\tau)\widehat{U}^\dagger_{-\mathbf{q},\nu}(0)\rangle = \mathcal{G}^M_{-\mathbf{q},\nu',\nu}(\tau). \end{aligned} \tag{E.17}$$

This property implies for the Matsubara function

$$\mathcal{G}^M_{\mathbf{q},\nu,\nu'}(E) = \mathcal{G}^M_{-\mathbf{q},\nu',\nu}(E). \tag{E.18}$$

By analytic continuation to the advanced and retarded Greens function, and subtraction of both one finds for the spectral density

$$\mathcal{S}_{\mathbf{q},\nu,\nu'}(\mathcal{E}) = \mathcal{S}_{-\mathbf{q},\nu',\nu}(\mathcal{E}) = -\mathcal{S}_{\mathbf{q},\nu,\nu'}(-\mathcal{E}), \tag{E.19}$$

and, as a result, all even moments of the distribution vanish. On top of this, one has for the averaged propagator

$$\mathcal{G}_{\mathbf{q},\nu,\nu'}(\mathcal{E}) = \mathcal{G}_{\mathbf{q},\nu,\nu'}(-\mathcal{E}). \tag{E.20}$$

Reference (170) has shown, that the phonon propagator in the mode basis, transforms like a scalar under space-group operations of the crystal:

$$\mathcal{G}_{S\mathbf{q},\nu,\nu'}(\mathcal{E}) = \mathcal{G}_{\mathbf{q},\nu,\nu'}(\mathcal{E}), \tag{E.21}$$

for any space-group rotation S. Recall the transformation law of the phonon polarization vectors (171)

$$\mathbf{e}_\nu(S\mathbf{q}) = \Gamma_S(\mathbf{q})\mathbf{e}_\nu(\mathbf{q}), \tag{E.22}$$

where **e** is the vector version of the phonon polarization e and the matrix Γ_S is defined in Ref. (171)

$$\Gamma_S^{\kappa\alpha\kappa'\alpha'}(\mathbf{q}) = S_{\alpha\alpha'}\delta_{\kappa',\mathcal{O}(\kappa)}, \tag{E.23}$$

where $\mathcal{O}(\kappa)$ is the index of the nucleus κ after the space-group transformation $\mathcal{O}$ (including a potential translation). Then, I find, that the phonon propagator in the displacement basis transforms just like the dynamical matrix, as

$$\mathcal{G}_{S\mathbf{q}}(\mathcal{E}) = \Gamma_S(\mathbf{q})\mathcal{G}_{\mathbf{q}}(\mathcal{E})\Gamma_S^\dagger(\mathbf{q}). \tag{E.24}$$

E.3 PROPERTIES OF THE SELF-ENERGY

As discussed above, the interacting propagator in matrix form is, in my work, obtained by using Dyson's Eq. (2.51), as

$$\left[\mathcal{G}_{\mathbf{q}}(\mathcal{E})\right]^{-1} = \left[\mathcal{G}_{\mathbf{q}}^{(0)}(\mathcal{E})\right]^{-1} - \Sigma_{\mathbf{q}}(\mathcal{E}). \tag{E.25}$$

The task is to prove the properties of the self-energy Σ in the displacement basis from the properties of the phonon propagator $\mathcal{G}$. This is useful, because in displacement basis the self-energy can be interpolated (because of the absence of the impact of degeneracy in the definition of Σ's elements).

The two representations are related

$$\Sigma_{\mathbf{q}\kappa\kappa'}^{\alpha\alpha'}(\mathcal{E}) = \frac{2}{\hbar}\sum_{\nu\nu'} e_{\kappa\nu}^{\alpha}(\mathbf{q})e_{\kappa'\nu'}^{\alpha'}(-\mathbf{q})(\omega_{\mathbf{q}\nu}\omega_{\mathbf{q}\nu'})^{1/2}\Sigma_{\mathbf{q}\nu\nu'}(\mathcal{E}), \tag{E.26}$$

which follows directly from Dyson's equation. In what follows, the self-energy is assumed to be in displacement basis, if not stated differently.

By the transformation law of the phonon propagator

$$\begin{aligned}
\mathcal{G}_{S\mathbf{q}}(\mathcal{E}) &= \left[\left[\mathcal{G}_{S\mathbf{q}}^{(0)}(\mathcal{E})\right]^{-1} - \Sigma_{S\mathbf{q}}(\mathcal{E})\right]^{-1} \\
&= \Gamma_S(\mathbf{q})\mathcal{G}_{\mathbf{q}}(\mathcal{E})\Gamma_S^\dagger(\mathbf{q}) \\
&= \Gamma_S(\mathbf{q})\left[\left[\mathcal{G}_{\mathbf{q}}^{(0)}(\mathcal{E})\right]^{-1} - \Sigma_{\mathbf{q}}(\mathcal{E})\right]^{-1}\Gamma_S^\dagger(\mathbf{q}) \\
&= \left[\Gamma_S(\mathbf{q})\left[\mathcal{G}_{\mathbf{q}}^{(0)}(\mathcal{E})\right]^{-1}\Gamma_S^\dagger(\mathbf{q}) - \Gamma_S(\mathbf{q})\Sigma_{\mathbf{q}}(\mathcal{E})\Gamma_S^\dagger(\mathbf{q})\right]^{-1} \\
&= \left[\left[\mathcal{G}_{S\mathbf{q}}^{(0)}(\mathcal{E})\right]^{-1} - \Gamma_S(\mathbf{q})\Sigma_{\mathbf{q}}(\mathcal{E})\Gamma_S^\dagger(\mathbf{q})\right]^{-1},
\end{aligned} \tag{E.27}$$

and by comparing the first and the last line, one can see that the self-energy transforms like the dynamical matrix

$$\Sigma_{S\mathbf{q}}(\mathcal{E}) = \Gamma_S(\mathbf{q})\Sigma_{\mathbf{q}}(\mathcal{E})\Gamma_S^\dagger(\mathbf{q}). \tag{E.28}$$

Maradudin *et. al* (172) have studied how to compute the self-energy of a phonon - to understand neutron scattering. Their result for the one-loop self-energy can be applied also to higher-order calculations. The self-energy of a phonon $\Sigma_{\mathbf{q}}(\mathcal{E})$ can be separated in a term constant in $\mathcal{E}$ and a varying part:

$$\Sigma_{\mathbf{q}}(\mathcal{E}) = \Sigma^{c}_{\mathbf{q}} + \Sigma^{v}_{\mathbf{q}}(\mathcal{E}). \tag{E.29}$$

The second term is a function that is analytic in the upper half complex plane, and obeys

$$\lim_{|\mathcal{E}|\to\infty} |\mathcal{E}\Sigma^{v,\alpha,\alpha'}_{\mathbf{q},\kappa,\kappa'}(\mathcal{E})| \leq C, \tag{E.30}$$

where C is a constant. This can be shown order by order in perturbation theory, and is an important general constraint to the self-energy (2). For this reason, the variable part of $\Sigma_{\mathbf{q}}(\mathcal{E})$ obeys Kramers-Kronig relations, and the imaginary part and real part are Hilbert-transforms of each other.

This turns out to be a useful result, because of Maradudin *et. al*'s (172) work: In the calculation, the (analytically continued) energy $\mathcal{E}$ appears only in denominators. For this, one can write

$$\frac{1}{\mathcal{E} + i0^{+} - \alpha} = \mathcal{P}\frac{1}{\mathcal{E} - \alpha} - i\pi\delta(\mathcal{E} - \alpha). \tag{E.31}$$

The argument, α, is bounded, by a multiple of the maximum phonon frequency. Hence, the self-energy can be expanded by functions, that build a complete orthogonal system on $[-1, +1]$, such as Legendre polynomials. The other part can then be computed immediately, as the Hilbert-transform of the Legendre polynomial is a Legendre function of the second kind.

The self-energy then reads in matrix form

$$\Sigma^{v}_{\mathbf{q}}(\mathcal{E}) = \sum_{n} \mathbb{A}^{n}_{\mathbf{q}} \left(Q_n(\mathcal{E}/\mathcal{E}_{\max}) + iP_n(\mathcal{E}/\mathcal{E}_{\max}) \right). \tag{E.32}$$

What are the properties of the parameter matrices $\mathbb{A}^n$? Again from the spectral representation one finds

$$\mathcal{G}^{r}_{\mathbf{q}}(\mathcal{E}) = \mathcal{G}^{r}_{\mathbf{q}}(-\mathcal{E})^{\dagger}, \tag{E.33}$$

and therefore

$$\Sigma^{r}_{\mathbf{q}}(\mathcal{E}) = \Sigma^{r}_{\mathbf{q}}(-\mathcal{E})^{\dagger}. \tag{E.34}$$

This yields

$$\begin{aligned}\Sigma^v_{\mathbf{q}}(\mathcal{E}) &= \sum_n \mathbb{A}^n_{\mathbf{q}} \left(Q_n(\mathcal{E}/\mathcal{E}_{\max}) + iP_n(\mathcal{E}/\mathcal{E}_{\max})\right) \\ &= \Sigma^v_{\mathbf{q}}(-\mathcal{E})^\dagger \\ &= \sum_n (\mathbb{A}^n_{\mathbf{q}})^\dagger \left(Q_n(-\mathcal{E}/\mathcal{E}_{\max}) - iP_n(-\mathcal{E}/\mathcal{E}_{\max})\right) \\ &= \sum_n (\mathbb{A}^n_{\mathbf{q}})^\dagger \left((-1)^{n+1} Q_n(\mathcal{E}/\mathcal{E}_{\max}) - (-1)^n iP_n(\mathcal{E}/\mathcal{E}_{\max})\right).\end{aligned} \tag{E.35}$$

Then by comparing lines 1 and 4, one finds

$$\mathbb{A}^n_{\mathbf{q}} + (-1)^n (\mathbb{A}^n_{\mathbf{q}})^\dagger = 0, \tag{E.36}$$

which means, that for odd n the parameter matrix is Hermitian, and for even n it is anti-Hermitian. It turns out that in perturbation theory, all $\mathbb{A}^n_{\mathbf{q}}$ with even n vanish.

The symmetry transformation laws of the $\mathbb{A}^n_{\mathbf{q}}$ follow directly from those of the self-energy, such that all matrices $\mathbb{A}^n_{\mathbf{q}}$ transform under the space-group like the dynamical matrix, which is explained in detail in Ref. (171), and used in Sec. 5.2.

F

LIMITS OF PERTURBATION THEORY

The perturbation theory in this thesis is not a Taylor-expansion with a well-defined convergence radius, but instead an asymptotic series, which is proven by an argument by Dyson (67): assume I have the Hamiltonian of the harmonic crystal $\widehat{H}^0$. Now I add a term $\alpha \sum_{n=3}^{N_B} \widehat{V}^{(n)}$ to this Hamiltonian (up to some even number N_B), where α is some real parameter. The eigenstates of the system as a function of α can not be interpreted in the sense of a Taylor expansion in the parameter α, because, if the result would exist for any positive value of α then there would be a continuous transformation to the result for $-\alpha$. But the potential energy for large displacements is dominated by the highest term. That means, if the crystal is stable for $+\alpha$ it cannot be stable for $-\alpha$, and so the series cannot be interpreted as a Taylor series (as for $-\alpha$ the series cannot converge, no matter how small α is, see Fig. F.1).

Indeed the perturbation expansion constitutes an asymptotic series. These series do not possess these continuous transforms (by Stokes phenomenon (190)). The treatment of asymptotic series (that usually do not converge) is often encountered in engineering and physics and some observations have been made in practice (25):

- One (usually) cannot guarantee convergence of the series against the correct result.
- The best approximation to the correct result is obtained by truncating the series at the smallest term.
- The size of the error of the approximation is usually of the order of the smallest term.

It is possible to construct examples where these observations are invalid. But in practice, this behavior is especially encountered in quantum electrodynamics (269) and also for simple mathematical models like the Stieltjes integral.

Therefore, it is expected that, if the first term of a perturbation expansion is much larger than the second, the correct result of the approximated quantity is close to the first term with an uncertainty of the size of the second term.

While this cannot be guaranteed, it still motivates this work to obtain a second order correction to the thermal conductivity of crystals. The size of the second term of the expansion gives a hint on how good the first order approximation (the BTE) actually is.

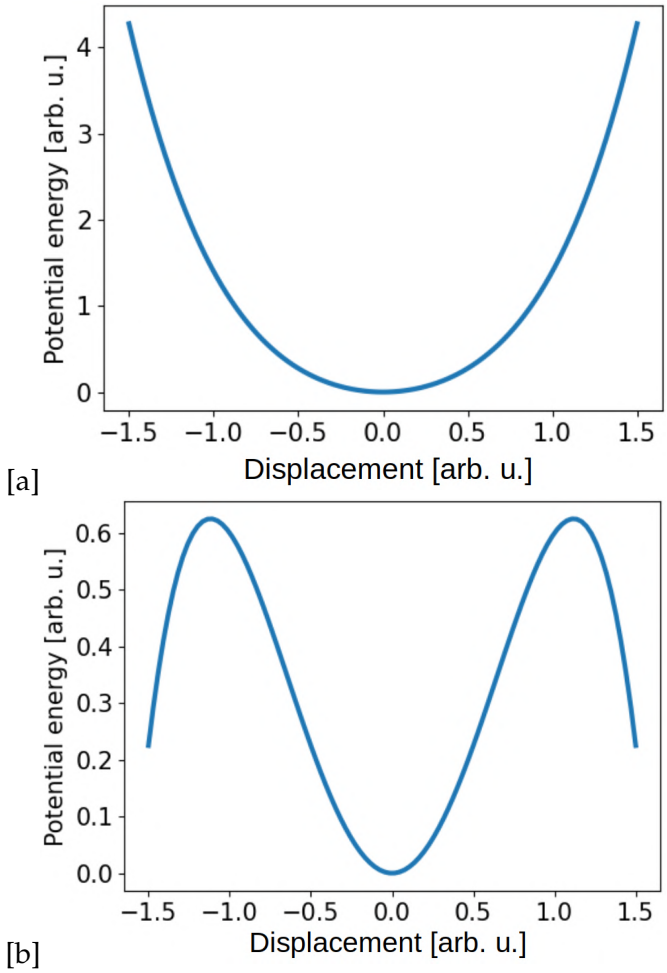

Figure F.1: Illustration of the potential energy as a function of the displacement of some nucleus, when the Taylor expansion of the BO surface is truncated at some term. This illustrates the argument by Dyson. In the case (a) of positive α the perturbation expansion has the chance to converge - but in case (b), for negative α the actual ground-state is not close to the equilibrium (as for large displacements lower energies can be achieved). This means, for arbitrarily small $-\alpha$ the series can never converge. Consequently, the expansion cannot be a Taylor expansion.

G

DERIVATION OF THE THERMAL CONDUCTIVITY

The aim of this section is to clarify what assumptions underlie the formalism presented in this thesis and how it relates to the classical limit of the thermal conductivity. For this I derive the definition of the thermal conductivity, following the path of Onsager (206) and Kubo (147). De Groot has clarified many arguments concerning the thermal conductivity (55, 57), and Luttinger (161) defended the formalism against questions of Prigogine (227) and Cohen (49). To the best of my knowledge, the formalism is generally accepted nowadays (4, 31).

I consider an adiabatically insulated and aged system. The important quantity to be studied is the rate of change of the entropy (55, 57). I use the assumption on the regression of fluctuations, sometimes called Onsagers assumption (206): The fluctuations of a thermodynamic quantity are governed by the same law, as the quantity itself. This is an assumption, as noted by Casimir (34). It is likely to hold true, if the transport equations are linear in the perturbations.

In equilibrium, the entropy of the system is extremal. For the classical case, this can be mathematically written as follows: assume one considers the deviations α_i of all thermodynamic observables of a system from their equilibrium value. If these deviations are small, one can assume that the entropy can be written as

$$S \approx S_0 + \frac{1}{2}\sum_{i,j}\frac{\partial S}{\partial\alpha_i\partial\alpha_j}\alpha_i\alpha_j =: S_0 + \frac{1}{2}\sum_{i,j}\beta_{i,j}\alpha_i\alpha_j. \tag{G.1}$$

Over time spans that are large compared to molecular collision times, but small compared to the relaxation time of a fluctuation, the rate of change of the fluctuations is linear in the fluctuations if these are sufficiently small (55):

$$\frac{\partial\alpha_i}{\partial t} = -\sum_j \lambda_{i,j}\alpha_j. \tag{G.2}$$

If one introduces thermodynamic forces

$$A_i = -k_B^{-1}\frac{\partial S}{\partial\alpha_i} = \sum_k \beta_{i,k}\alpha_k, \tag{G.3}$$

one finally obtains the relation between the forces A_i and the regression of the deviations α_i:

$$\frac{\partial\alpha_i}{\partial t} = \sum_j G_{i,j}A_j, \tag{G.4}$$

where **G** is the matrix of transport coefficients. This is the basis for further manipulation - one can, for example, multiply with α_l and average over configuration space to obtain **G** (147). To generalize this to the quantum case, the values α_i may be replaced by expectation values of operators:

$$\alpha_i(t) = \mathrm{Tr}\left(\widehat{\rho}(\vec{\alpha}|t)\widehat{\alpha}_i\right)/\mathrm{Tr}\widehat{\rho}. \tag{G.5}$$

Then, the quantized version of Eq. (G.4) would be

$$\alpha_i(t+\Delta t) - \alpha_i(t) = \mathrm{Tr}\left((\widehat{\rho}(\vec{\alpha}|t+\Delta t) - \widehat{\rho}(\vec{\alpha}|t))\widehat{\alpha}_i\right) = \sum_l G_{i,l}\frac{\partial S}{\partial \alpha_l}\Delta t. \tag{G.6}$$

The entropy of a system in quantum mechanics (von Neumann entropy) has the form (132)

$$S = -\frac{k_B}{\mathrm{Tr}\widehat{\rho}}\mathrm{Tr}\left(\widehat{\rho}\log\widehat{\rho}\right). \tag{G.7}$$

Kubo argued that, if the quantum version of the theory shall have a similar shape as the classical expression, where $\frac{\partial S}{\partial \alpha_l}$ is linear in the α's, then, the density matrix has to have the form (147)

$$\widehat{\rho}(\vec{\alpha}|t) = \exp\left(-\beta\widehat{H} - \beta\sum_j A_j\widehat{\alpha}_j\right), \tag{G.8}$$

with A_j being some coefficient. The task is now to derive a couple $(A_j, \widehat{\alpha}_j)$ that matches these conditions for thermal transport, and additionally agrees with the experimental observations. The operator $A_j\widehat{\alpha}_j = \widehat{H}'$ is called the effective perturbing Hamiltonian. To find such an operator, I follow Allen and Feldman (4) and Mori *et. al* (56, 187). (Luttinger derived the formula also, but using a gravitational field ansatz (161).) Their ansatz is to write the density matrix as

$$\begin{aligned}\widehat{\rho} &= \exp\left(-\int_\Omega \beta(\mathbf{x})\widehat{\mathcal{H}}(\mathbf{x})d\mathbf{x}\right)\\ &= \exp(-\beta(\widehat{H}+\widehat{H}'))\\ \rightarrow \widehat{H}' &= -k_B\beta\int_\Omega \delta T(\mathbf{x})\widehat{\mathcal{H}}(\mathbf{x})d\mathbf{x},\end{aligned} \tag{G.9}$$

where $\beta = (k_B T)^{-1}$, Ω is the crystal volume. $\widehat{\mathcal{H}}(\mathbf{x})$ is the Hamiltonian density, whose volume integral is the system Hamiltonian $\widehat{H}$. $\widehat{H}$ will not be specified in the argumentation. Ref. (4) then considers the local

conservation of energy, by introducing a local heat-flux operator $\widehat{\mathbf{j}}(\mathbf{x},t)$, that fulfills

$$\frac{d}{dt}\widehat{\mathcal{H}}(\mathbf{x},t)+\nabla\cdot\widehat{\mathbf{j}}(\mathbf{x},t)=0$$
$$\Leftrightarrow\ \widehat{\mathcal{H}}(\mathbf{x},t)=-\int_{-\infty}^{t}\nabla\cdot\widehat{\mathbf{j}}(\mathbf{x},t')dt'. \tag{G.10}$$

For convenience, I write $\widehat{\mathcal{H}}(\mathbf{x},0)=\widehat{\mathcal{H}}(\mathbf{x})$. Inserting Eq. (G.10) into Eq. (G.9) one obtains

$$\begin{aligned}\widehat{H}' &= -k_B\beta\int_\Omega \delta T(\mathbf{x})\widehat{\mathcal{H}}(\mathbf{x})d\mathbf{x}\\ &= k_B\beta\int_\Omega\int_{-\infty}^{0}\delta T(\mathbf{x})\nabla\cdot\widehat{\mathbf{j}}(\mathbf{x},t)dtd\mathbf{x}\\ &= -k_B\beta\int_\Omega\int_{-\infty}^{0}\nabla T(\mathbf{x})\cdot\widehat{\mathbf{j}}(\mathbf{x},t)dtd\mathbf{x}\\ &= -k_B\beta\nabla T\int_\Omega\int_{-\infty}^{0}\widehat{\mathbf{j}}(\mathbf{x},t)dtd\mathbf{x}.\end{aligned} \tag{G.11}$$

Let us assume that the interaction and kinetic energy in the system is associated to the nuclei. In this case, the volume integral of the local heat-flux was found by Hardy (102) and is

$$\begin{aligned}\widehat{\mathbf{J}} &= \frac{1}{\Omega}\int_\Omega\widehat{\mathbf{j}}(\mathbf{x})d\mathbf{x}\\ &= \frac{1}{2\Omega}\left\{\sum_i\frac{\widehat{\mathbf{p}}_i}{M_i}\left(\frac{\widehat{\mathbf{p}}_i^2}{2M_i}+\widehat{V}_i\right)+\sum_{i,j}(\widehat{\mathbf{r}}_i-\widehat{\mathbf{r}}_j)\frac{1}{i\hbar}\left[\frac{\widehat{\mathbf{p}}_i^2}{2M_i},\widehat{V}_j\right]\right\}+\text{h.c.}\end{aligned} \tag{G.12}$$

Here, $\widehat{\mathbf{r}}_i$ and $\widehat{\mathbf{p}}_i$ are the position and momentum operator of nucleus i, M_i is its mass, and $\widehat{V}_i$ the potential energy associated to the nucleus. The potential energy can be distributed arbitrarily between the nuclei, so that the heat-flux operator *is not unique*. The origin of this peculiarity is, that the Hamiltonian density $\widehat{\mathcal{H}}(\mathbf{x})$ is not unique in an interacting system, as the interaction potential depends on more than one particle coordinate. It will be shown in Sec. 3.1, that the thermal conductivity does not change, if the potential energy is distributed in a different way. In fact, no observable should be dependent on such a reshuffling: The Hamiltonian density may be changed in a microscopic volume, but on any mesoscopic volume, the energy of the crystal has to stay the same, as it is measurable.

A concise way to write the flux operator $\widehat{\mathbf{J}}$ is in terms of an operator $\widehat{\mathbf{P}}$, which I call the „energetic polarization", as

$$\widehat{\mathbf{J}}=\frac{1}{i\hbar\Omega}\left[\widehat{\mathbf{P}},\widehat{H}\right]\leftrightarrow\widehat{\mathbf{J}}(t)=\frac{1}{\Omega}\frac{d}{dt}\widehat{\mathbf{P}}(t)$$
$$\text{if}\ \ \widehat{\mathbf{P}}=\frac{1}{2}\sum_k\left(\frac{\widehat{\mathbf{p}}_k^2}{2M_k}+\widehat{V}_k\right)\widehat{\mathbf{r}}_k+\text{h.c.} \tag{G.13}$$

$\widehat{\mathbf{P}}$ may be interpreted as an energetic polarization, similar to an electrical one (137, 235, 236). With this operator $\widehat{\mathbf{P}}$, inserted in Eq. (G.11) I find the perturbing Hamiltonian to the system is

$$\widehat{H}' = -k_B\beta\nabla T \cdot \widehat{\mathbf{P}}. \tag{G.14}$$

I have set $\widehat{\mathbf{P}}(-\infty) = \mathbf{0}$, for convenience. This is possible, because one is only interested in the difference between two operators $\widehat{\mathbf{P}}(t)$ and $\widehat{\mathbf{P}}(t')$, see below. Here, the perturbing Hamiltonian has the form $A_j\widehat{\alpha}_j$ with $A_j = -k_B\beta\nabla T$ and $\widehat{\alpha}_j = \widehat{\mathbf{P}}$, as formulated by Kubo above. This is an important result, because now I can use the mathematical machinery of linear response to obtain the thermal conductivity κ^{ij} as a response of the system to the perturbing Hamiltonian $\widehat{H}'$.

To clarify, that I actually derive the thermal conductivity that an experimentalist means, consider: According to Onsagers assumption, one finds the heat flux $\langle\widehat{\mathbf{J}}\rangle$ proportional to the derivative of the entropy S:

$$\begin{aligned} S &= -\frac{k_B}{\mathrm{Tr}\widehat{\rho}}\mathrm{Tr}(\widehat{\rho}\log(\widehat{\rho})) \\ &= k_B\beta\langle\widehat{H}\rangle - k_B^2\beta^2\nabla T\cdot\langle\widehat{\mathbf{P}}\rangle \\ \Rightarrow \frac{\partial S}{\partial\langle\widehat{\mathbf{P}}\rangle} &= -k_B^2\beta^2\nabla T = k_B^2\nabla\beta. \end{aligned} \tag{G.15}$$

This can be cast in Onsagers assumption (147)

$$\begin{aligned} \langle\widehat{\mathbf{P}}\rangle(\Delta t) - \langle\widehat{\mathbf{P}}\rangle(0) &= \mathbf{G}\frac{\partial S}{\partial\langle\widehat{\mathbf{P}}\rangle}\Delta t \\ \Rightarrow \langle\widehat{\mathbf{J}}\rangle &= -\frac{k_B^2\beta^2}{\Omega}\mathbf{G}\nabla T. \end{aligned} \tag{G.16}$$

Hence, the heat flux is proportional to the thermal force, which is $\mathbf{F}_T = -k_B^2\beta^2\nabla T$. $\mathbf{G}$ is positive definite here, as the change in entropy from Eq. (G.15) is positive

$$\frac{dS}{dt} = \Omega\langle\widehat{\mathbf{J}}\rangle\cdot\mathbf{F}_T = k_B^4\beta^4\nabla T\mathbf{G}\nabla T \geq 0. \tag{G.17}$$

The proportionality constant $\frac{k_B^2\beta^2}{\Omega}\mathbf{G}$ between heat-flux $\langle\widehat{\mathbf{J}}\rangle$ and temperature gradient ∇T is defined as thermal conductivity κ^{ij}.

G.1 LINEAR RESPONSE FORMULA

The thermal conductivity κ^{ij} can be obtained from the standard formalism for linear response, using the perturbation Hamiltonian $\widehat{H}'$ from Eq. (G.14). In analogy to Nolting's derivation of the electrical conductivity (204, pg. 121), the system is perturbed by a force $\mathbf{f}(t) = k_B\beta\nabla T$, which couples to an operator $\widehat{\mathbf{P}}$, such that $\widehat{H}' = -\mathbf{f}(t)\cdot\widehat{\mathbf{P}}$. The heat-

flux operator is related to the coupling operator by Eq. (G.13). Then, after the perturbation is turned on, the heat-flux is (assuming a linear response)

$$\langle \widehat{J}^i(t) \rangle = -\frac{1}{\hbar} \sum_j \int_{\mathbb{R}} dt' f_j(t') G^{r,ij}_{\widehat{\mathbf{J}},\widehat{\mathbf{P}}}(t,t'), \tag{G.18}$$

where the average $\langle \widehat{\mathbf{J}} \rangle$ is computed in first order of the perturbation and $G^{r,ij}_{\widehat{\mathbf{J}},\widehat{\mathbf{P}}}(t,t')$ is the retarded Greens function defined by

$$G^{r,ij}_{\widehat{\mathbf{J}},\widehat{\mathbf{P}}}(t-t') = -i\theta(t-t') \langle \left[\widehat{J}^i(t), \widehat{P}^j(t') \right] \rangle. \tag{G.19}$$

The thermal conductivity is defined by

$$\kappa^{ij}(\mathcal{E}) = -\frac{1}{\hbar T} G^{r,ij}_{\widehat{\mathbf{J}},\widehat{\mathbf{P}}}(\mathcal{E}). \tag{G.20}$$

It can be shown (204), that this Fourier transformed Greens function can be written as a flux-flux correlation function plus a fully imaginary term

$$G^{r,ij}_{\widehat{\mathbf{J}},\widehat{\mathbf{P}}}(\mathcal{E}) = -i\hbar\Omega \frac{G^{r,ij}_{\widehat{\mathbf{J}},\widehat{\mathbf{J}}}(\mathcal{E})}{\mathcal{E}+i0} - \frac{\langle \left[\widehat{J}^i, \widehat{P}^j \right] \rangle}{\mathcal{E}+i0}. \tag{G.21}$$

The flux-flux correlation function $\Omega G^{r,ij}_{\widehat{\mathbf{J}},\widehat{\mathbf{J}}}(\mathcal{E})$ will from now on be called $\Pi^{ij}_r(\mathcal{E})$. As I am interested in the real part of the DC conductivity, it follows (166, pg. 212)

$$\kappa^{ij} = -\frac{1}{T} \lim_{\mathcal{E}\to 0} \frac{1}{\mathcal{E}} \mathrm{Im}(\Pi^{ij}_r(\mathcal{E})). \tag{G.22}$$

To evaluate the retarded Greens function $\Pi^{ij}_r(\mathcal{E})$, I will compute its twin, the Matsubara function $\Pi^{ij}_M(E)$, see Secs. 3, 4 and 5, and analytically continue this function, see Sec. 2.2.2.

G.2 CLASSICAL LIMIT

In this section I will show the equivalence between Eq. (G.22) and the result of Refs. (4, 147). Then, I will show, that the classical limit of Eq. (G.22) is indeed the GK equation.

THE EQUIVALENCE of Eq. (G.22) with the result from Refs. (4, 147) is best shown by writing both results in terms of eigenfunctions. I start with the formula from Refs.(4, 147):

$$\begin{aligned}\kappa^{ij} &= \frac{\Omega}{T}\int_0^\beta d\lambda \int_0^\infty dt \langle \exp(\lambda \widehat{H})\widehat{J}^i \exp(-\lambda \widehat{H})\widehat{J}^j(t)\rangle \\ &= \frac{\Omega}{T\mathrm{Tr}\widehat{\rho}}\int_0^\beta d\lambda \int_0^\infty dt \sum_{\gamma,\xi}\widehat{J}^i_{\gamma\xi}\widehat{J}^j_{\xi\gamma}\exp(-\beta E_\gamma)\exp(\lambda(E_\gamma - E_\xi))\times \\ &\qquad \times \exp(i(E_\gamma - E_\xi)t - 0^+ t) \\ &= \frac{\Omega}{T\mathrm{Tr}\widehat{\rho}}\int_0^\beta d\lambda \sum_{\gamma,\xi}\widehat{J}^i_{\gamma\xi}\widehat{J}^j_{\xi\gamma}\exp(-\beta E_\gamma)\exp(\lambda(E_\gamma - E_\xi))\times \\ &\qquad \times \frac{1}{i(E_\gamma - E_\xi) - 0^+}. \end{aligned} \tag{G.23}$$

I only ask for the real part of this

$$\begin{aligned}\kappa^{ij} &= \frac{\pi\Omega}{T\mathrm{Tr}\widehat{\rho}}\int_0^\beta d\lambda \sum_{\gamma,\xi}\mathrm{Re}(\widehat{J}^i_{\gamma\xi}\widehat{J}^j_{\xi\gamma})\exp(-\beta E_\gamma)\exp(\lambda(E_\gamma - E_\xi))\times \\ &\qquad \times \delta(E_\gamma - E_\xi) \\ &= \frac{\pi\Omega\beta}{T\mathrm{Tr}\widehat{\rho}}\sum_{\gamma,\xi}\mathrm{Re}(\widehat{J}^i_{\gamma\xi}\widehat{J}^j_{\xi\gamma})\exp(-\beta E_\gamma)\delta(E_\gamma - E_\xi). \end{aligned} \tag{G.24}$$

The step from Eq. (G.23) to (G.24) is indeed accurate, as the term from the imaginary part of $\widehat{J}^i_{\gamma\xi}\widehat{J}^j_{\xi\gamma}$ cancels precisely against the term with interchanged indices. Now compare to Eq. (G.22). The time-correlation function reads

$$\begin{aligned}\Pi_r^{ij}(t-t') &= -i\Omega\theta(t-t')\langle\left[\widehat{J}^i(t),\widehat{J}^j(t')\right]\rangle \\ &= -i\Omega\theta(t-t')\langle\left[\widehat{J}^i(t-t'),\widehat{J}^j(0)\right]\rangle \\ &= \frac{-i\Omega\theta(t-t')}{\mathrm{Tr}\widehat{\rho}}\sum_{\gamma,\xi}\exp(-\beta E_\gamma) \\ &\times \{\exp(i(E_\gamma - E_\xi)(t-t'))\widehat{J}^i_{\gamma\xi}\widehat{J}^j_{\xi\gamma} \\ &\quad - \exp(i(E_\xi - E_\gamma)(t-t'))\widehat{J}^j_{\gamma\xi}\widehat{J}^i_{\xi\gamma}\}. \end{aligned} \tag{G.25}$$

Now I switch indices in the second line to obtain

$$\begin{aligned}\Pi_r^{ij}(t-t') &= \frac{-i\Omega\theta(t-t')}{\mathrm{Tr}\widehat{\rho}}\sum_{\gamma,\xi}\left(\exp(-\beta E_\gamma) - \exp(-\beta E_\xi)\right)\times \\ &\quad \times \exp(i(E_\gamma - E_\xi)(t-t'))\widehat{J}^i_{\gamma\xi}\widehat{J}^j_{\xi\gamma}. \end{aligned} \tag{G.26}$$

Then, the Fourier transform is

$$\Pi_r^{ij}(\mathcal{E}) = -\frac{\Omega}{\mathrm{Tr}\widehat{\rho}} \sum_{\gamma,\xi} \left(\exp(-\beta E_\gamma) - \exp(-\beta E_\xi)\right) \frac{\widehat{J}^i_{\gamma\xi}\widehat{J}^j_{\xi\gamma}}{\mathcal{E} + (E_\gamma - E_\xi) + i0^+}. \tag{G.27}$$

The imaginary part of this function is (the term $\mathrm{Im}(\widehat{J}^i_{\gamma\xi}\widehat{J}^j_{\xi\gamma})$ cancels against its index-interchanged twin)

$$\begin{aligned}\mathrm{Im}(\Pi_r^{ij}(\mathcal{E})) &= -\frac{\pi\Omega}{\mathrm{Tr}\widehat{\rho}} \sum_{\gamma,\xi} \left(\exp(-\beta E_\gamma) - \exp(-\beta E_\xi)\right) \times \\ &\quad \times \delta(\mathcal{E} + (E_\gamma - E_\xi))\mathrm{Re}(\widehat{J}^i_{\gamma\xi}\widehat{J}^j_{\xi\gamma}) \\ &= -\frac{\pi\Omega}{\mathrm{Tr}\widehat{\rho}}(1 - \exp(-\beta\mathcal{E})) \sum_{\gamma,\xi} \exp(-\beta E_\gamma) \\ &\quad \times \delta(\mathcal{E} + (E_\gamma - E_\xi))\mathrm{Re}(\widehat{J}^i_{\gamma\xi}\widehat{J}^j_{\xi\gamma}).\end{aligned} \tag{G.28}$$

Then, use that $\lim_{\mathcal{E}\to 0}(1 - \exp(-\beta\mathcal{E}))/\mathcal{E} = \beta$, to obtain for κ^{ij}

$$\kappa^{ij} = \frac{\pi\Omega\beta}{T\mathrm{Tr}\widehat{\rho}} \sum_{\gamma,\xi} \mathrm{Re}(\widehat{J}^i_{\gamma\xi}\widehat{J}^j_{\xi\gamma}) \exp(-\beta E_\gamma)\delta(E_\gamma - E_\xi). \tag{G.29}$$

which is identical to Eq. (G.24).

THE CLASSICAL LIMIT of this formalism indeed gives the GK formula. This is now trivial: Start at Eq. (G.23)

$$\kappa^{ij} = \frac{\Omega}{T}\int_0^\beta d\lambda \int_0^\infty dt \langle \exp(\lambda\widehat{H})\widehat{J}^i \exp(-\lambda\widehat{H})\widehat{J}^j(t)\rangle, \tag{G.30}$$

and assume that β is small (which is true in the classical limit). Then $\exp(\pm\lambda\widehat{H}) \approx \mathbf{1}$:

$$\kappa^{ij} \approx \frac{\Omega}{k_B T^2}\int_0^\infty dt \langle \widehat{J}^i\widehat{J}^j(t)\rangle. \tag{G.31}$$

Now, one can just use the correspondence principle (202, pg. 120): the trace of the operators becomes a phase space integral, and the operators the corresponding phase-space functions:

$$\kappa^{ij} \approx \frac{\Omega}{k_B T^2}\int_0^\infty dt \langle J^i J^j(t)\rangle_c. \tag{G.32}$$

where $\langle ... \rangle_c$ is a phase-space average. Now, its just important to interpret the operator $\widehat{\mathbf{J}}$. Here, Eq. (G.13) gives insight:

$$\begin{aligned} \widehat{\mathbf{J}}(t) &= \frac{1}{\Omega}\frac{d}{dt}\widehat{\mathbf{P}}(t), \\ \text{with } \widehat{\mathbf{P}} &= \frac{1}{2}\sum_k \widehat{H}_k \widehat{\mathbf{r}}_k + \text{h.c.} \end{aligned} \tag{G.33}$$

Here, $\widehat{H}_k$ is the local Hamiltonian of lattice point k. The classical heat-flux is defined as (32)

$$\mathbf{J}(t) = \frac{d}{dt}\sum_k E_k \mathbf{r}_k, \tag{G.34}$$

where E_k is the local energy of lattice point k. Therefore, $\widehat{\mathbf{J}}$ is the manifest quantization of the classical heat-flux $\mathbf{J}$, and the GK formula (32, 93, 94) is the classical limit of the methodology, described in this thesis.

H

VERTEX FUNCTIONS

H.1 HEAT-FLUX VERTICES

The task of this section is to rephrase the heat-flux operator $\widehat{\mathbf{J}}$ in terms of the interaction vertex φ^n. This turns out to always be possible, such that the theoretical formulation used in this thesis is independent of the definitions of phonons, given a vibration or phonon propagator. This propagator, however, is of course calculated by perturbation theory, where the non-interacting phonon system is the starting point of the perturbation expansion. The heat-flux operator was first derived by Hardy, to be

$$\widehat{\mathbf{J}} = \frac{1}{2\Omega}\left\{\sum_i \frac{\widehat{\mathbf{p}}_i}{M_i}\left(\frac{\widehat{\mathbf{p}}_i^2}{2M_i} + \widehat{V}_i\right) + \sum_{i,j}(\widehat{\mathbf{r}}_i - \widehat{\mathbf{r}}_j)\frac{1}{i\hbar}\left[\frac{\widehat{\mathbf{p}}_i^2}{2M_i}, \widehat{V}_j\right]\right\} + \text{h.c.} \tag{H.1}$$

I want to Fourier-transform this operator. The indices of the nuclei i and j may be identified with $\{\kappa, p\}$, where κ is the index of the nucleus in the unit cell and p is the index of the unit cell itself. To start, I will derive the commutator $\left[\frac{\widehat{\mathbf{p}}_i^2}{2M_i}, \widehat{V}_j\right]$ (where $i \neq j$ is assumed, as the prefactor is zero otherwise). I define the local potential energy $\widehat{V}_j = \sum_{n=2}^{N_B} \widehat{V}_j^{(n)}$ as (N_B is the order at which the Taylor expansion of the BO surface is truncated)

$$\widehat{V}_{\kappa,p}^{(n)} = \frac{1}{n!}\sum_{\{\kappa,\alpha,p\}}^{*} \Phi_{\alpha_1,\ldots,\alpha_n}^{\kappa_1,p_1,\ldots,\kappa,p}\, \widehat{u}_{\kappa_1,p_1}^{\alpha_1} \times \ldots \times \widehat{u}_{\kappa,p}^{\alpha_n}. \tag{H.2}$$

The asterisk means, that the pair (κ,p) is not summed. Then, the commutator becomes

$$\left[\widehat{p}_{\kappa,p}^{\alpha}, \widehat{V}_{\kappa',p'}^{(n)}\right] = \frac{1}{n!}\sum_{\{\kappa,\alpha,p\}}^{**} \Phi_{\alpha_1,\ldots,\alpha_n}^{\kappa_1,p_1,\ldots,\kappa',p'}\, \widehat{u}_{\kappa',p'}^{\alpha_n}\left[\widehat{p}_{\kappa,p}^{\alpha}, \widehat{u}_{\kappa_1,p_1}^{\alpha_1}\ldots\widehat{u}_{\kappa_{n-1},p_{n-1}}^{\alpha_{n-1}}\right]. \tag{H.3}$$

Here, the $**$ denotes that no summation takes place over $\kappa, \alpha, p, \kappa', p'$. The commutator can be evaluated

$$\begin{aligned}\left[\widehat{p}_{\kappa,p}^{\alpha}, \widehat{u}_{\kappa_1,p_1}^{\alpha_1}\ldots\widehat{u}_{\kappa_{n-1},p_{n-1}}^{\alpha_{n-1}}\right] &= \sum_{i=1}^{n-1}\left[\widehat{p}_{\kappa,p}^{\alpha}, \widehat{u}_{\kappa_i,p_i}^{\alpha_i}\right]\prod_{l=1,l\neq i}^{n-1}\widehat{u}_{\kappa_l,p_l}^{\alpha_l} \\ &= -i\hbar\sum_{i=1}^{n-1}\delta_{\kappa,\kappa_i}\delta^{\alpha,\alpha_i}\delta_{p,p_i}\prod_{l=1,l\neq i}^{n-1}\widehat{u}_{\kappa_l,p_l}^{\alpha_l}. \end{aligned} \tag{H.4}$$

Reinserting this into Eq. (H.3) I find

$$\left[\widehat{p}^{\alpha}_{\kappa,p},\widehat{V}^{(n)}_{\kappa',p'}\right]=\frac{-i\hbar}{n!}\sum_{i=1}^{n-1}\sum_{\{\kappa,\alpha,p\}}^{**}\Phi^{\kappa_1,p_1,\ldots,\kappa_{i-1},p_{i-1},\kappa,p,\kappa_{i+1},p_{i+1},\ldots,\kappa_{n-1},p_{n-1},\kappa',p'}_{\alpha_1,\ldots,\alpha_{i-1},\alpha,\alpha_{i+1}\ldots\alpha_n}\times \\ \times\,\widehat{u}^{\alpha_n}_{\kappa',p'}\prod_{l=1,l\neq i}^{n-1}\widehat{u}^{\alpha_l}_{\kappa_l,p_l}. \tag{H.5}$$

IFCs are derivatives of the Born-Oppenheimer energy surface E_B. As a consequence, I can change the index i to be just $n-1$, as E_B is a smooth function.

$$\begin{aligned}\left[\widehat{p}^{\alpha}_{\kappa,p},\widehat{V}^{(n)}_{\kappa',p'}\right]&=\frac{-i\hbar}{n!}\sum_{i=1}^{n-1}\sum_{\{\kappa,\alpha,p\}}^{**}\Phi^{\kappa_1,p_1,\ldots\kappa_{n-2},p_{n-2},\kappa,p,\kappa',p'}_{\alpha_1,\ldots\alpha_{n-2},\alpha,\alpha_n}\widehat{u}^{\alpha_n}_{\kappa',p'}\prod_{l=1}^{n-2}\widehat{u}^{\alpha_l}_{\kappa_l,p_l}\\&=\frac{-i\hbar}{n((n-2)!)}\sum_{\{\kappa,\alpha,p\}}^{**}\Phi^{\kappa_1,p_1,\ldots\kappa_{n-2},p_{n-2},\kappa,p,\kappa',p'}_{\alpha_1,\ldots\alpha_{n-2},\alpha,\alpha_n}\widehat{u}^{\alpha_n}_{\kappa',p'}\prod_{l=1}^{n-2}\widehat{u}^{\alpha_l}_{\kappa_l,p_l}\end{aligned} \tag{H.6}$$

$$\frac{1}{i\hbar}\left[\frac{\widehat{\mathbf{p}}^2_{\kappa,p}}{2M_\kappa},\widehat{V}^{(n)}_{\kappa',p'}\right]=\sum_{\alpha}\frac{\widehat{p}^{\alpha}_{\kappa,p}}{2M_\kappa}\frac{1}{i\hbar}\left[\widehat{p}^{\alpha}_{\kappa,p},\widehat{V}^{(n)}_{\kappa',p'}\right]+\text{h.c.} \tag{H.7}$$

I want to calculate the contribution to the heat-flux operator $\widehat{\mathbf{J}}$ in terms of phonon operators $\widehat{P}^{\alpha}_{\mathbf{q},\kappa}$, such that the vertex function can be interpolated as a function of its momenta in the Brillouin zone. The prefactor of the commutator is $(\widehat{\mathbf{r}}_{\kappa,p}-\widehat{\mathbf{r}}_{\kappa',p'})=(\mathbf{x}_{\kappa,p}-\mathbf{x}_{\kappa',p'})+(\widehat{\mathbf{u}}_{\kappa,p}-\widehat{\mathbf{u}}_{\kappa',p'})$, where $\mathbf{x}$ denotes the equilibrium position of a nucleus. Then, the contributions to the heat-flux are

$$\widehat{\mathbf{J}}=\frac{1}{2\Omega}\left[\widehat{\mathbf{J}}^1+\widehat{\mathbf{J}}^2+\widehat{\mathbf{J}}^3+\widehat{\mathbf{J}}^4\right]+\text{h.c.}, \tag{H.8}$$

with

$$\begin{aligned}\widehat{J}^{i,1}_{n-1}&=\frac{1}{(n-1)!}\frac{n-1}{n}\sum_{\{\kappa,\alpha,p\}}\left(x^i_{\kappa_n p_n}-x^i_{\kappa_1 p_1}\right)\Phi^{\kappa_1,p_1,\ldots\kappa_n,p_n}_{\alpha_1,\ldots\alpha_n}\frac{\widehat{p}^{\alpha_1}_{\kappa_1,p_1}}{M_{\kappa_1}}\prod_{l=2}^{n}\widehat{u}^{\alpha_l}_{\kappa_l,p_l}\\&=\frac{N_p^{-n/2}}{(n-1)!}\frac{n-1}{n}\sum_{\{\kappa,\alpha,\mathbf{q}\}}\widehat{P}_{\kappa_1,\alpha_1,\mathbf{q}_1}\prod_{l=2}^{n}\widehat{U}_{\kappa_l,\alpha_l,\mathbf{q}_l}\prod_{l=1}^{n}M_{\kappa_l}^{-1/2}\times\\&\quad\times\sum_{\{p\}}\left(x^i_{\kappa_n p_n}-x^i_{\kappa_1 p_1}\right)\Phi^{\kappa_1,p_1,\ldots\kappa_n,p_n}_{\alpha_1,\ldots\alpha_n}\exp\left(i\sum_l\mathbf{q}_l\cdot(\mathbf{R}_{p_l}+\boldsymbol{\tau}_{\kappa_l})\right),\end{aligned} \tag{H.9}$$

where $\mathbf{R}_{p_l} + \boldsymbol{\tau}_{\kappa_l} = \mathbf{x}_{\kappa_l p_l}$, and because the quantity must be invariant under lattice translations, one can require that $\sum_l \mathbf{q}_l = 0$, (see Appendix H.3). This leads, by comparison, to

$$\widehat{J}^{i,1}_{n-1} = \frac{N_p^{-n/2}}{(n-1)!}(-i)\frac{n-1}{n}\sum_{\{\kappa,\alpha,\mathbf{q}\}} \widehat{P}_{\kappa_1,\alpha_1,\mathbf{q}_1}\prod_{l=2}^{n}\widehat{U}_{\kappa_l,\alpha_l,\mathbf{q}_l}\times \\ \times \frac{d}{dq^i_n}\varphi^n(\mathbf{q}_1,\kappa_1,\alpha_1;...;\mathbf{q}_n,\kappa_n,\alpha_n). \tag{H.10}$$

The second contribution, where the equilibrium positions $\mathbf{x}$ are replaced by the displacement operators $\widehat{\mathbf{u}}$, gives the contribution

$$\widehat{J}^{i,2}_{n} = \frac{1}{n!}(1-n)\sum_{\{\kappa,\alpha,p\}}\Phi^{\kappa_1,p_1,...\kappa_n,p_n}_{\alpha_1,...\alpha_n}\frac{\widehat{p}^{\alpha_n}_{\kappa_n,p_n}}{M_{\kappa_n}}\left(\widehat{u}^i_{\kappa_n,p_n} - \widehat{u}^i_{\kappa_{n-1},p_{n-1}}\right)\prod_{l=1}^{n-1}\widehat{u}^{\alpha_l}_{\kappa_l,p_l}. \tag{H.11}$$

For each term in the difference, I obtain a term. The first is

$$\psi_1 = \frac{1}{n!}(1-n)\sum_{\{\kappa,\alpha,p\}}\Phi^{\kappa_1,p_1,...\kappa_n,p_n}_{\alpha_1,...\alpha_n}\frac{\widehat{p}^{\alpha_n}_{\kappa_n,p_n}}{M_{\kappa_n}}\widehat{u}^i_{\kappa_n,p_n}\prod_{l=1}^{n-1}\widehat{u}^{\alpha_l}_{\kappa_l,p_l} \\ = \frac{N_p^{-(n+1)/2}}{n!}(1-n)\sum_{\{\kappa,\alpha,\mathbf{q}\}}\widehat{P}_{\kappa_n,\alpha_n,\mathbf{q}_n}\widehat{U}_{\kappa_n,i,\mathbf{q}_0}\prod_{l=1}^{n-1}\widehat{U}_{\kappa_l,\alpha_l,\mathbf{q}_l}M_{\kappa_n}^{-1/2}\prod_{l=1}^{n}M_{\kappa_l}^{-1/2} \\ \times\sum_{\{p\}}\Phi^{\kappa_1,p_1,...\kappa_n,p_n}_{\alpha_1,...\alpha_n}\exp(i(\mathbf{q}_0+\mathbf{q}_n)\cdot(\mathbf{R}_{p_n}+\boldsymbol{\tau}_{\kappa_n}))\exp(i\sum_{l=1}^{n-1}\mathbf{q}_l\cdot(\mathbf{R}_{p_l}+\boldsymbol{\tau}_{\kappa_l})) \\ = \frac{N_p^{-(n+1)/2}}{n!}(1-n)\sum_{\{\kappa,\alpha,\mathbf{q}\}}\widehat{P}_{\kappa_n,\alpha_n,\mathbf{q}_n}\widehat{U}_{\kappa_n,i,\mathbf{q}_0}\prod_{l=1}^{n-1}\widehat{U}_{\kappa_l,\alpha_l,\mathbf{q}_l}\times \\ \times M_{\kappa_n}^{-1/2}\varphi^n(\mathbf{q}_1,\kappa_1,\alpha_1;...;\mathbf{q}_0+\mathbf{q}_n,\kappa_n,\alpha_n), \tag{H.12}$$

and the other contribution is

$$\begin{aligned}
\psi_2 &= \frac{1}{n!}(n-1)\sum_{\{\kappa,\alpha,p\}}\Phi^{\kappa_1,p_1,\dots\kappa_n,p_n}_{\alpha_1,\dots\alpha_n}\frac{\widehat{p}^{\alpha_n}_{\kappa_n,p_n}}{M_{\kappa_n}}\widehat{u}^{i}_{\kappa_{n-1},p_{n-1}}\prod_{l=1}^{n-1}\widehat{u}^{\alpha_l}_{\kappa_l,p_l}\\
&= \frac{N_p^{-(n+1)/2}}{n!}(n-1)\sum_{\{\kappa,\alpha,\mathbf{q}\}}\widehat{P}_{\kappa_n,\alpha_n,\mathbf{q}_n}\widehat{U}_{\kappa_{n-1},i,\mathbf{q}_0}\prod_{l=1}^{n-1}\widehat{U}_{\kappa_l,\alpha_l,\mathbf{q}_l}M_{\kappa_{n-1}}^{-1/2}\\
&\quad\times\prod_{l=1}^{n}M_{\kappa_l}^{-1/2}\sum_{\{p\}}\Phi^{\kappa_1,p_1,\dots\kappa_n,p_n}_{\alpha_1,\dots\alpha_n}\exp(i(\mathbf{q}_0+\mathbf{q}_{n-1})\cdot(\mathbf{R}_{p_{n-1}}+\boldsymbol{\tau}_{\kappa_{n-1}}))\times\\
&\qquad\times\exp(i\sum_{l=1;l\neq n-1}^{n}\mathbf{q}_l\cdot(\mathbf{R}_{p_l}+\boldsymbol{\tau}_{\kappa_l}))\\
&= \frac{N_p^{-(n+1)/2}}{n!}(n-1)\sum_{\{\kappa,\alpha,\mathbf{q}\}}\widehat{P}_{\kappa_n,\alpha_n,\mathbf{q}_n}\widehat{U}_{\kappa_{n-1},i,\mathbf{q}_0}\prod_{l=1}^{n-1}\widehat{U}_{\kappa_l,\alpha_l,\mathbf{q}_l}\times\\
&\quad\times M_{\kappa_{n-1}}^{-1/2}\varphi^n(\mathbf{q}_1,\kappa_1,\alpha_1;\dots;\mathbf{q}_0+\mathbf{q}_{n-1},\kappa_{n-1},\alpha_{n-1};\mathbf{q}_n,\kappa_n,\alpha_n).
\end{aligned}\tag{H.13}$$

The final result is the sum of these contributions. The third term is found as

$$\begin{aligned}
\widehat{J}^{i,3} &= \sum_{\kappa,\alpha,p}\frac{\widehat{p}^{i}_{\kappa p}}{M_\kappa}\frac{\widehat{p}^{\alpha}_{\kappa p}}{2M_\kappa}\\
&= \frac{1}{2}N_p^{-3/2}\sum_{\kappa,\alpha,p,\{\mathbf{q}\}}M_\kappa^{-1/2}\widehat{P}_{\kappa i\mathbf{q}_1}\widehat{P}_{\kappa\alpha\mathbf{q}_2}\widehat{P}_{\kappa\alpha\mathbf{q}_3}\times\\
&\quad\times\exp(i(\mathbf{q}_1+\mathbf{q}_2+\mathbf{q}_3)\cdot(\mathbf{R}_p+\boldsymbol{\tau}_\kappa))\\
&= \frac{1}{2}N_p^{-1/2}\sum_{\kappa,\alpha,p,\{\mathbf{q}\}}M_\kappa^{-1/2}\widehat{P}_{\kappa i\mathbf{q}_1}\widehat{P}_{\kappa\alpha\mathbf{q}_2}\widehat{P}_{\kappa\alpha(-\mathbf{q}_1-\mathbf{q}_2)},
\end{aligned}\tag{H.14}$$

where the last step is possible, as the sum of momenta can be forced to vanish: $\mathbf{q}_1+\mathbf{q}_2+\mathbf{q}_3=0$. And the last term (for potential energy transport) is

$$\begin{aligned}
\widehat{J}^{i,4}_n &= \frac{1}{n!}\sum_{\{\kappa,\alpha,p\}}\Phi^{\kappa_1,p_1,\dots\kappa_n,p_n}_{\alpha_1,\dots\alpha_n}\frac{\widehat{p}^{i}_{\kappa_n,p_n}}{M_{\kappa_n}}\prod_{l=1}^{n}\widehat{u}^{\alpha_l}_{\kappa_l,p_l}\\
&= \frac{N_p^{-(n+1)/2}}{n!}\sum_{\{\kappa,\alpha,\mathbf{q}\}}\widehat{P}_{\kappa_n,i,\mathbf{q}_0}\left(\prod_{l=1}^{n}M_{\kappa_l}^{-1/2}\widehat{U}_{\kappa_l,\alpha_l,\mathbf{q}_l}\right)M_{\kappa_n}^{-1/2}\times\\
&\quad\times\sum_{\{p\}}\Phi^{\kappa_1,p_1,\dots\kappa_n,p_n}_{\alpha_1,\dots\alpha_n}\exp(i\sum_{l=1}^{n-1}\mathbf{q}_l\cdot(\mathbf{R}_{p_l}+\boldsymbol{\tau}_{\kappa_l}))\times\\
&\qquad\times\exp(i(\mathbf{q}_0+\mathbf{q}_n)\cdot(\mathbf{R}_{p_n}+\boldsymbol{\tau}_{\kappa_n}))\\
&= \frac{N_p^{-(n+1)/2}}{n!}\sum_{\{\kappa,\alpha,\mathbf{q}\}}\widehat{P}_{\kappa_n,i,\mathbf{q}_0}\prod_{l=1}^{n}\widehat{U}_{\kappa_l,\alpha_l,\mathbf{q}_l}M_{\kappa_n}^{-1/2}\times\\
&\qquad\times\varphi^n(\mathbf{q}_1,\kappa_1,\alpha_1;\dots;\mathbf{q}_0+\mathbf{q}_n,\kappa_n,\alpha_n).
\end{aligned}\tag{H.15}$$

H.1.1 *Phonon group velocities*

The task here is to show that

$$\widehat{J}_1^{i,1} = \frac{-i}{2} \sum_{\{\kappa,\alpha\},\mathbf{q}} \widehat{P}_{\kappa_1,\alpha_1,-\mathbf{q}} \widehat{U}_{\kappa_2,\alpha_2,\mathbf{q}} \frac{d}{dq^i} D_{\kappa_1,\alpha_1,\kappa_2,\alpha_2}(\mathbf{q}) \tag{H.16}$$

can be rephrased approximately in terms of phonon group velocities in the mode basis. This was done by Hardy (102), before.

$$\widehat{J}_1^{i,1} = \frac{-i\hbar}{4} \sum_{\{\kappa,\alpha,\nu\},\mathbf{q}} \widehat{P}_{-\mathbf{q}\nu_1} \widehat{U}_{\mathbf{q}\nu_2} (\omega_{\mathbf{q}\nu_1}\omega_{\mathbf{q}\nu_2})^{-1/2} e^{\alpha_1}_{\kappa_1\nu_1}(-\mathbf{q}) e^{\alpha_2}_{\kappa_2\nu_2}(\mathbf{q}) \times \\ \times \frac{d}{dq^i} D_{\kappa_1,\alpha_1,\kappa_2,\alpha_2}(\mathbf{q}). \tag{H.17}$$

Recall the eigenvalue equation of the dynamical matrix

$$\sum_{\kappa_2,\alpha_2} D_{\kappa_1,\alpha_1,\kappa_2,\alpha_2}(\mathbf{q}) e^{\alpha_2}_{\kappa_2,\nu}(\mathbf{q}) = \omega^2_{\mathbf{q},\nu} e^{\alpha_1}_{\kappa_1,\nu}(\mathbf{q}). \tag{H.18}$$

This can be rephrased, using Eq. (A.2), by multiplying with $\left(e^{\alpha_1}_{\kappa_1,\nu}(\mathbf{q})\right)^*$ and summing over κ_1, α_1:

$$\sum_{\kappa_1,\alpha_1,\kappa_2,\alpha_2} D_{\kappa_1,\alpha_1,\kappa_2,\alpha_2}(\mathbf{q}) e^{\alpha_2}_{\kappa_2,\nu}(\mathbf{q}) \left(e^{\alpha_1}_{\kappa_1,\nu}(\mathbf{q})\right)^* = \omega^2_{\mathbf{q},\nu}. \tag{H.19}$$

If one considers $\omega_{\mathbf{q},\nu}$ as a continuous function of $\mathbf{q}$, one finds

$$\begin{aligned} &\sum_{\kappa_1,\alpha_1,\kappa_2,\alpha_2} \partial_{\mathbf{q}} D_{\kappa_1,\alpha_1,\kappa_2,\alpha_2}(\mathbf{q}) e^{\alpha_2}_{\kappa_2,\nu}(\mathbf{q}) \left(e^{\alpha_1}_{\kappa_1,\nu}(\mathbf{q})\right)^* + \\ &\sum_{\kappa_1,\alpha_1,\kappa_2,\alpha_2} D_{\kappa_1,\alpha_1,\kappa_2,\alpha_2}(\mathbf{q}) \partial_{\mathbf{q}} e^{\alpha_2}_{\kappa_2,\nu}(\mathbf{q}) \left(e^{\alpha_1}_{\kappa_1,\nu}(\mathbf{q})\right)^* + \\ &\sum_{\kappa_1,\alpha_1,\kappa_2,\alpha_2} D_{\kappa_1,\alpha_1,\kappa_2,\alpha_2}(\mathbf{q}) e^{\alpha_2}_{\kappa_2,\nu}(\mathbf{q}) \partial_{\mathbf{q}} \left(e^{\alpha_1}_{\kappa_1,\nu}(\mathbf{q})\right)^* \\ &= 2\omega_{\mathbf{q},\nu} \partial_{\mathbf{q}} \omega_{\mathbf{q},\nu}. \end{aligned} \tag{H.20}$$

In line 2 and 3 of the above equation, one can multiply the dynamical matrix with the non-differentiated eigenvectors.

$$\begin{aligned} &\omega^2_{\mathbf{q},\nu} \sum_{\kappa_2,\alpha_2} \partial_{\mathbf{q}} e^{\alpha_2}_{\kappa_2,\nu}(\mathbf{q}) \left(e^{\alpha_2}_{\kappa_2,\nu}(\mathbf{q})\right)^* + \\ &\omega^2_{\mathbf{q},\nu} \sum_{\kappa_1,\alpha_1} e^{\alpha_1}_{\kappa_1,\nu}(\mathbf{q}) \partial_{\mathbf{q}} \left(e^{\alpha_1}_{\kappa_1,\nu}(\mathbf{q})\right)^* \\ &= \omega^2_{\mathbf{q},\nu} \partial_{\mathbf{q}} \sum_{\kappa,\alpha} e^{\alpha}_{\kappa,\nu}(\mathbf{q}) \left(e^{\alpha}_{\kappa,\nu}(\mathbf{q})\right)^* = \omega^2_{\mathbf{q},\nu} \partial_{\mathbf{q}} 1 = 0. \end{aligned} \tag{H.21}$$

This then leads to

$$\sum_{\{\kappa\alpha\}} e^{\alpha_1}_{\kappa_1\nu}(-\mathbf{q}) e^{\alpha_2}_{\kappa_2\nu}(\mathbf{q}) \frac{d}{dq^i} D_{\kappa_1,\alpha_1,\kappa_2,\alpha_2}(\mathbf{q}) = \\ = \frac{d}{dq^i} \sum_{\{\kappa\alpha\}} e^{\alpha_1}_{\kappa_1\nu}(-\mathbf{q}) e^{\alpha_2}_{\kappa_2\nu}(\mathbf{q}) D_{\kappa_1,\alpha_1,\kappa_2,\alpha_2}(\mathbf{q}). \tag{H.22}$$

Then, for the diagonal term of this heat-flux contribution I find

$$\widehat{J}^{i,1}_1 \approx -\frac{i\hbar}{2} \sum_{\mathbf{q}\nu} \widehat{P}_{-\mathbf{q}\nu} \widehat{U}_{\mathbf{q},\nu} \partial_{\mathbf{q}} \omega_{\mathbf{q},\nu}. \tag{H.23}$$

H.2 IMPLEMENTATION OF THE DYNAMICAL TENSOR

The dynamical tensor that I construct may be defined as

$$\varphi^n(\mathbf{q}_1, \kappa_1, \alpha_1, ..., \mathbf{q}_n, \kappa_n, \alpha_n) = \sum_{\{p\}} \Phi^{0...p_n}_{\kappa_1\alpha_1...\kappa_n\alpha_n} \vartheta^{\kappa_1,...\kappa_n}_{p_2...p_n}(\mathbf{q}_1, ..., \mathbf{q}_n). \tag{H.24}$$

Two implementations of ϑ are given. First the rigorous one via

$$\vartheta^{\kappa_1,...,\kappa_n}_{p_2,...,p_n}(\mathbf{q}_1, ..., \mathbf{q}_n) = N_p^{-1} \sum_{p_1} \theta(\mathbf{q}_1, \mathbf{R}_{p_1}) \prod_{l=2}^{n} \theta(\mathbf{q}_l, \mathbf{R}_{p_l} + \mathbf{R}_{p_1} + \boldsymbol{\tau}_{\kappa_l} - \boldsymbol{\tau}_{\kappa_1}). \tag{H.25}$$

This is derived directly from the definition of the vertex function:

$$\varphi^n(\mathbf{q}_1, \kappa_1, \alpha_1, ..., \mathbf{q}_n, \kappa_n, \alpha_n) = N^{-1} \sum_{\{p\}} \Phi^{p_1...p_n}_{\kappa_1\alpha_1...\kappa_n\alpha_n} \prod_{l=1}^{n} \exp(i\mathbf{q}_l \cdot (\mathbf{R}_{p_l} + \boldsymbol{\tau}_{\kappa_l})). \tag{H.26}$$

Now use translation invariance

$$\begin{aligned} \varphi^n(\mathbf{q}_1, \kappa_1, \alpha_1, ..., \mathbf{q}_n, \kappa_n, \alpha_n) &= N^{-1} \sum_{p_1} \sum_{\{p\}} \Phi^{0p_2-p_1...p_n-p_1}_{\kappa_1\alpha_1...\kappa_n\alpha_n} \times \\ &\qquad \times \prod_{l=1}^{n} \exp(i\mathbf{q}_l \cdot (\mathbf{R}_{p_l} + \boldsymbol{\tau}_{\kappa_l})) \\ &= N^{-1} \sum_{p_1} \exp(i\mathbf{q}_1 \cdot \mathbf{R}_{p_1}) \sum_{\{p'\}} \Phi^{0p'_2...p'_n}_{\kappa_1\alpha_1...\kappa_n\alpha_n} \times \\ &\qquad \prod_{l=2}^{n} \exp(i\mathbf{q}_l \cdot (\mathbf{R}_{p'_l} + \mathbf{R}_{p_1} + \boldsymbol{\tau}_{\kappa_l} - \boldsymbol{\tau}_{\kappa_1})) \\ &= \sum_{\{p\}} \Phi^{0...p_n}_{\kappa_1\alpha_1...\kappa_n\alpha_n} \vartheta^{\kappa_1,...\kappa_n}_{p_2...p_n}(\mathbf{q}_1, ..., \mathbf{q}_n), \end{aligned} \tag{H.27}$$

where the last step is true on the $\mathbf{q}$-grid commensurate with the supercell. There is also a simpler implementation for ϑ, that varies less with its arguments:

$$\vartheta^{\kappa_1,\ldots,\kappa_n}_{p_2,\ldots,p_n}(\mathbf{q}_1,\ldots,\mathbf{q}_n) = \prod_{l=2}^{n} \theta(\mathbf{q}_l, \mathbf{R}_{p_l} + \boldsymbol{\tau}_{\kappa_l} - \boldsymbol{\tau}_{\kappa_1}). \tag{H.28}$$

The properties that the ϑ must fulfill are simply found:

TRANSLATION INVARIANCE leads to the requirement that

$$\sum_{\kappa} \varphi^n(\mathbf{q}_1, \kappa_1, \alpha_1, \ldots, \mathbf{0}, \kappa, \alpha, \ldots) = 0. \tag{H.29}$$

This is manifestly true, for the rigorous implementation, and for the simple implementation for all momentum arguments, except the first one. (The function ϑ is a constant, independent of the l-indices if $\mathbf{q}_l = 0$.)

SYMMETRY OPERATIONS give, for an operation $\mathcal{O} = \{S|v_S\}$, the relation

$$\begin{aligned}
\varphi^n(S\mathbf{q}_1,\mathcal{O}(\kappa_1),\alpha_1,\ldots,S\mathbf{q}_n,\mathcal{O}(\kappa_n),\alpha_n) &= \sum_{\{p\}} \Phi^{0,p_2,\ldots,p_n}_{\mathcal{O}(\kappa_1),\alpha_1,\ldots,\mathcal{O}(\kappa_n),\alpha_n} \times \\
&\quad \times \vartheta^{\mathcal{O}(\kappa_1),\ldots,\mathcal{O}(\kappa_n)}_{p_2,\ldots,p_n}(S\mathbf{q}_1,\ldots,S\mathbf{q}_n) \\
&= \sum_{\{\nu\}} \left(\prod_{l=1}^{n} S_{\nu_l,\alpha_l} \right) \varphi^n(\mathbf{q}_1,\kappa_1,\nu_1,\ldots,\mathbf{q}_n,\kappa_n,\nu_n) \\
&= \sum_{\{\nu\}} \left(\prod_{l=1}^{n} S_{\nu_l,\alpha_l} \right) \sum_{\{p\}} \Phi^{p_1\ldots p_n}_{\kappa_1\nu_1\ldots\kappa_n\nu_n} \vartheta^{\kappa_1,\ldots\kappa_n}_{p_2\ldots p_n}(\mathbf{q}_1,\ldots,\mathbf{q}_n).
\end{aligned} \tag{H.30}$$

So, if the sets of points p and $\mathcal{O}(p)$ are identical, i.e. if the supercell is *closed under all operations of the space-group*, then one can obtain a condition that guarantees correct space-group transformations of φ^n:

$$\vartheta^{\mathcal{O}(\kappa_1),\ldots\mathcal{O}(\kappa_n)}_{\mathcal{O}(p_2)\ldots\mathcal{O}(p_n)}(S\mathbf{q}_1,\ldots,S\mathbf{q}_n) = \vartheta^{\kappa_1,\ldots\kappa_n}_{p_2\ldots p_n}(\mathbf{q}_1,\ldots,\mathbf{q}_n). \tag{H.31}$$

I apply this rule explicitly to both definitions of ϑ. First, in the rigorous case

$$\begin{aligned}
\vartheta^{\mathcal{O}(\kappa_1),\ldots,\mathcal{O}(\kappa_n)}_{\mathcal{O}(p_2),\ldots,\mathcal{O}(p_n)}(S\mathbf{q}_1,\ldots,S\mathbf{q}_n) &= N_p^{-1} \sum_{p_1} \theta(S\mathbf{q}_1, \mathbf{R}_{p_1}) \times \\
&\quad \times \prod_{l=2}^{n} \theta(S\mathbf{q}_l, S(\mathbf{R}_{p_l} + \boldsymbol{\tau}_{\kappa_l} - \boldsymbol{\tau}_{\kappa_1}) + \mathbf{R}_{p_1}).
\end{aligned} \tag{H.32}$$

If the two sets of points $\mathbf{R}_{p_1}$ and $S\mathbf{R}_{p_1}$ are identical, this is manifestly identical to $\vartheta^{\kappa_1,\ldots\kappa_n}_{p_2\ldots p_n}(\mathbf{q}_1,\ldots,\mathbf{q}_n)$, because

$$\theta(S\mathbf{q},S\mathbf{x}) = \theta(\mathbf{q},\mathbf{x}). \tag{H.33}$$

The simple case is, with this equation, manifestly transforming correctly. The nuclei-masses can be ignored in this multiplication, because the symmetry operations can only transform nuclei of the same type onto each other.

PERMUTATION INVARIANCE is almost a tautology, given the permutation invariance of the IFCs. The simplified implementation breaks the permutation invariance with respect to the first index for all vertices with more than two momentum arguments.

H.3 USING TRANSLATION SYMMETRY

Consider a general physical quantity, that depends on multiple unit cell indices p, $\Psi_{p_1\ldots p_n}$. This might be a contribution to the heat-flux operator or whatever other quantity. The Fourier transform is

$$\psi(\mathbf{q}_1\ldots\mathbf{q}_n) = N_p^{-1}\sum_{\{p\}}\Psi_{p_1\ldots p_n}\exp(i\sum_l \mathbf{q}_l\cdot\mathbf{R}_{p_l}). \tag{H.34}$$

Because of the translation symmetry, a shift of the lattice by a lattice vector must leave ψ invariant, or it must be zero because otherwise $\psi = \alpha\psi$ with $\alpha \neq 1$. This means in turn, that $\exp(i\sum_l \mathbf{q}_l\cdot\mathbf{R}_p) = 1$ for every lattice vector $\mathbf{R}_p$, and that means, that $\sum_l \mathbf{q}_l$ must be a reciprocal lattice vector $\mathbf{R}_\mathbf{q}$, that fulfills

$$\mathbf{R}_{p_i}\cdot\mathbf{R}_\mathbf{q} = 2\pi n\delta_{i,j}, \tag{H.35}$$

with $n \in \widehat{\mathrm{Tr}}$. I reinsert this consideration into the above formula

$$\psi(\mathbf{q}_1\ldots\mathbf{q}_n) = N_p^{-1}\sum_{p_1}\sum_{\{p\}}\Psi_{p_1\ldots p_n}\exp(i\sum_{l=2}^{n}\mathbf{q}_l\cdot(\mathbf{R}_{p_l}-\mathbf{R}_{p_1}))\Delta(\sum_l \mathbf{q}_l). \tag{H.36}$$

I used that $\exp(i\mathbf{R}_\mathbf{q}\cdot\mathbf{R}_{p_1}) = 1$, and $\Delta(\mathbf{x})$ is one if the argument is a reciprocal lattice vector, and otherwise zero. By translation invariance

$$\psi(\mathbf{q}_1\ldots\mathbf{q}_n) = N_p^{-1}\sum_{p_1}\sum_{\{p\}}\Psi_{0p_2-p_1\ldots p_n-p_1}\exp(i\sum_{l=2}^{n}\mathbf{q}_l\cdot(\mathbf{R}_{p_l}-\mathbf{R}_{p_1}))\Delta(\sum_l \mathbf{q}_l). \tag{H.37}$$

The summation can be shifted $p'_l = p_l - p_1$ such that

$$\begin{aligned}\psi(\mathbf{q}_1 ... \mathbf{q}_n) &= N_p^{-1} \sum_{p_1} \sum_{\{p\}} \Psi_{0 p_2 ... p_n} \exp(i \sum_{l=2}^{n} \mathbf{q}_l \cdot \mathbf{R}_{p_l}) \Delta(\sum_l \mathbf{q}_l) \\ &= \sum_{\{p\}} \Psi_{0 p_2 ... p_n} \exp(i \sum_{l=2}^{n} \mathbf{q}_l \cdot \mathbf{R}_{p_l}) \Delta(\sum_l \mathbf{q}_l),\end{aligned} \tag{H.38}$$

with the constraint that the set of unit-cell positions contains the origin.

I

IMAGINARY PART

It is the task of this section to reason, why, for the imaginary part of the diagram, it is enough to take the imaginary part of the product of denominators. This was motivated by the cutting rules for Feynman diagrams in quantum field theory (44).

A diagram consists of vertices and propagators. Propagators have a start and an end index ν_n^s and ν_n^e. Every vertex has the property that under inversion of all momenta $\mathbf{q}$ it becomes its own complex conjugate. This is easy to see for the phonon vertices. Recall the properties of the boson spectral densities:

$$\mathcal{S}^{\widehat{A}\widehat{B}}_{\mathbf{q},\nu,\nu'}(\mathcal{E}) = -(\mathcal{S}^{\widehat{A}\widehat{B}}_{-\mathbf{q},\nu,\nu'}(-\mathcal{E}))^*, \tag{I.1}$$

where $\widehat{A}$ and $\widehat{B}$ can be $\widehat{P}$ or $\widehat{U}$. For the propagators one has

$$\mathcal{G}^{M,\widehat{A}\widehat{B}}_{\mathbf{q},\nu,\nu'}(E) = (\mathcal{G}^{M,\widehat{A}\widehat{B}}_{-\mathbf{q},\nu,\nu'}(-E))^* = \mathcal{G}^{M,\widehat{B}\widehat{A}}_{-\mathbf{q},\nu',\nu}(-E). \tag{I.2}$$

Every diagram, that contributes to the correlation function, has the form:

$$\begin{aligned} D^M_{12}(E) = \sum_{\{\mathbf{q},\nu\}} \sum_{\{E_p\}} & J_L(\mathbf{q}_1^1\nu_1^1, ...\mathbf{q}_1^{l_1}\nu_1^{l_1})\; J_R(\mathbf{q}_2^1\nu_2^1, ...\mathbf{q}_2^{l_2}\nu_2^{l_2}) \times \\ & \times \prod_{v=3}^{n_v} \tilde{\Phi}(\mathbf{q}_v^1\nu_v^1, ...\mathbf{q}_v^{l_v}\nu_v^{l_v}) \prod_{p=1}^{n_p} \mathcal{G}^{M,\widehat{A}_p\widehat{B}_p}_{\mathbf{q}_p,\nu_p^s,\nu_p^e}(E_p(E)), \end{aligned} \tag{I.3}$$

where n_v is the number of vertices and l_v the number of legs of the vertex v. n_p is the number of propagators. $J_{L/R}$ denotes the left and right heat-flux vertex. The energies at the heat-flux vertices sum to $\pm E$, so that the Matsubara energies E_p of the propagators depend on E. The sums of all D^M_{12} and D^M_{21} are related: According to Eq. (2.33), one has for the correlation function in total:

$$\begin{aligned} G^M_{21}(\tau - \tau') = -\frac{1}{\mathrm{Tr}(\widehat{\rho})} \sum_{n=0}^{\infty} \frac{1}{n!} \left(-\frac{1}{\hbar}\right)^n \int_0^{\hbar\beta} d\tau_1 ... d\tau_n \\ \times \mathrm{Tr}\left[\widehat{\rho}_0 T_\tau(\widehat{V}^D(\tau_1)...\widehat{V}^D(\tau_n)\widehat{A}^D(\tau')\widehat{B}^D(\tau))\right], \end{aligned}$$

while

$$\begin{aligned} G^M_{12}(\tau - \tau') = -\frac{1}{\mathrm{Tr}(\widehat{\rho})} \sum_{n=0}^{\infty} \frac{1}{n!} \left(-\frac{1}{\hbar}\right)^n \int_0^{\hbar\beta} d\tau_1 ... d\tau_n \\ \times \mathrm{Tr}\left[\widehat{\rho}_0 T_\tau(\widehat{V}^D(\tau_1)...\widehat{V}^D(\tau_n)\widehat{A}(\tau)\widehat{B}(\tau'))\right], \end{aligned}$$

which implies in the time domain

$$G_{21}^{M}(-\tau) = G_{12}^{M}(\tau). \tag{I.4}$$

This implies for the Fourier decomposition:

$$\begin{aligned} G_{12}^{M}(\tau) &= \frac{1}{\hbar\beta}\sum_{E}\exp(-\frac{iE\tau}{\hbar})G_{12}^{M}(E) = G_{21}^{M}(-\tau) \\ &= \frac{1}{\hbar\beta}\sum_{E}\exp(\frac{iE\tau}{\hbar})G_{21}^{M}(E) \\ &= \frac{1}{\hbar\beta}\sum_{E}\exp(-\frac{iE\tau}{\hbar})G_{21}^{M}(-E), \end{aligned} \tag{I.5}$$

or, by inversion, simply $G_{21}^{M}(-E) = G_{12}^{M}(E)$. As the correlation function is the sum of all diagrams, the sum of all the diagrams fulfills $\sum_D D_{21}^{M}(-E) = \sum_D D_{12}^{M}(E)$. Lets return to Eq. (I.3) and take the complex conjugate:

$$\begin{aligned} (D_{12}^{M}(E))^* = \sum_{\{\mathbf{q},\nu\}}\sum_{\{E_p\}} & J_L(-\mathbf{q}_1^1\nu_1^1,\ldots-\mathbf{q}_1^{l_1}\nu_1^{l_1})\; J_R(-\mathbf{q}_2^1\nu_2^1,\ldots-\mathbf{q}_2^{l_2}\nu_2^{l_2})\times \\ & \times\prod_{v=3}^{n_v}\tilde{\Phi}(-\mathbf{q}_v^1\nu_v^1,\ldots-\mathbf{q}_v^{l_v}\nu_v^{l_v})\prod_{p=1}^{n_p}\mathcal{G}^{M,\widehat{A}_p\widehat{B}_p}_{-\mathbf{q}_p,\nu_p^s,\nu_p^e}(-E_p(E)). \end{aligned} \tag{I.6}$$

After this, invert E, $\mathbf{q}$:

$$\begin{aligned} (D_{12}^{M}(-E))^* = \sum_{\{\mathbf{q},\nu\}}\sum_{\{E_p\}} & J_L(\mathbf{q}_1^1\nu_1^1,\ldots\mathbf{q}_1^{l_1}\nu_1^{l_1})\; J_R(\mathbf{q}_2^1\nu_2^1,\ldots\mathbf{q}_2^{l_2}\nu_2^{l_2})\times \\ & \times\prod_{v=3}^{n_v}\tilde{\Phi}(\mathbf{q}_v^1\nu_v^1,\ldots\mathbf{q}_v^{l_v}\nu_v^{l_v})\prod_{p=1}^{n_p}\mathcal{G}^{M,\widehat{A}_p\widehat{B}_p}_{\mathbf{q}_p,\nu_p^s,\nu_p^e}(E_p(E)). \end{aligned} \tag{I.7}$$

This step is possible, because at first, every propagator has its own independent energy, but the vertex functions carry a prefactor of the type

$$d(E+\sum_{p=1}^{n_p}\sigma_p^1E_p)d(-E+\sum_{p=1}^{n_p}\sigma_p^2E_p)\prod_{v=3}^{n_v}d(\sum_{p=1}^{n_p}\sigma_p^vE_p), \tag{I.8}$$

where $d(x)$ is one if $x=0$ and otherwise it is zero and σ_p^v is either $+1$, 0 or -1. Now, if the energy arguments of the propagators are all inverted *and* the energy E is inverted, this prefactor remains the same, as d is symmetric in its argument.

Then, I find that the sum of all diagrams

$$\sum_D D_{12}^{M}(E) + D_{21}^{M}(E) \in \mathbb{R} \qquad \forall E, \tag{I.9}$$

where E can be any Matsubara energy. On top of that

$$\sum_D D_{12}^M(E) + D_{21}^M(E) = \sum_D D_{12}^M(E) + D_{12}^M(-E). \tag{I.10}$$

Now, consider

$$\begin{aligned} D_{12}^M(-E) = &\sum_{\{\mathbf{q},\nu\}} \sum_{\{E_p\}} J_L(\mathbf{q}_1^1\nu_1^1, ...\mathbf{q}_1^{l_1}\nu_1^{l_1})\ J_R(\mathbf{q}_2^1\nu_2^1, ...\mathbf{q}_2^{l_2}\nu_2^{l_2}) \\ &\times \prod_{v=3}^{n_v} \tilde{\Phi}(\mathbf{q}_v^1\nu_v^1, ...\mathbf{q}_v^{l_v}\nu_v^{l_v}) \prod_{p=1}^{n_p} \mathcal{G}^{M,\widehat{A}_p\widehat{B}_p}_{\mathbf{q}_p,\nu_p^s,\nu_p^e}(-E_p(E)), \end{aligned} \tag{I.11}$$

and insert the spectral representation for the propagators Eq. (2.26):

$$\begin{aligned} D_{12}^M(-E) = &\sum_{\{\mathbf{q},\nu\}} \sum_{\{E_p\}} J_L(\mathbf{q}_1^1\nu_1^1, ...\mathbf{q}_1^{l_1}\nu_1^{l_1})\ J_R(\mathbf{q}_2^1\nu_2^1, ...\mathbf{q}_2^{l_2}\nu_2^{l_2}) \\ &\times \prod_{v=3}^{n_v} \tilde{\Phi}(\mathbf{q}_v^1\nu_v^1, ...\mathbf{q}_v^{l_v}\nu_v^{l_v}) \prod_{p=1}^{n_p} \int_{\mathbb{R}} d\mathcal{E}_p \frac{\mathcal{S}^{\widehat{A}_p\widehat{B}_p}_{\mathbf{q}_p,\nu_p^s,\nu_p^e}(\mathcal{E}_p)}{-E_p(E) - \mathcal{E}_p} \\ = &\sum_{\{\mathbf{q},\nu\}} \sum_{\{E_p\}} J_L(\mathbf{q}_1^1\nu_1^1, ...\mathbf{q}_1^{l_1}\nu_1^{l_1})\ J_R(\mathbf{q}_2^1\nu_2^1, ...\mathbf{q}_2^{l_2}\nu_2^{l_2}) \times \\ &\times \prod_{v=3}^{n_v} \tilde{\Phi}(\mathbf{q}_v^1\nu_v^1, ...\mathbf{q}_v^{l_v}\nu_v^{l_v}) \prod_{p=1}^{n_p} \int_{\mathbb{R}} d\mathcal{E}_p \mathcal{S}^{\widehat{A}_p\widehat{B}_p}_{\mathbf{q}_p,\nu_p^s,\nu_p^e}(\mathcal{E}_p) \left(\frac{1}{E_p(E) - \mathcal{E}_p}\right)^*, \end{aligned} \tag{I.12}$$

which is true for all Matsubara frequencies E_p, that are fully imaginary. Under summation (for Matsubara energies):

$$\begin{aligned} D_{12}^M(E) + D_{12}^M(-E) = 2 &\sum_{\{\mathbf{q},\nu\}} J_L(\mathbf{q}_1^1\nu_1^1, ...\mathbf{q}_1^{l_1}\nu_1^{l_1})\ J_R(\mathbf{q}_2^1\nu_2^1, ...\mathbf{q}_2^{l_2}\nu_2^{l_2}) \times \\ &\times \prod_{v=3}^{n_v} \tilde{\Phi}(\mathbf{q}_v^1\nu_v^1, ...\mathbf{q}_v^{l_v}\nu_v^{l_v}) \times \\ &\times \prod_{p=1}^{n_p} \int_{\mathbb{R}} d\mathcal{E}_p \mathcal{S}^{\widehat{A}_p\widehat{B}_p}_{\mathbf{q}_p,\nu_p^s,\nu_p^e}(\mathcal{E}_p) \mathrm{Re}\left(\mathcal{F}^M(E, \mathcal{E}_1, ..., \mathcal{E}_p)\right). \end{aligned} \tag{I.13}$$

Here I defined

$$\begin{aligned} \mathcal{F}^M(E, \mathcal{E}_1, ..., \mathcal{E}_p) = &\sum_{\{E_p\}} \prod_{p=1}^{n_p} \frac{1}{E_p(E) - \mathcal{E}_p} \times \\ &\times d(E + \sum_{p=1}^{n_p} \sigma_p^1 E_p) d(-E + \sum_{p=1}^{n_p} \sigma_p^2 E_p) \prod_{v=3}^{n_v} d(\sum_{p=1}^{n_p} \sigma_p^v E_p). \end{aligned} \tag{I.14}$$

The d functions of the vertices have been taken into the Matsubara sum above. $D_{12}^M(E) + D_{12}^M(-E)$ is real. This means, I can divide by two, and add the complex conjugate, or:

$$\begin{aligned} D_{12}^M(E) + D_{12}^M(-E) = \mathrm{Re}\Big(\sum_{\{\mathbf{q},\nu\}} & J_L(\mathbf{q}_1^1\nu_1^1, ...\mathbf{q}_1^{l_1}\nu_1^{l_1})\; J_R(\mathbf{q}_2^1\nu_2^1, ...\mathbf{q}_2^{l_2}\nu_2^{l_2}) \times \\ & \times \prod_{v=3}^{n_v} \tilde{\Phi}(\mathbf{q}_v^1\nu_v^1, ...\mathbf{q}_v^{l_v}\nu_v^{l_v}) \prod_{p=1}^{n_p} \int_{\mathbb{R}} d\mathcal{E}_p \mathcal{S}^{\widehat{A}_p\widehat{B}_p}_{\mathbf{q}_p,\nu_p^s,\nu_p^e}(\mathcal{E}_p)) \times \\ & \times \Big(\mathcal{F}^M(E, \mathcal{E}_1, ..., \mathcal{E}_p) + \mathcal{F}^M(-E, \mathcal{E}_1, ..., \mathcal{E}_p) \Big) , \end{aligned} \tag{I.15}$$

where in the last line, I have reinserted the meaning of the real part of the Matsubara sums, and the real part operation Re acts on all objects that occur before the Matsubara sum. This representation and the representation without the real part operation need to be completely identical for all complex values $E \to z$ in the complex plane, as the set of Matsubara energies contains an accumulation point and the analytic continuation of the correlation function $\Pi_M^{ij}(E)$ ($\Pi^{ij}(z)$) is analytic at the accumulation point (190) (i.e. for large absolute values z):

$$\Pi^{ij}(z) = \frac{1}{\mathrm{Tr}(\widehat{\rho})} \sum_{\gamma,\xi} \langle\gamma|\widehat{J}^i|\xi\rangle\langle\xi|\widehat{J}^j|\gamma\rangle \frac{\exp(-\beta E_\xi) - \exp(-\beta E_\gamma)}{E_\gamma - E_\xi - z}, \tag{I.16}$$

where E_γ denotes an eigenenergy of the system, corresponding to the eigenstate $|\gamma\rangle$. If the contribution of the states of extremely high energy to the correlation function can be neglected (which should be possible if perturbation theory is ever to be applicable (218)), the function becomes zero if $|z| \to \infty$, and is therefore analytic near the accumulation point ∞.

Under analytic continuation the sum of diagrams acquires an imaginary part, which is

$$\begin{aligned} \mathrm{Im}(D_{12}^r(\mathcal{E}) + D_{21}^r(\mathcal{E})) = 2 \sum_{\{\mathbf{q},\nu\}} & J_L(\mathbf{q}_1^1\nu_1^1, ...\mathbf{q}_1^{l_1}\nu_1^{l_1})\; J_R(\mathbf{q}_2^1\nu_2^1, ...\mathbf{q}_2^{l_2}\nu_2^{l_2}) \times \\ & \times \prod_{v=3}^{n_v} \tilde{\Phi}(\mathbf{q}_v^1\nu_v^1, ...\mathbf{q}_v^{l_v}\nu_v^{l_v}) \prod_{p=1}^{n_p} \int_{\mathbb{R}} d\mathcal{E}_p \mathcal{S}^{\widehat{A}_p\widehat{B}_p}_{\mathbf{q}_p,\nu_p^s,\nu_p^e}(\mathcal{E}_p) \times \\ & \times \mathrm{Im}\mathcal{F}^r(\mathcal{E}, \mathcal{E}_1, ..., \mathcal{E}_p). \end{aligned} \tag{I.17}$$

J

A SECOND ORDER CONTRIBUTION

I exemplify here the calculation of a second order diagram. For brevity, the mode basis has been chosen. Any index ν may also be interpreted as combined index $\kappa\alpha$. I use the diagram shown in Fig. J.1, which has the value

$$\begin{aligned} D^{M,ij}(E) = \frac{1}{\hbar^4\beta^2 N_p^2 \Omega_c^2} \sum_{\{\mathbf{q}\nu\}} \sum_{\{E_n\}} (-36)\, J_1^i(-\mathbf{q}_0,\nu_0;\mathbf{q}_0,\nu_2)\times \\ v^3(\mathbf{q}_0,\nu_1;-\mathbf{q}_2,\nu_4;\mathbf{q}_2-\mathbf{q}_0,\nu_6)\times \\ v^3(-\mathbf{q}_0,\nu_3;\mathbf{q}_2,\nu_5;\mathbf{q}_0-\mathbf{q}_2,\nu_8)\times \\ J_1^j(\mathbf{q}_0-\mathbf{q}_2,\nu_7;\mathbf{q}_2-\mathbf{q}_0,\nu_9)\times \\ \mathcal{G}^{\widehat{P}\widehat{U}}_{\mathbf{q}_0,\nu_0,\nu_1}(E_0)\mathcal{G}_{-\mathbf{q}_0,\nu_2,\nu_3}(E-E_0)\times \\ \mathcal{G}_{\mathbf{q}_2,\nu_4,\nu_5}(E_2)\mathcal{G}^{\widehat{U}\widehat{P}}_{\mathbf{q}_0-\mathbf{q}_2,\nu_6,\nu_7}(E_0-E_2)\times \\ \mathcal{G}_{\mathbf{q}_2-\mathbf{q}_0,\nu_8,\nu_9}(E+E_2-E_0). \end{aligned} \tag{J.1}$$

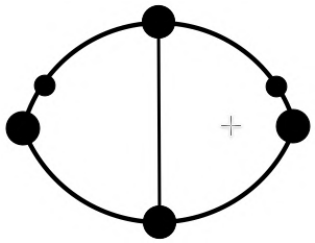

Figure J.1: Second order example diagram.

In order to use the Matsubara summation technique, I apply the spectral representation of the propagators Eq. (2.26):

$$
\begin{aligned}
D^{M,ij}(E) = \frac{1}{\hbar^4\beta^2 N_p^2 \Omega_c^2} \int_{\mathbb{R}} d\mathcal{E} \sum_{\{\mathbf{q}\nu\}} (-36)\, J_1^i(-\mathbf{q}_0,\nu_0;\mathbf{q}_0,\nu_2)\times \\
v^3(\mathbf{q}_0,\nu_1;-\mathbf{q}_2,\nu_4;\mathbf{q}_2-\mathbf{q}_0,\nu_6)\times \\
v^3(-\mathbf{q}_0,\nu_3;\mathbf{q}_2,\nu_5;\mathbf{q}_0-\mathbf{q}_2,\nu_8)\times \\
J_1^j(\mathbf{q}_0-\mathbf{q}_2,\nu_7;\mathbf{q}_2-\mathbf{q}_0,\nu_9)\times \\
\mathcal{S}^{\widehat{P}\widehat{U}}_{\mathbf{q}_0,\nu_0,\nu_1}(\mathcal{E}_0)\mathcal{S}_{-\mathbf{q}_0,\nu_2,\nu_3}(\mathcal{E}_1)\times \\
\mathcal{S}_{\mathbf{q}_2,\nu_4,\nu_5}(\mathcal{E}_2)\mathcal{S}^{\widehat{U}\widehat{P}}_{\mathbf{q}_0-\mathbf{q}_2,\nu_6,\nu_7}(\mathcal{E}_3)\times \\
\mathcal{S}_{\mathbf{q}_2-\mathbf{q}_0,\nu_8,\nu_9}(\mathcal{E}_4)\times \\
\sum_{\{E_n\}} (E_0-\mathcal{E}_0)^{-1}\,(E-E_0-\mathcal{E}_1)^{-1}\times \\
(E_2-\mathcal{E}_2)^{-1}\,(E_0-E_2-\mathcal{E}_3)^{-1}\times \\
(E+E_2-E_0-\mathcal{E}_4)^{-1}\,. \qquad \text{(J.2)}
\end{aligned}
$$

Executing the Matsubara summation leads to a total of 12 contributions:

$$
\begin{aligned}
&\beta^{-2}\sum_{E_0,E_2} (E_0-\mathcal{E}_0)^{-1}\,(E-E_0-\mathcal{E}_1)^{-1}\,(E_2-\mathcal{E}_2)^{-1}\times \\
&(E_0-E_2-\mathcal{E}_3)^{-1}\,(E+E_2-E_0-\mathcal{E}_4)^{-1} = \\
&\frac{n_B(\mathcal{E}_0)n_B(\mathcal{E}_2)}{(E-\mathcal{E}_0-\mathcal{E}_1)\,(\mathcal{E}_0-\mathcal{E}_2-\mathcal{E}_3)\,(E+\mathcal{E}_2-\mathcal{E}_0-\mathcal{E}_4)}+ \\
&\frac{-n_B(\mathcal{E}_0)n_B(\mathcal{E}_0-\mathcal{E}_3)}{(E-\mathcal{E}_0-\mathcal{E}_1)\,(\mathcal{E}_0-\mathcal{E}_2-\mathcal{E}_3)\,(E-\mathcal{E}_3-\mathcal{E}_4)}+ \\
&\frac{n_B(\mathcal{E}_0)n_B(\mathcal{E}_0+\mathcal{E}_4)}{(E-\mathcal{E}_0-\mathcal{E}_1)\,(\mathcal{E}_0+\mathcal{E}_4-E-\mathcal{E}_2)\,(E-\mathcal{E}_3-\mathcal{E}_4)}+ \\
&\frac{-n_B(-\mathcal{E}_1)n_B(\mathcal{E}_2)}{(E-\mathcal{E}_0-\mathcal{E}_1)\,(E-\mathcal{E}_1-\mathcal{E}_2-\mathcal{E}_3)\,(\mathcal{E}_1+\mathcal{E}_2-\mathcal{E}_4)}+ \\
&\frac{n_B(-\mathcal{E}_1)n_B(-\mathcal{E}_1-\mathcal{E}_3)}{(E-\mathcal{E}_0-\mathcal{E}_1)\,(E-\mathcal{E}_1-\mathcal{E}_2-\mathcal{E}_3)\,(E-\mathcal{E}_3-\mathcal{E}_4)}+ \\
&\frac{-n_B(-\mathcal{E}_1)n_B(\mathcal{E}_4-\mathcal{E}_1)}{(E-\mathcal{E}_0-\mathcal{E}_1)\,(\mathcal{E}_4-\mathcal{E}_1-\mathcal{E}_2)\,(E-\mathcal{E}_3-\mathcal{E}_4)}+ \\
&\frac{n_B(\mathcal{E}_3)n_B(\mathcal{E}_0-\mathcal{E}_3)}{(E-\mathcal{E}_0-\mathcal{E}_1)\,(\mathcal{E}_0-\mathcal{E}_2-\mathcal{E}_3)\,(E-\mathcal{E}_3-\mathcal{E}_4)}+
\end{aligned}
$$

$$\frac{-n_B(\mathcal{E}_3)n_B(-\mathcal{E}_1-\mathcal{E}_3)}{(E-\mathcal{E}_0-\mathcal{E}_1)\,(E-\mathcal{E}_1-\mathcal{E}_2-\mathcal{E}_3)\,(E-\mathcal{E}_3-\mathcal{E}_4)}+$$

$$\frac{n_B(\mathcal{E}_3)n_B(\mathcal{E}_2)}{(\mathcal{E}_2+\mathcal{E}_3-\mathcal{E}_0)\,(E-\mathcal{E}_1-\mathcal{E}_2-\mathcal{E}_3)\,(E-\mathcal{E}_3-\mathcal{E}_4)}+$$

$$\frac{-n_B(-\mathcal{E}_4)n_B(\mathcal{E}_0+\mathcal{E}_4)}{(E-\mathcal{E}_0-\mathcal{E}_1)\,(\mathcal{E}_0+\mathcal{E}_4-E-\mathcal{E}_2)\,(E-\mathcal{E}_3-\mathcal{E}_4)}+$$

$$\frac{n_B(-\mathcal{E}_4)n_B(\mathcal{E}_4-\mathcal{E}_1)}{(E-\mathcal{E}_0-\mathcal{E}_1)\,(\mathcal{E}_4-\mathcal{E}_1-\mathcal{E}_2)\,(E-\mathcal{E}_3-\mathcal{E}_4)}+$$

$$\frac{-n_B(-\mathcal{E}_4)n_B(\mathcal{E}_2)}{(E+\mathcal{E}_2-\mathcal{E}_0-\mathcal{E}_4)\,(\mathcal{E}_4-\mathcal{E}_1-\mathcal{E}_2)\,(E-\mathcal{E}_3-\mathcal{E}_4)}. \tag{J.3}$$

Consider the first term only and take the imaginary part (after analytic continuation)

$$\frac{-\pi n_B(\mathcal{E}_0)n_B(\mathcal{E}_2)\delta\,(\mathcal{E}-\mathcal{E}_0-\mathcal{E}_1)}{(\mathcal{E}+\mathcal{E}_2-\mathcal{E}_0-\mathcal{E}_4)\,(\mathcal{E}_0-\mathcal{E}_2-\mathcal{E}_3)}+$$

$$\frac{-\pi n_B(\mathcal{E}_0)n_B(\mathcal{E}_2)\delta\,(\mathcal{E}+\mathcal{E}_2-\mathcal{E}_0-\mathcal{E}_4)}{(\mathcal{E}-\mathcal{E}_0-\mathcal{E}_1)\,(\mathcal{E}_0-\mathcal{E}_2-\mathcal{E}_3)}. \tag{J.4}$$

It is now possible to remove the rest of the denominators by reintegration, see Sec. 4.3.5. In our example I obtain (for the first contribution of the formula above, where $\mathcal{E}_3$ and $\mathcal{E}_4$ can be reintegrated)

$$\begin{aligned}\frac{1}{\hbar^4 N_p^2 \Omega_c^2}\int_{\mathbb{R}} d\mathcal{E} \sum_{\{\mathbf{q}\nu\}} (36\pi)\, & J_1^j(-\mathbf{q}_0,\nu_0;\mathbf{q}_0,\nu_2)\times \\ & v^3(\mathbf{q}_0,\nu_1;-\mathbf{q}_2,\nu_4;\mathbf{q}_2-\mathbf{q}_0,\nu_6)\times \\ & v^3(-\mathbf{q}_0,\nu_3;\mathbf{q}_2,\nu_5;\mathbf{q}_0-\mathbf{q}_2,\nu_8)\times \\ & J_1^j(\mathbf{q}_0-\mathbf{q}_2,\nu_7;\mathbf{q}_2-\mathbf{q}_0,\nu_9)\times \\ & \mathcal{S}^{\widehat{P}\widehat{U}}_{\mathbf{q}_0,\nu_0,\nu_1}(\mathcal{E}_0)\mathcal{S}_{-\mathbf{q}_0,\nu_2,\nu_3}(\mathcal{E}-\mathcal{E}_0)\times \\ & \mathcal{S}_{\mathbf{q}_2,\nu_4,\nu_5}(\mathcal{E}_2)n_B(\mathcal{E}_0)n_B(\mathcal{E}_2)\times \\ & \mathcal{G}^{\widehat{U}\widehat{P}}_{\mathbf{q}_0-\mathbf{q}_2,\nu_6,\nu_7}(\mathcal{E}_0-\mathcal{E}_2)\times \\ & \mathcal{G}_{\mathbf{q}_2-\mathbf{q}_0,\nu_8,\nu_9}(\mathcal{E}+\mathcal{E}_2-\mathcal{E}_0).\end{aligned} \tag{J.5}$$

The next task is to apply the limit necessary to calculate the contribution to the thermal conductivity. Afterwards the interrelations between the spectral densities and propagators are applied. I only consider

the term, that is proportional to the derivative of $\mathcal{S}_{-\mathbf{q}_0,\nu_2,\nu_3}(\mathcal{E}-\mathcal{E}_0)$ at $\mathcal{E}=0$:

$$\begin{aligned}\frac{1}{\hbar^6 N_p^2 \Omega_c^2}\int_{\mathbb{R}} d\mathcal{E} \sum_{\{\mathbf{q}\nu\}} (-36\mathcal{E}_0\pi(\mathcal{E}_0-\mathcal{E}_2))\, J_1^i(-\mathbf{q}_0,\nu_0;\mathbf{q}_0,\nu_2)\times \\ v^3(\mathbf{q}_0,\nu_1;-\mathbf{q}_2,\nu_4;\mathbf{q}_2-\mathbf{q}_0,\nu_6)\times \\ v^3(-\mathbf{q}_0,\nu_3;\mathbf{q}_2,\nu_5;\mathbf{q}_0-\mathbf{q}_2,\nu_8)\times \\ J_1^j(\mathbf{q}_0-\mathbf{q}_2,\nu_7;\mathbf{q}_2-\mathbf{q}_0,\nu_9)\times \\ \mathcal{S}_{\mathbf{q}_0,\nu_0,\nu_1}(\mathcal{E}_0)\mathcal{S}^{(1)}_{-\mathbf{q}_0,\nu_2,\nu_3}(-\mathcal{E}_0)\times \\ \mathcal{S}_{\mathbf{q}_2,\nu_4,\nu_5}(\mathcal{E}_2) n_B(\mathcal{E}_0) n_B(\mathcal{E}_2)\times \\ \mathcal{G}_{\mathbf{q}_0-\mathbf{q}_2,\nu_6,\nu_7}(\mathcal{E}_0-\mathcal{E}_2)\times \\ \mathcal{G}_{\mathbf{q}_2-\mathbf{q}_0,\nu_8,\nu_9}(\mathcal{E}_2-\mathcal{E}_0). \end{aligned} \tag{J.6}$$

Then I observe, that the integration energies fulfill the same kinetics as the momenta (and Matsubara energies). To simplify I define a normal form, that enforces all momenta and integration energies to sum up. A detailed description is found in Appendix M and Sec. 4.3.7. Then, all arguments of the contributing propagators and spectral densities can be made positive

$$\begin{aligned}\frac{1}{\hbar^6 N_p^2 \Omega_c^2}\int_{\mathbb{R}} d\mathcal{E} \sum_{\{\mathbf{q}\nu\}} (36\mathcal{E}_0\pi(\mathcal{E}_0+\mathcal{E}_1))\, J_1^i(\mathbf{q}_0,\nu_2;-\mathbf{q}_0,\nu_0)\times \\ J_1^j(\mathbf{q}_0+\mathbf{q}_1,\nu_7;-\mathbf{q}_0-\mathbf{q}_1,\nu_9)\times \\ v^3(\mathbf{q}_0,\nu_1;\mathbf{q}_1,\nu_4;-\mathbf{q}_0-\mathbf{q}_1,\nu_6)\times \\ v^3(\mathbf{q}_0+\mathbf{q}_1,\nu_8;-\mathbf{q}_1,\nu_5;-\mathbf{q}_0,\nu_3)\times \\ \mathcal{S}_{\mathbf{q}_1,\nu_5,\nu_4}(\mathcal{E}_1)\mathcal{S}_{\mathbf{q}_0,\nu_0,\nu_1}(\mathcal{E}_0)\times \\ \mathcal{S}^{(1)}_{\mathbf{q}_0,\nu_3,\nu_2}(\mathcal{E}_0) n_B(\mathcal{E}_1) n_B(\mathcal{E}_0)\times \\ \mathcal{G}_{\mathbf{q}_0+\mathbf{q}_1,\nu_6,\nu_7}(\mathcal{E}_0+\mathcal{E}_1)\times \\ \mathcal{G}_{\mathbf{q}_0+\mathbf{q}_1,\nu_9,\nu_8}(\mathcal{E}_0+\mathcal{E}_1), \end{aligned} \tag{J.7}$$

which is one part of the result of the diagram in Fig. J.1. For the final contributions, partial integration can be applied, see Sec. 4.3.8. For some reason, the final terms always have derivatives *on the occupa-*

tion functions. For example, a final contribution (that the above term contributes to) is

$$\begin{aligned}\frac{1}{\hbar^6 N_p^2 \Omega_c^2} \int_{\mathbb{R}} d\mathcal{E} \sum_{\{\mathbf{q}\nu\}} (-144 \mathcal{E}_1 \pi(\mathcal{E}_0 + \mathcal{E}_1))\, J_1^i(\mathbf{q}_1, \nu_0; -\mathbf{q}_1, \nu_1) \times \\ J_1^j(\mathbf{q}_0 + \mathbf{q}_1, \nu_2; -\mathbf{q}_0 - \mathbf{q}_1, \nu_3) \times \\ v^3(\mathbf{q}_0, \nu_4; \mathbf{q}_1, \nu_5; -\mathbf{q}_0 - \mathbf{q}_1, \nu_6) \times \\ v^3(\mathbf{q}_0 + \mathbf{q}_1, \nu_7; -\mathbf{q}_1, \nu_8; -\mathbf{q}_0, \nu_9) \times \\ \mathcal{S}_{\mathbf{q}_1, \nu_1, \nu_5}(\mathcal{E}_1) \mathcal{S}_{\mathbf{q}_1, \nu_8, \nu_0}(\mathcal{E}_1) \times \\ \mathcal{S}_{\mathbf{q}_0, \nu_9, \nu_4}(\mathcal{E}_0) n_B^{(1)}(\mathcal{E}_1) n_B(\mathcal{E}_0) \times \\ \mathcal{G}_{\mathbf{q}_0 + \mathbf{q}_1, \nu_3, \nu_7}(\mathcal{E}_0 + \mathcal{E}_1) \times \\ \mathcal{G}_{\mathbf{q}_0 + \mathbf{q}_1, \nu_6, \nu_2}(\mathcal{E}_0 + \mathcal{E}_1). \end{aligned} \tag{J.8}$$

Only terms of the kind $g(\mathcal{E}_0) h(\mathcal{E}_0 + \mathcal{E}_1) k(\mathcal{E}_1)$ remain in the final expressions of the second order, which is used in Sec. 5.3.1. You can obtain a full, explanatory step-by-step calculation of the entire second order contribution to the lattice thermal conductivity together with all contributing diagrams, upon request (126).

K

EXCLUDED DIAGRAMS

Three types of diagrams are excluded before they are transferred to terms: Diagrams that contain sub-diagrams that are already included via Dyson's equation for the propagator are excluded, see Fig. K.1. Another type of diagram that is not included, is a disconnected diagram, as no energy can flow through it, see Fig. K.2. The third excluded diagram type are those that contain equal-time $\widehat{P}\widehat{U}$ propagators, see Fig. K.3. In terms of Matsubara sums, this diagram is proportional to

$$I = \sum_E \mathcal{G}^{\widehat{P}\widehat{U}}(E), \tag{K.1}$$

but the sum can be taken for negative E as well - which must be identical, but is at the same time $-I$ by the symmetry of $\mathcal{G}^{\widehat{P}\widehat{U}}$, and so $I = 0$, which is why the entire diagram has no contribution.

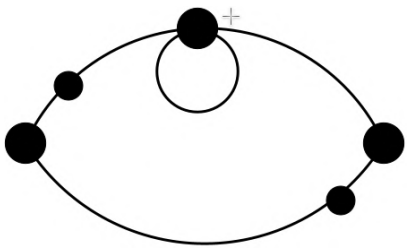

Figure K.1: A diagram that contains a sub-diagram that is already included in the propagator. The smaller bubble is already contained in the propagator line on top, so this diagram does not need to be included in the expansion anymore.

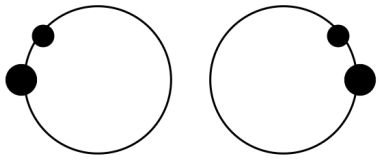

Figure K.2: A disconnected diagram is a diagram where not all vertices can be reached from all other vertices by travelling over connecting propagators.

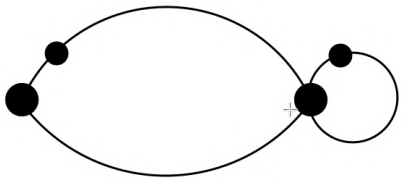

Figure K.3: A diagram that contains a vanishing equal-time $\widehat{P}\widehat{U}$ contraction (the right bubble).

L

CONSTANT IN $\mathcal{G}^{\widehat{P}\widehat{P}}$

Recall the relations of the propagators:

$$\mathcal{G}^{r/a,\widehat{P}\widehat{P}}_{\mathbf{q},\nu,\nu'}(\mathcal{E}) = \frac{\mathcal{E}^2}{\hbar^2}\mathcal{G}^{r/a}_{\mathbf{q},\nu,\nu'}(\mathcal{E}) - 2\omega_{\mathbf{q},\nu}\delta_{\nu,\nu'}.$$

For the lattice thermal conductivity κ^{ij} the constant contribution $-2\omega_{\mathbf{q},\nu}\delta_{\nu,\nu'}$ in $\mathcal{G}^{\widehat{P}\widehat{P}}$ can safely be ignored. I will reason here for this: Consider we just created terms from diagrams. There are four options how many $\mathcal{G}^{\widehat{P}\widehat{P}}$-objects appear in a term, namely up to three (as there are at most $6\widehat{P}$ to contract).

If there are no $\mathcal{G}^{\widehat{P}\widehat{P}}$ objects, the constant cannot matter, of course.

If there is one $\mathcal{G}^{\widehat{P}\widehat{P}}$, the Feynman rules can be applied in such a way, that only this $\mathcal{G}^{\widehat{P}\widehat{P}}$-object depends on the argument of $\Pi^{ij}_M(E)$. Then Eq. (2.12) is applied to this object and the Matsubara summation is performed. Then there are two cases to consider: First, the residue operation removed the denominator that originally belonged to the $\mathcal{G}^{\widehat{P}\widehat{P}}$. Then, the corresponding spectral density has no denominator to apply Eq. (4.23), and the contribution does not contain any $\mathcal{G}^{\widehat{P}\widehat{P}}$ in the end. Secondly, if the denominator of the spectral density remained untouched by the Matsubara summation, the imaginary part operation will remove the denominator, as it is the only object dependent on the argument of $\Pi^{ij}_r(\mathcal{E})$. This means, for terms with one $\mathcal{G}^{\widehat{P}\widehat{P}}$, the constant contribution does not matter.

For two $\mathcal{G}^{\widehat{P}\widehat{P}}$ objects the constant is also irrelevant: In order to have two $\mathcal{G}^{\widehat{P}\widehat{P}}$, at least one contribution $\widehat{\mathbf{J}}^3$ is necessary. Now, if there is one $\widehat{\mathbf{J}}^3$, there can be at most two $\mathcal{G}^{\widehat{P}\widehat{P}}$ objects, where one of them is the only object dependent on a Matsubara energy E_i. After Eq. (2.12) has been applied, the Matsubara summation must remove the corresponding denominator, according to Eq. (4.17). Therefore no reintegration takes place, and a spectral density occurs in the final term. For the other $\mathcal{G}^{\widehat{P}\widehat{P}}$ object, the reasoning of above applies. If one evaluates the expectation value $\langle\widehat{\mathbf{J}}^3(\tau)\widehat{\mathbf{J}}^3(\tau')\rangle$, there cannot be two $\mathcal{G}^{\widehat{P}\widehat{P}}(\tau-\tau')$, because the third $\widehat{P}$-pair would contract with a self-energy contribution. This is already included in the propagator itself, and therefore discarded.

For the term with three $\mathcal{G}^{\widehat{P}\widehat{P}}$ objects, either one or three connect the two vertices. In the case of one, the reasoning for one and two $\mathcal{G}^{\widehat{P}\widehat{P}}$ objects applies. If there are three connecting $\mathcal{G}^{\widehat{P}\widehat{P}}$, there is only one diagram, shown in Fig. L.1. Here, the constant contribution does not matter either, because the two Matsubara summations remove two

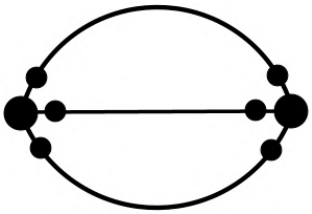

Figure L.1: Diagram with three $\mathcal{G}^{\widehat{P}\widehat{P}}$ propagators.

denominators, and the imaginary part operation takes the last. So there are no denominators left to reintegrate.

In total, the constant contribution of $\mathcal{G}^{\widehat{P}\widehat{P}}$ cannot contribute to κ^{ij}.

M

NORMAL FORM OF A TERM

Even though the precise definition of the normal form does not affect the results of the calculation, the normal form is listed here to rule out any questions on what is done in the CAS system, described in Sec. 4.

$$\begin{aligned}\frac{1}{\hbar^4 N_p^2 \Omega_c^2} \int_{\mathbb{R}} d\mathcal{E} \sum_{\{\mathbf{q}\nu\}} &(-144\mathcal{E}_1 \pi(\mathcal{E}_0+\mathcal{E}_1))\, J_1^i(\mathbf{q}_0,\nu_0;-\mathbf{q}_0,\nu_1)\times \\ &J_1^j(\mathbf{q}_0+\mathbf{q}_1,\nu_2;-\mathbf{q}_0-\mathbf{q}_1,\nu_3)\times \\ &v^3(\mathbf{q}_0,\nu_4;\mathbf{q}_1,\nu_5;-\mathbf{q}_0-\mathbf{q}_1,\nu_6)\times \\ &v^3(\mathbf{q}_0+\mathbf{q}_1,\nu_7;-\mathbf{q}_1,\nu_8;-\mathbf{q}_0,\nu_9)\times \\ &\mathcal{S}_{\mathbf{q}_1,\nu_1,\nu_5}(\mathcal{E}_1)\mathcal{S}_{\mathbf{q}_1,\nu_8,\nu_0}(\mathcal{E}_1)\times \\ &\mathcal{S}_{\mathbf{q}_0,\nu_9,\nu_4}(\mathcal{E}_0)n_B^{(1)}(\mathcal{E}_1)n_B(\mathcal{E}_0)\times \\ &\mathcal{G}_{\mathbf{q}_0+\mathbf{q}_1,\nu_3,\nu_7}(\mathcal{E}_0+\mathcal{E}_1)\times \\ &\mathcal{G}_{\mathbf{q}_0+\mathbf{q}_1,\nu_6,\nu_2}(\mathcal{E}_0+\mathcal{E}_1). \end{aligned} \tag{M.1}$$

The normal form is constructed from the order relations of all contributing quantities, the spectral densities $\mathcal{S}$, phonon propagators $\mathcal{G}$, vertices V and J and occupation functions. The first thing, that all quantities share, are their arguments. Arguments are compared by comparing the variables and prefactors used in them. I arbitrarily define

$$\begin{aligned} &\mathcal{E}_0 < \mathcal{E}_1, \\ -\mathbf{q}_1 < 0\mathbf{q}_1 < &+\mathbf{q}_1. \end{aligned} \tag{M.2}$$

This does not mean anything for the numerical calculation and is only a symbolic comparison within the CAS. The arguments can then be compared element-wise. If two arguments can be compared like this, the larger one is written on the left. For vertices, additionally, the order relation of the operators $\hat{P}$ and $\hat{U}$ is taken into account and dominant over the argument order, *i.e.*

$$J^{\hat{U}\hat{P}} < J^{\hat{P}\hat{U}} \tag{M.3}$$

no matter what the argument is. Indices are also compared element-wise by comparing the strings of the variables in the sense of `Python`'s default `__lt__` for strings, but are dominated by both other `__lt__`'s. An occupation with a derivative is always larger than one without a derivative. As all lists in the term objects can be compared, the terms can be compared by element-wise comparison of these list. The

prefactor does not matter for the term-'<'. To obtain the normal form, every renaming of the integration energies and momenta is tested and the smallest term in the sense of '<' is chosen as the normal form of the term.

N

CALCULATION PARAMETERS AND RESULTS

This section aims at tabulating reproducible results for the calculations of the thermal conductivity. All calculations, where the DFT functional has not been named explicitly, have been done with the PBEsol implementation of `FHI-aims`. The force models for the materials can be found in table N.2, the lattice vectors and the nuclei positions for each material in its own table, and are all fully relaxed using the BFGS implementation of `FHI-aims`. The general calculation parameters are in tables N.3, N.4 and N.5.

Table N.1: Calculation parameters for the electronic structure. All calculations have been performed with "light" atom settings of FHI-aims. Other parameters always had the same value, for all DFT calculations: *sc_acc_forces* was set to 10^{-6}, *sc_acc_rho* was set to 10^{-4} and *sc_init_iter* was set to 10. The version of FHI-aims was 12/24/2017. If "Zora?" is true, the parameter "relativistic" was set to "atomic_zora_scalar", otherwise "relativistic" was not specified in `control.in`. The parameter *k*-grid corresponds to the setting of k_grid in the `control.in` file. All these specifications are for the supercell calculations.

	Zora?	*k*-grid
PbTe	yes	2x2x2
Bi_2Te_3	yes	2x2x2
SnSe	yes	3x3x3
KF	no	3x3x3
MgO	no	3x3x3
La_3Te_4	yes	3x3x3
B_4C	no	4x4x4

Table N.2: The force models used for the different calculations in the materials. Distances are in Bohr. $r_c^{(i)}$ is the cutoff radius for the i^{th} order IFCs used in the `ALM` fit. The cutoff radii are in my calculations independent of the atom types. $n_{\text{max}}^{(i)}$ corresponds to the maximum number of interacting atoms included. For PbTe, both the LDA and PBEsol calculations have been performed with the same parameters. N_{SC} is the size of the supercell (in directions according to the definition in Sec. 6), and n_{DFT} is the number of DFT calculations necessary to realize this force model. C3B12 has not been calculated with the possible number of IFCs, because the fit in `ALM` was not possible (as the amount necessary amount of RAM exceeded my resources).

	KF	MgO	PbTe	Bi_2Te_3	SnSe	La_3Te_4	B_4C
$r_c^{(3)}$	11.0	11.0	20.0	11.2	11.2	13.0	11.0
$n_{\text{max}}^{(3)}$	3	3	3	3	3	3	3
$r_c^{(4)}$	11.0	11.0	10.0	5.6	5.6	6.5	5.5
$n_{\text{max}}^{(4)}$	2	2	2	2	2	2	2
N_{SC}	4x4x4	4x4x4	4x4x4	2x4x4	2x3x3	2x2x2	2x2x2
n_{DFT}	191	417	243	536	958	1045	3544

Table N.3: Calculation parameters for the self-energy. All integrations have been performed with the `cuhre` routine with a cubature rule of degree 11. N_{eval} is the maximum number of integrand evaluations used (that was always completely used). n_{max} is the number of the Legendre polynomials used in the expansion, so if $n_{\text{max}} = 300$, P_{300} is the last used polynomial. $N_{\mathbf{q}}$ denotes the size of the $\mathbf{q}$-grid on which the self-energy is computed. Z_κ? says yes, if effective charges (and the dielectric tensor) have been calculated and used to obtain LO-TO splitting. 'Off-d.' is yes, if the DPA has not been used, otherwise it is 'no'. The same setting has then been used for the thermal conductivity calculations in the material. 'Shifts' is true, if the constant part of the self-energy has been calculated. 'SCPT' is true, if self-consistent phonon theory was applied and A2 is set true, if the the second algorithm from Sec. 5.2.6 has been used. The self-energy as calculated here, is used in this same manner for the thermal conductivity calculations.

	KF	MgO	PbTe	Bi_2Te_3	SnSe	La_3Te_4	B_4C
N_{eval}	40000	40000	40000	30000	30000	20000	20000
n_{max}	300	300	300	240	240	240	240
$N_{\mathbf{q}}$	12x12x12	12x12x12	12x12x12	16x16x8	6x12x12	8x8x8	8x8x8
Z_κ?	no	no	yes	no	no	no	no
Off-d.	yes	yes	yes	no	no	no	no
Shifts	yes	yes	yes	yes	no	no	no
SCPT	no	no	yes	yes	no	no	no
A2	no	no	no	yes	no	no	no

Table N.4: Parameters of the BTE calculation for each material, given the self-energy from table N.3. r is the relative error that the CUBA routines tried to achieve. N_{eval} is the number of $\mathbf{q}$-points the integrand is evaluated on. $N_\mathcal{E}$ is the number of energies the integrand is evaluated on for a certain $\mathbf{q}$ point. 'Int' is the integrator from CUBA used in the calculation. 'Pts' gives the number of points the integrand is evaluated at in any iteration. 'RNG' is the random number generator. In the cases used here, only the Sobol quasi-random number generator is used, as implemented in CUBA. 'F' is the flatness parameter used in suave calculations. N_{new} is the number of new evaluations of the integrand used in the suave integration.

	KF	MgO	PbTe	Bi_2Te_3	SnSe	La_3Te_4	B_4C
r	0.05	0.05	0.05	0.05	0.05	0.05	0.05
N_{eval}	30000	30000	30000	30000	30000	30000	30000
$N_\mathcal{E}$	1024	1024	1024	1024	1024	1024	1024
Int	vegas	vegas	vegas	suave	suave	vegas	vegas
Pts	1024	1024	1024	1024	1024	1024	1024
RNG	sobol	sobol	sobol	sobol	sobol	sobol	sobol
F				20	20		
N_{new}				128	128		

Table N.5: Parameters of the BTE correction calculation for each material, given the self-energy from table N.3. r is the relative error that the CUBA routines tried to achieve. N_{eval} is the number of $\mathbf{q}_1, \mathbf{q}_2$ point sets the integrand is evaluated on. $N_\mathcal{E}$ is the number of energies the integrand is evaluated on each axis ($N_\mathcal{E}^2$ evaluations in total) for a certain $\mathbf{q}_1, \mathbf{q}_2$ point set. 'Int' is the integrator from CUBA used in the calculation. 'Pts' gives the number of points the integrand is evaluated at in any iteration. 'RNG' is the random number generator. In the cases used here, only the Sobol quasi-random number generator is used, as implemented in CUBA. 'F' is the flatness parameter used in suave calculations. N_{new} is the number of new evaluations of the integrand used in the suave integration.

	KF	MgO	PbTe	Bi_2Te_3	SnSe	La_3Te_4	B_4C
r	0.3	0.3	0.3	0.3	0.05	0.3	0.3
N_{eval}	100000	100000	100000	100000	30000	8192	8192
$N_\mathcal{E}$	1024	1024	1024	1024	1024	1024	1024
Int	suave	suave	suave	suave	suave	suave	suave
Pts	128	128	128	128	128	128	128
RNG	sobol	sobol	sobol	sobol	sobol	sobol	sobol
F	20	20	20	20	20	20	20
N_{new}	128	128	128	128	128	128	128

Table N.6: Face-centered cubic lattice structure, where d is a constant. x, y and z correspond to the respective components of the vectors. The nuclei in the unit cell are always at $(0,0,0)$ and $(0.5,0.5,0.5)d$.

	x	y	z
a	0	d	d
b	d	0	d
c	d	d	0

Table N.7: Lattice parameters of fcc crystals that calculations have been performed for. In PbTe both LDA and PBEsol were relaxed with the same lattice parameter. The values are given in Å.

Material	d
AgCl	2.73476186
KF	2.65636874
MgO	2.11315
PbTe	3.25685

Table N.8: The lattice vectors of Bi_2Te_3, as used in the calculations. x, y and z correspond to the respective components of the vectors. All values are given in Å. The nuclei positions are given in table N.9.

	x	y	z
a	-2.16132552	-3.74352512	0
b	2.16132592	-3.74352581	0
c	0	-2.4008157	9.94443426

Table N.9: Absolute positions of the nuclei in the Bi_2Te_3 calculations. x, y and z correspond to the respective components of the position. All values are given in Å. The corresponding lattice vectors are given in table N.8.

x	y	z	type
9.36E-06	-4.90170292	7.94414947	Bi
3.72E-06	-4.98614427	2.0002647	Bi
-1.174E-05	-7.37E-06	1.971E-05	Te
2.89E-06	-7.40657749	6.20340789	Te
-3.44E-06	-2.48130123	3.74102677	Te

Table N.10: The lattice vectors of SnSe, as used in the calculations. x, y and z correspond to the respective components of the vectors. All values are given in Å. The nuclei positions are given in table N.11.

	x	y	z
a	11.4314830575263	0	0
b	0	4.17724931369833	0
c	0	0	4.28743757980503

Table N.11: Fractional positions of the nuclei in the SnSe calculations. x, y and z correspond to the respective components of the position. The corresponding lattice vectors are given in table N.10.

x	y	z	type
0.360004252078553	0.25	0.021305888545553	Se
0.139995747921454	0.75	0.521305888545545	Se
0.639995747921447	0.75	0.978694111454433	Se
0.860004252078566	0.25	0.478694111454455	Se
0.119867679287597	0.25	0.072883065159428	Sn
0.380132320712398	0.75	0.572883065159424	Sn
0.880132320712388	0.75	0.927116934840576	Sn
0.619867679287602	0.25	0.427116934840576	Sn

Table N.12: The lattice vectors of La_3Te_4, as used in the calculations. x, y and z correspond to the respective components of the vectors. All values are given in Å. The nuclei positions are given in table N.13.

	x	y	z
a	-4.76385243	4.76385243	4.76385243
b	4.76384012	-4.76384012	4.76384012
c	4.76384459	4.76384459	-4.76384459

Table N.13: Absolute positions of the nuclei in the La_3Te_4 calculations. x, y and z correspond to the respective components of the position. All values are given in Å. The corresponding lattice vectors are given in table N.12.

x	y	z	type
2.38205251	3.57299827	0.0001386	La
7.14589868	1.19112072	0.0001347	La
0.00012757	2.38206353	3.5730441	La
0.00012751	7.14591037	1.19109088	La
3.57301544	0.00013668	2.38205829	La
1.19108991	0.00014141	7.14591019	La
0.73719666	0.73719349	0.73719727	Te
0.73719756	-0.73691473	4.0269169	Te
-0.73693631	4.02692894	0.73720105	Te
4.0269071	0.73719338	-0.73693319	Te
3.11911855	3.1191307	3.1191177	Te
-1.64473213	1.64500631	6.40885234	Te
6.40882757	-1.64471476	1.64499904	Te
1.64498924	6.40884575	-1.644724	Te

Table N.14: The lattice vectors of B_4C, as used in the calculations. x, y and z correspond to the respective components of the vectors. All values are given in Å. The nuclei positions are given in table N.15.

	x	y	z
a	2.81302994	1.6241038	4.02636052
b	-2.81302994	1.6241038	4.02636052
c	0	-3.24822016	4.02637733

Table N.15: Absolute positions of the nuclei in the B_4C calculations. x, y and z correspond to the respective components of the position. All values are given in Å. The corresponding lattice vectors are given in table N.14.

x	y	z	type
-1.39808009	0.80766117	4.34251686	B
0	-1.61390342	4.34252838	B
1.39808009	0.80766117	4.34251686	B
-1.39808089	-0.80672919	7.73707188	B
0	1.61483641	7.73705961	B
1.39808089	-0.80672919	7.73707188	B
-0.91041851	0.52606638	1.3759307	B
0	-1.05081397	1.37596034	B
0.91041851	0.52606638	1.3759307	B
-0.91041863	-0.52513401	10.70365783	B
0	1.05174696	10.70362846	B
0.91041863	-0.52513401	10.70365783	B
0	0.00046561	6.03979512	C
0	0.0004517	4.70596034	C
0	0.00048166	7.37362853	C

Table N.16: Results of the BTE calculations κ_{BTE} and the correction κ_{Corr} in MgO. The uncertainties Δ_{BTE} and Δ_{Corr} stand next to them, with the same units. The uncertainty only includes the uncertainty of the integration as reported by the `CUBA` library, and nothing else. As MgO crystallizes in an fcc structure, the thermal conductivity is isotropic.

T[K]	κ_{BTE} [W/(m K)]	Δ_{BTE}	κ_{Corr} [mW/(m K)]	Δ_{Corr}
300	77.3	1.6	-1	77
600	44.2	0.8	11	28
900	30.8	0.3	3	21
1200	24.8	0.3	-3	13
1500	21.3	0.3	3	9
1800	19.5	0.2	-1	6
2100	17.4	0.2	4	5
2400	16.4	0.2	6	6
2700	15.4	0.2	2	3
3000	14.9	0.2	2	3

Table N.17: Results of the BTE calculations κ_{BTE} and the correction κ_{Corr} in KF. The uncertainties Δ_{BTE} and Δ_{Corr} stand next to them, with the same units. Constant contributions to the self-energy have not been considered in this calculation. The uncertainty only includes the uncertainty of the integration as reported by the `CUBA` library, and nothing else. As KF crystallizes in an fcc structure, the thermal conductivity is isotropic.

T[K]	κ_{BTE} [W/(m K)]	Δ_{BTE}	κ_{Corr} [μW/(m K)]	Δ_{Corr}
100	14.05	0.2	79	41
300	4.82	0.07	9	55
500	3.02	0.04	-0.5	12
700	2.32	0.03	0.05	1
900	1.91	0.03	0.0007	0.09
1100	1.62	0.02	0.002	0.02

Table N.18: Results of the BTE calculations κ_{BTE} and the correction κ_{Corr} in PbTe. All BTE results are in units [W/(m K)], the correction is in units [mW/(m K)]. The superscript refers to the used functional. If a † is displayed, SCPT as described in Sec. 5.2.6 was applied. The uncertainties Δ_{BTE} and Δ_{Corr} stand next to them, with the same units. The uncertainty only includes the uncertainty of the integration as reported by the `CUBA` library, and nothing else. As PbTe crystallizes in an fcc structure, the thermal conductivity is isotropic. At 400K I did not obtain stable phonon bands with SCPT.

T[K]	κ_{BTE}^{PBEsol}	Δ_{BTE}^{PBEsol}	κ_{BTE}^{LDA} †	Δ_{BTE}^{LDA}	κ_{BTE}^{PBEsol} †	Δ_{BTE}^{PBEsol}	κ_{Corr}^{PBEsol} †	Δ_{Corr}^{PBEsol}
100	4.26	0.03	2.74	0.03	4.36	0.04	0.5	1.3
200	2.29	0.02	1.48	0.02	1.98	0.02	0.2	0.9
300	1.61	0.02	0.69	0.01	0.66	0.01	0.9	0.4
400	1.25	0.01						
500	1.034	0.007	0.336	0.009	0.269	0.008	0.6	0.1
600	0.878	0.006	0.212	0.008	0.192	0.007	0.4	0.08
700	0.755	0.006	0.172	0.007	0.176	0.007	0.29	0.05
800	0.660	0.005	0.253	0.008	0.199	0.007	0.9	0.5

Table N.19: Results of the BTE calculations κ_{BTE} in Bi_2Te_3. All BTE results are in units [W/(m K)]. The uncertainties Δ_{BTE} stand next to them, with the same units. SCPT was used to obtain the results, as described in Sec. 5.2.6. The uncertainty only includes the uncertainty of the integration as reported by the `CUBA` library, and nothing else. The superscript denotes the tensor element. The corresponding lattice vectors are tabulated in table N.8.

T[K]	$\kappa^{xx}_{\mathrm{BTE}}$	$\Delta^{xx}_{\mathrm{BTE}}$	$\kappa^{yy}_{\mathrm{BTE}}$	$\Delta^{yy}_{\mathrm{BTE}}$	$\kappa^{zz}_{\mathrm{BTE}}$	$\Delta^{zz}_{\mathrm{BTE}}$
50	2.24	0.03	0.95	0.01	2.58	0.06
150	1.14	0.02	1.096	0.009	1.41	0.03
250	1.01	0.01	0.987	0.02	1.45	0.04
350	0.89	0.01	0.88	0.01	1.41	0.04
500	0.74	0.02	0.81	0.02	1.42	0.04

Table N.20: Results of the correction calculations κ_{Corr} in Bi_2Te_3. All results are in units [10^{-4}W/(m K)]. The uncertainties Δ_{Corr} stand next to them, with the same units. SCPT was used to obtain the results, as described in Sec. 5.2.6. The uncertainty only includes the uncertainty of the integration as reported by the `CUBA` library, and nothing else. The superscript denotes the tensor element. The corresponding lattice vectors are tabulated in table N.8.

T[K]	$\kappa^{xx}_{\mathrm{Corr}}$	$\Delta^{xx}_{\mathrm{Corr}}$	$\kappa^{yy}_{\mathrm{Corr}}$	$\Delta^{yy}_{\mathrm{Corr}}$	$\kappa^{zz}_{\mathrm{Corr}}$	$\Delta^{zz}_{\mathrm{Corr}}$
50	3	17	1	50	2	25
150	3	0.6	4	1	3	1
250	2.8	0.3	1.5	1.4	2.1	0.6
350	3.9	0.5	3	1	3	1
500	2.4	0.3	2	1	2.1	0.8

Table N.21: Results of the BTE calculations κ_{BTE} in SnSe. All BTE results are in units [W/(m K)]. The uncertainties Δ_{BTE} stand next to them, with the same units. Constant contributions to the self-energy have been ignored in these calculations. The uncertainty only includes the uncertainty of the integration as reported by the `CUBA` library, and nothing else. The superscript denotes the tensor element. The corresponding lattice vectors are tabulated in table N.10. As Sn_4Se_4 has orthorhombic symmetry, only the diagonal elements of the thermal conductivity can be non-zero.

T[K]	$\kappa^{xx}_{\mathrm{BTE}}$	$\Delta^{xx}_{\mathrm{BTE}}$	$\kappa^{yy}_{\mathrm{BTE}}$	$\Delta^{yy}_{\mathrm{BTE}}$	$\kappa^{zz}_{\mathrm{BTE}}$	$\Delta^{zz}_{\mathrm{BTE}}$
100	6.3	0.05	2.65	0.1	1.94	0.07
200	3.07	0.04	1.52	0.03	1.08	0.04
300	2.45	0.03	1.13	0.03	0.81	0.03
400	2.14	0.03	0.84	0.02	0.64	0.02
500	1.67	0.01	0.69	0.01	0.55	0.01
600	1.34	0.01	0.56	0.02	0.37	0.01
700	1.28	0.01	0.55	0.02	0.41	0.01
800	0.978	0.007	0.49	0.01	0.35	0.01
900	1.08	0.01	0.44	0.01	0.326	0.008

Table N.22: Results of the correction calculations κ_{Corr} in SnSe. All correction results are in units [mW/(m K)]. The uncertainties Δ_{Corr} stand next to them, with the same units. Constant contributions to the self-energy have been ignored in these calculations. The uncertainty only includes the uncertainty of the integration as reported by the `CUBA` library, and nothing else. The superscript denotes the tensor element. The corresponding lattice vectors are tabulated in table N.10. As Sn_4Se_4 has orthorhombic symmetry, only the diagonal elements of the thermal conductivity can be non-zero.

T[K]	$\kappa^{xx}_{\mathrm{Corr}}$	$\Delta^{xx}_{\mathrm{Corr}}$	$\kappa^{yy}_{\mathrm{Corr}}$	$\Delta^{yy}_{\mathrm{Corr}}$	$\kappa^{zz}_{\mathrm{Corr}}$	$\Delta^{zz}_{\mathrm{Corr}}$
100	2	1	-2	2	-0.2	2
200	0.3	0.3	-0.6	0.5	-0.1	0.3
300	0.05	0.2	-0.09	0.3	-0.02	0.3
400	0.3	0.3	-1.2	0.3	-0.8	0.4
500	0.3	0.2	-0.7	0.3	-1	0.3
600	0.3	0.1	-0.2	0.1	-0.2	0.1
700	0.08	0.07	-0.2	0.2	-0.3	0.2
800	0.46	0.08	-0.2	0.2	-0.3	0.1
900	0.13	0.07	-0.6	0.2	-0.3	0.1

Table N.23: Results of the BTE calculations κ_{BTE} in La_6Te_8. All BTE results are in units [W/(m K)]. The uncertainties Δ_{BTE} stand next to them, with the same units. Constant contributions to the self-energy have been ignored in these calculations. The uncertainty only includes the uncertainty of the integration as reported by the `CUBA` library, and nothing else. The superscript denotes the tensor element. The corresponding lattice vectors are tabulated in table N.12. As lanthanum telluride almost crystallizes in a bcc structure, the diagonal elements of the thermal conductivity are almost identical, which is why I display also the average of them κ_{BTE}. The results of the self-energy calculations in La_3Te_4 seem not to be trustworthy, such that this result can not be considered trustworthy and is presented only for completeness.

T[K]	$\kappa^{xx}_{\mathrm{BTE}}$	$\Delta^{xx}_{\mathrm{BTE}}$	$\kappa^{yy}_{\mathrm{BTE}}$	$\Delta^{yy}_{\mathrm{BTE}}$	$\kappa^{zz}_{\mathrm{BTE}}$	$\Delta^{zz}_{\mathrm{BTE}}$	κ_{BTE}
300	0.118	0.004	0.113	0.003	0.118	0.004	0.116
600	0.044	0.001	0.044	0.001	0.044	0.001	0.044
800	0.03	0.001	0.0298	0.0008	0.0286	0.0008	0.0295
1000	0.0212	0.0007	0.0212	0.0007	0.0210	0.0007	0.0211
1200	0.0153	0.0006	0.0156	0.0006	0.0148	0.0004	0.0152
1400	0.0115	0.0003	0.0123	0.0004	0.0123	0.0004	0.0120
1600	0.0095	0.0004	0.0088	0.0002	0.0085	0.0002	0.0089

Table N.24: Results of the correction calculations κ_{Corr} in La_3Te_4. All correction results are in units [mW/(m K)]. The uncertainties Δ_{Corr} stand next to them, with the same units. Constant contributions to the self-energy have been ignored in these calculations. The uncertainty only includes the uncertainty of the integration as reported by the `CUBA` library, and nothing else. The superscript denotes the tensor element. The corresponding lattice vectors are tabulated in table N.12. The results of the self-energy calculations in La_3Te_4 seem not to be trustworthy, such that this result can not be considered trustworthy and is presented only for completeness.

T[K]	$\kappa^{xx}_{\mathrm{Corr}}$	$\Delta^{xx}_{\mathrm{Corr}}$	$\kappa^{yy}_{\mathrm{Corr}}$	$\Delta^{yy}_{\mathrm{Corr}}$	$\kappa^{zz}_{\mathrm{Corr}}$	$\Delta^{zz}_{\mathrm{Corr}}$
300	0.12	0.02	0.08	0.02	0.12	0.03
600	0.03	0.01	0.08	0.02	0.07	0.03
800	0.031	0.003	0.033	0.006	0.040	0.004
1000	0.018	0.002	0.019	0.004	0.015	0.004
1200	0.012	0.001	0.014	0.002	0.013	0.002
1400	0.011	0.001	0.014	0.002	0.015	0.002
1600	0.004	0.001	0.007	0.001	0.003	0.001

Table N.25: Results of the BTE calculations κ_{BTE} in B_4C. All BTE results are in units [W/(m K)]. The uncertainties Δ_{BTE} stand next to them, with the same units. Constant contributions to the self-energy have been ignored in these calculations. The uncertainty only includes the uncertainty of the integration as reported by the `CUBA` library, and nothing else. The superscript denotes the tensor element. The corresponding lattice vectors are tabulated in table N.14. As measurements would usually not distinguish the lattice directions, I display also the average of the thermal conductivity κ_{BTE}.

T[K]	$\kappa^{xx}_{\mathrm{BTE}}$	$\Delta^{xx}_{\mathrm{BTE}}$	$\kappa^{yy}_{\mathrm{BTE}}$	$\Delta^{yy}_{\mathrm{BTE}}$	$\kappa^{zz}_{\mathrm{BTE}}$	$\Delta^{zz}_{\mathrm{BTE}}$	κ_{BTE}
300	12.7	0.6	12.4	0.5	13.7	0.6	12.9
600	6.2	0.3	6.1	0.2	6.6	0.2	6.3
800	4.9	0.1	5.2	0.2	5.7	0.1	5.3
1000	4.6	0.2	4.2	0.1	5.0	0.2	4.6
1200	3.7	0.1	3.8	0.1	4.2	0.1	3.9
1400	3.16	0.08	3.11	0.09	3.9	0.1	3.39
1600	3.1	0.1	2.8	0.1	3.1	0.1	3.0
1800	2.74	0.09	2.8	0.1	3.4	0.1	2.98
2000	2.7	0.1	2.7	0.1	3.3	0.1	2.9

Table N.26: Results of the correction calculations κ_{Corr} in B_4C. All correction results are in units [mW/(m K)]. The uncertainties Δ_{Corr} stand next to them, with the same units. Constant contributions to the self-energy have been ignored in these calculations. The uncertainty only includes the uncertainty of the integration as reported by the `CUBA` library, and nothing else. The superscript denotes the tensor element. The corresponding lattice vectors are tabulated in table N.14.

T[K]	$\kappa^{xx}_{\mathrm{Corr}}$	$\Delta^{xx}_{\mathrm{Corr}}$	$\kappa^{yy}_{\mathrm{Corr}}$	$\Delta^{yy}_{\mathrm{Corr}}$	$\kappa^{zz}_{\mathrm{Corr}}$	$\Delta^{zz}_{\mathrm{Corr}}$
300	5	2	15	6	21	44
600	2.8	0.8	6	1	7	5
800	5.4	0.6	7	0.8	7	4
1000	5.9	0.6	14	1	15	7
1200	4	1	7	2	16	8
1400	12	1	11	2	33	8
1600	10.2	0.8	9.30	0.09	24	4
1800	11	1	14	2	20	5
2000	11	1	11	1	17	2

O

DENSITY FUNCTIONAL THEORY

DFT is a very effective methodology for modelling materials, that can be used for a wide range of materials. Even though it does not provide an exact solution to the quantum mechanical many-body problem it is especially suited to reliably calculate vibrational properties of materials (87). For simplicity I assume here that the nuclei in the material are clamped at fixed positions. The basic idea of DFT is then based on the Hohenberg-Kohn theorem (120), which states that the ground-state energy of a material is uniquely determined by the electron density in the material, and that the electron density is uniquely determined by the *external* potential that is the sum of the nuclei Coulomb potentials. Hence, the ground-state energy can be interpreted as a functional of the ground-state electron density. The minimization of this functional then finds the ground-state electron density of the inspected material. Unfortunately, the exact functional that has to be minimized is not known, and therefore approximations to this functional have been constructed. More explicitly, the problem boils down to find an exchange-correlation potential V_{xc} in the Kohn-Sham equation (142)

$$\left[-\frac{\nabla^2}{2} + V_n(\mathbf{r}) + V_H(\mathbf{r}) + V_{xc}(\mathbf{r})\right]\phi_i(\mathbf{r}) = E_i\phi_i(\mathbf{r}) \tag{O.1}$$

where V_n is the Coulomb potential of the nuclei, V_H is the Hartree-potential, that is generated by the electrons, ϕ_i is the Kohn-Sham wavefunction and E_i is the Kohn-Sham eigenenergy. This equation has to be solved self-consistently. The wavefunctions and eigenenergies do not have a direct physical meaning.

There are multiple famous approximations to V_{xc}. For this work I used the *local density approximation* (LDA) (35, 215) and the PBEsol functional (216). More accurate approximations are known. In the LDA, V_{xc} is calculated from the local exchange potential, which the homogeneous electron gas would have at the same density. In PBEsol, the gradient of the electron density is also taken into account. Both functionals have been scanned for numerous materials and have proven useful and accurate in many occasions. However, as the thermal conductivity is very sensitive on the IFCs used in the calculation, the choice of the approximation has still significant impact on the final result of the thermal conductivity, see Ref. (294) or Sec. 6.1.

BIBLIOGRAPHY

1. M. Abramowitz, I. A. Stegun, Handbook of mathematical functions (National Bureau of Standards Applied Mathematics series 55, 1965).
2. A. A. Abrikosov, L. P. Gorkov, I. E. Dzyaloshinski, Methods of Quantum Field Theory in Statistical Physics, vol. 40.
3. S. L. Adler, Physical Review **126**, 413 (1962).
4. P. B. Allen, J. L. Feldman, Physical Review B **48**, 12581 (1993).
5. P. B. Allen, J. L. Feldman, J. Fabian, F. Wooten, Philosophical Magazine B **79**, 1715–1731 (1999).
6. A. Altland, B. Simons, Condensed Matter Field Theory (Cambridge University Press, 2010).
7. J. An, A. Subedi, D. J. Singh, Solid State Communications **148**, 417–419 (2008).
8. P. W. Anderson, Science **177**, 393–396 (1972).
9. F. Aryasetiawan, L. Hedin, K. Karlsson, Physical Review Letters **77**, 2268 (1996).
10. M. Asheghi, Y. K. Leung, S. S. Wong, K. E. Goodson, Applied Physics Letters **71**, 1798–1800 (1997).
11. T. Baba, A. Ono, Measurement Science and Technology **12**, 2046 (2001).
12. R. Badeau, R. Boyer, SIAM Journal on Matrix Analysis and Applications **30**, 1008–1021 (2008).
13. M. Balkanski, R. F. Wallis, E. Haro, Physical Review B **28**, 1928 (1983).
14. A. Banik, B. Vishal, S. Perumal, R. Datta, K. Biswas, Energy & Env Sci **9**, 2011–2019 (2016).
15. J. Bardeen, D. Pines, Physical Review **99**, 1140 (1955).
16. S. Baroni, S. De Gironcoli, A. Dal Corso, P. Giannozzi, Rev. Mod. Phys. **73**, 515 (2001).
17. G. Baumgartner, D. E. Bernholdt, D. Cociorva, R. Harrison, S. Hirata, C. C. Lam, M. Nooijen, R. Pitzer, J. Ramanujam, P. Sadayappan, presented at the SC'02: Proceedings of the 2002 ACM/IEEE Conference on Supercomputing, pp. 5–5.
18. M. Beekman, G. S. Nolas, Journal of Materials Chemistry **18**, 842–851 (2008).

19. J. Berntsen, T. O. Espelid, A. Genz, ACM TOMS **17**, 437–451 (1991).
20. C. M. Bhandari, D. M. Rowe, Journal of Physics. C: Solid State Physics **11**, 1787 (1978).
21. V. Blum, R. Gehrke, F. Hanke, P. Havu, V. Havu, X. Ren, K. Reuter, M. Scheffler, Computer Physics Communications **180**, 2175–2196 (2009).
22. I. Bogaert, B. Michiels, J. Fostier, SIAM Journal on Scientific Computing **34**, C83–C101 (2012).
23. M. Born, K. Huang, Dynamical theory of crystal lattices (Clarendon press, 1954).
24. M. Bouchacourt, F. Thevenot, Journal of Materials Science **20**, 1237–1247 (1985).
25. J. P. Boyd, Acta Applicandae Mathematica **56**, 1–98 (1999).
26. E. S. Božin, C. D. Malliakas, P. Souvatzis, T. Proffen, N. A. Spaldin, M. G. Kanatzidis, S. J. L. Billinge, Science **330**, 1660–1663 (2010).
27. S. R. Brown, S. M. Kauzlarich, F. Gascoin, G. J. Snyder, Chemistry of Materials **18**, 1873–1877 (2006).
28. F. Buccioni, J.-N. Lang, J. M. Lindert, P. Maierhöfer, S. Pozzorini, H. Zhang, M. F. Zoller, The European Physical Journal C **79**, 866 (2019).
29. R. E. Caflisch, Acta numerica **7**, 1–49 (1998).
30. T. Caillat, J.-P. Fleurial, A. Borshchevsky, Journal of Physics and Chemistry of Solids **58**, 1119–1125 (1997).
31. G. Caldarelli, M. Simoncelli, N. Marzari, F. Mauri, L. Benfatto, arXiv preprint arXiv:2202.02246 (2022).
32. C. Carbogno, R. Ramprasad, M. Scheffler, Physical Review Letters **118**, 175901 (2017).
33. F. Caruso, F. Giustino, The European Physical Journal B **89**, 238 (2016).
34. H. B. G. Casimir, Reviews of Modern Physics **17**, 343 (1945).
35. D. M. Ceperley, B. J. Alder, Physical Review Letters **45**, 566 (1980).
36. D. J. Chadi, M. L. Cohen, Physical Review B **8**, 5747 (1973).
37. C. Chang, L.-D. Zhao, Materials Today Physics **4**, 50–57 (2018).
38. L. Chaput, Physical Review Letters **110**, 265506 (2013).
39. A. S. Chaves, A. Antonelli, D. T. Larson, E. Kaxiras, Physical Review B **102**, 125116 (2020).
40. J. Che, T. Çağın, W. Deng, W. A. Goddard III, Journal of Chemical Physics **113**, 6888–6900 (2000).

41. G. Chen, Semiconductors and Semimetals **71**, 203 (2001).

42. J. Chen, G. Zhang, B. Li, Physical Letters A **374**, 2392–2396 (2010).

43. Y. Chen, D. Li, J. R. Lukes, A. Majumdar, Journal of Heat Transfer **127**, 1129–1137 (2005).

44. U. Chowdhury, MA thesis, 2010.

45. D.-Y. Chung, L. Iordanidis, K.-S. Choi, M. G. Kanatzidis, Bulletin of the Korean Chemical Society **19**, 1283–1293 (1998).

46. D. Cociorva, J. Wilkins, G. Baumgartner, P. Sadayappan, J. Ramanujam, M. Nooijen, D. Bernholdt, R. Harrison, presented at the International Conference on High-Performance Computing, pp. 237–248.

47. D. Cociorva, G. Baumgartner, C.-C. Lam, P. Sadayappan, J. Ramanujam, M. Nooijen, D. E. Bernholdt, R. Harrison, Acm Sigplan Notices **37**, 177–186 (2002).

48. A. J. Cohen, P. Mori-Sánchez, W. Yang, Chemical Reviews **112**, 289–320 (2012).

49. E. G. D. Cohen, M. H. J. J. Ernst, Physical Letters **5** (1963).

50. R. A. Cowley, Reports on Progress in Physics **31**, 123 (1968).

51. G. Cullen, N. Greiner, G. Heinrich, G. Luisoni, P. Mastrolia, G. Ossola, T. Reiter, F. Tramontano, The European Physical Journal C **72**, 1889 (2012).

52. R. Cuscó, J. H. Edgar, S. Liu, J. Li, L. Artús, Physical Review Letters **124**, 167402 (2020).

53. P. Cvitanović, B. Lautrup, R. B. Pearson, Physical Review D **18**, 1939 (1978).

54. J. Dangić, O. Hellman, S. Fahy, I. Savić, npj Computational Materials **7**, 1–8 (2021).

55. S. R. De Groot, Thermodynamics of irreversible processes (North-Holland Amsterdam, 1951), vol. 336.

56. J. de Boer, G. E. Uhlenbeck, Studies in statistical mechanics (North-Holland, 1962), vol. 1.

57. S. R. de Groot, P. Mazur, Non-Equilibrium Thermodynamics, 1962.

58. A. Debernardi et al., Anharmonic prop. of semiconductors from DFPT (SISSA, 1995).

59. G. Deinzer, M. Schmitt, A. P. Mayer, D. Strauch, Physical Review B **69**, 014304 (2004).

60. O. Delaire, J. Ma, K. Marty, A. F. May, M. A. McGuire, M.-H. Du, D. J. Singh, A. Podlesnyak, G. Ehlers, M. D. Lumsden, et al., Nature Materials **10**, 614–619 (2011).

61. A. Dhar, K. Saito, P. Hänggi, Physical Review E **85**, 011126 (2012).

62. F. J. DiSalvo, Science **285**, 703–706 (1999).

63. J. Dong, O. F. Sankey, G. K. Ramachandran, P. F. McMillan, Journal of Applied Physics **87**, 7726–7734 (2000).

64. D. L. Donoho et al., IEEE Transactions on Information Theory **52**, 1289–1306 (2006).

65. M. S. Dresselhaus, Y. M. Lin, T. Koga, S. B. Cronin, O. Rabin, M. R. Black, G. Dresselhaus, Recent Trends in Thermoelectric Materials Research III **71** (2001).

66. Z. H. Dughaish, Physica B **322**, 205–223 (2002).

67. F. J. Dyson, Physical Review **85**, 631 (1952).

68. H. Eck, PhD thesis, 1995.

69. L. Ercole, A. Marcolongo, P. Umari, S. Baroni, Journal of Low Temperature Physics **185**, 79–86 (2016).

70. I. Errea, B. Rousseau, A. Bergara, Physical Review Letters **106**, 165501 (2011).

71. K. Esfarjani, H. T. Stokes, Physical Review B **77**, 144112 (2008).

72. K. Esfarjani, G. Chen, H. T. Stokes, Physical Review B **84**, 085204 (2011).

73. A. Faghaninia, C. S. Lo, Journal of Physics: Condensed Matter **27**, 125502 (2015).

74. Z. Fan, H. Dong, A. Harju, T. Ala-Nissila, Physical Review B **99**, 064308 (2019).

75. J. Fernandez Troncoso, P. Aguado-Puente, presented at the APS March Meeting Abstracts, vol. 2019, S47.003.

76. M. Fishman, S. R. White, E. M. Stoudenmire, arXiv preprint arXiv:2007.14822 (2020).

77. E. Flenner, L. Wang, G. Szamel, Soft Matter (2020).

78. J. P. Fleurial, L. Gailliard, R. Triboulet, H. Scherrer, S. Scherrer, Journal of Physics and Chemistry of Solids **49**, 1237–1247 (1988).

79. D. R. Fredkin, N. R. Werthamer, Physical Review **138**, A1527 (1965).

80. J. Gao, P. Qi, G. He, Mathematical Problems in Engineering **2016** (2016).

81. A. García, N. Papior, A. Akhtar, E. Artacho, V. Blum, E. Bosoni, P. Brandimarte, M. Brandbyge, J. I. Cerdá, F. Corsetti, et al., Journal of Chemical Physics **152**, 204108 (2020).

82. J. Garg, N. Bonini, B. Kozinsky, N. Marzari, Physical Review Letters **106**, 045901 (2011).

83. A. Genz, R. E. Kass, Journal of Computational and Graphical Statistics **6**, 92–111 (1997).
84. P. Giannozzi, S. Baroni, N. Bonini, M. Calandra, R. Car, C. Cavazzoni, D. Ceresoli, G. L. Chiarotti, M. Cococcioni, I. Dabo, et al., Journal of Physics: Condensed matter **21**, 395502 (2009).
85. P. Giannozzi, O. Baseggio, P. Bonfà, D. Brunato, R. Car, I. Carnimeo, C. Cavazzoni, S. De Gironcoli, P. Delugas, F. Ferrari Ruffino, et al., The Journal of Chemical Physics **152**, 154105 (2020).
86. N. S. Gillis, N. R. Werthamer, Physical Review **167**, 607 (1968).
87. F. Giustino, Materials modelling using density functional theory (Oxford University Press, 2014).
88. F. Giustino, Reviews of Modern Physics **89**, 015003 (2017).
89. G. Goldberg, Physical Review D **32**, 3331 (1985).
90. H. J. Goldsmid, Proceedings of the Physical Society. Section B **69**, 203 (1956).
91. X. Gonze, C. Lee, Physical Review B **55**, 10355 (1997).
92. J. L. Greathouse, M. Daga, presented at the SC'14: Proceedings of the International Conference for High Performance Computing, Networking, Storage and Analysis, pp. 769–780.
93. M. S. Green, The Journal of Chemical Physics **20**, 1281–1295 (1952).
94. M. S. Green, The Journal of Chemical Physics **22**, 398–413 (1954).
95. G. Grimvall, Thermophysical Properties of Materials, ed. by E. P. Wohlfarth (Elsevier Science Publisher BV, 1986).
96. A. Gulans, S. Kontur, C. Meisenbichler, D. Nabok, P. Pavone, S. Rigamonti, S. Sagmeister, U. Werner, C. Draxl, Journal of Physics: Condensed Matter **26**, 363202, (http://stacks.iop.org/0953-8984/26/i=36/a=363202) (2014).
97. G. Haase, M. Liebmann, G. Plank, International Journal of Parallel, Emergent and Distributed Systems **22**, 213–220 (2007).
98. J. Hafner, Journal of Computational Chemistry **29**, 2044–2078 (2008).
99. T. Hahn, Computer Physics Communications **140**, 418–431 (2001).
100. T. Hahn, Computer Physics Communications **168**, 78–95 (2005).
101. T. Hahn, Computer Physics Communications **207**, 341–349 (2016).

102. R. J. Hardy, Physical Review **132**, 168 (1963).

103. R. J. Hardy, R. J. Swenson, W. C. Schieve, Journal of Mathematical Physics **6**, 1741–1748 (1965).

104. V. J. Härkönen, A. J. Karttunen, Physical Review B **93**, 024307 (2016).

105. V. Havu, V. Blum, P. Havu, M. Scheffler, Journal of Computational Physics **228**, 8367–8379 (2009).

106. B. Hay, J. R. Filtz, J. Hameury, L. Rongione, International Journal of Thermophysics **26**, 1883–1898 (2005).

107. Y. He, I. Savić, D. Donadio, G. Galli, Physical Chemistry Chemical Physics **14**, 16209–16222 (2012).

108. L. Hedin, Physical Review **139**, A796 (1965).

109. L. Hedin, Physica Scripta **21**, 477 (1980).

110. L. Hedin, Journal of Physics: Condensed Matter **11**, R489 (1999).

111. P. F. Heiter, S. A. Funken, Bachelor Thesis, Universität Ulm (2010).

112. E. Helfand, Physical Review **119**, 1 (1960).

113. O. Hellman, I. A. Abrikosov, Physical Review B **88**, 144301 (2013).

114. O. Hellman, P. Steneteg, I. A. Abrikosov, S. I. Simak, Physical Review B **87**, 104111 (2013).

115. J. P. Heremans, V. Jovovic, E. S. Toberer, A. Saramat, K. Kurosaki, A. Charoenphakdee, S. Yamanaka, G. J. Snyder, Science **321**, 554–557 (2008).

116. L. D. Hicks, M. S. Dresselhaus, Physical Review B **47**, 12727 (1993).

117. S. Hirata, The Journal of Physical Chemistry A **107**, 9887–9897 (2003).

118. S. Hirata, A. E. Doran, P. J. Knowles, J. V. Ortiz, Journal of Chemical Physics **147**, 044108 (2017).

119. P. D. Hislop, O. Lenoble, Journal of Mathematical Physics **47**, 112106 (2006).

120. P. Hohenberg, W. Kohn, Physical Review **136**, B864 (1964).

121. P. C. Howell, The Journal of Chemical Physics **137**, 2129 (2012).

122. J. Hromkovič, Algorithmics for hard problems (Springer Science & Business Media, 2013).

123. B. L. Huang, M. Kaviany, Physical Review B **77**, 125209 (2008).

124. K. Huang, Statistical mechanics, p. 10.

125. A. Hübner, S. Rigamonti, C. Draxl, arXiv:2210.06854 (2022).

126. A. Hübner, B. Maurer, S. Rigamonti, C. Draxl, Perturbation expansion for the lattice thermal conductivity, 2022.

127. Intel(R) Math Kernel Library 2021 Update 4.0 for Linux*.

128. K. W. Jacobsen, P. Stoltze, J. K. Nørskov, Surface Science **366**, 394–402 (1996).

129. H. A. Jahn, E. Teller, Proceedings of the Royal Society of London A **161**, 220–235 (1937).

130. W. Jeitschko, Metallurgical Transactions **1**, 3159–3162 (1970).

131. J. J. Jorgensen, J. E. Christensen, T. J. Jarvis, G. L. W. Hart, arXiv preprint arXiv:2104.05856 (2021).

132. R. Jozsa, J. Schlienz, Physical Review A **62**, 012301 (2000).

133. P. L. Kapitza, Journal of Physics of the USSR **4**, 181 (1941).

134. H. Kargaran, A. Minuchehr, A. Zolfaghari, AIP Advances **6**, 045101 (2016).

135. B. Kastening, Physical Review E **61**, 3501 (2000).

136. T. Katsura, Physics of the Earth and Planetary Interiors **101**, 73–77 (1997).

137. R. D. King-Smith, D. Vanderbilt, Physical Review B **47**, 1651 (1993).

138. C. Kittel et al., Introduction to solid state physics (Wiley New York, 1976), vol. 8.

139. H. Kleinert, Particles and quantum fields (World Scientific Singapore, 2016).

140. H. Kleinert, A. Pelster, B. Kastening, M. Bachmann, Physical Review E **62**, 1537 (2000).

141. F. Knoop, PhD thesis, 2021.

142. W. Kohn, L. J. Sham, Physical Review **140**, A1133 (1965).

143. P. Konsin, physica status solidi (b) **86**, 57–66 (1978).

144. R. Kubo, Journal of the Physical Society of Japan **12**, 570–586 (1957).

145. R. Kubo, Journal of the Physical Society of Japan **17**, 1100–1120 (1962).

146. R. Kubo, Reports on Progress in Physics **29**, 255 (1966).

147. R. Kubo, M. Yokota, S. Nakajima, Journal of The Physical Society of Japan **12**, 1203–1211 (1957).

148. G. S. Kumar, G. Prasad, R. O. Pohl, Journal of Materials Science **28**, 4261–4272 (1993).

149. A. D. LaLonde, Y. Pei, H. Wang, G. J. Snyder, Materials Today **14**, 526–532 (2011).

150. D. Lacroix, K. Joulain, D. Terris, D. Lemonnier, Applied Physics Letters **89**, 103104 (2006).

151. A. H. Larsen, J. J. Mortensen, J. Blomqvist, I. E. Castelli, R. Christensen, M. Dułak, J. Friis, M. N. Groves, B. Hammer, C. Hargus, et al., Journal of Physics: Condensed Matter **29**, 273002 (2017).

152. M. Lax, Symmetry principles in solid state and molecular physics (Courier Corporation, 2001).

153. S. Lepri, Thermal transport in low dimensions (Springer, 2016), vol. 921.

154. C. W. Li, J. Ma, H. B. Cao, A. F. May, D. L. Abernathy, G. Ehlers, C. Hoffmann, X. Wang, T. Hong, A. Huq, et al., Physical Review B **90**, 214303 (2014).

155. C. W. Li, O. Hellman, J. Ma, A. F. May, H. B. Cao, X. Chen, A. D. Christianson, G. Ehlers, D. J. Singh, B. C. Sales, et al., Physical Review Letters **112**, 175501 (2014).

156. C. W. Li, J. Hong, A. F. May, D. Bansal, S. Chi, T. Hong, G. Ehlers, O. Delaire, Nature Physics **11**, 1063 (2015).

157. D. O. Lindroth, J. Brorsson, E. Fransson, F. Eriksson, A. Palmqvist, P. Erhart, Physical Review B **100**, 045206 (2019).

158. W. Liu, M. Asheghi, Applied Physics Letters **84**, 3819–3821 (2004).

159. L. Lu, W. Yi, D. L. Zhang, Review of Scientific Instruments **72**, 2996–3003 (2001).

160. X. Lu, D. T. Morelli, Y. Xia, F. Zhou, V. Ozolins, H. Chi, X. Zhou, C. Uher, Advanced Energy Materials **3**, 342–348, eprint: https://onlinelibrary.wiley.com/doi/pdf/10.1002/aenm.201200650, (https://onlinelibrary.wiley.com/doi/abs/10.1002/aenm.201200650) (2013).

161. J. M. Luttinger, Physical Review **135**, A1505 (1964).

162. W. Lv, PhD thesis, Georgia Institute of Technology, 2017.

163. W. Lv, A. Henry, New Journal of Physics **18**, 013028 (2016).

164. T. Maehara, K. Murota, SIAM Journal on Matrix Analysis and Applications **32**, 605–620 (2011).

165. G. D. Mahan, Journal of Applied Physics **76**, 4362–4366 (1994).

166. G. D. Mahan, Many-particle physics (Springer Science & Business Media, 2013).

167. G. D. Mahan, J. O. Sofo, Proceedings of the National Academy of Sciences **93**, 7436–7439 (1996).

168. A. A. Maradudin, Journal of The American Chemical Society **86**, 3405–3413 (1964).

169. A. A. Maradudin, A. E. Fein, Physical Review **128**, 2589 (1962).

170. A. A. Maradudin, I. P. Ipatova, Journal of Mathematical Physics **9**, 525–532 (1968).

171. A. A. Maradudin, S. H. Vosko, Reviews of Modern Physics **40**, 1 (1968).

172. A. A. Maradudin, A. E. Fein, G. H. Vineyard, physica status solidi (b) **2**, 1479–1492 (1962).

173. A. Marcolongo, P. Umari, S. Baroni, Nature Physics **12**, 80 (2016).

174. Y. Marechal, The Journal of Chemical Physics **83**, 247–254 (1985).

175. T. Matsubara, Progress of Theoretical Physics **14**, 351–378 (1955).

176. F. Mauri, N. Vast, C. J. Pickard, Physical Review Letters **87**, 085506 (2001).

177. A. F. May, J.-P. Fleurial, G. J. Snyder, Physical Review B **78**, 125205 (2008).

178. S. McConnell, Code complete (Pearson Education, 2004).

179. R. J. Mehta, Y. Zhang, C. Karthik, B. Singh, R. W. Siegel, T. Borca-Tasciuc, G. Ramanath, Nature materials **11**, 233–240 (2012).

180. A. Meurer, C. P. Smith, M. Paprocki, O. Čertík, S. B. Kirpichev, M. Rocklin, A. Kumar, S. Ivanov, J. K. Moore, S. Singh, et al., PeerJ Computer Science **3**, e103 (2017).

181. M. Mikami, R. Funahashi, Journal of Solid State Chemistry **178**, 1670–1674 (2005).

182. S. K. Mishra, S. Satpathy, O. Jepsen, Journal of Physics: Condensed Matter **9**, 461 (1997).

183. K. Momma, F. Izumi, Journal of Applied Crystallography **44**, 1272–1276 (2011).

184. J. Moore, Nature Physics **5**, 378–380 (2009).

185. D. T. Morelli, V. Jovovic, J. P. Heremans, Physical Review Letters **101**, 035901 (2008).

186. D. Morgan, G. Ceder, S. Curtarolo, Measurement Science and Technology **16**, 296 (2004).

187. H. Mori, Physical Review **112**, 1829 (1958).

188. T. Mori, T. Nishimura, Journal of Solid State Chemistry **179**, 2908–2915 (2006).

189. W. J. Morokoff, R. E. Caflisch, Journal of Computational Physics **122**, 218–230 (1995).

190. P. M. Morse, H. Feshbach, Methods of theoretical physics (AAPT, 1954), vol. 22.

191. B. Mortazavi, M. Pötschke, G. Cuniberti, Nanoscale **6**, 3344–3352 (2014).

192. B. Mortazavi, M.-Q. Le, T. Rabczuk, L. F. C. Pereira, Physica E **93**, 202–207 (2017).

193. F. Müller-Plathe, The Journal of chemical physics **106**, 6082–6085 (1997).

194. J. Muscatello, F. Jaeger, O. K. Matar, E. A. Muller, ACS Applied Materials & Interfaces **8**, 12330–12336 (2016).

195. P. Q. Nguyen, D. Stehlé, ACM Transactions on algorithms (TALG) **5**, 1–48 (2009).

196. A. Nieto, arXiv preprint hep-ph/9311210 (1993).

197. W. Ning, H. Du, F. Kong, J. Yang, Y. Han, M. Tian, Y. Zhang, Scientific reports **3**, 1–6 (2013).

198. P. Nogueira, Journal of Computational Physics **105**, 279–289 (1993).

199. G. S. Nolas, D. T. Morelli, T. M. Tritt, Annual Review of Materials Science **29**, 89–116 (1999).

200. G. S. Nolas, M. Beekman, J. Gryko, G. A. Lamberton Jr, T. M. Tritt, P. F. McMillan, Applied Physics Letters **82**, 910–912 (2003).

201. G. S. Nolas, J. Sharp, J. Goldsmid, Thermoelectrics (Springer Science & Business Media, 2013), vol. 45.

202. W. Nolting, Grundkurs Theoretische Physik 6: Statistische Physik (Springer-Verlag, 2007).

203. W. Nolting, Grundkurs Theoretische Physik 5: Quantenmechanik Teil 2 (Springer-Verlag, 2013).

204. W. Nolting, Grundkurs Theoretische Physik 7: Viel-Teilchen-Theorie (Springer-Verlag, 2014).

205. P. Nozieres, D. Pines, Perseus Books Publishing, LLC (Cambridge, 1966) (1966).

206. L. Onsager, Physical Review **37**, 405 (1931).

207. H. H. Panjer, S. Wang, ASTIN Bulletin: The Journal of the IAA **23**, 227–258 (1993).

208. W. J. Parker, R. J. Jenkins, C. P. Butler, G. L. Abbott, Journal of Applied Physics **32**, 1679–1684 (1961).

209. K. Parlinski, Z. Q. Li, Y. Kawazoe, Physical Review Letters **78**, 4063 (1997).

210. R. H. Parmenter, Physical Review **100**, 573 (1955).

211. R. G. Parr, Annual Review of Physical Chemistry **34**, 631–656 (1983).

212. L. Paulatto, I. Errea, M. Calandra, F. Mauri, Physical Review B **91**, 054304 (2015).

213. Y. Pei, A. LaLonde, S. Iwanaga, G. J. Snyder, Energy & Environmental Science **4**, 2085–2089 (2011).

214. R. Peierls, Annalen der Physik **395**, 1055–1101 (1929).

215. J. P. Perdew, A. Zunger, Physical Review B **23**, 5048 (1981).

216. J. P. Perdew, A. Ruzsinszky, G. I. Csonka, O. A. Vydrov, G. E. Scuseria, L. A. Constantin, X. Zhou, K. Burke, Physical Review Letters **100**, 136406 (2008).

217. A. Pereverzev, T. Sewell, Physical Review B **97**, 104308 (2018).

218. M. E. Peskin, D. V. Schroeder, An Introduction to Quantum Field Theory (Westview Press, 1995).

219. R. N. C. Pfeifer, J. Haegeman, F. Verstraete, Physical Review E **90**, 033315 (2014).

220. D. Pines, Theory of Quantum Liquids: Normal Fermi Liquids (CRC Press, 2018).

221. S. Pisana, M. Lazzeri, C. Casiraghi, K. S. Novoselov, A. K. Geim, A. C. Ferrari, F. Mauri, Nature Materials **6**, 198–201 (2007).

222. N. M. Plakida, T. Siklós, physica status solidi (b) **33**, 103–112 (1969).

223. V. Pokorný, V. Janiš, Journal of Physics: Condensed Matter **25**, 175502 (2013).

224. B. Poudel, Q. Hao, Y. Ma, Y. Lan, A. Minnich, B. Yu, X. Yan, D. Wang, A. Muto, D. Vashaee, et al., Science **320**, 634–638 (2008).

225. N. Prasad, K. Balasubramanian, Journal of Raman Spectroscopy **47**, 1266–1270 (2016).

226. W. H. Press, G. R. Farrar, Computers in Physics **4**, 190–195 (1990).

227. I. Prigogine, G. Severne, Physical Letters **6** (1963).

228. M. Puligheddu, Y. Xia, M. Chan, G. Galli, Physical Review Materials **3**, 085401 (2019).

229. G. Qin, Z. Qin, H. Wang, M. Hu, Physical Review B **95**, 195416 (2017).

230. J. Ranninger, Physical Review **140**, A2031 (1965).

231. J. Ranninger, Annals of Physics **45**, 452–478 (1967).

232. H. Rauh, R. Geick, H. Kohler, N. Nucker, N. Lehner, Journal of Physics C: Solid State Physics **14**, 2705 (1981).

233. Y. I. Ravich, B. A. Efimova, I. A. Smirnov, Semiconducting lead chalcogenides, 1970.

234. N. K. Ravichandran, D. Broido, Physical Review X **10**, 021063 (2020).

235. R. Resta, Reviews of Modern Physics **66**, 899 (1994).

236. R. Resta, D. Vanderbilt, in Physics of Ferroelectrics (Springer, 2007), pp. 31–68.

237. J.-F. Richard, W. Zhang, Journal of Econometrics **141**, 1385–1411 (2007).

238. A. H. Romero, E. K. U. Gross, M. J. Verstraete, O. Hellman, Physical Review B **91**, 214310 (2015).

239. J. M. Rondinelli, A. S. Eidelson, N. A. Spaldin, Physical Review B **79**, 205119 (2009).

240. S. Roszeitis, B. Feng, H.-P. Martin, A. Michaelis, Journal of The European Ceramic Society **34**, 327–336 (2014).

241. D. M. Rowe, CRC Handbook of Thermoelectrics: Macro to Nano CRC.

242. B. C. Sales, D. Mandrus, B. C. Chakoumakos, V. Keppens, J. R. Thompson, Physical Review B **56**, 15081 (1997).

243. C. B. Satterthwaite, R. W. Ure Jr, Physical Review **108**, 1164 (1957).

244. W. C. Schieve, R. L. Peterson, Physical Review **126**, 1458 (1962).

245. D. P. Sellan, E. S. Landry, J. E. Turney, A. J. H. McGaughey, C. H. Amon, Physical Review B **81**, 214305 (2010).

246. B. S. Semwal, P. K. Sharma, Physical Review B **5**, 3909 (1972).

247. H. Sevinçli, S. Roche, G. Cuniberti, M. Brandbyge, R. Gutierrez, L. M. Sandonas, Journal of Physics: Condensed Matter **31**, 273003 (2019).

248. H. R. Seyf, L. Yates, T. L. Bougher, S. Graham, B. A. Cola, T. Detchprohm, M.-H. Ji, J. Kim, R. Dupuis, W. Lv, et al., npj Computational Materials **3**, 1–8 (2017).

249. H. R. Seyf, K. Gordiz, F. DeAngelis, A. Henry, Journal of Applied Physics **125**, 081101 (2019).

250. A. Shakouri, Annual Review of Materials Research **41**, 399–431 (2011).

251. L. J. Sham, Physical Review **139**, A1189 (1965).

252. L. J. Sham, Physical Review **156**, 494 (1967).

253. L. J. Sham, Physical Review **163**, 401 (1967).

254. L. J. Sham, J. M. Ziman, in Solid State Physics (Elsevier, 1963), vol. 15, pp. 221–298.

255. T. Shiga, J. Shiomi, J. Ma, O. Delaire, T. Radzynski, A. Lusakowski, K. Esfarjani, G. Chen, Physical Review B **85**, 155203 (2012).

256. M. Simoncelli, N. Marzari, F. Mauri, Nature Physics **15**, 809–813 (2019).

257. G. J. Snyder, E. S. Toberer, in Materials for Sustainable Energy (World Scientific, 2011), pp. 101–110.

258. F. Song-Ke, L. Shuang-Ming, F. Heng-Zhi, Chinese Physics B **23**, 086301 (2014).

259. J. R. Sootsman, R. J. Pcionek, H. Kong, C. Uher, M. G. Kanatzidis, Chemistry of Materials **18**, 4993–4995 (2006).

260. J. R. Sootsman, D. Y. Chung, M. G. Kanatzidis, Angewandte Chemie International Edition **48**, 8616–8639 (2009).

261. A. C. Sparavigna, Mechanics, Materials Science & Engineering Journal **2016**, 34–45 (2016).

262. A. Stan, P. Romaniello, S. Rigamonti, L. Reining, J. A. Berger, New Journal of Physics **17**, 093045 (2015).

263. H. T. Stokes, B. J. Campbell, R. Cordes, Acta Crystallographica A **69**, 388–395 (2013).

264. M. Stordeur, M. Stölzer, H. Sobotta, V. Riede, physica status solidi (b) **150**, 165–176 (1988).

265. M. D. Sturge, in Solid state physics (Elsevier, 1968), vol. 20, pp. 91–211.

266. E. T. Swartz, R. O. Pohl, Reviews of Modern Physics **61**, 605 (1989).

267. T. Tadano, S. Tsuneyuki, Physical Review B **92**, 054301 (2015).

268. T. Tadano, Y. Gohda, S. Tsuneyuki, Journal of Physics: Condensed Matter **26**, 225402 (2014).

269. M. Tanabashi, K. Hagiwara, K. Hikasa, K. Nakamura, Y. Sumino, F. Takahashi, J. Tanaka, K. Agashe, G. Aielli, C. Amsler, et al., Physical Review D **98**, 030001 (2018).

270. P. L. Taylor, Quantum approach to the solid state (New Jersey, Prentice-Hall, 1970).

271. A. Togo, phonopy manual, 2013.

272. A. Togo, I. Tanaka, Scripta Materialia **108**, 1–5 (2015).

273. A. Togo, I. Tanaka, arXiv preprint arXiv:1808.01590 (2018).

274. A. Togo, F. Oba, I. Tanaka, Physical Review B **78**, 134106 (2008).

275. M. Troppenz, S. Rigamonti, C. Draxl, Chemistry of Materials **29**, 2414–2424 (2017).

276. C. Uher, in Semiconductors and semimetals (Elsevier, 2001), vol. 69, pp. 139–253.

277. C. Uher, J. Yang, S. Hu, D. T. Morelli, G. P. Meisner, Physical Review B **59**, 8615 (1999).

278. D. Vashaee, A. Shakouri, Physical Review Letters **92**, 106103 (2004).

279. R. Venkatasubramanian, Semiconductors and semimetals **71**, 175–201 (2001).

280. R. Viennois, K. Niedziolka, P. Jund, Physical Review B **88**, 174302 (2013).

281. S. Volz, Thermal nanosystems and nanomaterials (Springer Science & Business Media, 2009), vol. 118.

282. C. T. Walker, R. O. Pohl, Physical Review **131**, 1433 (1963).

283. S. Wang, Z. Wang, W. Setyawan, N. Mingo, S. Curtarolo, Physical Review X **1**, 021012 (2011).

284. X. Wang, K.-T. Fang, Journal of Complexity **19**, 101–124 (2003).

285. Y. Wang, J. J. Wang, W. Y. Wang, Z. G. Mei, S. L. Shang, L. Q. Chen, Z. K. Liu, Journal of Physics: Condensed Matter **22**, 202201 (2010).

286. Y. Wang, S.-L. Shang, H. Fang, Z.-K. Liu, L.-Q. Chen, npj Computational Materials **2**, 1–10 (2016).

287. A. Ward, D. A. Broido, D. A. Stewart, G. Deinzer, Physical Review B **80**, 125203 (2009).

288. H. Werheit, Materials Science and Engineering: B **29**, 228–232 (1995).

289. N. R. Werthamer, Physical Review B **1**, 572 (1970).

290. I. T. Witting, T. C. Chasapis, F. Ricci, M. Peters, N. A. Heinz, G. Hautier, G. J. Snyder, Advanced Electronic Materials **5**, 1800904 (2019).

291. Y. Xia, Applied Physics Letters **113**, 073901 (2018).

292. B. Xiao, H. Wang, S.-H. Zhu, Computer Physics Communications **184**, 1966–1972 (2013).

293. H. Xie, T. Ouyang, E. Germaneau, G. Qin, M. Hu, H. Bao, Physical Review B **93**, 075404 (2016).

294. H. Xie, X. Gu, H. Bao, Computational Materials Science **138**, 368–376 (2017).

295. L. Xue, PhD thesis, Rensselaer Polytechnic Institute, 2004.

296. M. Zebarjadi, K. Esfarjani, A. Shakouri, J.-H. Bahk, Z. Bian, G. Zeng, J. Bowers, H. Lu, J. Zide, A. Gossard, Applied Physics Letters **94**, 202105 (2009).

297. M. Zebarjadi, K. Esfarjani, M. S. Dresselhaus, Z. F. Ren, G. Chen, Energy & Environmental Science **5**, 5147–5162 (2012).

298. Y. Zeng, J. Dong, Physical Review B **99**, 014306 (2019).

299. C. Zhang, L. Sun, Z. Chen, X. Zhou, Q. Wu, W. Yi, J. Guo, X. Dong, Z. Zhao, Physical Review B **83**, 140504 (2011).

300. L.-C. Zhang, G. Qin, W.-Z. Fang, H.-J. Cui, Q.-R. Zheng, Q.-B. Yan, G. Su, Scientific Reports **6**, 19830 (2016).

301. L.-D. Zhao, S.-H. Lo, Y. Zhang, H. Sun, G. Tan, C. Uher, C. Wolverton, V. P. Dravid, M. G. Kanatzidis, Nature **508**, 373 (2014).

302. F. Zhou, W. Nielson, Y. Xia, V. Ozoliņš, et al., Physical Review Letters **113**, 185501 (2014).

303. J. M. Ziman, Electrons and phonons: the theory of transport phenomena in solids (Oxford university press, 2001).

304. R. Zwanzig, The Journal of Chemical Physics **40**, 2527–2533 (1964).

305. R. Zwanzig, Annual Review of Physical Chemistry **16**, 67–102 (1965).

EIGENSTÄNDIGKEITSERKLÄRUNG

Ich erkläre hiermit ausdrücklich, dass es sich bei der von mir eingereichten schriftlichen Arbeit mit dem Titel

"Many-body theory for the lattice thermal conductivity of crystalline thermoelectrics"

um eine von mir erstmalig, selbstständig und ohne fremde Hilfe verfasste Arbeit handelt.

Ich erkläre ausdrücklich, dass ich sämtliche in der oben genannten Arbeit verwendeten fremden Quellen, auch aus dem Internet (einschließlich Tabellen, Grafiken u. Ä.) als solche kenntlich gemacht habe. Insbesondere bestätige ich, dass ich ausnahmslos sowohl bei wörtlich übernommenen Aussagen bzw. unverändert übernommenen Tabellen, Grafiken u. Ä. (Zitaten) als auch bei in eigenen Worten wiedergegebenen Aussagen bzw. von mir abgewandelten Tabellen, Grafiken u. Ä. anderer Autorinnen und Autoren (Paraphrasen) die Quelle angegeben habe.

Mir ist bewusst, dass Verstöße gegen die Grundsätze der Selbstständigkeit als Täuschung betrachtet und entsprechend der fachspezifischen Prüfungsordnung und/oder der Allgemeinen Satzung für Studien- und Prüfungsangelegenheiten der HU (ASSP) bzw. der Fächerübergreifenden Satzung zur Regelung von Zulassung, Studium und Prüfung der Humboldt-Universität (ZSP-HU) geahndet werden.

Berlin, Dezember 2022

Axel Hübner

COLOPHON

This document was typeset using the typographical look-and-feel `classicthesis` developed by André Miede and Ivo Pletikosić. The style was inspired by Robert Bringhurst's seminal book on typography "The Elements of Typographic Style".